1-1-2002

Investigations into the mechanical and physical behavior of thermoplastic elastomers.

Kathryn J. Wright
University of Massachusetts Amherst

INVESTIGATIONS INTO THE MECHANICAL AND PHYSICAL BEHAVIOR OF THERMOPLASTIC ELASTOMERS

A Dissertation Presented

By

KATHRYN J. WRIGHT

Submitted to the Graduate School of the
University of Massachusetts Amherst in partial fulfillment
Of the requirements for the degree of

DOCTOR OF PHILOSOPHY

May 2002

Polymer Science & Engineering

INVESTIGATIONS INTO THE MECHANICAL AND PHYSICAL BEHAVIOR OF THERMOPLASTIC ELASTOMERS

A Dissertation Presented

By

KATHRYN J. WRIGHT

Approved as to style and content by:

Alan J. Lesser, Chair

E. Bryan Coughlin, Member

James A. Donovan, Member

Thomas J. McCarthy, Department Head
Polymer Science & Engineering

DEDICATION

To my patient and loving husband and my parents who taught me the value of education.

ACKNOWLEDGMENTS

This dissertation would not have been possible without the help and encouragement of many people. First I would like to thank my husband, Michael, for his patience and love and for the many discussions regarding my research and its issues. I value his opinion not only as a scientist but also as a soul mate. My parents not only taught me the importance of gaining a solid education but also taught me to set high standards for myself and to not accept anything less. For this I am grateful because it has helped make me the person that I am. I also thank them for their continued encouragement and interest in everything that I do. The Ward family and the Wright family have also been of great encouragement.

Professor Alan Lesser has been the best advisor I could have asked for. He was available when I needed direction but allowed me enough freedom to explore and become a researcher in my own right. His constant jovial attitude always brings a smile to my face, and I always knew that when anything went wrong I could discuss it with him. My other committee members have been a delight to work with and a pleasure to know. I thank both Professor Bryan Coughlin and Professor James Donovan for their input and attention to detail. I must acknowledge the ExxonMobil Chemical Company and Advanced Elastomer Systems, for they provided funding and materials for this research. I would like to especially thank Dr. Andrew Peacock, Dr. Andy Tsou, Dr. Michael Lyon, and Dr. Maria Ellul for their help and guidance throughout the work.

One of the things that really attracted me to the PSE department when I was looking at graduate programs was the shared facilities. I certainly made use of them

through out my studies. In doing so I was able to interface with so many graduate students and learn something about their research as well. Many of them were instrumental in training me on equipment and to all of them I am grateful. I have so many fond memories of working in the Lesser research group. I must thank all of my fellow group members both past and present. It was a pleasure to work closely with Kishore Indukuri during my last year and a half on the modeling study. Of course there are several people with whom I became very close friends: Adam Zerda, Terry Caskey, and Jeremy Morin. Adam has been a terrific person to share my office with. Terry always made conversation interesting. Jeremy made the 30 minute ride to school each day a pleasure. Adam, Terry, and I have been together almost everyday of each week since we joined the Lesser group. I will miss them greatly but am sure we will stay in touch. Many thanks should be given to John Domian without whom I may never have rebuilt the Dynastat. Lou Raboin provided a great deal of insight in the microscopy studies, as did Alan Waddon in the initial x-ray analysis. Eileen Besse, Sophie Hsu, Ann Brainerd, and Jen Farner were all such a pleasure to be around. I thank each of them for all their hard work; without them graduate students would never finish on time. Finally, I would like to thank my Lord and Savior, Jesus Christ, without whom none of this would have been possible.

ABSTRACT

INVESTIGATIONS INTO THE MECHANICAL AND PHYSICAL BEHAVIOR OF THERMOPLASTIC ELASTOMERS

MAY 2002

KATHRYN J. WRIGHT, B.S., UNIVERISTY OF FLORIDA

M.S., UNIVERSITY OF MASSACHUSETTS

Ph.D., UNIVERSITY OF MASSACHUSETTS AMHERST

Directed by: Professor Alan J. Lesser

This thesis describes investigations into the physical and mechanical characteristics of two commercial thermoplastic elastomer (TPE) systems. Both systems studied exhibit elastomeric behavior similar to more traditional crosslinked elastomers; however, in these TPEs non-conventional polymer architectures and morphologies are used to produce their elastomeric behavior. The two TPEs of interest are ethylene-propylene random copolymers and dynamically vulcanized blends of ethylene-propylene-diene monomer (EPDM) and isotactic polypropylene (iPP). Very few studies have examined the mechanical behavior of these materials in terms of their composition and morphology. As such, the primary goal of this research is to both qualitatively and quantitatively understand the influence of composition and morphology on mechanical behavior. In additional very little information is available that compares their performance with that of crosslinked elastomers. As a result, the secondary goal is to qualitatively compare the mechanical responses of these TPEs with that of their more traditional counterparts.

The ethylene-propylene copolymers studied have very high comonomer contents and exhibit slow crystallization kinetics. Their morphology consists of nanoscale crystallites embedded in an amorphous rubbery matrix. These crystallites act as physical crosslinks that allow for elasticity. Slow crystallization causes subsequent changes in mechanical behavior that take place over days and even weeks. Physical responses (*e.g.*, density, crystallization kinetics, and crystal structure) of five copolymer compositions are investigated. Mechanical responses (*e.g.*, stiffness, ductility, yielding, and reversibility) are also examined. Finally, the influence of morphology on deformation is studied using *in situ* analytical techniques.

The EPDM/iPP blends are dynamically vulcanized which produces a complex morphology consisting of chemically crosslinked EPDM domains embedded within a semicrystalline iPP matrix. Six compositions are investigated as a function of three parameters: major volume fraction, iPP molecular weight, and EPDM cure state. The influence of these parameters on morphology and resulting mechanical behavior is examined. This work culminates in the development of a morphological model to describe the steady-state reversibility of these EPDM/iPP blends. The model is then evaluated in terms of composition and cure state.

TABLE OF CONTENTS

LIST OF TABLES

Table

page

LIST OF FIGURES

Figure

GLOSSARY OF TERMS

α – constraint factor

β – angle between transition moment of vibrational mode and chain axis

Δh_f – theoretical heat of fusion of a crystal

δ – phase angle

ε – axial strain of a strut

ε' – elastic strain with respect to previous extension

ε_a – dynamic strain amplitude

ε_f – maximum previous strain

ε_o – characteristic strain

γ – shear strain

γ_e – theoretical surface energy of a crystal

λ_i – extension or stretch ratios

ϕ – strain energy density function

σ_∞ – far-field stress

σ_a – dynamic stress amplitude

σ_i – principal stresses

σ_y – yield stress

2θ – Bragg angle

θ – strut angle

θ_{cp} – critical angle for plastic hinge formation

θ_{cs} – critical angle for strut yielding

$1/\rho$ -- curvature of strut

$A_{\perp}$ – absorbance with incident radiation polarized perpendicular to draw direction

$A_{||}$ – absorbance with incident radiation polarized parallel to draw direction

AFM – atomic force microscopy

C – iPP concentration

D – dichroic ratio

$d_{\perp}$ – dimension perpendicular to plane responsible for x-ray reflection

DMTA – dynamic mechanical thermal analysis

E – tensile modulus

E' – tensile storage modulus

E'_{∞} – high amplitude storage modulus

E'' – tensile loss modulus

E''_{m} – maximum loss modulus

E'_{o} – low amplitude storage modulus

EPDM – ethylene-propylene-diene monomer terpolymer

F – total force acting of representative volume element

f – Herman's orientation function

F_a – axial force on a strut

FEM – finite element modeling

FTIR – fourier transform infrared spectroscopy

FWHM – full width at high maximum

G –shear modulus

G' – shear storage modulus

HT – high temperature

I – moment of inertia

I_1 – first strain invariant

I_2 – second strain invariant

iPP – isotactic polypropylene

ℓ – strut length

LT – low temperature

M – rotational moment

m – shape parameter

m_e – normalized elastic rotational moment

MFR – melt flow rate

m_p – normalized plastic rotational moment

RPM – revolutions per minute

RVE – representative volume element

S – strut density

SCB – short chain branching

SEM – scanning electron microscopy

T – shear force acting on elastomer

t – strut thickness

$\tan \delta_m$ – maximum tan delta

TEM – transmission electron microscopy

$T_m(\infty)$ – theoretical melting point of an infinite crystal

TPE – thermoplastic elastomer

WAXD – wide angle x-ray diffraction

CHAPTER 1

INTRODUCTION

Over the past century numerous attempts have been published to characterize the mechanical deformation of traditional crosslinked elastomers. Efforts have also been made to understand their morphology in terms of filler/network interactions. While a great deal of progress has been made on phenomenologically characterizing filled crosslinked elastomers, thermoplastic elastomers (TPEs) have emerged on the market. Characterization of the morphology and deformation of two commercial TPE systems is the focus of this thesis. Qualitatively comparing the responses of these TPEs with more traditional crosslinked elastomers is also of interest.

Whether an elastomer is thermoset or thermoplastic, heterogeneity is necessary to enhance strength and improve reversibility while in most cases sacrificing ultimate elongation. Heterogeneity in crosslinked elastomers traditionally consists of particulate filler such as carbon black. Crosslinked elastomers excel in areas such as chemical resistance, heat distortion, and reversibility but lack ease of processability and reusability. Efforts have only recently begun to characterize the relationships between deformation and morphology of TPEs. Heterogeneity is also essential to the mechanical integrity and reversibility of TPEs and can exist at different length scales. In fact this heterogeneity is responsible for their elasticity. A classical TPE architecture consists of a phase separated structure such as immiscible block copolymer segments or crystalline and amorphous domain separation. The mechanical behavior of TPEs is determined by the morphology

of the resulting heterogeneity. The utility of thermoplastic elastomers originates from their physical crosslinks, which are thermally stable at use temperature and reversible at elevated temperatures allowing for processability.

1.1 Thermoplastic Elastomers

New TPEs have emerged on the market over the past three decades. Two of these are the focus of this research. The first class is random ethylene-propylene copolymers. The heterogeneity in these systems consists of crystalline regions embedded in an amorphous rubbery matrix. These crystalline regions evolve with time within several weeks after solidification. This evolving heterogeneity is examined in terms of mechanical behavior. The second class of TPEs consists of dynamically vulcanized blends of ethylene-propylene-diene-monomer (EPDM) terpolymer and isotactic polypropylene (iPP). The process of dynamic vulcanization produces a unique morphology; in these blends, chemically crosslinked EPDM rubber domains are embedded in a continuous semicrystalline iPP matrix. The origins of elasticity and energy dissipation in these systems are examined in terms of composition and morphology.

1.1.1 Ethylene-Propylene Copolymers

Ethylene-propylene random copolymers with various molecular architectures are being considered as a new class of thermoplastic elastomers. They behave as elastomeric materials because their maximum crystallinity is very low (less than 15%), and they are

well above their glass transition temperature (-55°C). Since these copolymers have a high degree of short chain branching and high comonomer content, crystallization is inhibited. Several weeks at ambient conditions are necessary to achieve maximum crystallinity due to their slow crystallization kinetics. This results in the formation of small crystals on the order of nanometers in thickness. These crystals not only serve to reinforce the copolymer but also serve as physical crosslinks contributing to its elastomeric nature.

The composition and architecture not only determine the ultimate crystallinity but also the rate at which this crystallinity is achieved. These materials are relatively new, and in depth crystallization studies of ethylene – α-olefin copolymers have only recently been conducted.[1-11] Ziegler/Natta based copolymers with high comonomer content exhibit bimodal crystallization kinetics.[1,2] This is attributed to the resulting branched architecture of the copolymers. Of the two observed crystallization exotherms, the first occurs at a high temperature (HT) with a relatively large exotherm and the second is depressed to a much lower temperature (LT) with a smaller exotherm. The HT exotherm is attributed to the crystallization of high molecular weight chains with low branching content while the LT exotherm is due to the crystallization of low molecular weight chains with high branching content.[1,2] For these copolymers, molecular segregation occurs so readily that these crystallization kinetics can be observed during nonisothermal conditions. The crystals that form coinciding with the HT exotherm are similar to those of linear low density polyethylene. Wide angle X-ray diffraction (WAXD) experiments show that by introducing short branches into polyethylene via propylene incorporation, unit cell dimensions slightly enlarge to accommodate the additional methyl groups.[12]

Recent studies on the crystallization of ethylene – α-olefin copolymers with relatively large side groups indicate the presence of four copolymer regimes.[10,11] This classification is based on density and in terms of crystal morphology. Copolymers in regime I have densities less than 0.89 g/cc and exhibit bundle-like crystals that can be described as fringed micelles. No spherulites are present in this regime and very low degrees of crystallinity are observed. No effects of cooling rate are observed and it is thought that these copolymers anneal at room temperature. Copolymers in regime II have densities between 0.89-0.91 g/cc and exhibit a mixed crystalline morphology of bundle-like crystals and lamellae. Poorly developed, unbanded spherulites are observed in this regime. A very broad range of melting temperatures is also observed. Regime III copolymers have densities between 0.91 g/cc and approximately 0.93 g/cc. Lamellar crystals similar to linear low density polyethylene are observed with small spherulite formation. Branching restricts crystallization to some extent but the ethylene segments are long enough to crystallize into lamellae. Regime IV copolymers have densities greater than 0.93 g/cc. They exhibit lamellar crystals with well defined spherulites similar to high density polyethylene. Lamellar thickness is strongly determined by crystallization kinetics.

Low density ethylene – α-olefin copolymers exhibit an "annealing" response when isothermally crystallized at ambient temperatures.[10] Secondary crystallization behavior of ethylene – 1-octene random copolymers has recently been investigated as a function of time after initial solidification.[13] A quenched sample exhibits a broad HT melting endotherm due to primary crystallization. Upon isothermal crystallization at room temperature for various times, heating thermograms reveal the emergence of a LT

endotherm even for crystallization times as short as one minute. As the crystallization time increases, this LT endotherm shifts to higher temperatures while its heat of fusion increases. While the LT endotherm evolves, no change is observed in the position of the HT endotherm.[13]

The structure of polyethylene (PE) is well characterized. The pressure-temperature phase diagram for PE is shown in Figure 1.1. PE exhibits a triple point at 230 °C and 360 MPa. Below this triple point crystals exist in the orthorhombic structure and above it in the hexagonal structure. High pressure WAXD experiments have been conducted to isolate the hexagonal phase.[14-17] The hexagonal phase of polyethylene has a characteristic d-spacing of 4.3 Å for the (100) reflection[16] while the orthorhombic phase has two characteristic d-spacings of 4.1 Å for the (110) reflection and 3.7 Å for the (200) reflection.[17] The conformation of the hexagonal phase has been studied by Raman spectroscopy[18-20] as well as by nuclear magnetic resonance.[21] The hexagonal phase, also referred to as the rotator phase or condis phase, consists of parallel packing of conformationally disordered chains. Within this packing, trans-gauche rotational isomers are randomly distributed with all trans sequences of five or fewer CH_2 units in length.[18] This distribution of gauche segments allows for high degrees of mobility through rotation along the chain axis.[21]

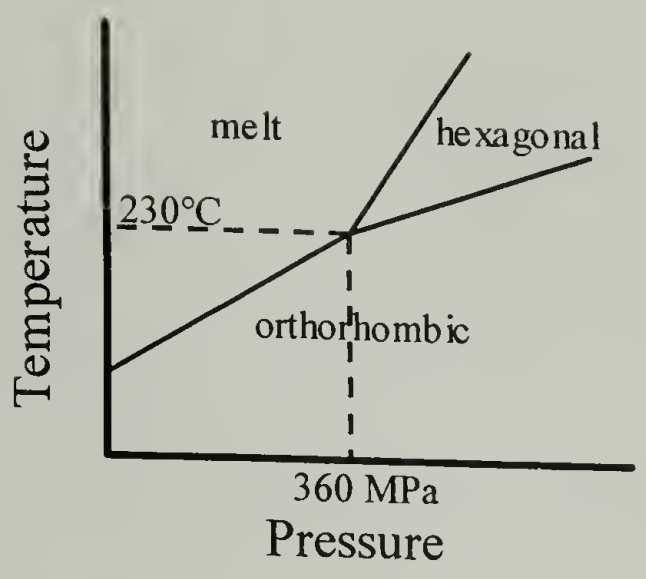

Figure 1.1: Phase diagram of polyethylene

Recently crystallization of ultrahigh molecular weight polyethylene through the hexagonal phase has been observed below its traditional triple point.[14] Occurrence of the hexagonal phase has also recently been reported in ethylene – 1-octene copolymers containing 7.3 mole percent 1-octene.[22] Wide and small angle X-ray scattering reveal the orthorhombic crystal structure in conjunction with the hexagonal mesophase. In these copolymers, the hexagonal phase is stable at room temperature. The amount of hexagonal crystals increases upon stretching and crystalline orientation is achieved. It is speculated that side chains excluded from the orthorhombic phase are accommodated by the hexagonal phase.[22]

Compared to other ethylene – α-olefin copolymers, little work has been done on ethylene – propylene copolymers to relate their composition and crystallinity to mechanical behavior. It is accepted that branched ethylene – propylene copolymers age at room temperature to achieve a maximum crystallinity which conventionally occurs over a two week period. The resulting crystal evolution will undoubtedly affect mechanical properties. For the context of this research the term "aging" is used to merely describe the length of time between solidification and experimentation. Time zero occurs

immediately after solidification, and the sample's age increases from this point until maximum crystallinity and mechanical behavior are achieved. Changes in crystal structure and mechanical behavior occur rapidly at first, and then slow down as the sample matures. The aim of this research is to completely characterize the evolving crystal structure and determine its influence on mechanical behavior.

1.1.2 Dynamically Vulcanized EPDM/iPP Blends

Dynamically vulcanized blends of EPDM terpolymer and iPP have emerged as a new class of TPEs with vastly different morphologies. The complex morphology of these blends is the result of the way in which they are produced, namely by dynamic vulcanization.

During the process of dynamic vulcanization a thermoplastic polymer (in this case iPP) and uncrosslinked rubber (usually EPDM) are heated and blended together in a masticating mixer. This mixing disperses EPDM particles within the iPP which reduces the mixing torque. Once the torque reaches a specific value, a curing agent is added which selectively cures the diene monomer in the EPDM resulting in a phase separated microstructure. This microstructure consists of chemically crosslinked EPDM rubber particles dispersed in a semicrystalline iPP matrix. Plasticizers or extender oils are added to the batch to reduce the viscosity in the melt state. Paraffin oil is commonly used and has been shown to have equal affinity for amorphous iPP and EPDM. When the dynamic vulcanizate is in the melt state, the oil is homogeneously dispersed throughout;[23] when the thermoplastic crystallizes, the processing oil is partitioned out of the crystals causing

the crosslinked elastomer domains to swell. As a result, the plasticizer is not only a processing aid but also a softener at use temperature.[24,25]

The process of dynamic vulcanization[24-26] produces very complex morphologies. These morphologies are influenced by composition and result in a wide range of mechanical behavior. The properties of these materials can also vary greatly depending on the cure state of the EPDM. A great deal of effort has been made in the literature to characterize the various morphologies of these specific systems.[23,27-31] In most cases iPP is observed to be the continuous phase in which 1-2 micrometer rubber particles are dispersed. Occasionally the constituents appear as two cocontinuous networks which has been attributed to the interaction of vulcanized elastomer particles to form a network during thermoplastic processing steps.[24,26,32] Upon regrinding, this network is destroyed allowing the material to be reprocessed as a thermoplastic. The appearance of a cocontinuous network could also be due to swelling of the EPDM domains by the processing oil. If swollen, they may impinge upon on one another but not actually be connected.

Compared to traditional crosslinked elastomers, little work has been done on EPDM/iPP TPEs to relate their composition and morphological structure to their mechanical behavior. Moreover, little information is available in the public literature that characterizes, compares, or contrasts how this class of thermoplastic elastomers behaves when compared to traditional crosslinked elastomers. The aim of this research is to phenomenologically characterize the mechanical behavior and morphology of six model dynamically vulcanized EPDM/iPP TPEs and to compare them with their more

traditional counterparts. A microcellular model is also developed and evaluated in an effort to understand the micromechanisms of deformation.

1.2 Phenomenological Responses of Rubber

Introduction of filler into an elastomer is known to increase its stiffness, change the strain history dependence of modulus, and affect time-dependent behavior such as hysteresis and stress relaxation.[33] Classical crosslinked systems have been investigated for the better part of the twentieth century in terms of stress-softening (Mullins Effect)[34] and dissipation (Payne Effect).[35] These investigations typically utilize cyclic loading conditions in order to investigate reversibility and the interactions between the introduced heterogeneity and the polymer matrix. The TPEs studied herein have fundamentally different types and length scales of heterogeneity. Since they are vying to replace crosslinked elastomers, a fundamental understanding of their mechanical behavior as compared with that of traditional crosslinked systems is necessary. As such each of these responses is discussed in detail.

1.2.1 Mullins Effect

The Mullins effect or stress-softening is a large strain phenomenon.[34] A schematic of the Mullins effect is shown in Figure 1.2.

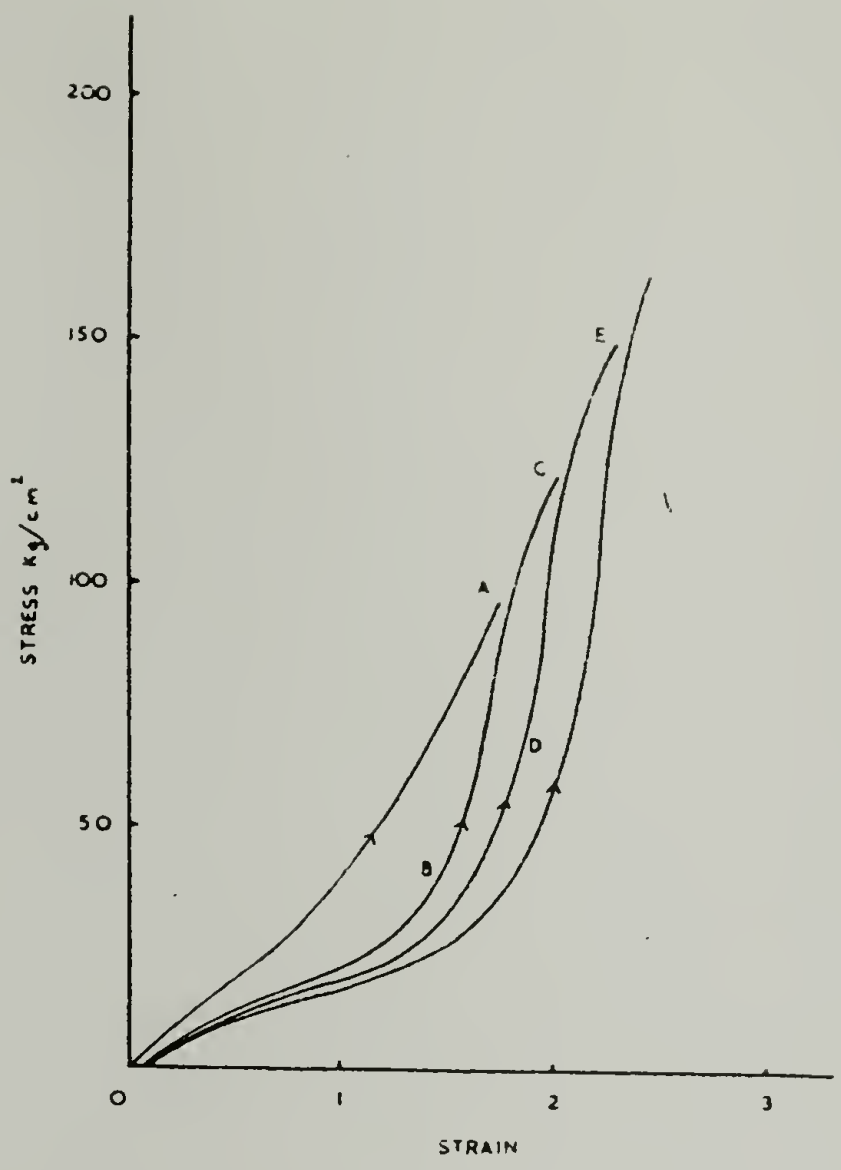

Figure 1.2: Schematic of Mullins effect – a stress-softening response

When a rubbery material is cycled, its compliance increases in each cycle until a steady-state response is reached. As a result the material supports a lower stress at a given strain than in the previous cycle. When the elastomer is cycled to strains higher than the maximum previous strain, the material returns to its virgin response. Several cycles are needed to achieve steady-state conditions so that a reproducible hysteresis loop may be obtained. Stress-softening is observed in all rubbers, crosslinked or uncrosslinked, with or without filler. It has been shown that stress-softening of unfilled crosslinked elastomers can be partially recovered by heating for extended periods of time. This recovery indicates that no breakdown process of the polymer chains occurs.[36] As a result, the response is attributed to quasi-irreversible rearrangements of molecular

networks due to localized non-affine deformation. However, stress-softening effects have been shown to increase upon addition of carbon black. In filled rubbers structural changes of the filler network are also believed to contribute to this response.[36]

1.2.2 Payne Effect

The energy dissipation and mechanical reversibility in crosslinked elastomers has been studied for many decades. Payne and Whittaker were some of the first to investigate the hysteresis and dynamic mechanical properties of crosslinked rubbers. They observed a sigmoidal dependence of the dynamic moduli on the dynamic strain amplitude,[35] which has become known as the "Payne effect." A schematic of the Payne effect is shown in Figure 1.3.

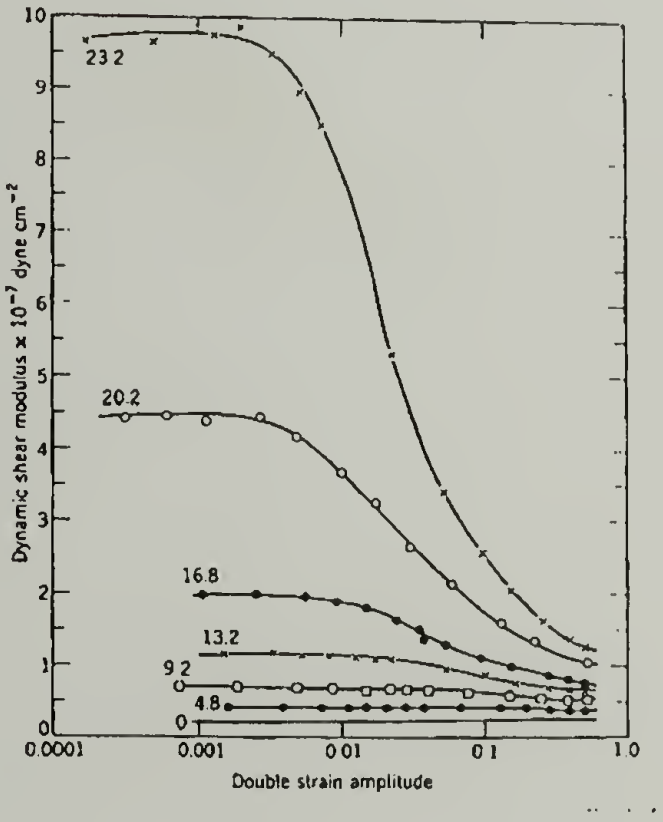

Figure 1.3: Schematic of the Payne effect – a sigmoidal dependence of storage modulus on dynamic strain amplitude exhibited by filled crosslinked elastomers

While the Mullins effect is generally referred to as a large strain phenomenon, the Payne effect is observed at small strains. An unfilled viscoelastic rubber exhibits a linear

response of its dynamic moduli on dynamic strain amplitude. As filler is introduced, the low amplitude modulus (E'_o) of the elastomer increases. While E'_o increases, the high amplitude modulus (E'_∞) remains relatively low. The difference between the low and high amplitude moduli (E'_o-E'_∞) increases as filler loading is increased. This is in conjunction with an increasing peak in the loss modulus indicates that more energy is being dissipated upon addition of filler. Frequency does not affect the overall response. Changing frequency simply shifts the entire curve up or down due to the viscoelasticity of the polymer matrix. It was found that only filled rubbers exhibit this nonlinear behavior and that filler characteristics affect the response. While previous literature studies have focused on nanoscale particulate fillers in a thermoset matrix, this research examines two different TPE morphologies: crosslinked elastomer domains embedded in a thermoplastic matrix and nanoscale crystallites in an amorphous rubbery matrix.

1.3 Modeling Attempts

1.3.1 Traditional Crosslinked Systems

Continuum Approach

Many attempts have been made to predict the mechanical behavior of crosslinked elastomers. Various modeling approaches have been utilized including thermodynamics, statistical mechanics, and continuum mechanics. Thermodynamics describes aspects of rubbery elasticity such as restoring force and entropic and enthalpic contributions to elasticity. The use of statistical mechanics and continuum mechanics has allowed many descriptions of the loading and unloading behavior of crosslinked elastomers. A

statistical mechanics approach assumes a structure of long molecular chains that are randomly oriented in space. Calculations are based on the probability distribution of end-to-end chain lengths. A continuum mechanics approach uses strain energy density functions that are dependent on stretch via one or more of the strain invariants to describe macroscopic deformation. The strain invariants are given in equations 1.1 and 1.2 where λ_i (i = 1-3) are the principal stretch ratios. The principal stretch ratios are equal to the final length divided by the initial length in the respective principal directions. Most derivations assume that the elastic material is incompressible, *i.e.*, $\lambda_1\lambda_2\lambda_3 = 1$.

$$I_1 = \lambda_1^{\,2} + \lambda_2^{\,2} + \lambda_3^{\,2} \qquad (1.1)$$

$$I_2 = \lambda_1^{\,-2} + \lambda_2^{\,-2} + \lambda_3^{\,-2} \qquad (1.2)$$

Treloar constructed a strain energy function[37] (eqn. 1.3) using molecular network theory and found it to be a function of the shear modulus (μ) and the first strain invariant (I_1).

$$\phi = \tfrac{1}{2}\mu(I_1 - 3) \qquad (1.3)$$

Mooney and Rivlin also described the macroscopic deformation of rubbers in terms of the first and second strain invariants as shown in equation 1.4.[38]

$$\phi = C_1(I_1 - 3) + C_2(I_2 - 3) \quad (1.4)$$

Equation 1.3 and the first term in equation 1.4 have the same form as the theoretical elastic free energy per unit volume when described in terms of statistical theory where $C_1 = kT\nu_e/2V$ and ν_e is the number of network chains.[39]

Ogden proposed a strain energy function for an incompressible elastic solid so that the relationship between principal stresses and strains is given by equation 1.5, where

ϕ is the strain energy function, P is an arbitrary hydrostatic pressure due to the incompressibility constraint, and no sum over i is implied.[40,41]

$$\sigma_i = \lambda_i \frac{\partial \phi}{\partial \lambda_i} - P \qquad (1.5)$$

The principal values of lagrangian strain (e_i) are given by equation 1.6 where α is any real number positive or negative.

$$e_i = \begin{cases} (\lambda_i^{\alpha} - 1)/\alpha \\ \ln \lambda_i \end{cases} \begin{matrix} (\alpha \neq 0) \\ (\alpha = 0) \end{matrix} \qquad (1.6)$$

Ogden proposes a strain energy function (eqn. 1.7) that is a linear combination of the first strain invariant of equation 1.6, where $I(\alpha)$ is the first strain invariant, μ_r's are constants, and summation over r is implied.

$$\phi = \mu_r I(\alpha_r) \qquad (1.7)$$

After partial differentiation and substitution into equation 1.5, the principal stresses are given by equation 1.8, where i = 1-3 with summation over r.

$$\sigma_i = \mu_r \lambda_i^{\alpha_r} - P \qquad (1.8)$$

When equation 1.8 is considered in terms of classical linear theory of isotropic elasticity the conventional shear modulus (μ) is given as $2\mu=\mu_r\alpha_r$. Ogden's continuum model accurately describes the loading curve of most traditional crosslinked elastomers under various loading conditions when r = 2. A two term Ogden model describes small and large strain behavior using a linear combination of only the first strain invariant; whereas, the Mooney-Rivlin equation (eqn. 1.4) utilizes two strain invariants and Treloar's strain energy function (eqn. 1.3) is only accurate at small strains.[40]

Filler Network Approach

Gerard Kraus proposed a model to explain the Payne effect as observed in filled crosslinked elastomers. Kraus attributes the decline in storage modulus and corresponding peak in loss modulus to the deformation of carbon black aggregate-aggregate contacts. He proposes that the resulting carbon black network is continuously broken and reformed under a periodic sinusoidal strain.[42] The Kraus model has successfully been applied to systems with particulate fillers other than carbon black in which the energy dissipation with increasing strain amplitude has been attributed to wetting and dewetting of the matrix and filler at interfaces.

In his derivation, Kraus assumes that the deagglomeration and reagglomeration rates of carbon black aggregates reach a steady-state under sinusoidal loading. The following equations are derived[42] to describe the drop in storage modulus (eqn. 1.9) and the peak in loss modulus (eqn. 1.10) as a function of dynamic strain. It should be noted that Kraus' original model described dynamic mechanical experiments under shear loading with the parameters G', G'', and γ that have been substituted here by the analogous parameters for tensile loading (E', E'', and ε) since the experiments herein are performed under tensile loading conditions.

$$\frac{E''-E''_{\infty}}{E''_{m}-E''_{\infty}} = \frac{2\left[\varepsilon/\varepsilon_{o}\right]^{m}}{1+\left[\varepsilon/\varepsilon_{o}\right]^{2m}} \qquad (1.9)$$

$$\frac{E'-E'_{\infty}}{E'_{o}-E'_{\infty}} = \frac{1}{1+\left[\varepsilon/\varepsilon_{o}\right]^{2m}} \qquad (1.10)$$

Each of the above equations has four parameters. The parameters in equation 1.9 are as follows:

- E'_o represents the low amplitude storage modulus.
- E'_∞ represents the high amplitude storage modulus.
- ε_o represents the characteristic strain at which the decline in E' is a maximum.
- m is a fitting parameter that determines the shape of the decline in E'.

The parameters in equation 1.10 are as follows:

- E''_m represents the maximum value of the loss modulus.
- E''_∞ represents the loss modulus at high strain amplitudes.
- ε_o represents the characteristic strain where the maximum in E'' occurs.
- m is a fitting parameter that determines the shape of the peak.

In a classical dynamic mechanical experiment, ε_o from the E' regression should equal ε_o from the E'' regression. In other words, the maximum in E'' should occur at the same strain as the maximum change in E'.[43]

1.3.2 Thermoplastic Elastomers

Even though many thermoset systems have been studied, comparatively little work has been done on TPEs. This is largely due to the complex morphologies and the viscoelastic nature of the constituents. An attempt to describe the deformation of ethylene – octene copolymers has recently been presented by Hiltner and Baer and

coworkers.[44] The origins of elasticity of EPDM/iPP blends have also been described recently though various constitutive and finite element efforts. Since the materials used for these modeling studies are similar to the TPEs in this research, each of these efforts will be described.

Slip-Link Theory Applied to Ethylene-Octene Copolymer Deformation

Slip-link theory was originally developed by Ball[45] and Edwards[46] to describe the elasticity of a crosslinked network. This was accomplished by considering additional contributions due to finite chain extensibility and entanglements. The entanglements are envisaged as links that can slide along the chain contour between crosslinks. Slip-link theory (eqn. 1.11) has four main parameters: the density of crosslinked chains (N_c), the density of slip-links (N_s), a slippage parameter (η), and an inextensibilitiy parameter (α).

$$\frac{F}{kT} = \frac{1}{2}N_s\left(\sum_i\left[\frac{\lambda_i^{\,2}(1-\alpha^2)(1+\eta)}{(1-\alpha^2\sum_i\lambda_i^{\,2})(1+\eta\lambda_i^{\,2})}+\log(1+\eta\lambda_i^{\,2})\right]+\log(1-\alpha^2\sum_i\lambda_i^{\,2})\right)+$$

$$\frac{1}{2}N_c\left(\frac{\sum_i\lambda_i^{\,2}(1-\alpha^2)}{(1-\alpha^2\sum_i\lambda_i^{\,2})}+\log(1-\alpha^2\sum_i\lambda_i^{\,2})\right) \qquad (1.11)$$

Summation is performed over the three Cartesian coordinates of strain, λ. Stress under uniaxial tension is obtained through equation 1.12 assuming incompressibility.

$$\sigma = \left(\frac{\partial F}{\partial \lambda}\right)_{T,V} \qquad (1.12)$$

If $\eta = 0$ the slip-links are rigid and act as crosslinks, and if $\alpha = 0$ the crosslink term reduces to that for a phantom network.

Eventhough ethylene – octene copolymers are not crosslinked, Hiltner and Baer used the slip-link theory to describe the deformation of these TPEs.[44] They first set $\alpha = 0$ to find approximate values for N_c and N_s at which point they performed a three parameter least-squares fit to obtain α and final values for N_s and N_c. The calculated stress-strain curves fit the experimental data well over the entire range of deformation. Their results indicate that the slip-link density is larger than the crosslink density by at least an order of magnitude and depends on the crystallinity. They also found that the inextensibility parameter increases with crystallinity. The density of the copolymers examined falls into regime I with bundle-like crystals as discussed earlier. They identified these crystals as slip-links since bundle-like crystals must form by the attachments of lateral segments. This would allow crystal segment attachment and detachment as a polymer chain "slipped" through the crystal. Their efforts successfully modeled the stress-strain response under uniaxial loading. No attempt was made to describe the unloading and recovery of the material and no other stress states were examined.

FEM of EPDM/iPP Deformation

Even though the matrix is a semicrystalline thermoplastic, EPDM/iPP dynamic vulcanizates behave elastically. Over the past several decades, the origins of this elasticity have been debated and several finite element studies and constitutive models have been proposed. A primary limitation of these studies is that none clearly identify how composition and morphology influence deformation characteristics.

Two different modeling approaches to explain the micromechanisms of deformation in EPDM/iPP TPEs have recently been presented. In the first approach Kikuchi[47] and Okamoto[48] focus on the origins of elasticity of EPDM/iPP thermoplastic

vulcanizates under uniaxial tension with two-dimensional finite element modeling. They set the following boundary conditions on a two phase model: identical constituent mechanical properties to that of the neat polymer, infinite adhesion between the rubber particles and the matrix, and von Mises criterion for shear yielding. Their results indicate that yielding in the thermoplastic matrix begins around the particles in an equatorial direction perpendicular to the applied load. This yielding is illustrated in Figure 1.4.

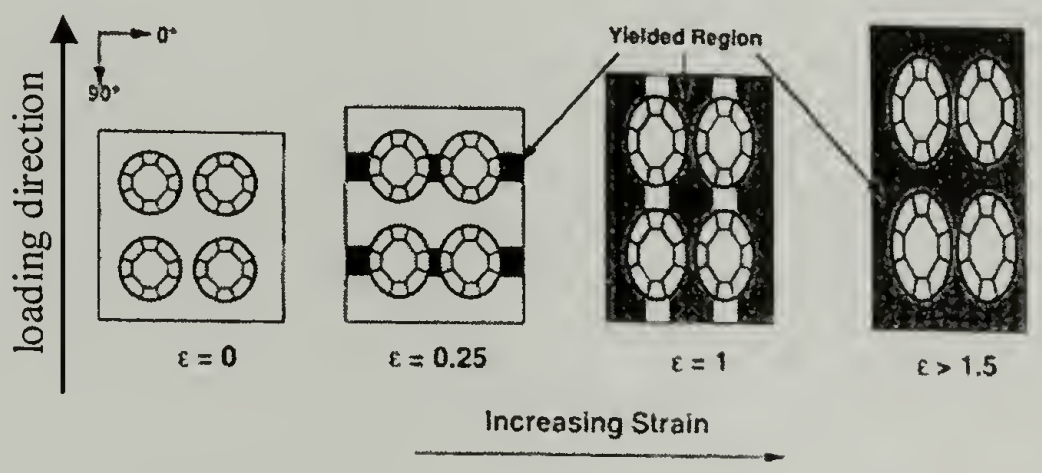

Figure 1.4: Illustration of matrix yielding in EPDM/iPP blends as modeled by Kikuchi and Okamoto

The yielding then propagates around the embedded rubber particles shifting toward the loading direction. Upon considerable strain the polar ligaments (matrix regions between particles that are parallel with the applied load) remain unyielded due to lower stress concentrations in that region. These unyielded polar ligaments serve as elastic domains and allow for elastic recovery. Once significant strain has been imposed on the system that causes yielding of the polar ligaments, no elastic recovery will take place. While this model qualitatively describes elasticity for one loading condition, it does not take composition, cure state, molecular weight, domain size, domain shape, or domain polydispersity into account. This approach also requires a significant amount of iPP

inelastic deformation to produce large strains. This is a direct consequence of the imposed representative volume element and loading configuration.

In the second modeling approach, Boyce[49-51] and coworkers have focused on constitutive modeling using viscoelastic elements composed of springs and dashpots in conjunction with finite element methods. They have attempted to model loading, unloading, and stress-softening for EPDM/iPP thermoplastic vulcanizates under uniaxial compression and plane-strain compression. Their one-dimensional model is composed of three elements and is shown in Figure 1.5.

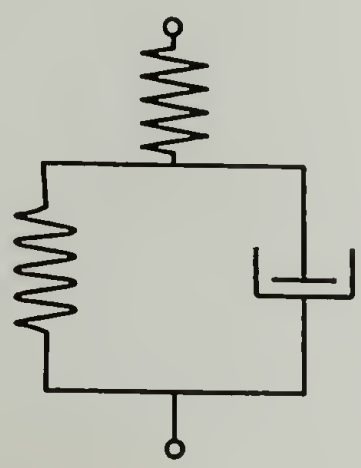

Figure 1.5: Spring and dashpot model used by Boyce and coworkers

The three elements of their model each correspond with a given aspect of morphological deformation. The linear spring represents the initial elastic response of both the EPDM and iPP phases. The viscoplastic dashpot is interpreted as yielding of the iPP matrix or matrix ligaments between particles. A nonlinear spring captures strain hardening once the iPP matrix has significantly yielded.[49]

Their experimental data show that stress state plays a significant role in the deformation. In plane-strain compression iPP exhibits a higher yield stress and a greater degree of strain hardening than in uniaxial compression. The EPDM exhibits a higher initial slope and a higher rate of slope increase with strain in plane-strain compression.

Both of these results are typical for thermoplastic polymers and elastomers. They describe the initial loading and unloading curves using the constitutive model shown above in conjunction with the Arruda-Boyce eight-chain network model of rubber elasticity.[52] This network model is based on statistical mechanics resulting in a strain energy density function with a nonlinear dependence on the first strain invariant. The calculated stress-strain response of the EPDM/iPP blends fits relatively well with the experimental data.

Next, Boyce and coworkers attempt to understand the micromechanisms of deformation and recovery in thermoplastic vulcanizates using finite element modeling. They impose a five-particle representative volume element assuming perfect adhesion between the EPDM domains and iPP matrix. They model the iPP behavior using the constitutive model for a rate-dependent elastic-viscoplastic glassy polymer[53] even though the iPP is semicrystalline. They again use the eight-chain network model of rubber elasticity for the EPDM phase.[52] Their simulations indicate that upon yielding a pseudo-continuous rubber phase develops due to the drawing of iPP ligaments and shear of rubber particles. This can be visualized in the top of Figure 1.6. The initial matrix ligament thickness also appears to control the initial stiffness and flow stress. Thinner ligaments result in earlier yielding. They also observe that the majority of the matrix material does not deform during large deformations but undergoes rigid body motion as the pseudo-continuous rubber phase shears and contorts around unyielded rigid matrix regions.

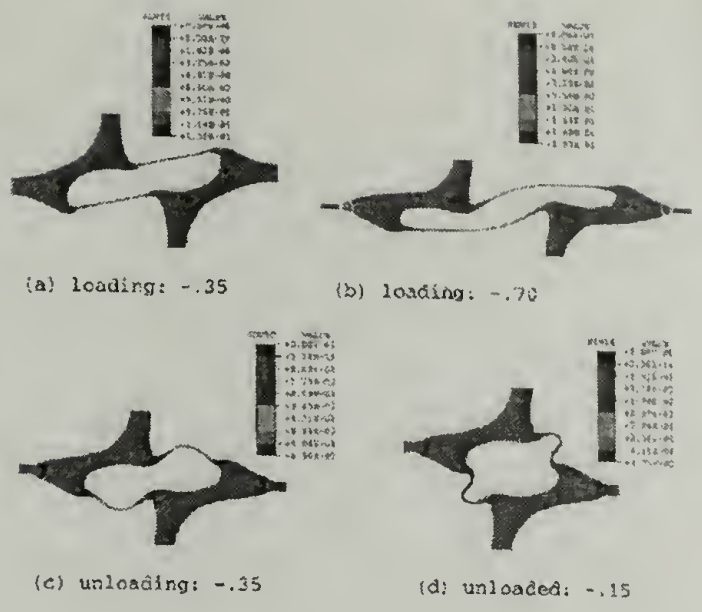

Figure 1.6: FEM contours of EPDM/iPP thermoplastic vulcanizate during first loading/unloading excursion as modeled by Boyce and coworkers

Finally, Boyce and coworkers take their finite element simulations one step further to describe stress-softening of thermoplastic vulcanizates in plane strain compression. They use the same micromechanical model briefly described above and subject the representative volume element to a given load, unload to zero, and allow a 15 minute relaxation period followed by continued reloading to simulate stress-softening. Figure 1.6 shows the initial loading and unloading contours while Figure 1.7 shows the reloading and unloading contours with an initial strain excursion of –0.70.

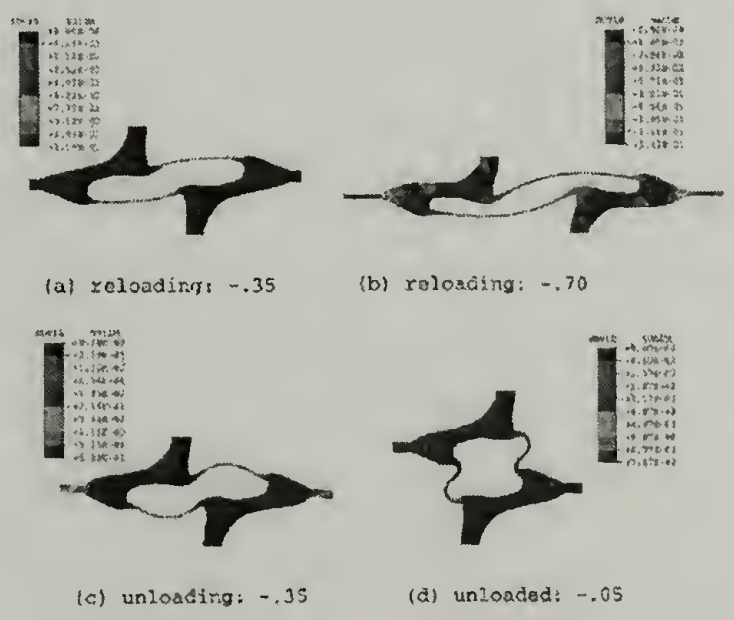

Figure 1.7: FEM contours of EPDM/iPP thermoplastic vulcanizate during second loading/unloading excursion as modeled by Boyce and coworkers

Their simulations show good correlation with experimentally observed stress-strain behavior. Additional compliance in the early stages of reloading are attributed to changes in the matrix/particle configuration induced during the initial loading cycle. The thinnest matrix ligaments are left in a configuration favorable for elastic bending and rotation upon reloading instead of additional plastic straining. These deformation modes occur at lower stress levels and would thus be responsible for increased compliance. After sufficient strain occurs upon reloading, the tangent modulus increases indicating that a strain has been reached where the particle/matrix interaction now requires additional plastic straining of the iPP ligaments.

The efforts of Kikuchi and Okamoto and Boyce are in stark contrast with one another. In the case of Kikuchi and Okamoto, the majority of the iPP matrix yields around the embedded rubber particles with the exception of unyielded ligaments at the particle poles. These unyielded polar ligaments connect the rubber domains and allow for elastic recovery.[24,47,48] The work of Boyce and coworkers indicates that the majority of the iPP matrix does not yield at all. Only thin ligaments between particles yield while the rubber domains shear around the undeformed iPP regions creating a pseudo-continuous EPDM phase. Their results indicate that matrix ligament yielding controls plastic flow while ligament bending, buckling, and rotation control the transition to nonlinear recovery during unloading; particle/matrix conformation leads to buckling and rotation of iPP ligaments producing the increased compliance observed as stress-softening.[49-51]

1.4 Research Objectives

There are two primary objectives of the research; each objective has several secondary goals. The first objective is to develop both a qualitative and quantitative understanding of the effect of composition and morphology on the mechanical and physical characteristics of selected TPEs. As mentioned earlier, the selected TPEs consist of ethylene – propylene copolymers and dynamically vulcanized EPDM/iPP blends. The mechanical characteristics of interest are stiffness, strength, and mechanical reversibility. The origins of elasticity in the EPDM/iPP systems are also of interest. Steady-state reversibility is evaluated through the development of a morphological model. The second objective is to qualitatively compare the behavior of the selected TPE formulations with the behavior of traditional crosslinked elastomers. This will be addressed in terms of the Mullins and Payne effects.

In the following chapters, each TPE class is presented separately beginning with the ethylene – propylene copolymers. For each, morphology characterization is presented first, followed by mechanical behavior evaluation and ensuing structure-property relationships.

CHAPTER 2

ETHYLENE-PROPYLENE COPOLYMERS

2.1 Materials

Four ethylene – propylene copolymer compositions are examined. The samples were produced by the ExxonMobil Chemical Company using a Ziegler-Natta catalyst. The compositions are listed in Table 2.1 where ethylene content is given in mole percent together with weight-average molecular weights, polydispersity indices, and numbers of short chain branches per 1000 carbon atoms. The sample name indicates the ethylene content as well as the comonomer distribution. Samples EP58.1R, EP68.6R, and EP79.8R have a more homogeneous or random comonomer distribution while samples EP68.6B and EP69.0B have a more heterogeneous or "blocky" distribution.

Table 2.1: Ethylene – propylene copolymer compositions

Sample	**mol% Ethylene**	**M_w**	**M_w/M_n**	**#SCB/ 1000C**	**Comonomer Distribution**
EP58.1R	58.1	153,000	2.1	210	random
EP68.6R	68.6	108,000	1.4	158	random
EP68.6B	68.6	108,000	1.4	158	blocky
EP69.0B	69.0	149,000	1.5	154	blocky
EP79.8R	79.8	111,000	1.9	99	random

2.2 Morphology Characterization

2.2.1 Experimental Procedures

Thermal analysis is performed using a Thermal Analysis 2910 differential scanning calorimeter (DSC). Indium is used as the calibration standard. Sample sizes between 5 and 8 mg are sealed in aluminum hermetic pans, and a nitrogen flow rate of 50 ml/min is maintained. All heating and cooling rates are 10 °C/min. DSC thermograms obtained immediately after solidification correspond to a second heating scan where samples are heated to 200 °C and equilibrated, cooled to 0 °C and equilibrated, and reheated to 200 °C. All other DSC thermograms obtained as a function of sample age correspond to first heating scans in order to preserve the crystallinity formed at room temperature.

Wide angle X-ray diffraction (WAXD) measurements are performed on a Rigaku RU-H3R rotating anode X-ray diffractometer equipped with an Osmic multilayer focusing optic and an evacuated Statton-type scattering camera. The incident beam wavelength is 1.54 Å, corresponding to 8 keV Cu Kα radiation. Scattering patterns are acquired with 10 cm x 15 cm Fuji ST-VA image plates in conjunction with a Fuji BAS-2500 image plate scanner. Intensity profiles are obtained from radial averages of the scattering pattern intensities. Samples for WAXD are compression molded into films approximately 0.6 mm thick at 190 °C for 10 minutes and then water-cooled in the melt press.

Density measurements are performed in an isopropanol-distilled water density column calibrated with glass floats. Temporal density measurements are made by inserting a sample into the density column immediately after solidification and reading its

position as it ages. The isopropanol-water solution does not swell the samples and crystallization is not inhibited by the presence of the fluid. This is determined by measuring the density of a sample that aged in the density column versus an identical one that aged in air. Samples for density measurement are first compression molded into 3 mm thick plaques at 190 °C and a pressure of 3.5 MPa for approximately 20 minutes and water-cooled in the melt press.

Similar compression molded samples for transmission electron microscopy (TEM) are stained in bulk prior to cryogenic microtoming using the Montezinos method.[54] Ruthenium tetroxide (RuO_4) for staining is produced by mixing 0.2 g of anhydrous ruthenium chloride with 10 mL of sodium hypochlorite solution. The samples are placed in the resulting RuO_4 vapor for 2 ½ hours. The stained samples are then cryogenically microtomed using a glass knife. Samples are collected dry onto 600 mesh copper grids. The thin sections are examined in a JEOL 100CX transmission electron microscope.

2.2.2 Crystallization Kinetics

Melting behaviors of the five copolymer compositions are shown in Figures 2.1-2.5 as a function of sample age. In order to accurately compare the DSC scans as a function of sample age, all scans shown correspond to the same set of samples (*i.e.*, all samples were treated identically and left at room temperature for the time indicated). Figure 2.1 shows that EP58.1R is an amorphous reference at all times.

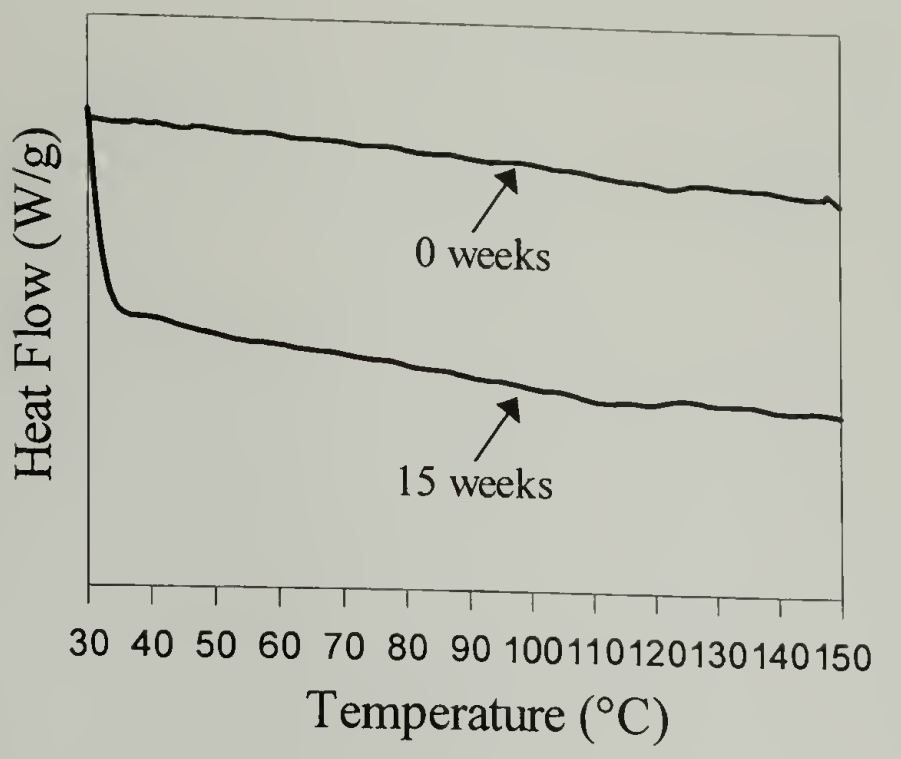

Figure 2.1: Melting behavior of amorphous reference, EP58.1R

Melting behaviors of EP68.6B and EP69.0B are shown in Figures 2.2 and 2.3, respectively. Both compositions have a blocky comonomer distribution and exhibit bimodal crystallization kinetics. Initially after solidification, a high temperature (HT) endotherm centered at approximately 130 °C is present in both of these samples while a low temperature (LT) endotherm develops over time.

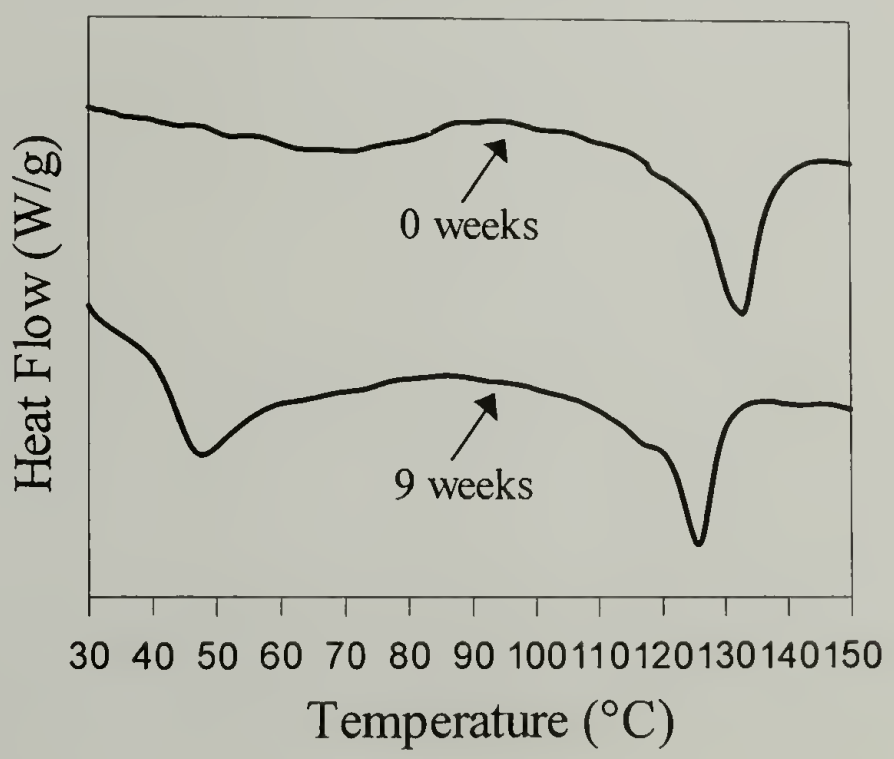

Figure 2.2: Melting behavior of EP68.6B illustrating aging through the development of a LT endotherm

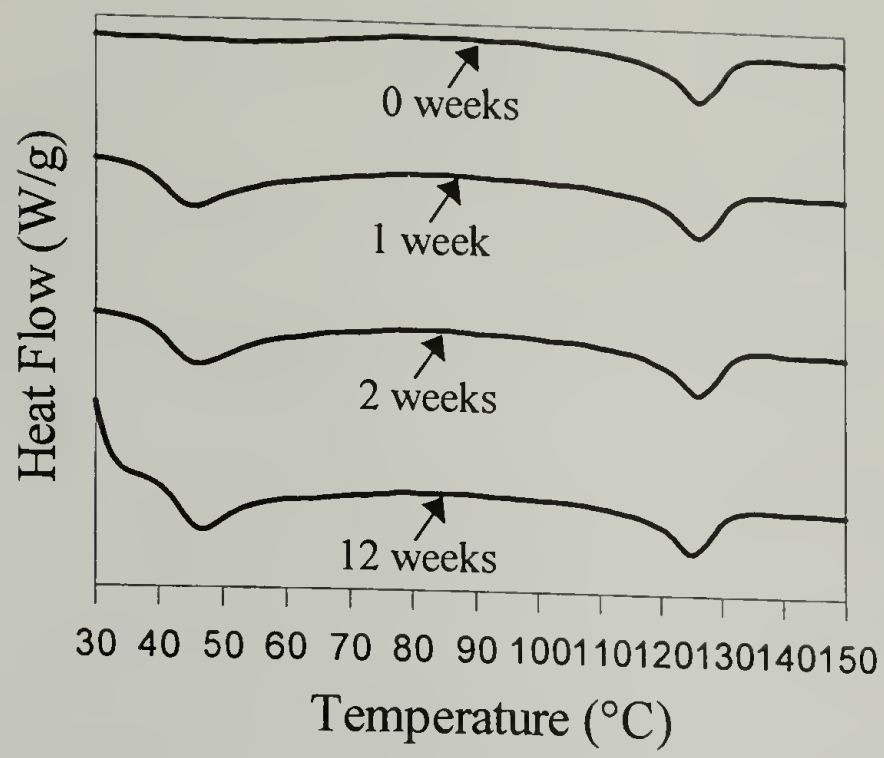

Figure 2.3: Melting behavior of EP69.0B illustrating aging through the development of a LT endotherm

Melting behaviors of EP68.6R and EP79.8R are shown in Figures 2.4 and 2.5, respectively. These compositions have a more random comonomer distribution and are essentially amorphous immediately after solidification. A negligible HT endotherm is observed while a LT endotherm centered at approximately 45 °C develops over time.

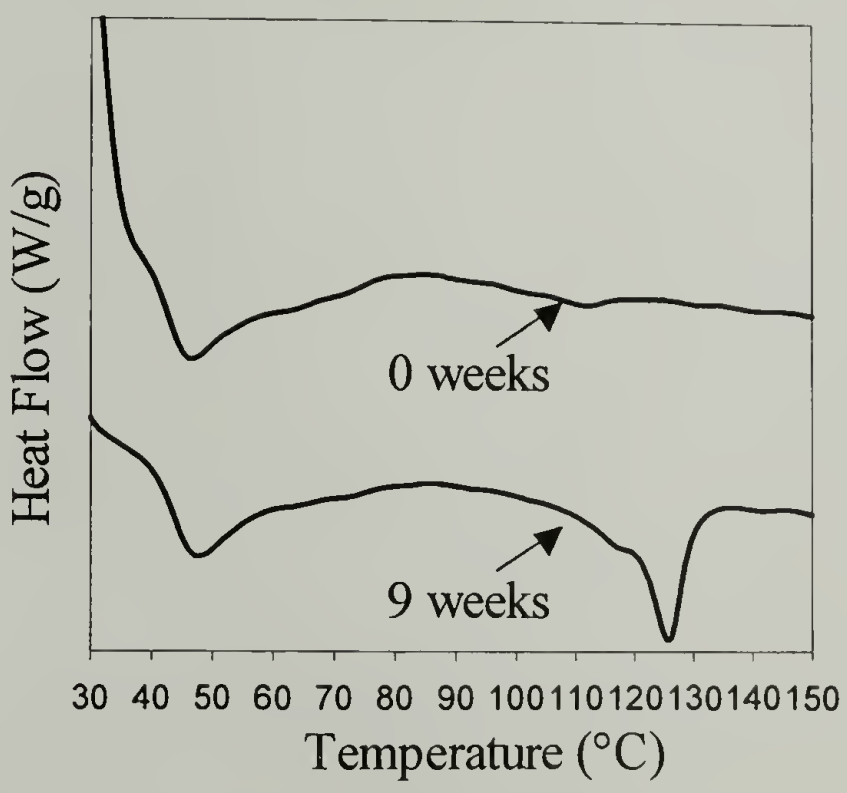

Figure 2.4: Melting behavior of EP68.6R illustrating aging through the development of a LT endotherm

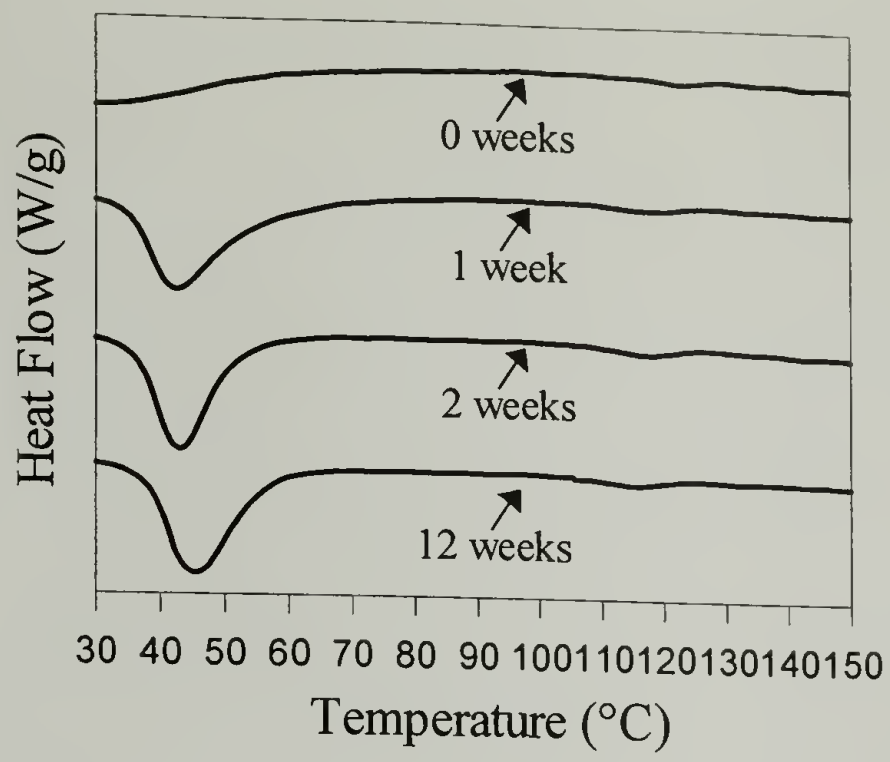

Figure 2.5: Melting behavior of EP79.8R illustrating aging through the development of a LT endotherm

All of the compositions (except the amorphous reference) exhibit both a LT and HT endotherm that increase in size and shift in temperature. The upper endotherm shifts to lower temperatures as time progresses and its area is only slightly increased; whereas, the lower endotherm shifts to higher temperatures and its heat of fusion is drastically increased. The endotherm shifts are illustrated in Figure 2.6, which is a plot of the HT and LT endotherm peak temperatures for EP69.0B and EP79.8R as a function of time.

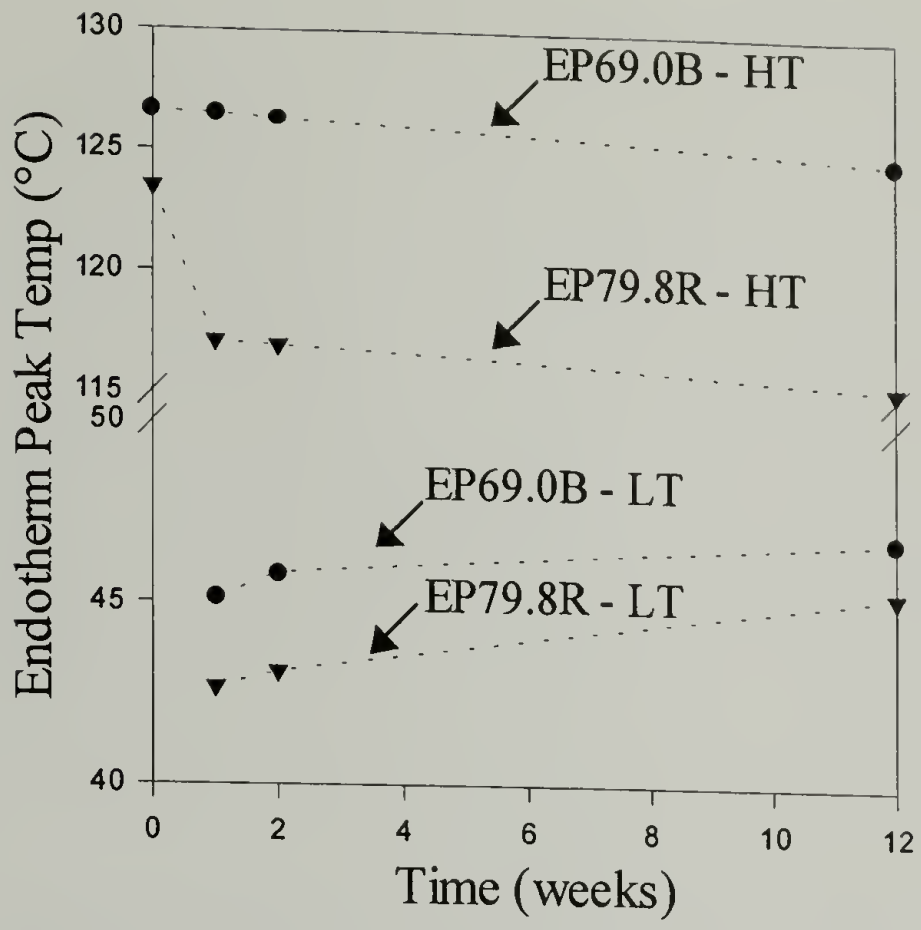

Figure 2.6: Shift in LT and HT endotherm positions

It is apparent that for both samples the HT endotherm shifts to lower temperatures over time while the LT endotherm shifts to higher temperatures over time. It is also observed that the decrease in peak temperature corresponding to EP69.0B occurs at a more uniform rate; whereas, that for EP79.8R decreases rapidly during the first week at which point the rate of decrease slows. The shift in the HT endotherm has not been reported prior to this study. Its exact origin has not yet been determined. However, since the heat of fusion of the HT endotherm increases with time and slight peak broadening is observed, smaller crystals could be forming thus shifting the average peak position to lower temperatures. The development of a lower endotherm and its shift to higher temperatures with annealing time has been observed previously for ethylene – 1-octene copolymers.[13]

Figure 2.7 shows the total heat of fusion as a function of time. The total heat of fusion is the sum of the HT and LT heats of fusion. Once again, EP58.1R is amorphous

at all times with no measurable heat of fusion. For the other compositions, the total heat of fusion increases rapidly within the first 7 days and then reaches a plateau value.

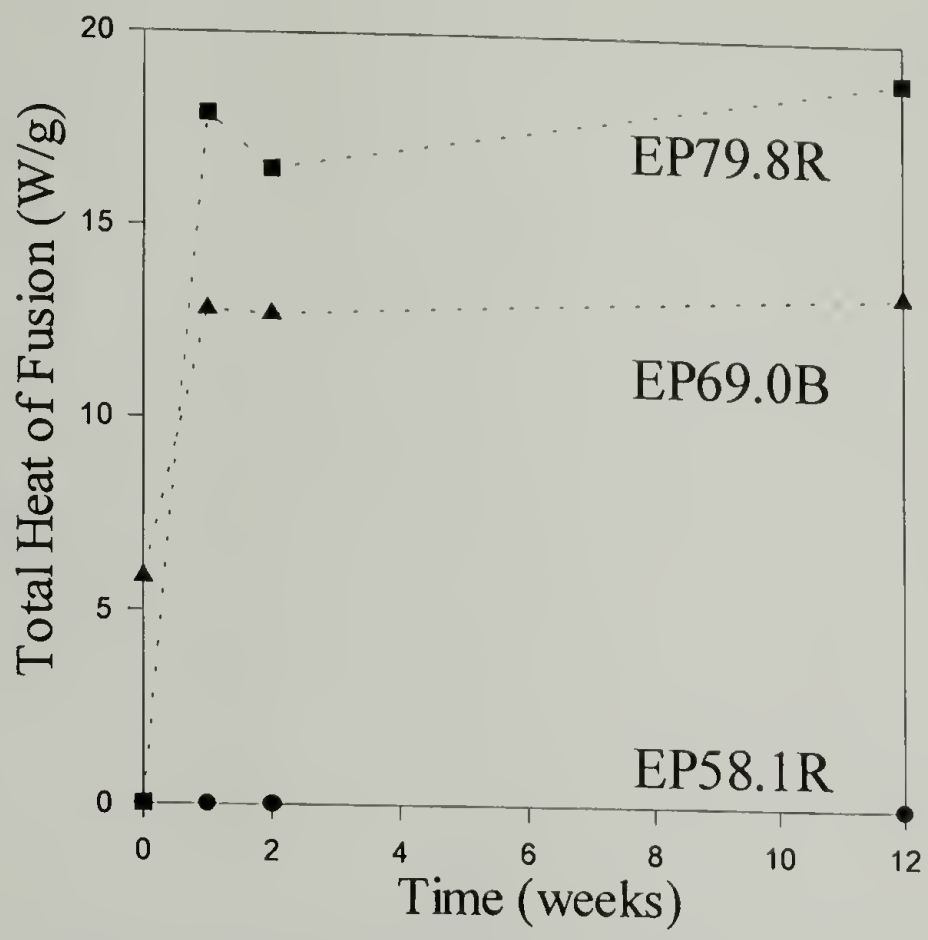

Figure 2.7: Total heat of fusion versus time for EP58.1R, EP69.0B, and EP79.8R

Two crystalline regimes exist. Both endotherms are relatively broad indicating a wide range of crystal sizes present. In order to compare the crystallinity between compositions, Table 2.2 shows the HT and LT endotherm heats of fusion (J/g) as well as the total heat of fusion immediately after solidification and after the samples have reached maturity. The crystallinity of these samples should be compared in terms of their total heats of fusion since the theoretical value for these crystals is unknown. However, a rough estimate of crystallinity is determined and listed in Table 2.2 by utilizing the heat of fusion of a perfect orthorhombic crystal (290 J/g). Crystallinity increases in the order of EP58.1R <<EP68.6R< EP69.0B < EP68.6B < EP79.8R.

Table 2.2: LT and HT endotherm heats of fusion and % crystallinity of copolymer compositions

Sample	After Solidification			At Maturity		
	LT†	HT†	%	LT†	HT†	%
EP58.1R	0	0	0	0	0	0
EP68.6R	0	0	0	9.22	0	3.18
EP68.6B	0	5.35	1.84	9.03	7.64	5.57
EP69.0B	0	5.85	2.01	8.19	5.17	4.60
EP79.8R	0	0.27	0.09	17.9	1.07	6.54

†Heat of fusion (J/g) from low and high temperature endotherms

2.2.3 Crystal Structure Analysis

WAXD measurements for four of the compositions as a function of time are shown in Figures 2.8-2.11. The inset in each figure is a 2θ expansion of the peak between 15° and 22° in order to show changes that occur in the crystal structure over time. The WAXD results for EP58.1R are shown in Figure 2.8. A very broad peak is observed at a 2θ of 18.2°. This type of amorphous halo has been observed for other ethylene – α-olefin copolymers at 18.5°.[9] For the purposes of this study this peak is assigned as the amorphous halo for all compositions. As expected no change is observed in the WAXD pattern for the amorphous sample as a function of time which is in agreement with the DSC results.

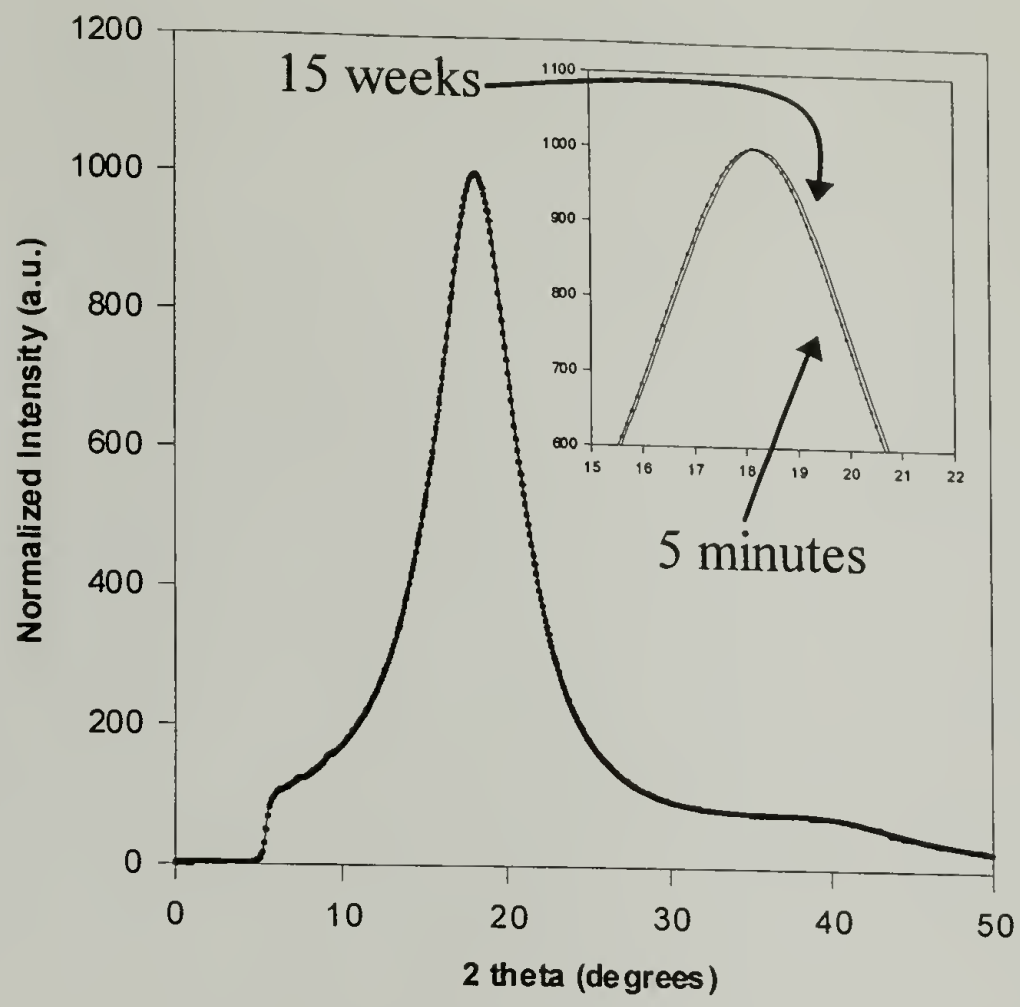

Figure 2.8: Initial and mature diffraction patterns of amorphous reference, EP58.1R

Figure 2.9 shows the WAXD pattern of EP68.6B as a function of time. Five minutes after solidification a small peak at 21.20° and a shoulder at 23.52° are observed. These two peaks correspond to the (110) and (200) reflections of orthorhombic polyethylene. After the sample has been aging at room temperature for 15 weeks, the WAXD pattern reveals the emergence of a peak at 20.56°. Using Bragg's Law, this reflection corresponds to a d-spacing of 4.3 Å which is the characteristic d-spacing of the (100) reflection for hexagonal polyethylene.[16] This hexagonal reflection is present in conjunction with the remaining orthorhombic (110) and (200) reflections, indicating that the hexagonal and orthorhombic crystals are in coexistence at maturity.

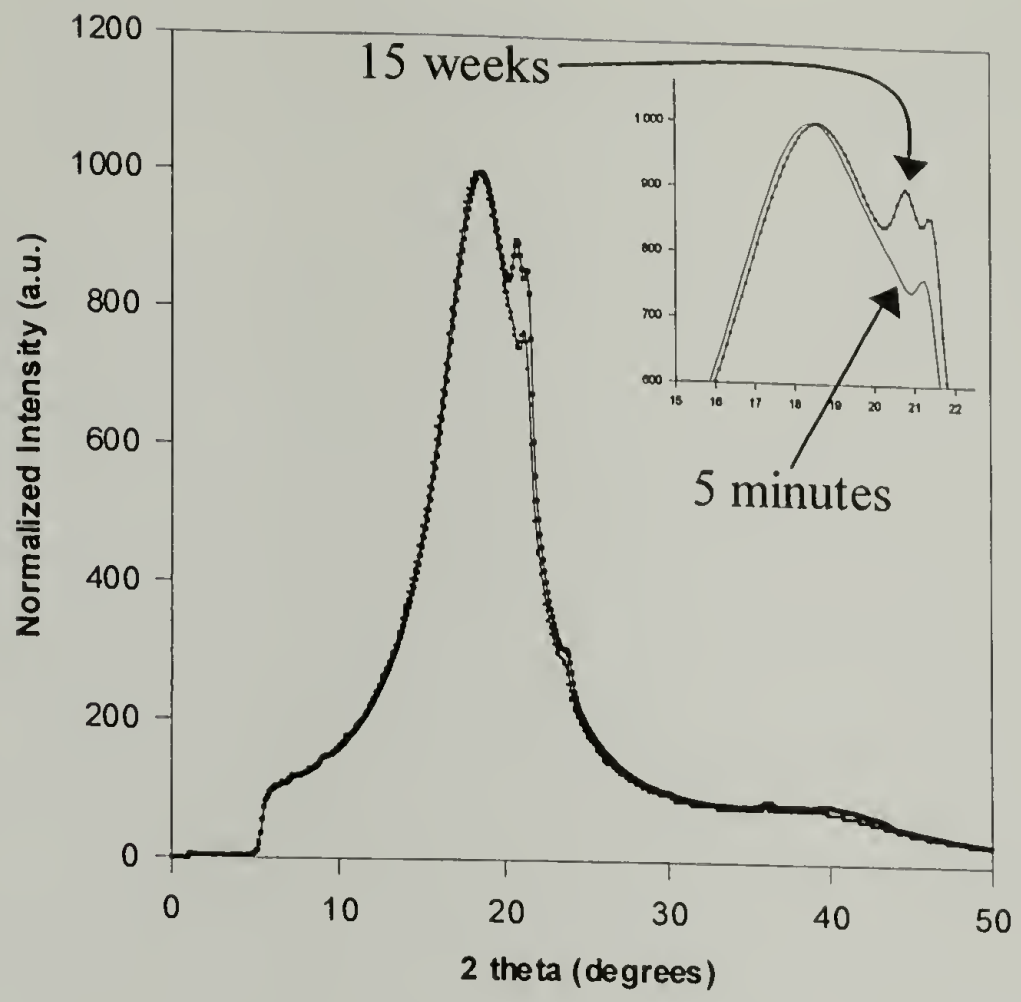

Figure 2.9: Initial and mature diffraction patterns of EP68.6B illustrating development of hexagonal crystal phase

Figure 2.10 shows a similar evolution in crystal structure for EP69.0B; except in this case only a shoulder corresponding to the (110) orthorhombic remains. The majority of the crystals present in EP69.0B appear to exist in the hexagonal phase. This is interesting considering that EP68.6R and EP69.0B are almost identical in composition.

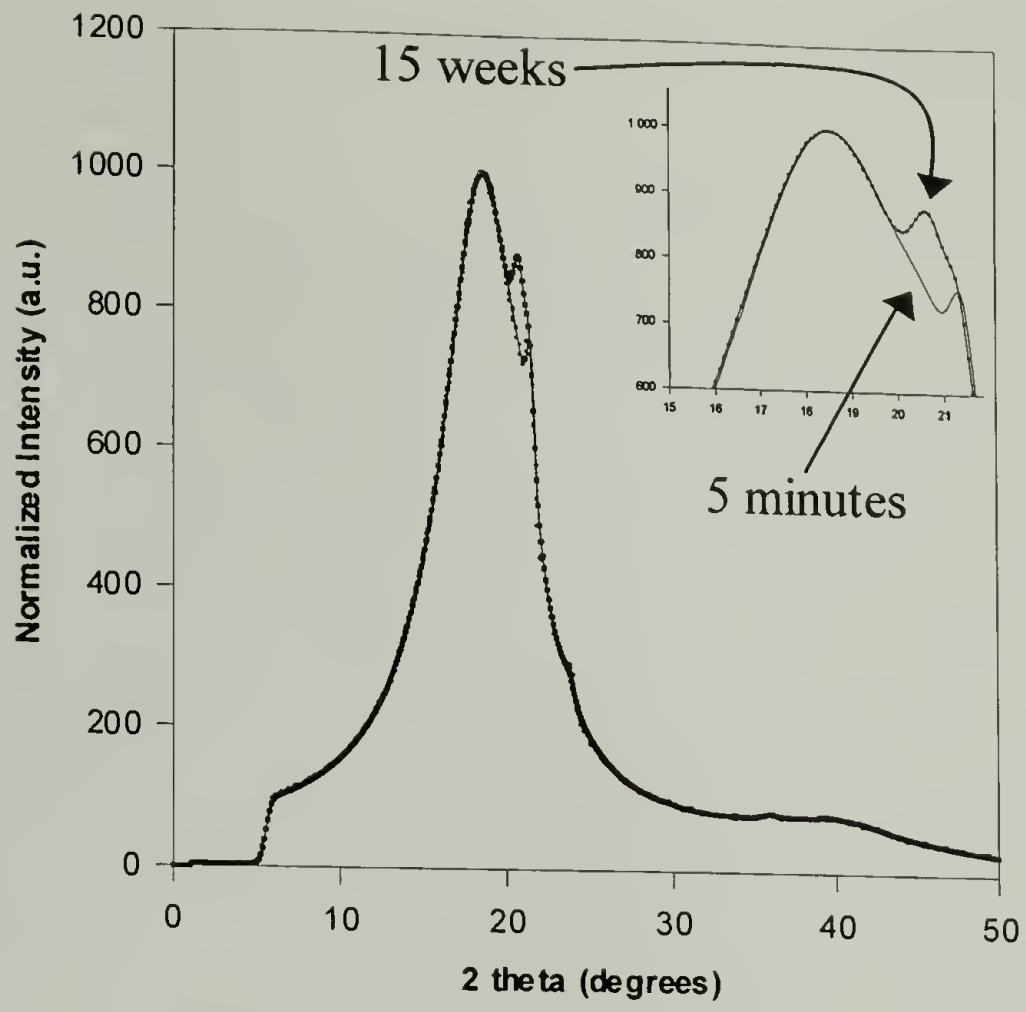

Figure 2.10: Initial and mature diffraction patterns of EP69.0B illustrating development of hexagonal crystal phase

Figure 2.11 shows the WAXD patterns of EP79.8R. Five minutes after solidification only a slight shoulder on the amorphous halo is observed indicating very little crystallinity, which is consistent with DSC results. However, after 15 weeks a sharp peak has developed at 20.67° corresponding to the hexagonal (100) reflection. It should be pointed out that the appearance of the hexagonal phase in these materials is occurring much below the triple point on the traditional PE phase diagram (see Figure 1.1). The occurrence of the hexagonal phase below the triple point has also recently been observed in UHMWPE[12] and ethylene – 1-octene copolymers.[22] This is the first observation of the coexistence of hexagonal and orthorhombic crystals in ethylene – propylene copolymers. Also, the crystal reflections present only correspond to the hexagonal and orthorhombic polyethylene structures; no polypropylene crystal structure is present. It should also be

noted that the amorphous halo shifts to slightly larger 2θ values as the ethylene content is increased.

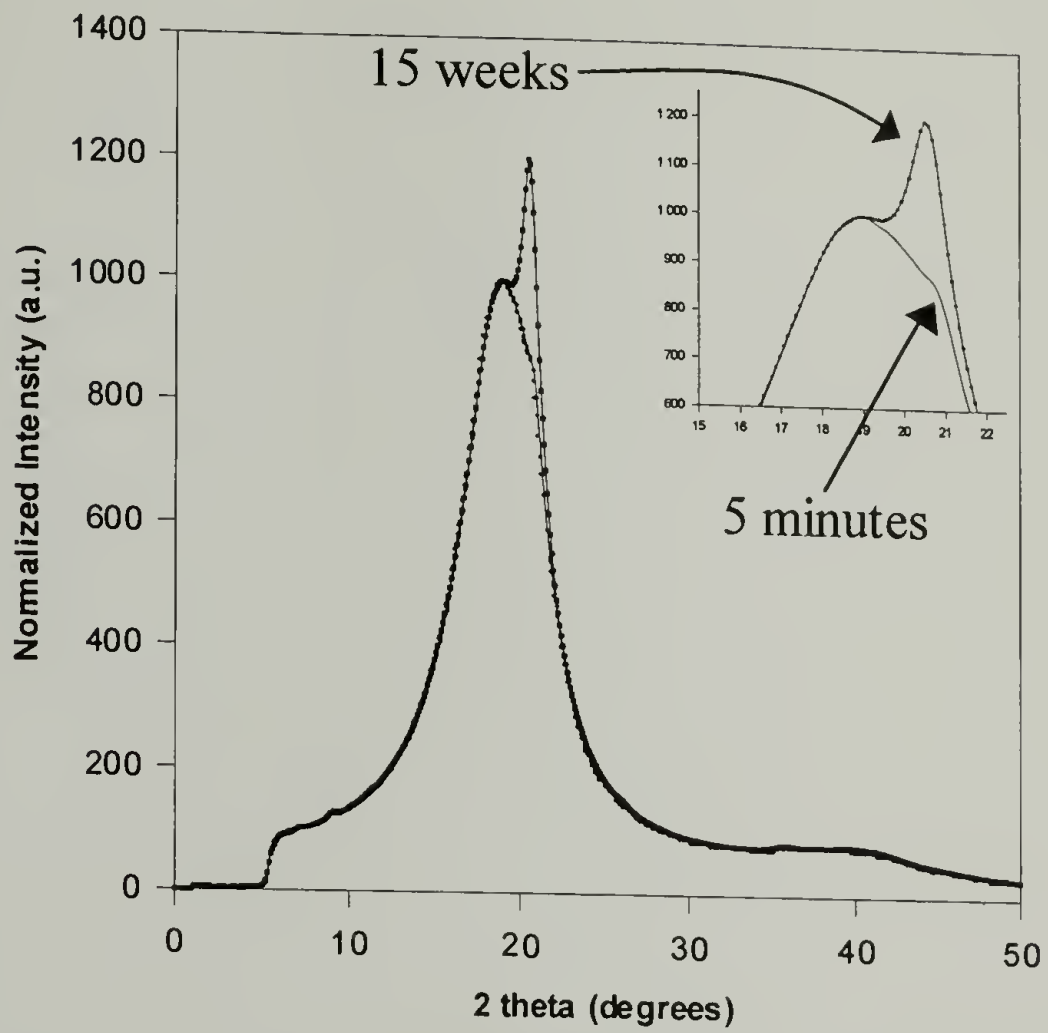

Figure 2.11: Initial and mature diffraction patterns of EP79.8R illustrating development of hexagonal crystal phase

While the ethylene content appears to dictate the mature level of crystallinity, comonomer distribution appears to be the most important parameter in determining crystal structure. This is examined more closely by looking at the crystallization behavior of EP68.6R and EP68.6B where the only difference between these compositions is comonomer distribution. Mature DSC thermograms for these two compositions are shown in Figure 2.12. EP68.6R exhibits only an LT endotherm while EP68.6B exhibits both LT and HT endotherms. Corresponding WAXD patterns at maturity are shown in Figure 2.13. EP68.6R exhibits crystals only in a hexagonal structure whereas EP68.6B exhibits orthorhombic and hexagonal crystals in coexistence. From this analysis, it

appears that the LT melting endotherm is due to melting of hexagonal crystals whereas the HT endotherm is due to melting of orthorhombic crystals.

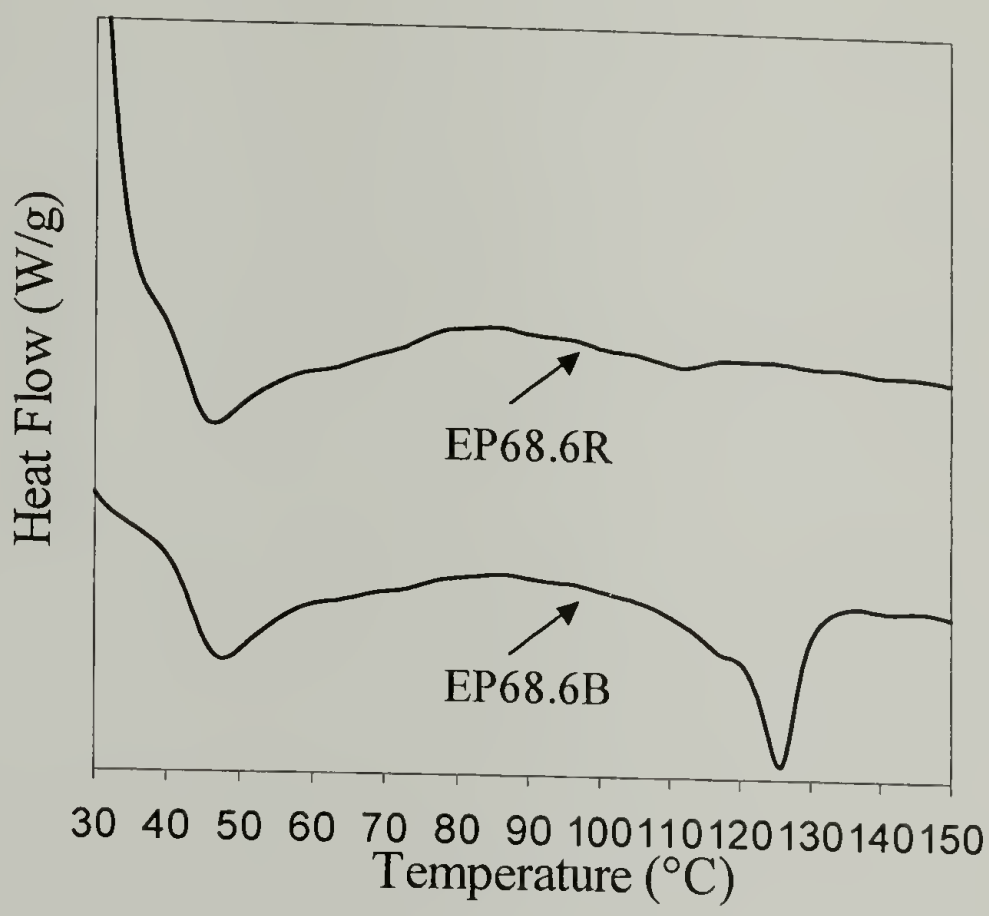

Figure 2.12: Melting behavior of EP68.6R and EP68.6B at maturity

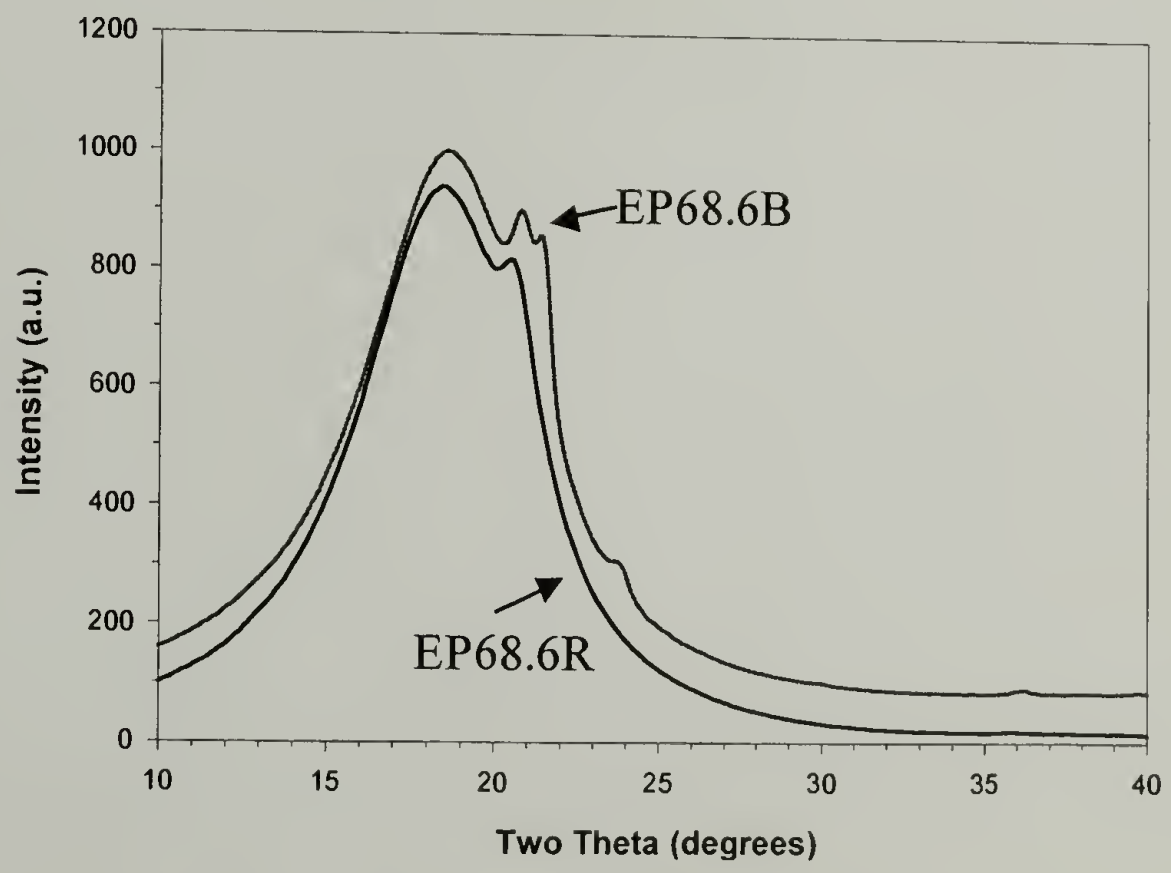

Figure 2.13: Mature diffraction patterns of EP68.6R and EP68.6B illustrating lack of orthorhombic phase for EP68.6R

A copolymer with a blocky comonomer distribution has segments that are composed only of ethylene units and other segments that are composed only of propylene units. As such, the ethylene sequences may be long enough to crystallize into a traditional orthorhombic unit cell for a composition with a blocky distribution. It is generally believed that the minimum CH_2 sequence length to form an orthorhombic crystal is between 22 and 44 units.[55] Methyl side groups can be incorporated into an expanded polyethylene unit cell. The orthorhombic unit cell has three crystallographic directions: a, b, and c where c is along the chain axis. When the orthorhombic unit cell is expanded such that $a = b\sqrt{3}$, the unit cell now has hexagonal structure and symmetry.[69,71] EP79.8R has the lowest branching content at approximately 1 branch for every 10 carbons. This leaves continuous CH_2 sequences that are too short to crystallize into an orthorhombic structure; as a result, only hexagonal crystals are observed in the WAXD patterns for EP79.8R and EP68.6R. Table 2.3 summarizes the various crystal structures present as a function of sample age for all five compositions.

Table 2.3: Crystal structure summary for copolymer compositions after solidification and at maturity

Sample	Initial Crystal Structures	Crystal Structures at Maturity
EP58.1R	Amorphous	Amorphous
EP68.6R	Amorphous	Hexagonal only
EP68.6B	Orthorhombic	Orthorhombic & hexagonal
EP69.0B	Orthorhombic	Orthorhombic & hexagonal
EP79.8R	Amorphous	Hexagonal only

Raman spectra for the four compositions are shown in Figure 2.14. All spectra have been normalized by dividing each by the integrated intensity of its 1295 cm^{-1} band.

The spectral region of interest is between 800 cm^{-1} and 1500 cm^{-1}. Each curve has been shifted vertically in order to easily visualize changes as a function of composition. All samples are 8 weeks old and all exhibit bands typical of polyethylene, which are listed in Table 2.4. It should be noted that for orthorhombic PE, the band at 1440 cm^{-1} (CH_2 bending) is usually split with a band at 1415 cm^{-1} due to the setting angle of the two polymer chains per unit cell. It usually requires at least 5% crystallinity in the orthorhombic phase to cause splitting. For hexagonal PE this splitting is not observed and only a band at 1440 cm^{-1} is observed.[18] In the four compositions examined no splitting band is observed at 1415 cm^{-1}.

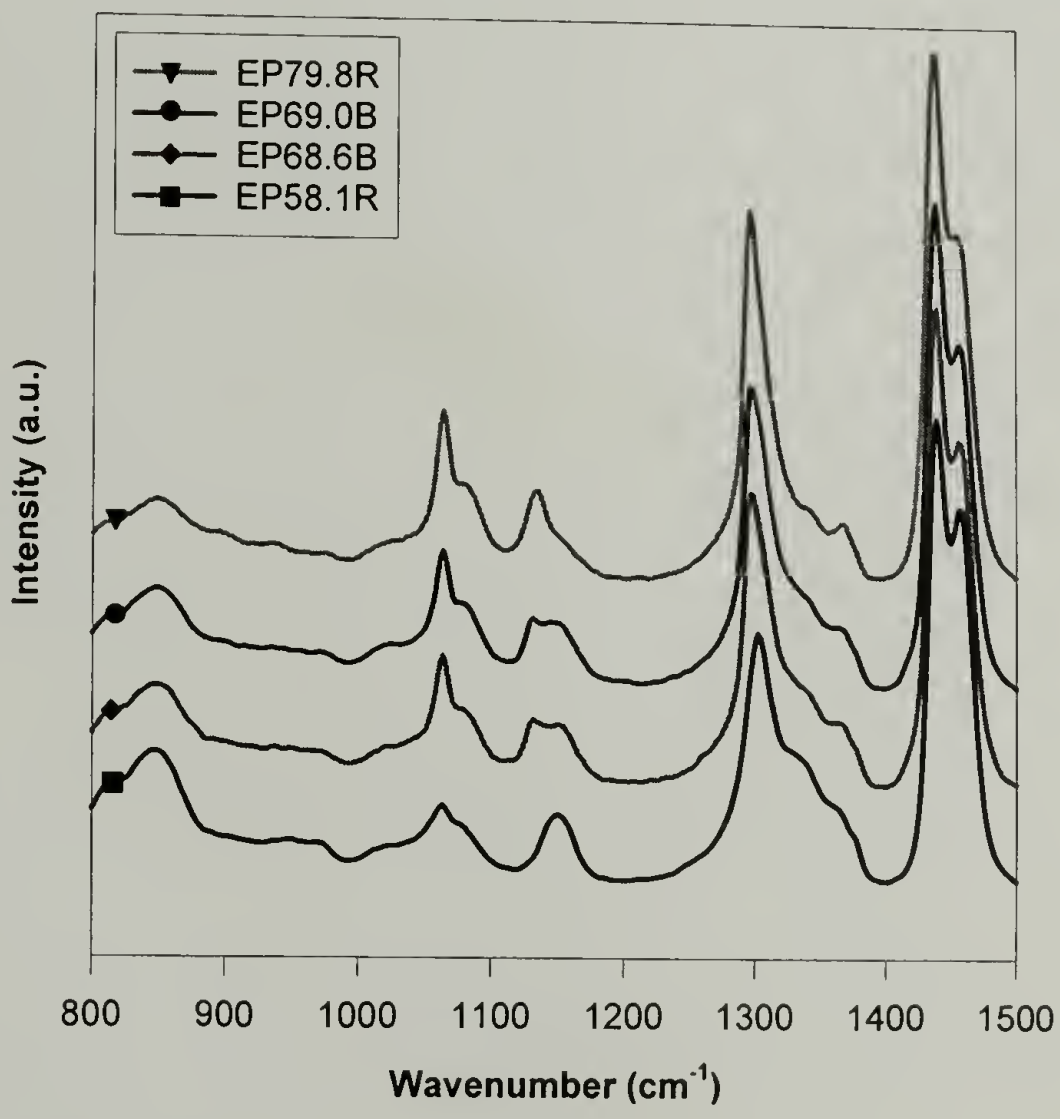

Figure 2.14: Raman analysis of copolymer compositions at maturity

The samples also exhibit a band at 1150 cm^{-1} which changes as a function of composition and is not present in a typical polyethylene spectrum. However, all types of polypropylene (isotactic, syndiotactic, and atactic) exhibit a vibrational band at 1153cm^{-1}. Bands in this region are often indicative of tertiary carbons. The 1153 cm^{-1} band in the polypropylene spectrum has been attributed to C-CH_3 vibrations coupled with skeletal carbon stretching which could be considered as the vibration of the C-C(CH_3)-C group.[21] Since these copolymers have high comonomer contents it is reasonable that the CH_3 side groups would contribute to the vibrational modes of the copolymer. As such, the intensity of the 1150 cm^{-1} band decreases as propylene content decreases.

Table 2.4: Raman bands typical of crystalline polyethylene

Band (cm^{-1})	**Contributing Vibration**
850	Amorphous gauche
1060	Symmetric skeletal stretch
1080	Amorphous gauche
1130	Anti-symmetric skeletal stretch
1297	CH_2 twisting
1415*	CH_2 bending
1440	CH_2 bending

*ocurs only in orthorhombic PE

Temporal Raman measurements are performed to monitor the influence of crystallization on the molecular vibrations. Raman spectra of EP68.6B at one hour and eight weeks after solidification are shown in Figure 2.15 while Figure 2.16 shows the Raman spectra of EP79.8R at five minutes, four hours, and eight weeks after

solidification. It can be observed from both samples that, as crystallization occurs, the 1150 cm^{-1} band remains essentially unchanged. However, the bands corresponding to all-trans skeletal vibrations at 1060 cm^{-1} and 1130 cm^{-1} increase with time, while the band associated with amorphous gauche vibrations decreases with time. This indicates that the polymer chains are becoming extended which would allow for more order. There is still a high fraction of gauche content as seen by the ratio of the 1080 cm^{-1} to 1060 cm^{-1} bands. This could account for the formation of the hexagonal unit cell instead of the orthorhombic as the samples crystallize over time. The hexagonal unit cell can accommodate a large content of gauche conformations while the orthorhombic cannot.

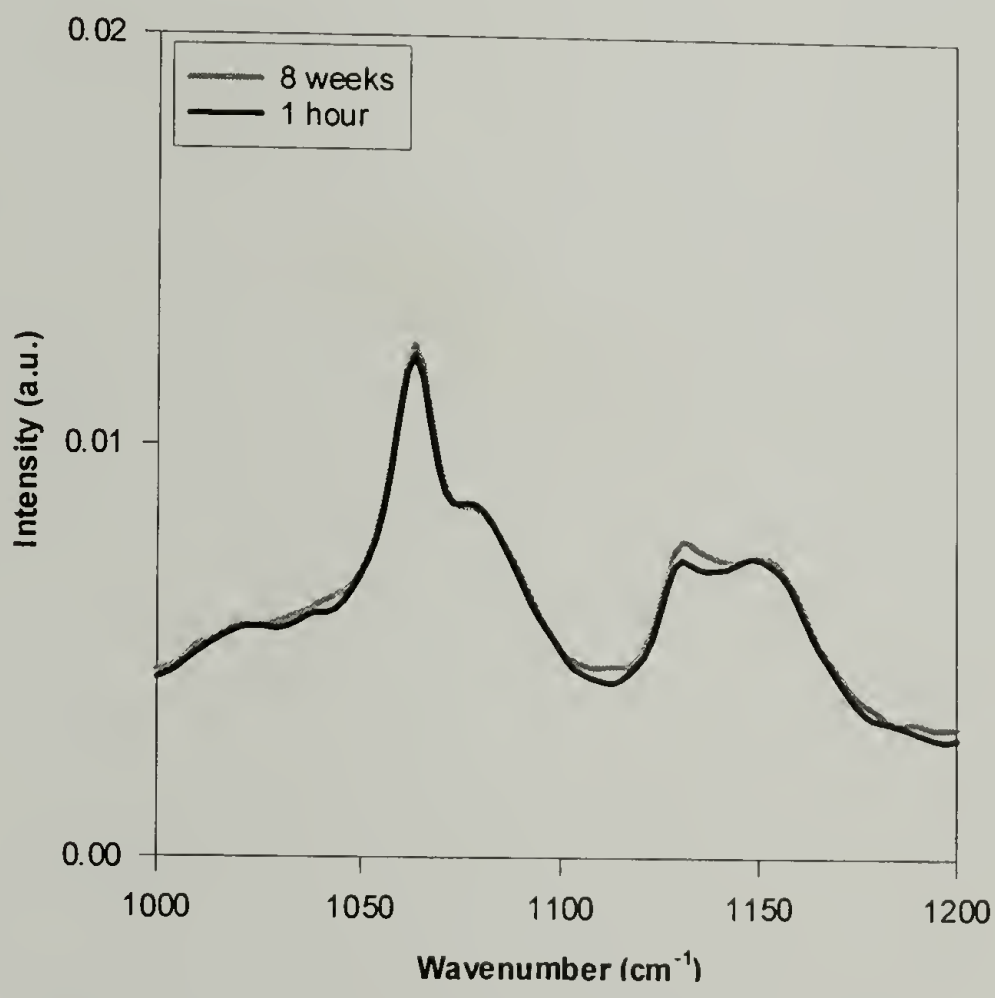

Figure 2.15: Raman analysis of EP68.6B as a function of sample age monitoring crystallization

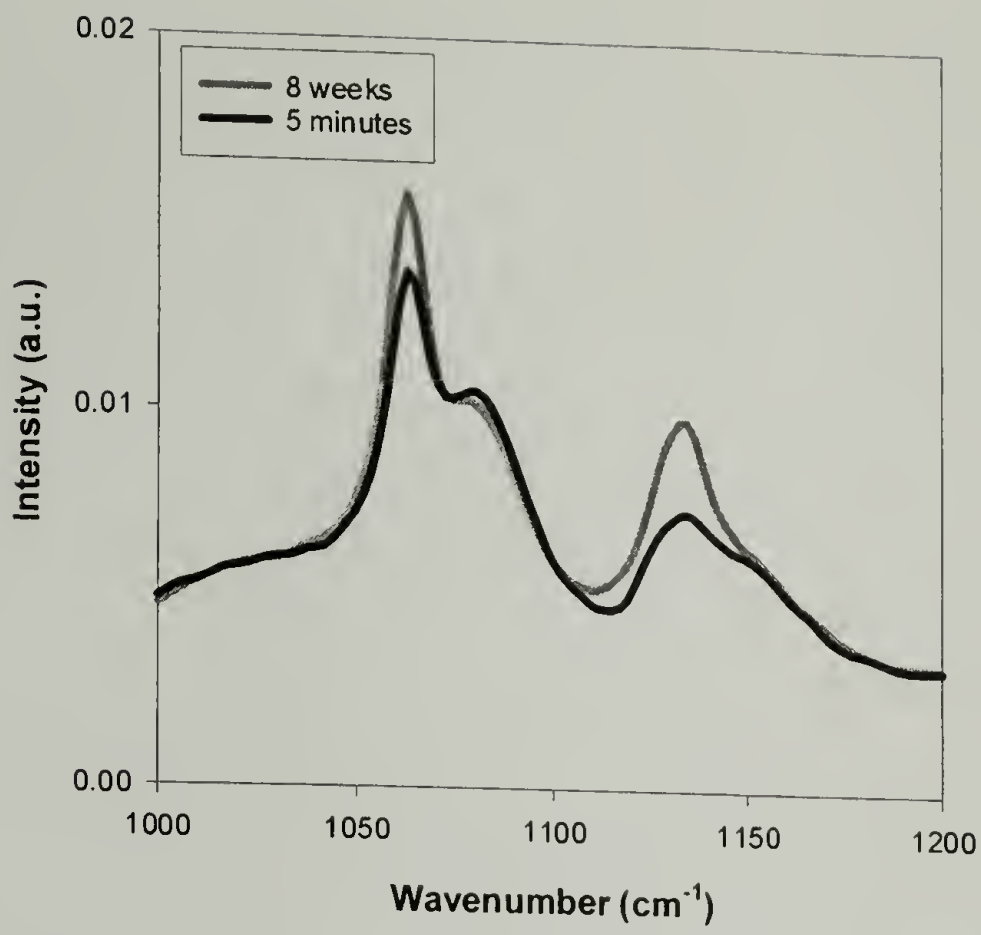

Figure 2.16: Raman analysis of EP79.8R as a function of sample age monitoring crystallization

Crystal dimensions perpendicular to the planes of reflection are calculated from the WAXD patterns using the Scherrer equation as shown below where λ is the wavelength of the incident radiation (1.54 Å), FWHM is the full width at half maximum, and θ is the relevant Bragg angle.

$$d_{\perp} = \frac{0.9\lambda}{FWHM\cos\theta} \qquad (2.1)$$

Line broadening in x-ray diffraction is due to finite crystal dimensions as well as crystal imperfection.[56] Third order reflections are necessary in order to deconvolute the influences of finite dimension and imperfection. Since third order reflections are rare in polymeric materials an approximation of the maximum crystal size will result assuming that all line broadening is due to crystal dimension. From this analysis, maximum

orthorhombic crystal dimensions perpendicular to the (110) reflection is shown in Figure 2.17. The crystals are initially 100 Å in dimension and enlarge slightly as the copolymers with a blocky comonomer distribution age. Likewise, mature hexagonal crystals perpendicular to the (10•0) reflection are approximately 50 Å in dimension as shown in Figure 2.18.

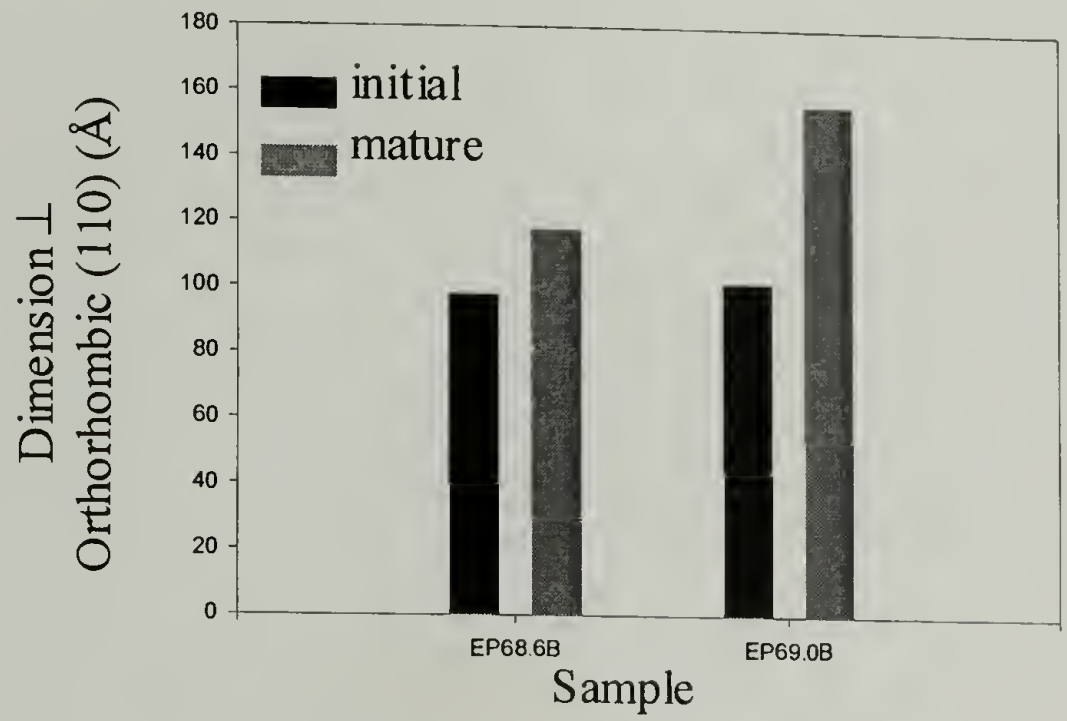

Figure 2.17: Change in orthorhombic crystal size perpendicular to (110) plane

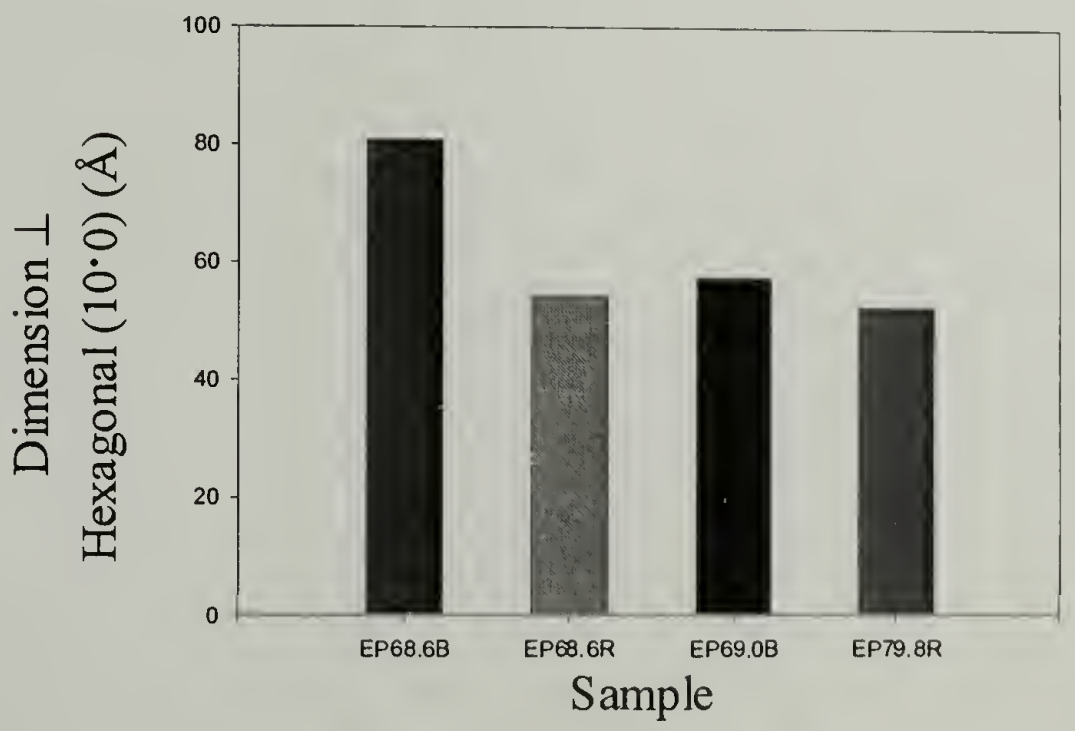

Figure 2.18: Mature hexagonal crystal size perpendicular to (110) plane

Crystal thickness (perpendicular to the (001) plane) can be estimated using the Thompson-Gibbs equation as shown below where γ_e is the theoretical surface energy of a polyethylene crystal, Δh_f is the theoretical heat of fusion, and $T_m(\infty)$ is the melting point of an infinite polyethylene crystal ($\gamma_e = 87.4$ erg/cm^2, $\Delta h_f = 2.79 \times 10^9$ erg/cm^3, and $T_m(\infty) = 414.2$ K).[57]

$$T_m(l) = T_m(\infty) - \frac{1}{l}\frac{2\gamma_e T_m(\infty)}{\Delta h_f} \qquad (2.2)$$

Melting point depression observed in ethylene – α-olefin copolymers with low comonomer contents obey the Thompson-Gibbs relationship.[57] As a result, this type of analysis will be applied to the copolymers herein to estimate crystal thickness. However, the result is merely an approximation since it must be assumed that hexagonal and orthorhombic crystals have the same surface energy. A melting point at approximately 125 °C corresponds to an average crystallite thickness of 167 Å while the melting point at approximately 45 °C corresponds to that of 27 Å.

2.2.4 Densification

Density as a function of sample age is shown in Figure 2.19 for the five compositions investigated. The density of the amorphous reference remains constant at 0.8563 ± 0.0002 g/cc. The other four samples have some initial density that increases rapidly within the first 50 hours and then slows reaching a plateau after 200 hours. An increase in density is expected due to the incorporation of crystallites as the copolymers age. For comparison the densities of amorphous polyethylene and polypropylene are

0.855 and 0.856 g/cc, respectively.[11,58] It appears that the initial densities of the five materials do not obey a rule of mixtures. For example, EP58.1R, EP68.6R, and EP79.8R are all amorphous immediately after solidification however they do not have the same densities.

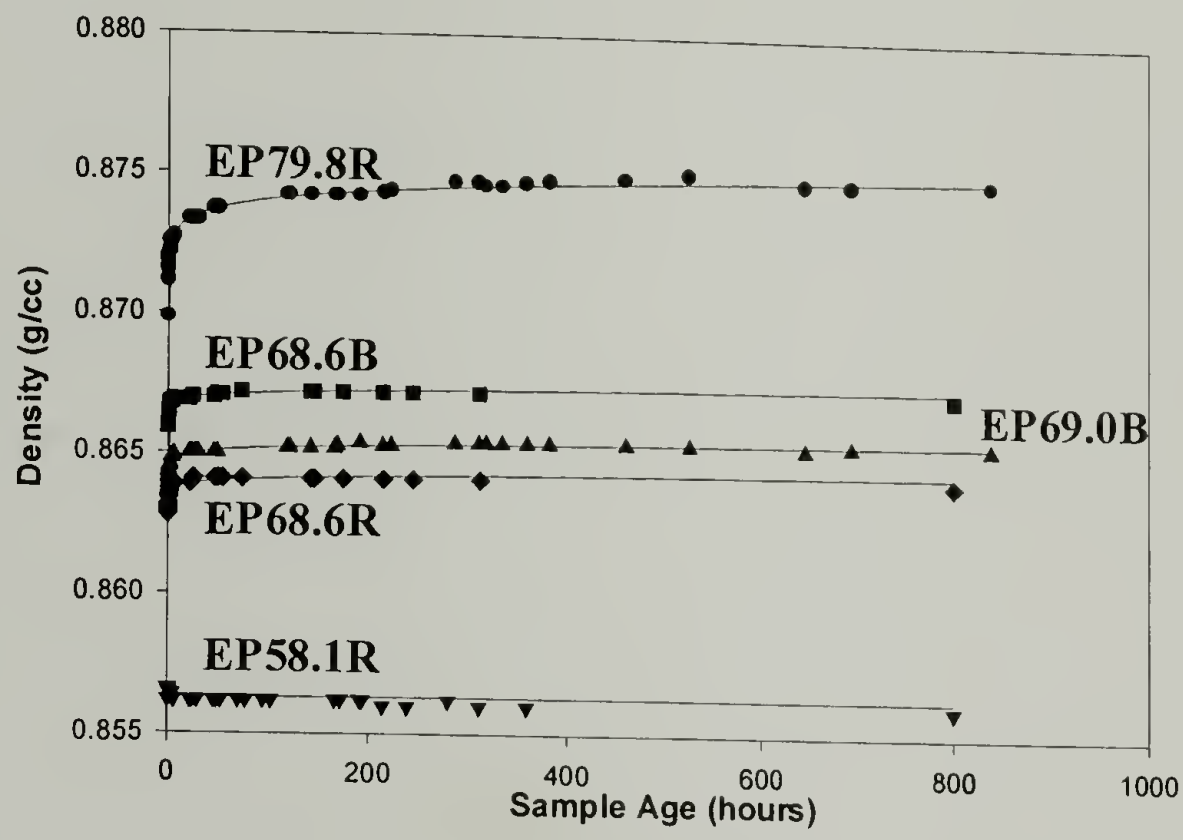

Figure 2.19: Density as a function of sample age for copolymers

Density as a function of branching content is shown in Figure 2.20. Initial density is decreases as branching density increases regardless of degree of crystallinity. If the regression for initial density is extrapolated to 333 branches per 1000 C (the branching density for linear polypropylene homopolymer) an amorphous density of 0.842 g/cc is calculated. This is slightly lower than the reported amorphous density for polypropylene of 0.855 g/cc. Samples EP68.6R, EP68.6B, and EP69.0B are all very similar in composition and initial density. As aging occurs, density increases commensurately with increasing content of hexagonal crystals.

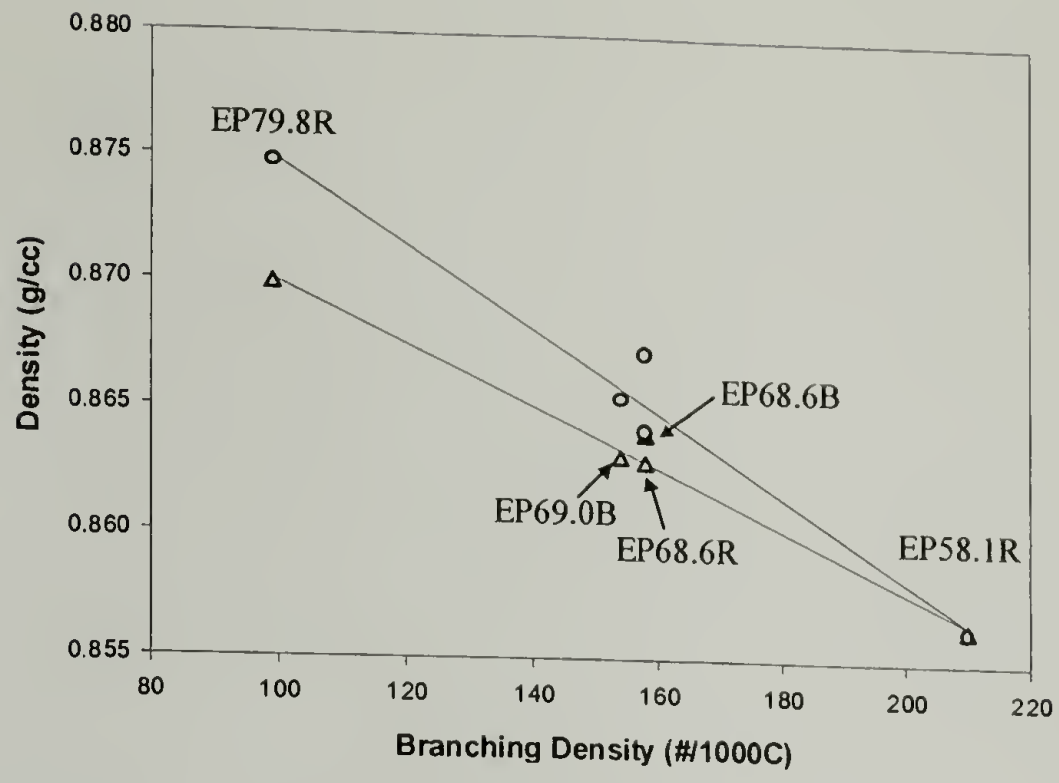

Figure 2.20: Initial (Δ) and mature (O) densities as a function of branching content

Figure 2.21 shows a correlation between the LT heat of fusion associated with hexagonal crystal melting and increasing density of EP69.0B. No correlation exists between the HT heat of fusion associated with orthorhombic crystal melting and increasing density. Perfect superposition of the hexagonal and orthorhombic responses is observed in the total heat of fusion as a function of density.

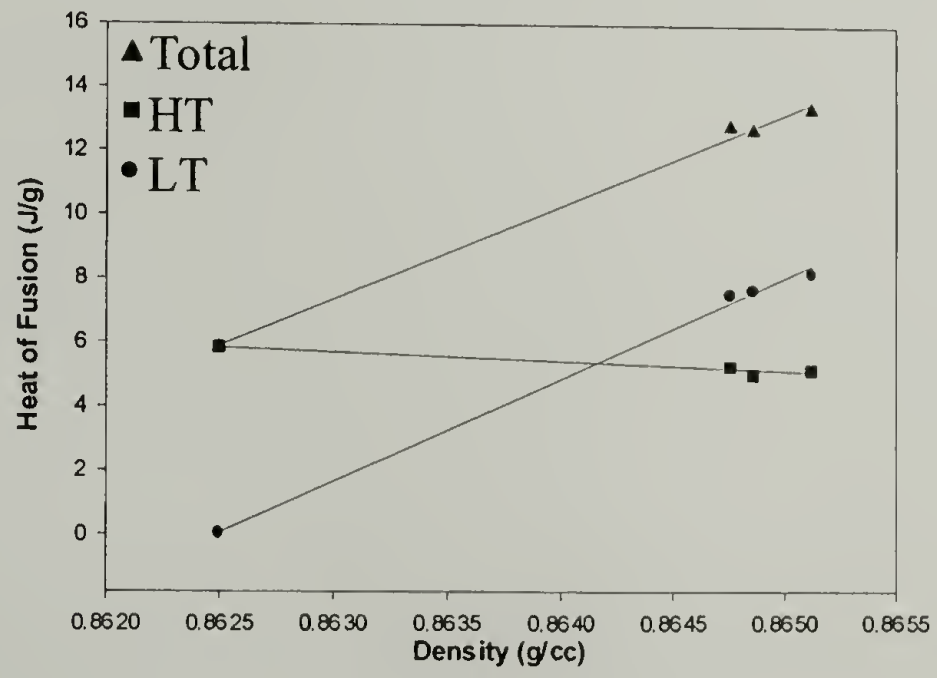

Figure 2.21: LT and HT heats of fusion as a function of density for EP69.0B

This suggests an empirical relationship for density where the initial density is solely a function of branching content and an increase in density is dictated by hexagonal crystal incorporation. For these materials, branching content is related to comonomer incorporation. As a result the following empirical equation is deduced for density as a function of comonomer and hexagonal crystal contents.

$$\rho = (0.062\frac{mol\%_{PE}}{100} + 0.820) + (\frac{0.00262}{2.87} Hex_{\%}) \qquad (2.3)$$

Figure 2.22 again plots density as a function of sample age. The dark symbols correspond with predicted density values from equation 2.3. The densities of EP58.1R, EP69.0B, and EP79.8R are predicted within experimental error. However, no distinction can be made between EP68.6R, EP68.6B, and EP69.0B. This is largely due to slight differences in initial density that are evident in Figure 2.20 which become amplified upon aging. The above empirical relationship does not capture the subtle differences within this narrow compositional range.

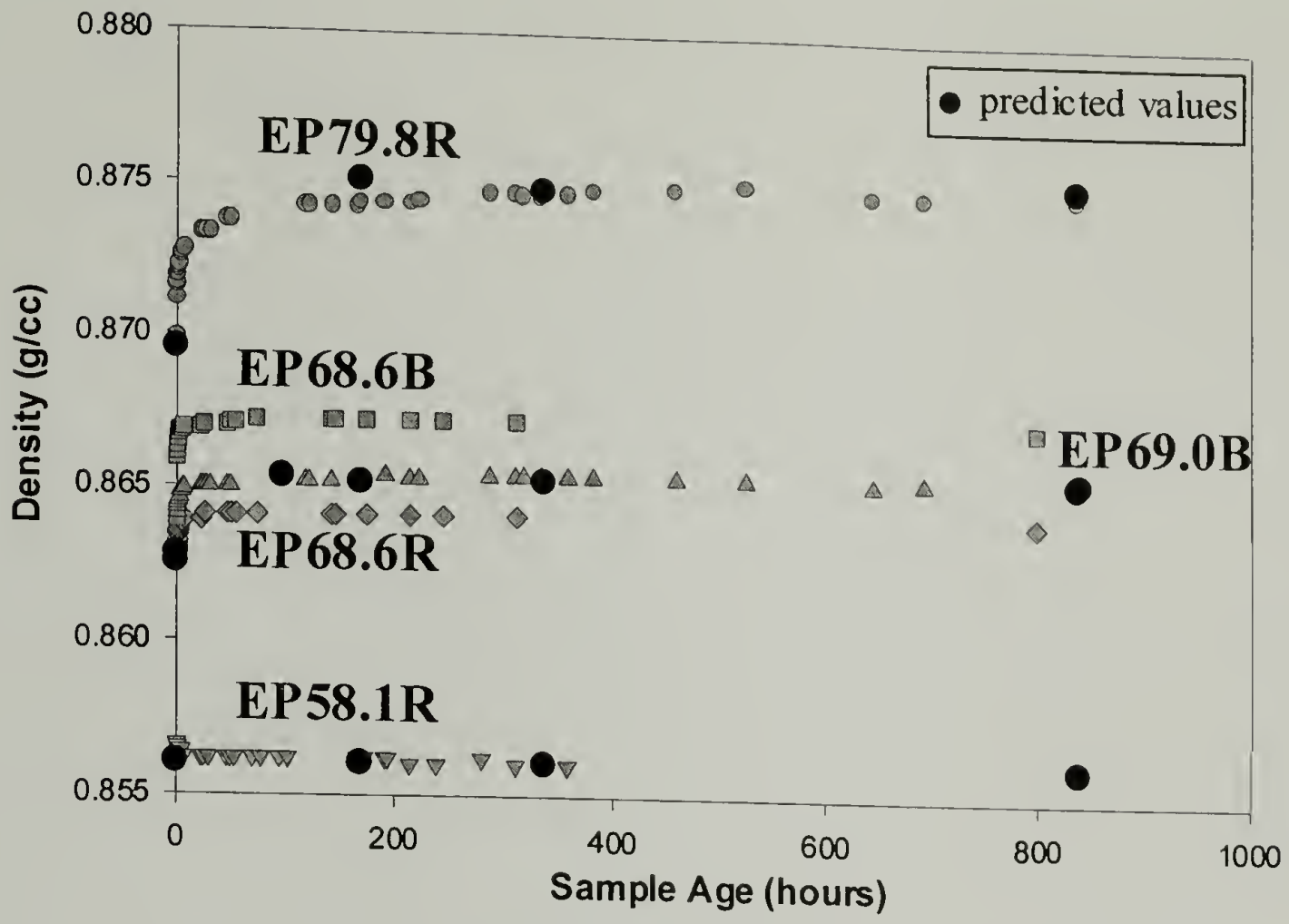

Figure 2.22: Predicted densities as a function of sample age

The fact that the initial density is independent of crystallinity may suggest the presence of a densified amorphous phase that is in between crystalline and amorphous. Crystallinity calculations based on density and heat of fusion measurements have not agreed for other ethylene – α-olefin copolymers. This has been attributed to crystallinity associated with both the crystal and the interfacial regions contributing to density measurements whereas the heat of fusion associated with the crystal only contributes to DSC measurements.[59,60] A densified amorphous phase may be similar to that which composes the interfacial region between a crystal and the surrounding amorphous material. A non-crystalline densified amorphous phase is observed in drawn polyethylene[61] and quenched polypropylene.[62,63] These non-crystalline densified amorphous phases are characterized with many techniques; all suggest the existence of an ordered amorphous phase that some have described as paracrystalline or smectic.[61,62]

This ordered amorphous phase in polypropylene exhibits a density (0.88 g/cc) in the range of those observed for the ethylene-propylene copolymers in this study. The ordered amorphous phase of polypropylene appears in x-ray diffraction as a very broad, low intensity peak at a 2θ value higher than the amorphous halo. This indicates a state of aggregation greater than that attained by a purely amorphous sample which possesses only an amorphous halo.[63] A low intensity reflection is observed in the WAXD data (Figures 2.8-2.11) at a 2θ of approximately 38° which corresponds to a d-spacing of 2.37Å. It is difficult to distinguish this reflection as that from a separate phase; however, *in situ* drawing studies (discussed in section 2.4) suggest that the length scale responsible for this reflection becomes highly oriented.

The morphology of the copolymers is examined using TEM as a function of comonomer distribution and sample age. TEM micrographs are shown in Figures 2.23-2.25 for EP58.1R, EP69.0B, and EP79.8R all at maturity; Figure 2.26 is a micrograph of EP79.8R that was stained and microtomed immediately after solidification. The RuO_4 stain should crosslink the amorphous regions thus preventing further crystallization. The amorphous reference, EP58.1R, shown in Figure 2.23 appears featureless.

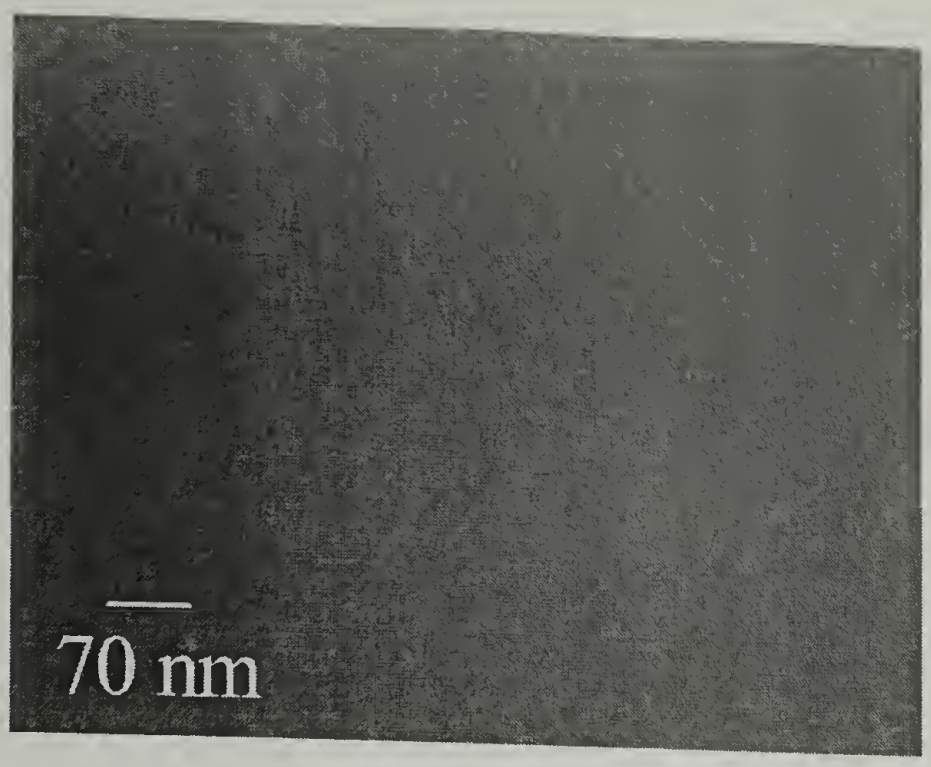

Figure 2.23: TEM micrograph of mature EP58.1R

A uniformly granular structure is observed for EP69.0B and EP79.8R both at maturity in Figures 2.24 and 2.25, respectively. The granular structure of EP79.8R appears slightly finer than that of EP69.0B.

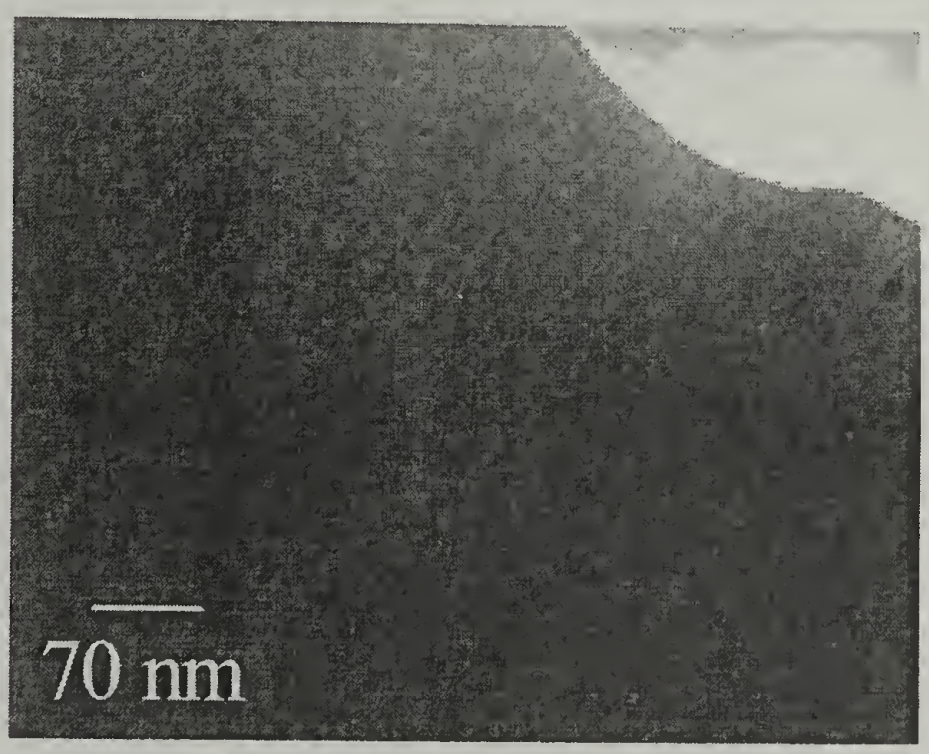

Figure 2.24: TEM micrograph of mature EP69.0B with uniformly granular structure observed

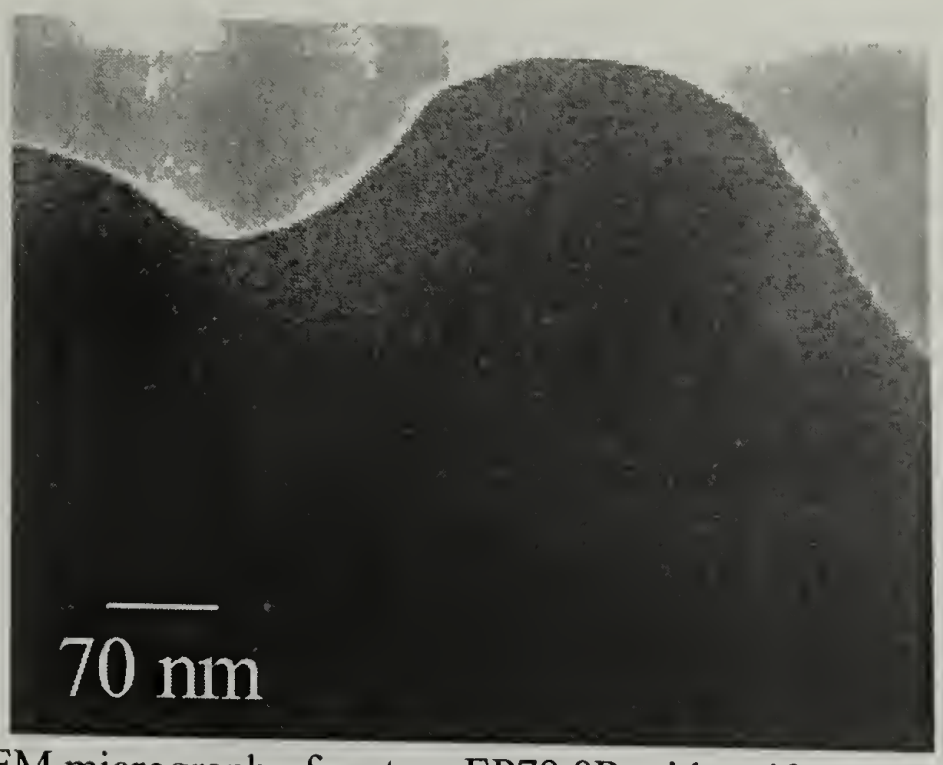

Figure 2.25: TEM micrograph of mature EP79.8R with uniformly granular structure observed

The initial morphology of EP79.8R is shown in Figure 2.26. Again a uniformly granular structure is observed.

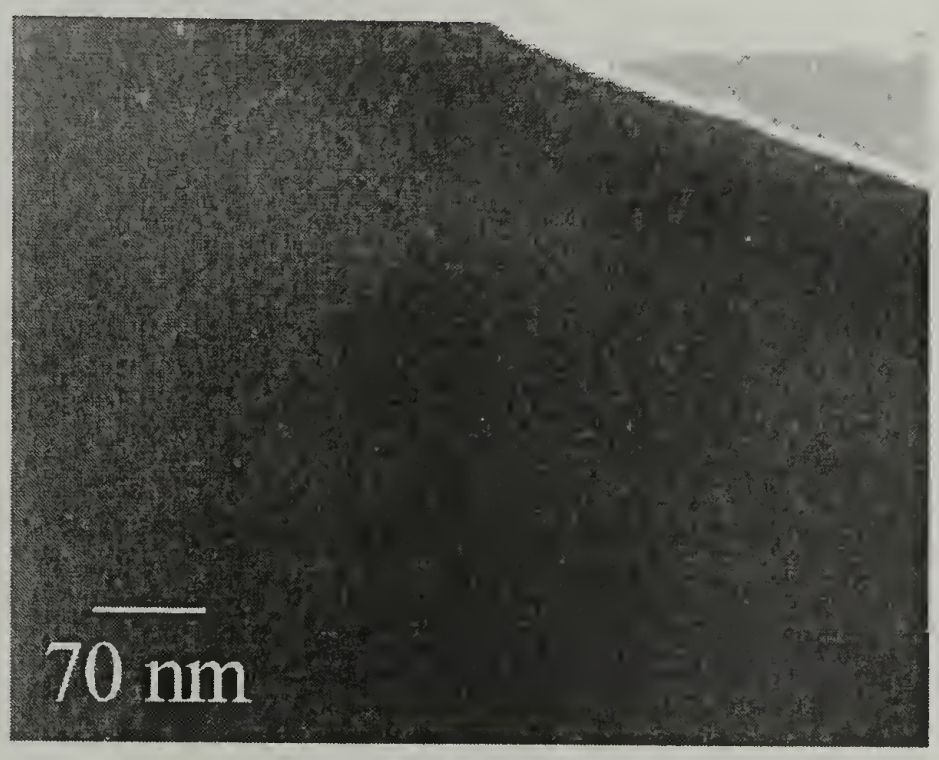

Figure 2.26: TEM micrograph of EP79.8R after solidification with uniformly granular structure observed

A similar granular structure has also been observed in ethylene – octene[10] and ethylene – propylene[9] copolymers. In ethylene – octene copolymers, the granules appear

to be aligned in beaded strings approximately 120 Å thick. The granules are assumed to be bundles of crystallized chain segments possibly resembling a fringed micelle concept.[10] The granular structures observed for the copolymers herein are approximately 150 Å in diameter which is of the same order of magnitude as that observed previously. However, since EP79.8R is initially amorphous and a granular structure is still observed, it is not directly evident that the observed structure is entirely due to crystallinity. Perhaps the structure is indicative of a densified amorphous phase that absorbs the RuO_4 stain at a different rate.

Figures 2.27-2.30 show TEM images of the same four samples at higher magnification. Again, the amorphous reference appears featureless in Figure 2.27. Structure in the form of unstained striations is evident in Figures 2.28 and 2.29 for both EP69.0B and EP79.8R at maturity.

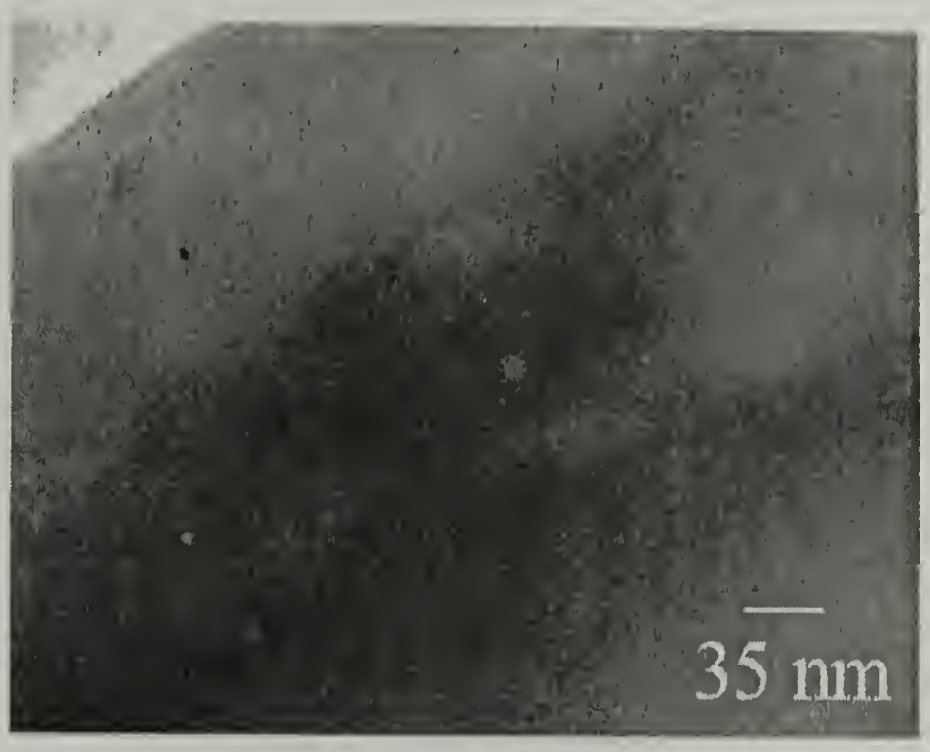

Figure 2.27: TEM micrograph of mature EP58.1R at high magnification

Figure 2.28: TEM micrograph of mature EP69.0B at high magnification

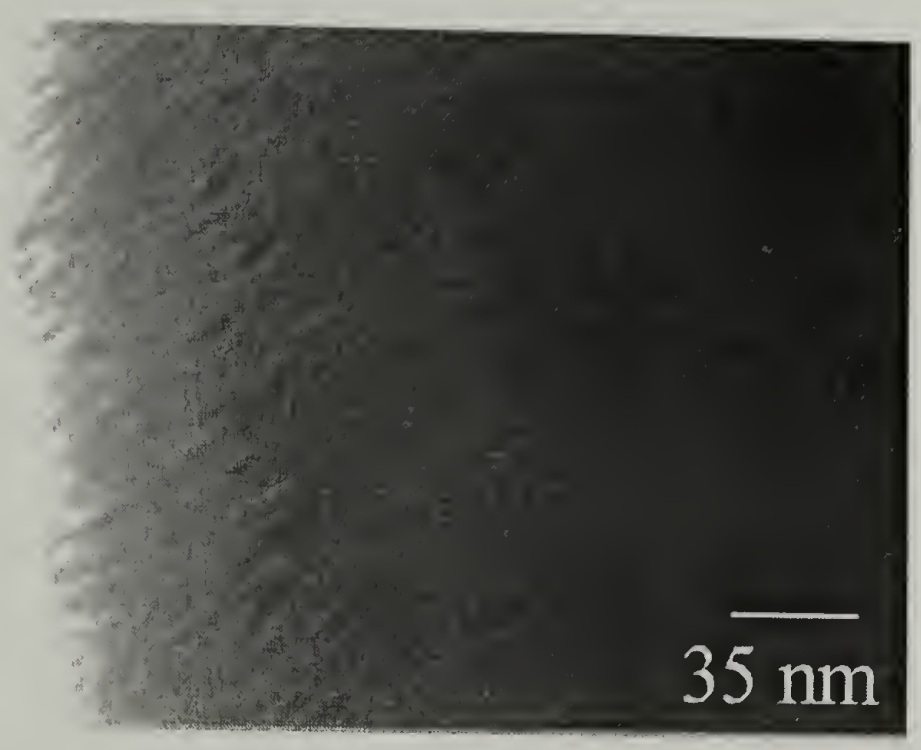

Figure 2.29: TEM micrograph of mature EP79.8R at high magnification

The striations appear to have some preferential alignment. The striations are approximately 50 Å in thickness and 150 Å in length. Structure is also observed in Figure 2.30 which shows the morphology of EP79.8R stained initially after solidification; this structure however appears smaller, less defined, and less oriented. In the initial morphology of EP79.8R, the striations are approximately 20 Å thick and 65 Å in length.

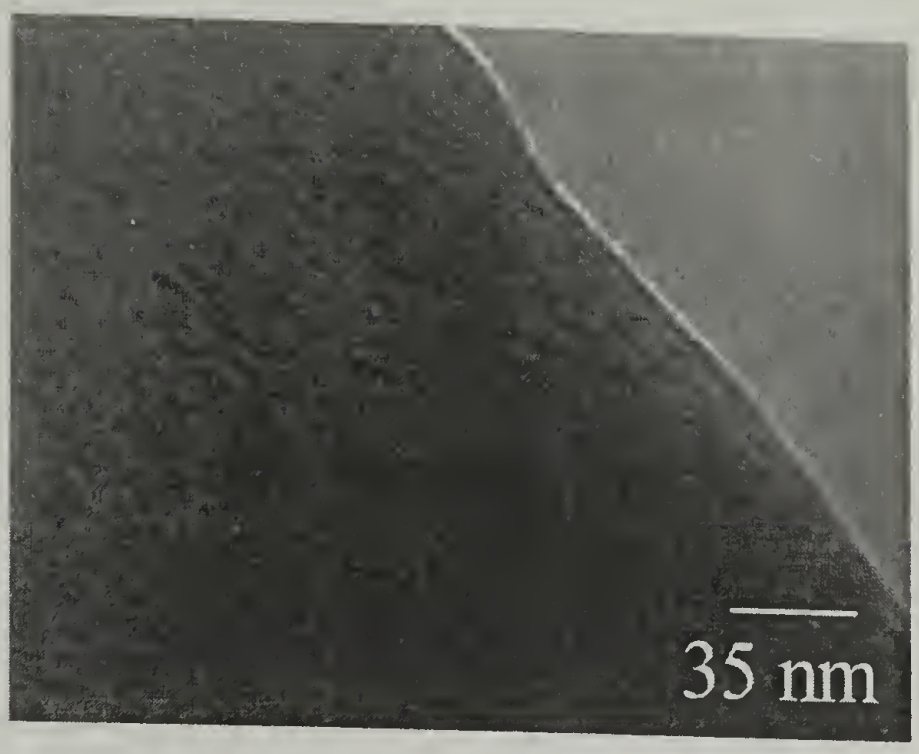

Figure 2.30: TEM micrograph of EP79.8R after solidification at high magnification

As described earlier crystal dimensions of the hexagonal crystals perpendicular to the (10•0) plane are estimated at 60-80 Å from line broadening in the WAXD patterns. Perhaps the striations viewed in Figures 2.28-2.30 are structures associated with hexagonal crystallinity. Structures of this length scale have not been reported previously since most morphological analyses have focused on copolymers with longer branches. Branch length directly influences the crystal structures present. It is generally thought that propyl and larger branches are excluded from the polyethylene unit cell whereas methyl branches can be accommodated by the unit cell. The incorporation of ethyl branches can be controlled by crystallization conditions.[64] Formation of the hexagonal crystal structure in ethylene – propylene copolymers is due to incorporation of methyl branches into the polyethylene unit cell while slightly enlarging its dimensions.

2.3 Mechanical Behavior Evaluation

2.3.1 Experimental Procedures

Tensile tests are conducted on an Instron 1123. Monotonic and cyclic tensile tests are conducted at a crosshead speed of 5 mm/min unless otherwise noted. All reported strains are calculated from crosshead displacement. Samples are compression molded into 3 mm thick plaques at 190 °C and a pressure of 3.5 MPa for approximately 20 minutes and water-cooled in the melt press. Tensile specimens are cut to an ASTM D638 type V geometry. Tests at different temperatures are conducted inside an environmental chamber with controlled heating and cooling capability within the Instron.

Cyclic compression tests are conducted on an Instron 1123 at a crosshead speed of 0.5 mm/min. Compression samples are prepared in accordance with ASTM D575 using the compression molding protocol described above. Compression platens are lubricated with silicone oil to minimize friction. Samples are cycled under load control with a peak value of the stress is equivalent to that at 50% strain on a first loading excursion.

Dynamic mechanical testing is performed at 1 Hz on a modified Dynastat (schematic shown in Figure 2.31). The Dynastat has a load frame with an air-supported piston driven by an electromagnetic motor.[65] A closed servo loop ensures stability of the piston and its motion. The instrument can interrogate high frequencies similar to a traditional DMTA, however, larger strains can also be achieved akin to a servo-hydraulic Instron. The original analog function generator for the Dynastat has been removed and the instrument is interfaced with a computer via a digital to analog converter. LabView software not only generates the waveform but also collects the incoming signals from the

load and displacement transducers. In order to remove the stress-softening response (Mullins effect), fifteen cycles are performed at each strain amplitude. Only the last two cycles are used to investigate the Payne effect under steady-state deformation. Samples are first compression molded in accordance with the above protocol and are tested in a tensile loading geometry.

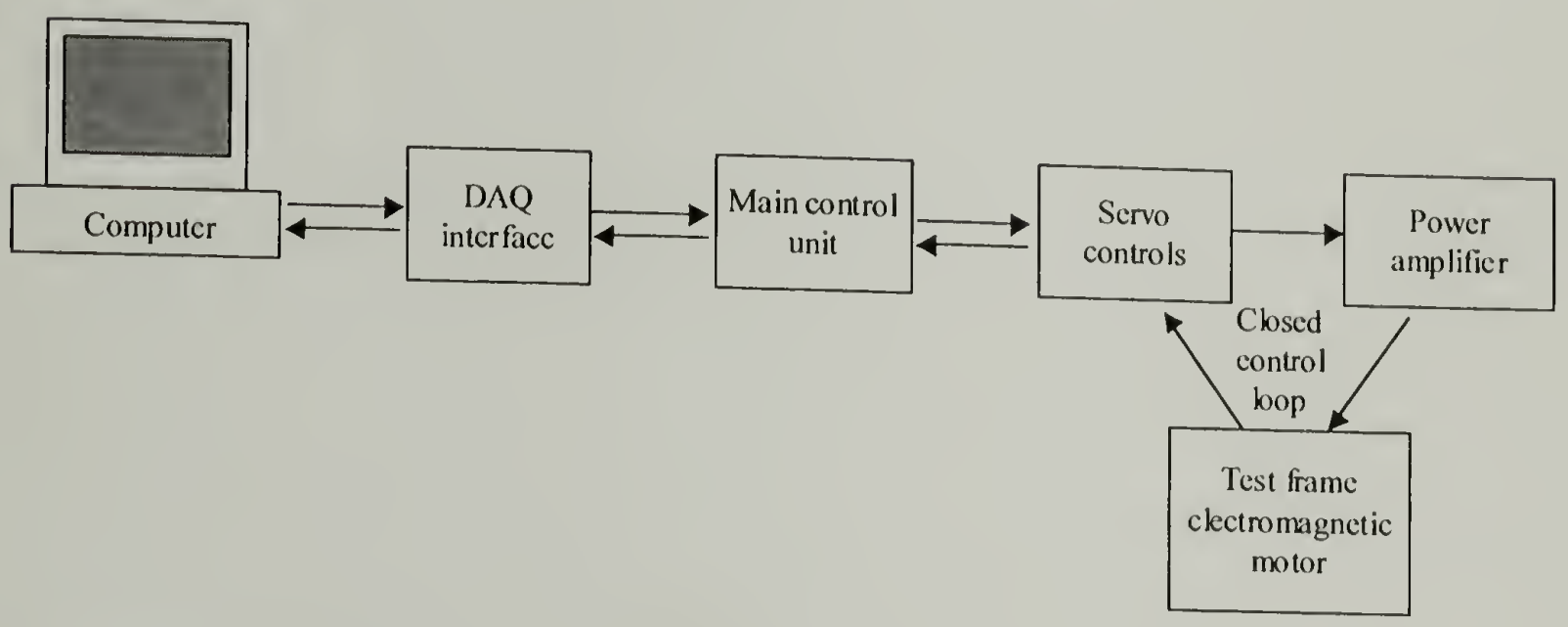

Figure 2.31: Schematic of modified Dynastat – dynamic mechanical testing apparatus

2.3.2 Static Loading

Since the copolymers anneal at room temperature, it is necessary to examine how the aging process affects mechanical behavior as a function of time. Figures 2.32-2.35 show engineering stress-strain curves for four of the compositions, each as a function of time. The stress-strain curves for the amorphous reference, EP58.1R, are shown in Figure 2.32. Over a five-week period the modulus ranges from 0.33 MPa to 0.65 MPa with an average value of 0.47 ± 0.12 MPa. This composition resembles a viscous fluid and as such the compression-molded plaque thins in some regions and not in others

which accounts for the unexplainable trend in elongation at failure over the five-week period.

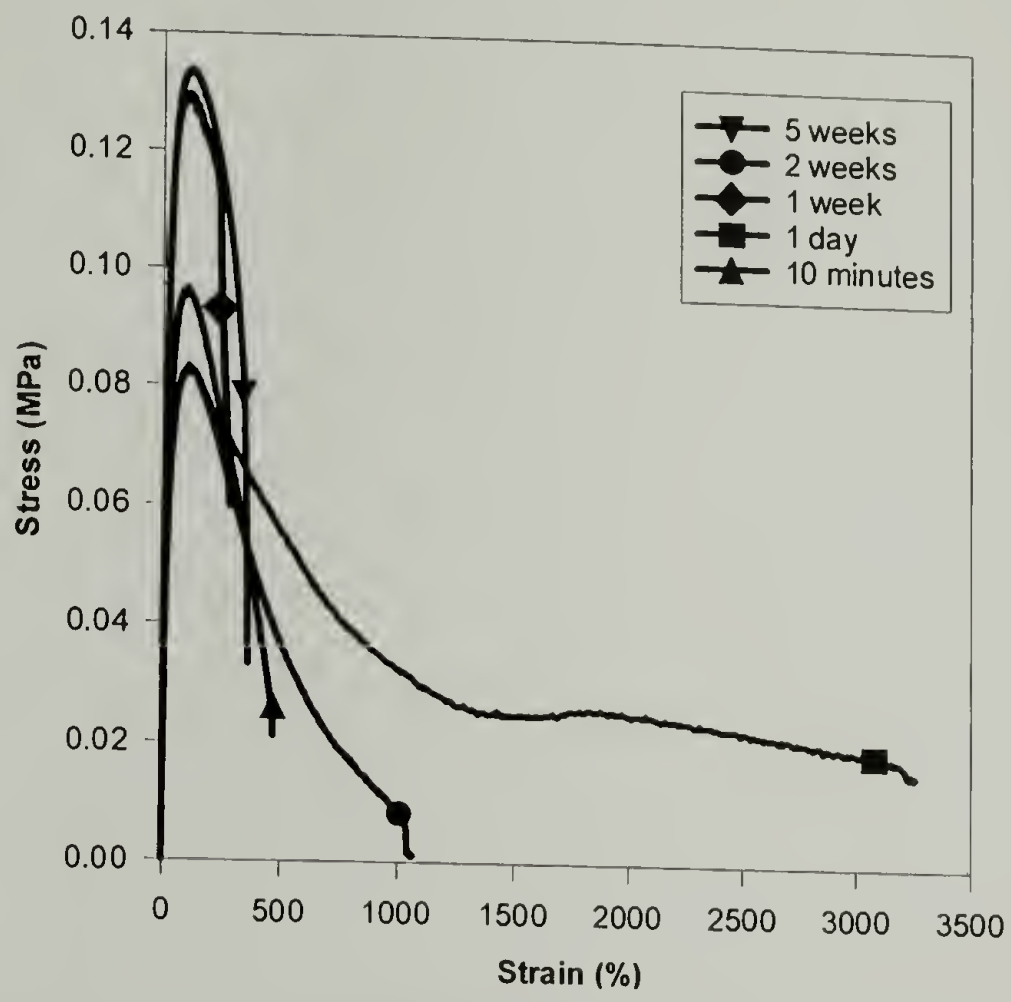

Figure 2.32: Mechanical behavior of EP58.1R as a function of sample age

The engineering stress-strain curves for EP68.6B and EP69.0B are shown in Figures 2.33 and 2.34, respectively. These two compositions behave similarly in the sense that 10 minutes after solidification they are relatively ductile and their moduli are low. As time progresses their moduli increase and they become more brittle which can be explained by increased reinforcement due to the incorporation of crystals. The modulus of EP68.6B is consistently higher than that of EP69.0B at all ages, which is also consistent with slightly higher amounts of crystallinity observed in DSC.

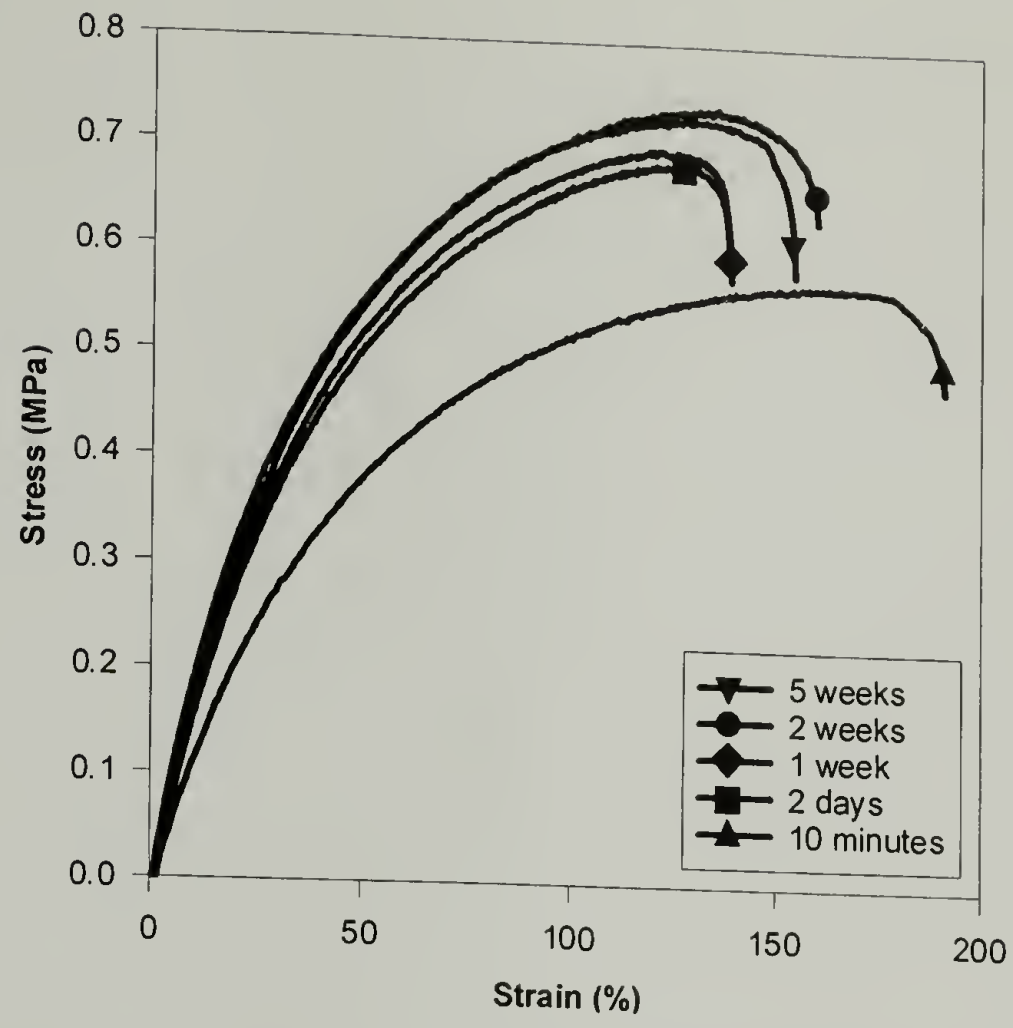

Figure 2.33: Mechanical behavior of EP68.6B as a function of sample age

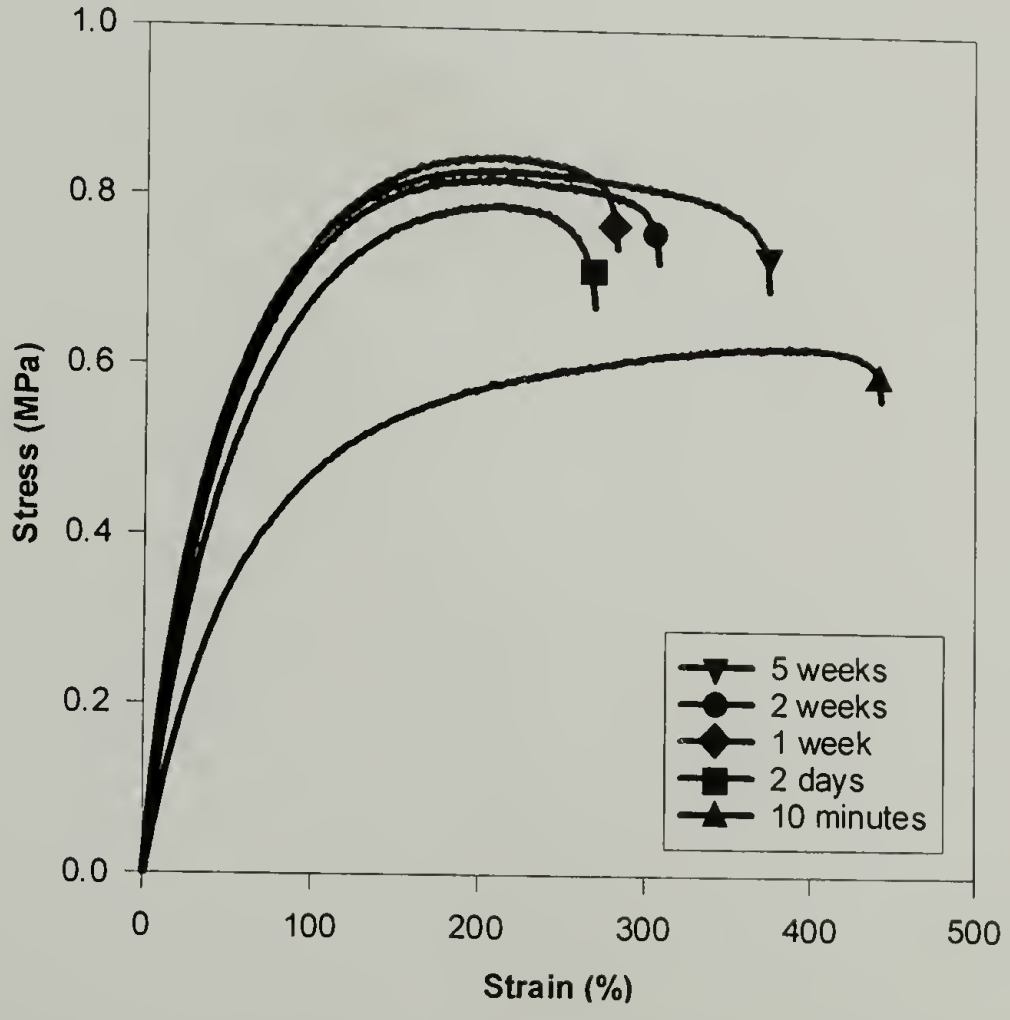

Figure 2.34: Mechanical behavior of EP69.0B as a function of sample age

The engineering stress-strain curves for EP79.8R are shown in Figure 2.35. This sample exhibits different crystallization kinetics where there is very little crystallinity immediately after solidification and a relatively large amount of hexagonal crystals form over time, eventually giving EP79.8R the highest crystallinity. Ten minutes after solidification the sample has a monotonically increasing stress-strain curve with no distinct yield point. The material is extremely ductile with a high elongation at failure. After one day the modulus has increased and a distinct yield point has emerged. Over a five-week period the modulus and yield stress increase while the elongation at failure remains essentially unchanged.

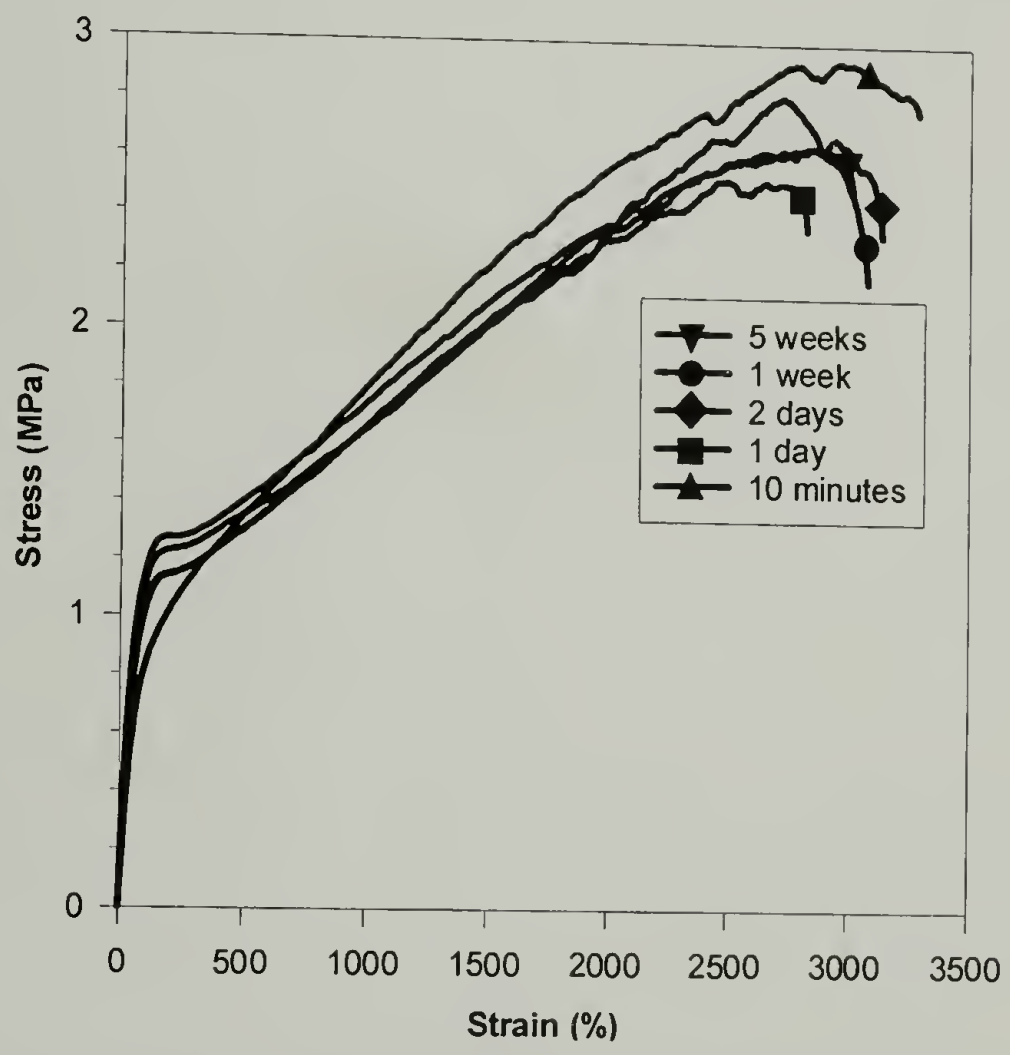

Figure 2.35: Mechanical behavior of EP79.8R as a function of sample age

The mature engineering stress-strain curves for EP68.6B and EP68.6R are shown in Figure 2.36. The only difference between these compositions is their comonomer

distribution. EP68.6R has only hexagonal crystals where as EP68.6B has orthorhombic and hexagonal crystals in coexistence. Both compositions have the same amount of hexagonal crystals as demonstrated by thermal analysis (Figure 2.12). The modulus increases with increasing crystal content regardless of crystal structure. Both compositions also have the same level of ductility despite having different crystal structures.

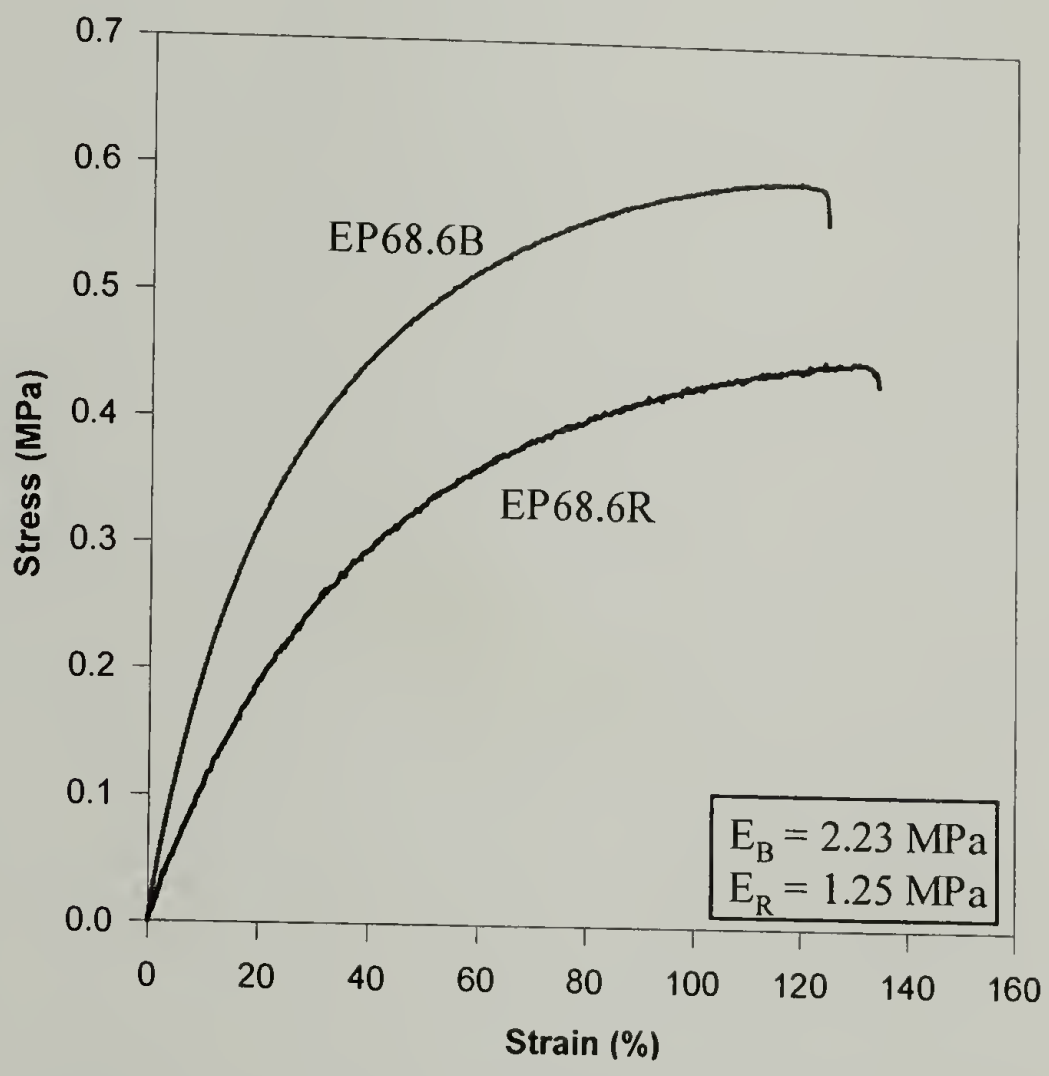

Figure 2.36: Comparison of mature EP68.6R and EP68.6B

Figure 2.37 plots modulus as a function of time for EP58.1, EP68.6B, EP69.0B, and EP79.8R. The modulus of the amorphous reference stays relatively constant over the five-week period while the moduli of the other three samples increase rapidly within the first week. The rate at which the moduli increase after the first week is gradually reduced as the samples mature.

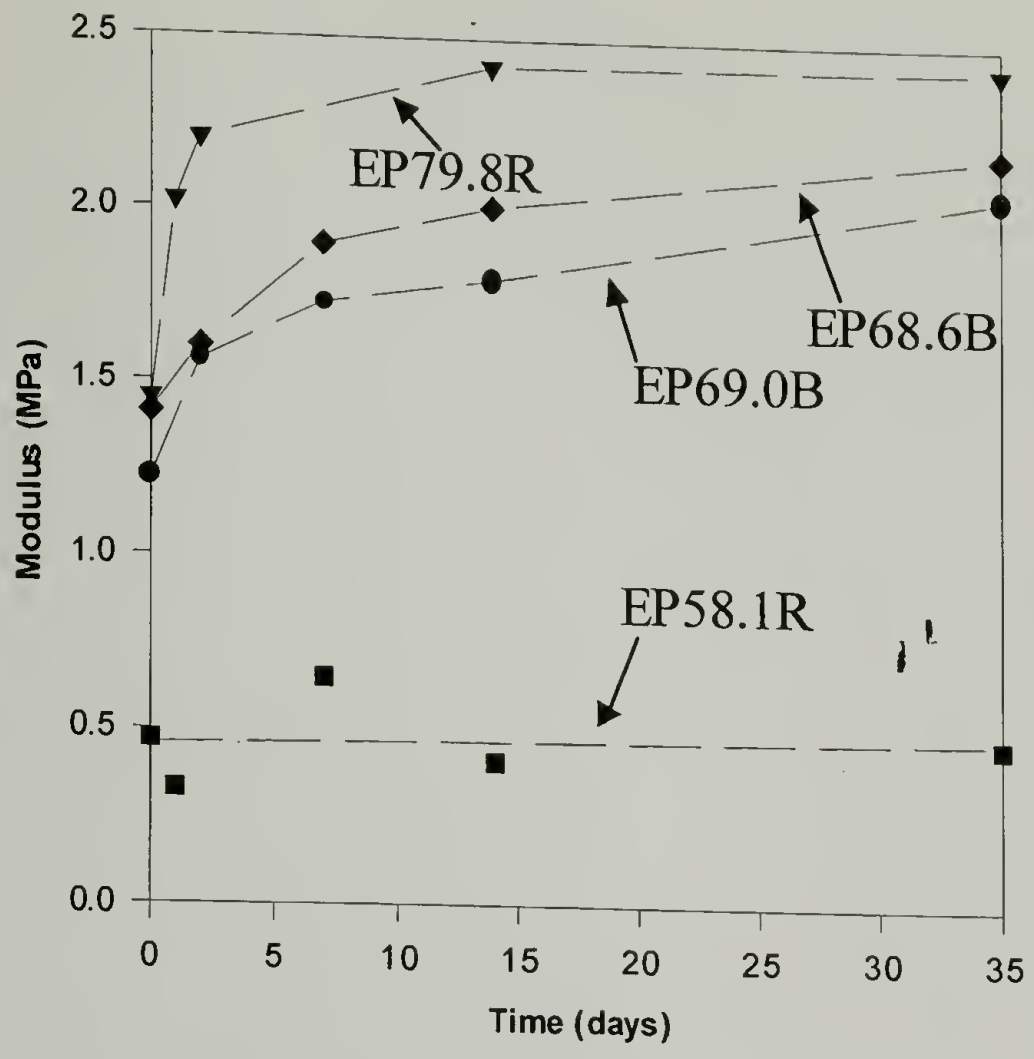

Figure 2.37: Change in modulus with sample age

The copolymers under investigation are being considered as a new class of thermoplastic elastomers. In fact their mechanical behavior is in between that of a true elastomer and a thermoplastic. They exhibit homogeneous deformation (*i.e.*, no visible neck formation) like most elastomers but show "yield-like" behavior similar to thermoplastics depending on composition. Figure 2.38 presents an overlay of the engineering stress versus engineering strain curves for the five compositions. The figure shows their yield responses in relation to composition. It should be pointed out that the full stress-strain curve is not shown for EP79.8R which continues to draw and strain harden. To describe this "yield-like" behavior, the yield point is defined as the point on the stress-strain curve with zero slope. All of the compositions achieve a zero-slope condition at a strain of approximately 175%.

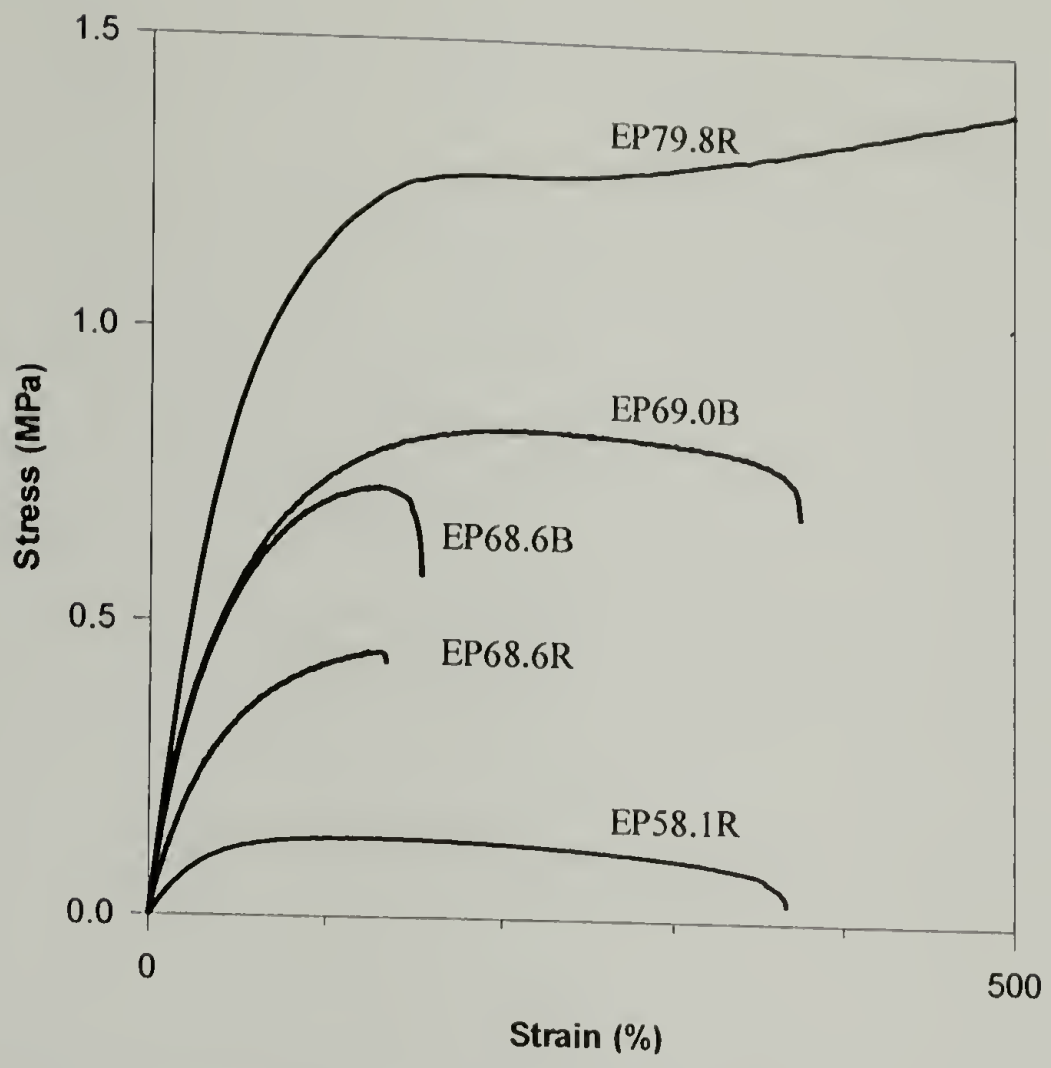

Figure 2.38: Stress-strain behavior of copolymers illustrating yield-like behavior

Yield stress, yield strain, and rupture energy density are monitored as a function of sample age in order to determine correlations with crystal changes. Figure 2.39 plots the yield stress for EP68.6B, EP69.0B, and EP79.8R as a function of time while Figure 2.40 plots the analogous yield strain as a function of time. For all three samples the yield stress increases within the first week and then remains relatively constant as the samples mature. The yield strain shows a different trend. For EP68.6B and EP69.0B yield strain decreases rapidly within the first two days as the samples become embrittled due to additional crystallinity. After two days, however, the yield strain remains constant while the yield stress continues to increase. EP79.8R behaves differently; its yield strain continues to increase within the first week exactly as its yield stress increases. After one week the yield strain of EP79.8R again reaches a plateau.

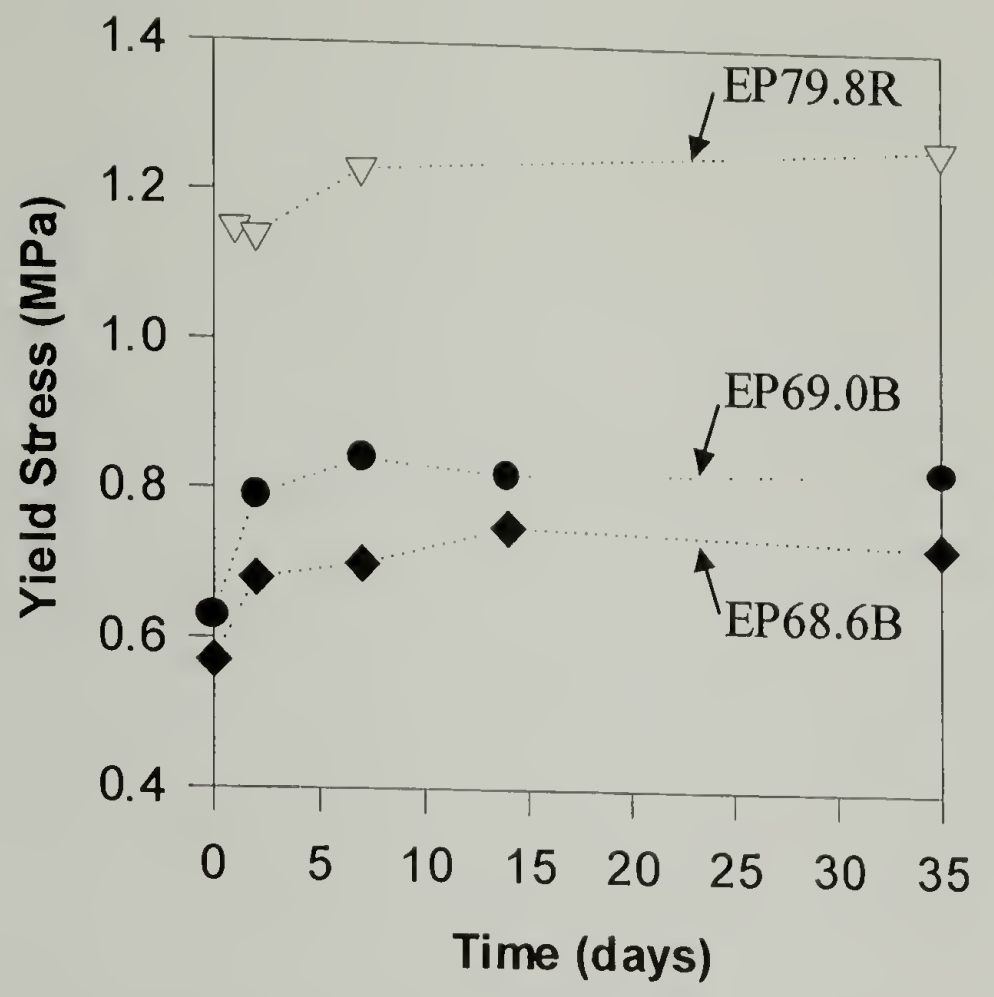

Figure 2.39: Yield stress as a function of sample age

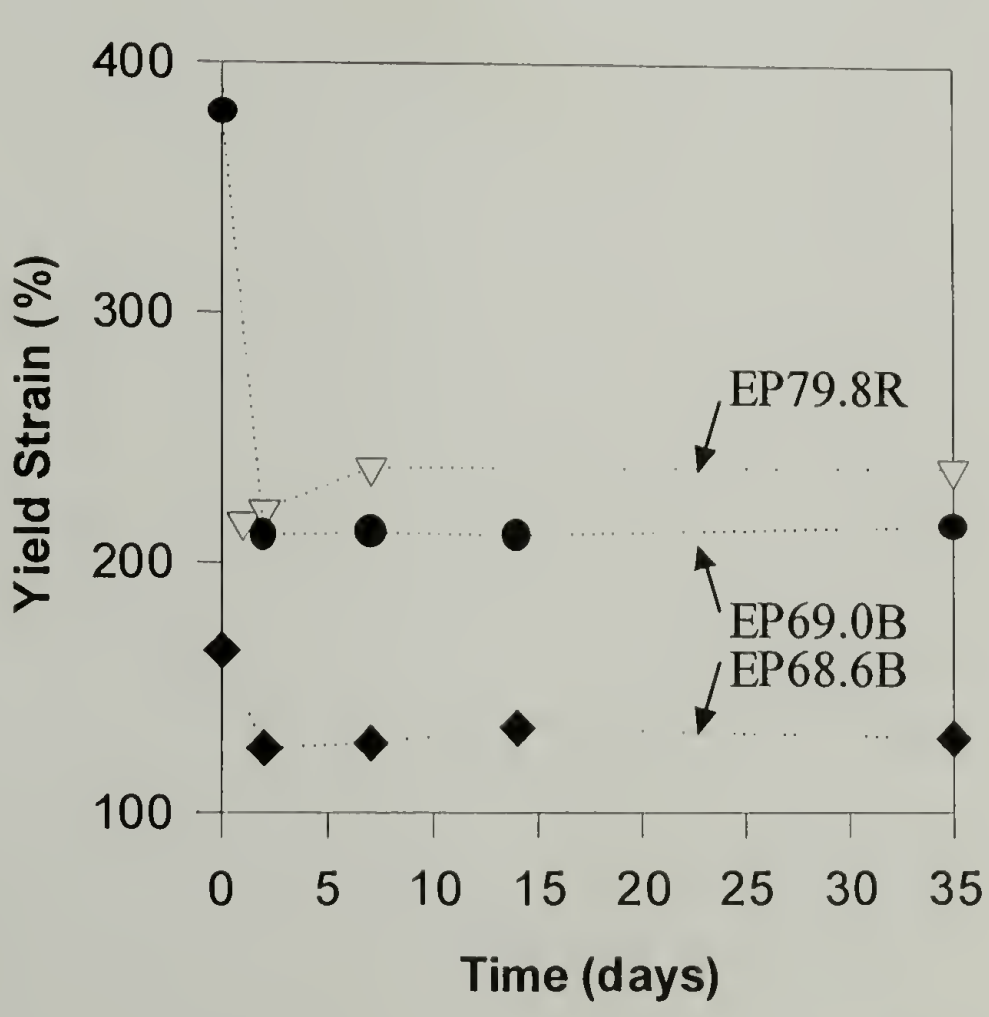

Figure 2.40: Yield strain as a function of sample age

The mechanical behavior is also examined in terms of the LT and HT endotherm heats of fusion as well as the total heat of fusion as a function of sample age. Figure 2.41 is a plot of the LT, HT, and total heats of fusion as a function of yield stress for EP69.0B. A linear regression is applied to the data and the corresponding R^2 values are as follows: LT – $R^2 = 0.9858$, HT – $R^2 = 0.8444$, Total – $R^2 = 0.9885$. There is strong correlation between the LT endotherm and the yield stress; as hexagonal crystal content increases the yield stress also increases. There is relatively little correlation between the HT endotherm and the yield stress. Perfect superposition of the LT and HT data is observed in the total heat of fusion as a function of yield stress. Consequently, the data suggest that the changes in yield stress are primarily due to the addition of hexagonal crystals.

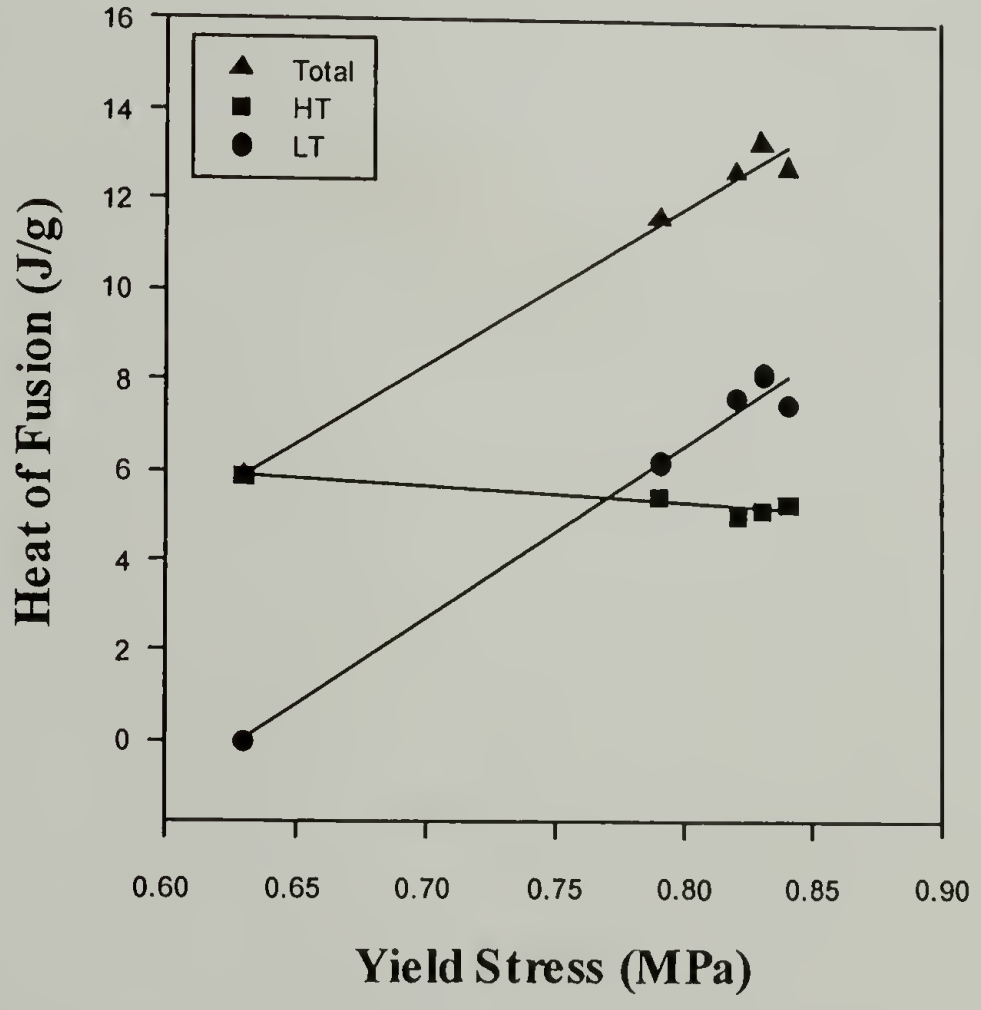

Figure 2.41: Correlation of increasing yield stress with incorporation of hexagonal content

The Rupture energy density of EP79.8R is plotted as a function of time in Figure 2.42. The rupture energy density of EP79.8R decreases exponentially as the sample ages in contrast to the behavior of EP68.6B and EP69.0B where the rupture energy density remains relatively constant within slight fluctuations (not shown on graph).

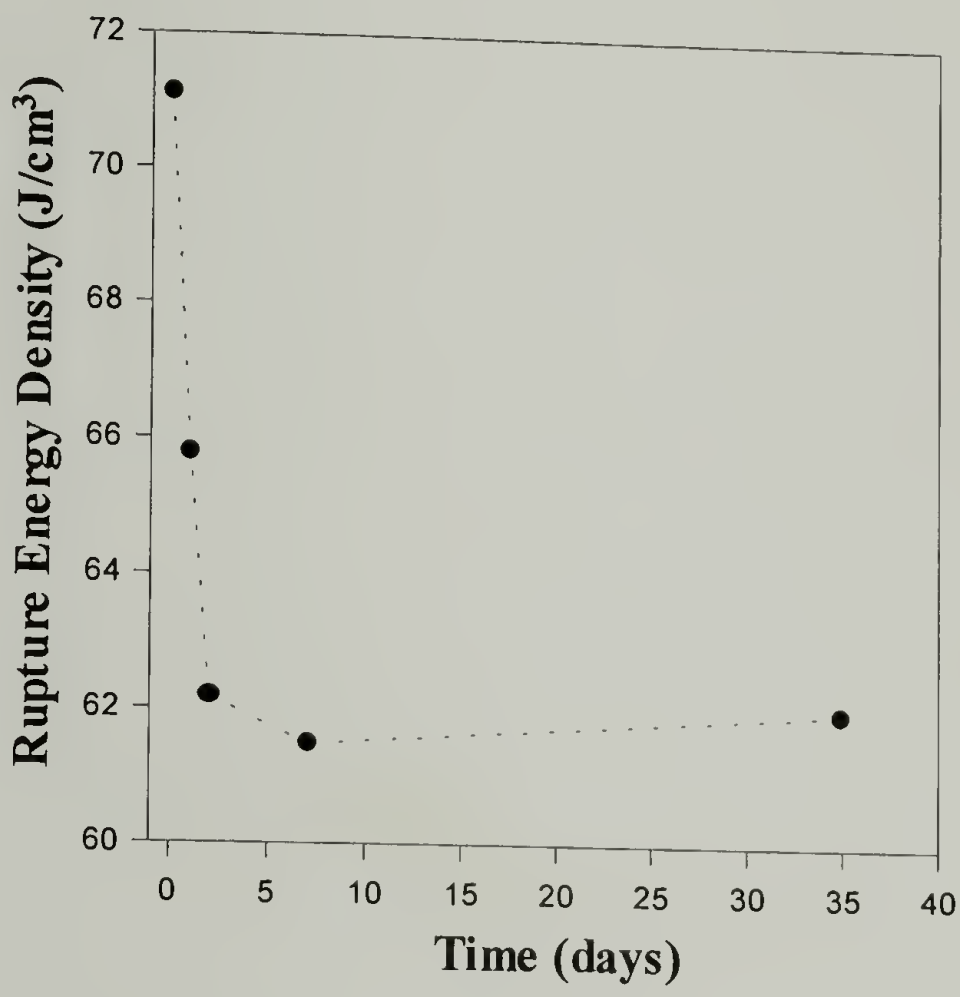

Figure 2.42: Rupture energy density as a function of sample age for EP79.8R

The LT, HT, and total heats of fusion are plotted as a function of rupture energy density for EP79.8R in Figure 2.43. A linear regression is again applied to the data and the corresponding R^2 values are as follows: LT – R^2 = 0.9241, HT – R^2 = 0.6502, Total – R^2 = 0.9392. Again a strong correlation exists between the evolution of the LT endotherm and the decreasing rupture energy density. There is little dependence on the HT endotherm. Subsequently, the data again suggest that changes in rupture energy density are the result of incorporation of hexagonal crystals.

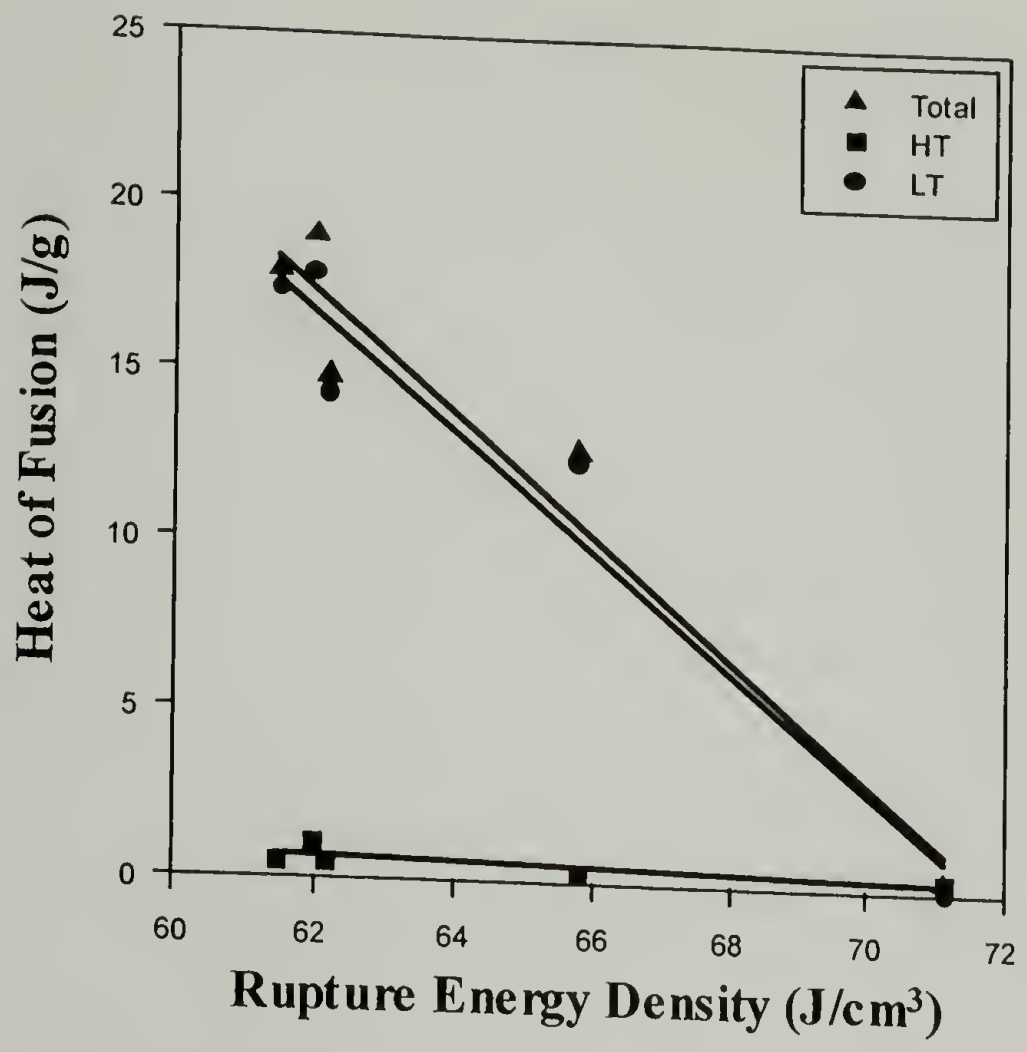

Figure 2.43: Correlation of decreasing rupture energy density with incorporation of hexagonal crystals

2.3.3 Quasi-Static Loading

Elastomeric materials are generally studied under cyclic loading conditions to interrogate mechanical reversibility in terms of energy dissipation and permanent set per cycle. The ethylene – propylene copolymers all exhibit substantial hysteresis when subjected to cyclic loading below their respective yield points indicating the presence of dissipative mechanisms. Their reversibility is less than that of traditional crosslinked elastomers but greater than a typical thermoplastic (*e.g.*, polypropylene). The energy loss densities per cycle are plotted as a function of sample age in Figures 2.44-2.48 for EP58.1R, EP68.6R, EP69.0B, and EP79.8R, respectively. All samples are cycled in tension under load control with a peak stress value equal to 70% of their respective yield

stresses. Figure 2.44 shows the energy dissipation density for EP58.1R immediately after solidification and after one day of aging. There is a decreasing trend in energy dissipation as the material is cycled and as it ages. This composition, however, does not appear to reach a true steady-state response due to its liquid-like nature.

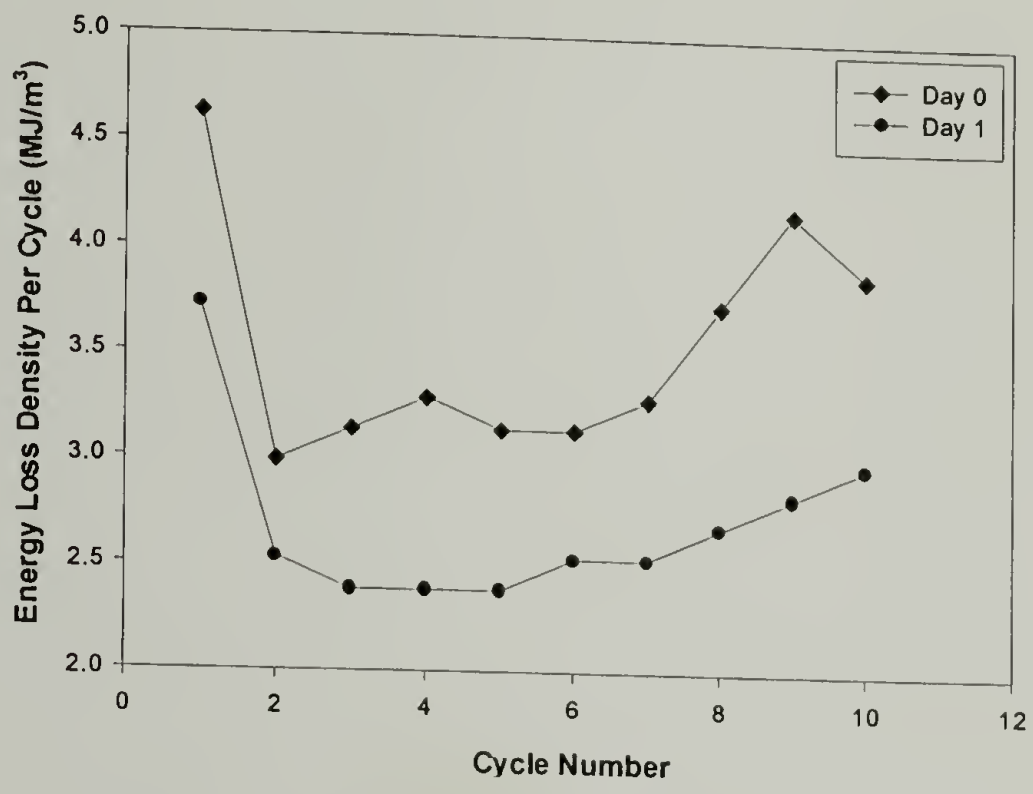

Figure 2.44: Energy dissipation of EP58.1R as a function of sample age

The energy loss density of EP68.6R, shown in Figure 2.45, reaches a steady-state value after approximately five cycles and decreases as aging occurs. A decrease in energy dissipation indicates enhanced elastomeric behavior. The development of physical crosslinks or crystallites is responsible for a decrease in steady-state energy dissipation. Similar behavior is observed for EP69.0B and EP79.8R as shown in Figures 2.46 and 2.47, respectively. For EP79.8R, it is apparent that the decrease in steady-state energy dissipation follows its crystallization kinetics, as there is a large decrease within the first day after solidification when a large majority of crystallization occurs.

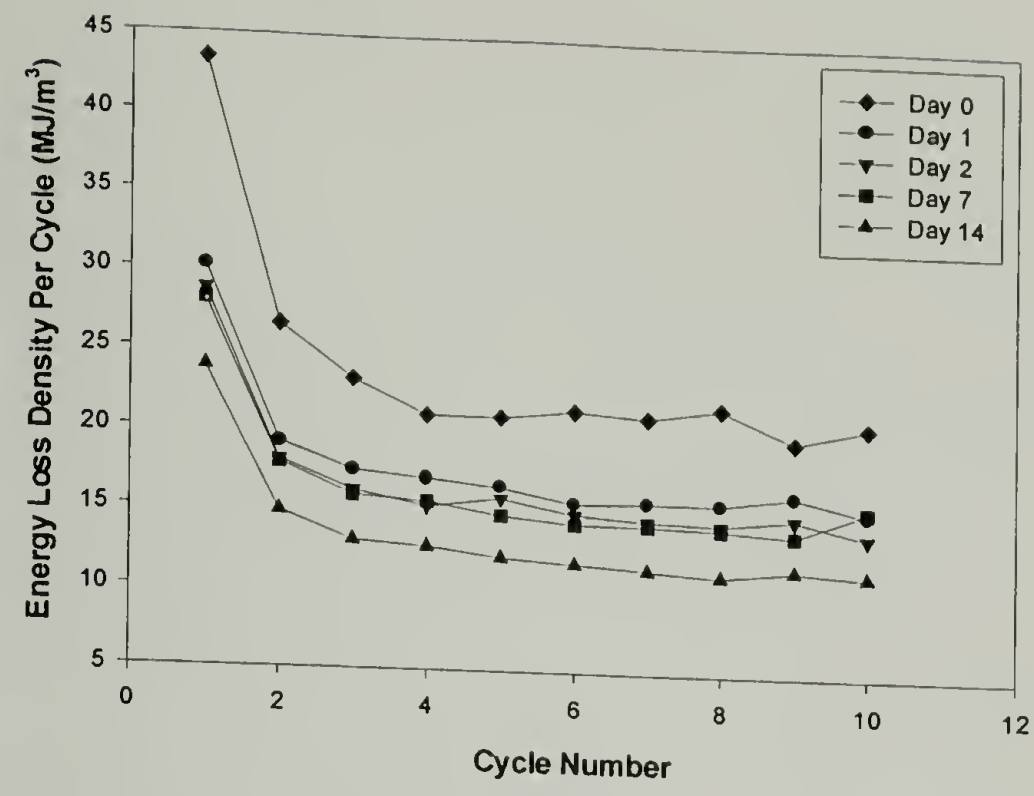

Figure 2.45: Energy dissipation of EP68.6R as a function of sample age

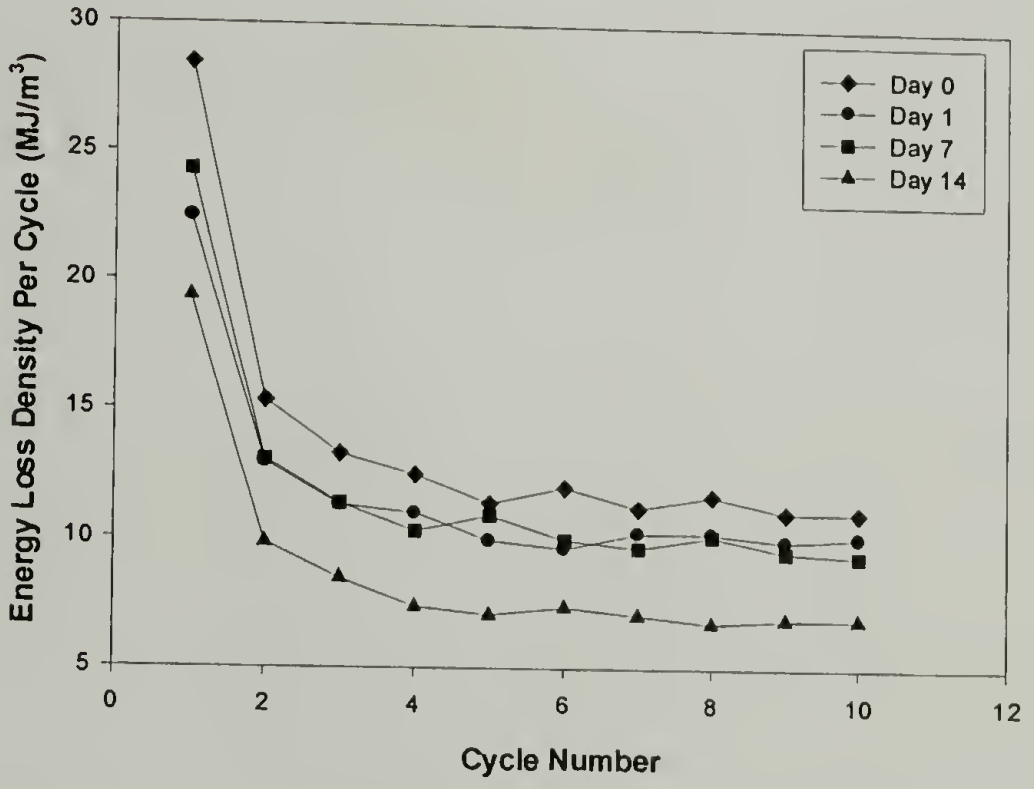

Figure 2.46: Energy dissipation of EP69.0B as a function of sample age

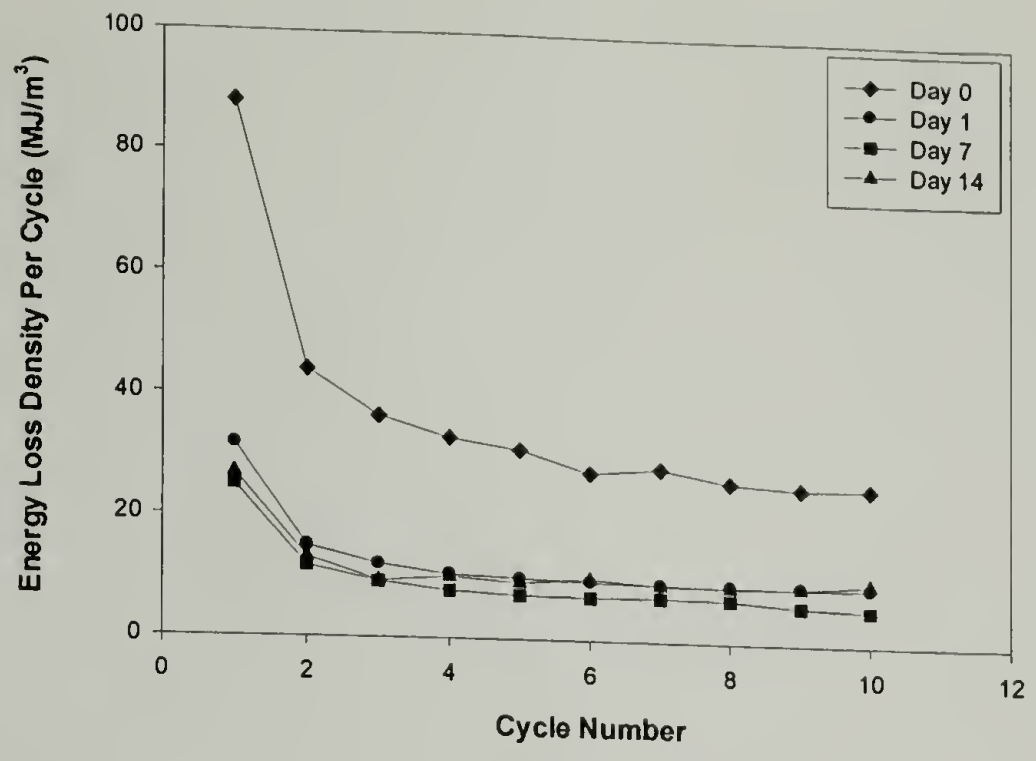

Figure 2.47: Energy dissipation of EP79.8R as a function of sample age

For EP79.8R cyclic loading is also performed subsequent to yielding. When cycled after yielding the steady-state energy dissipation density is not a strong function of sample age. This is most likely due to changes in crystallinity that occur during the yielding process which are discussed in section 2.4.3.

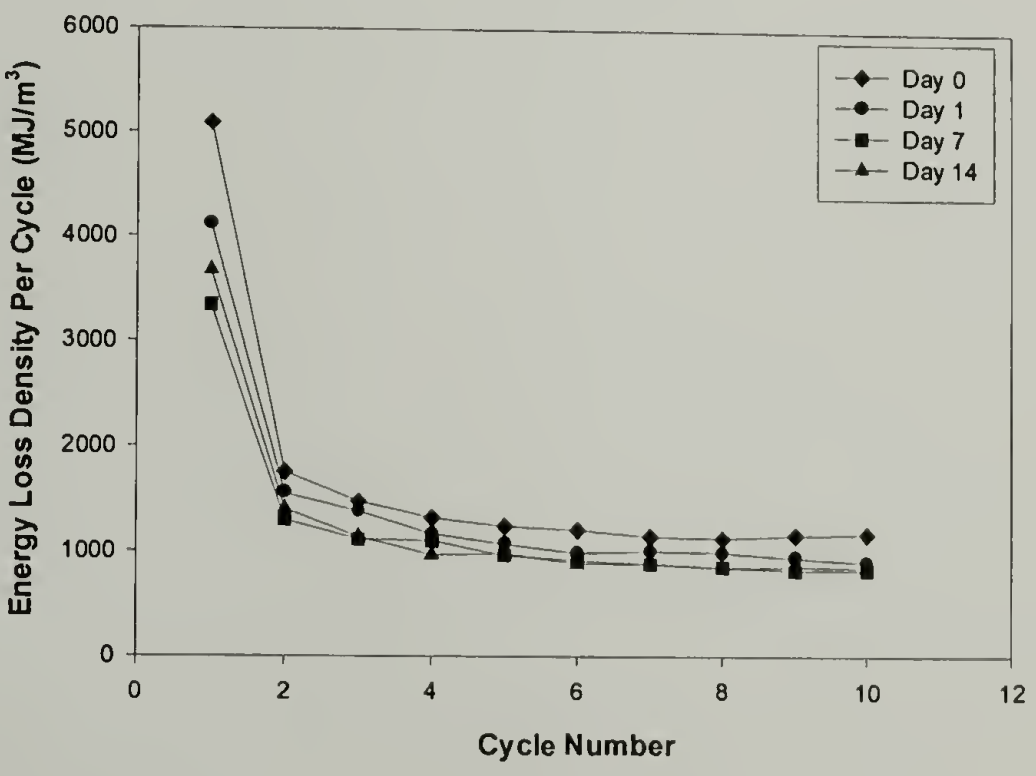

Figure 2.48: Energy dissipation of EP79.8R cycled post-yield

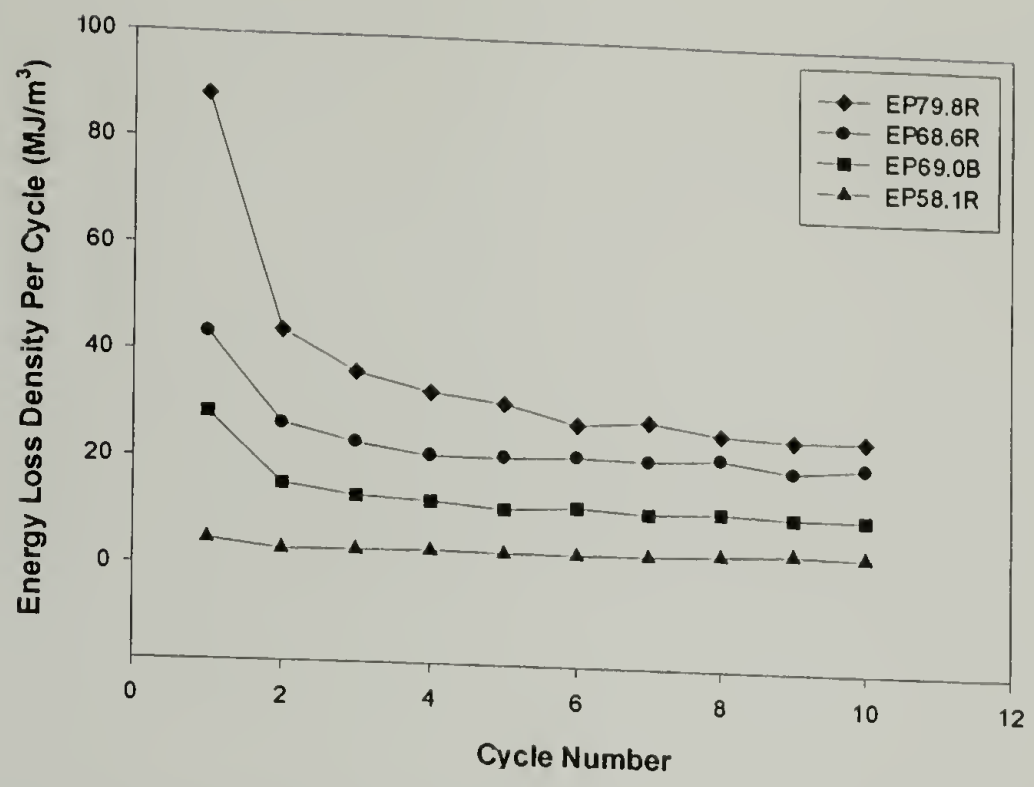

Figure 2.49: Compositional comparison of energy loss density immediately after solidification (day 0)

Compositional comparisons are shown immediately after solidification in Figure 2.49 and after two weeks in Figure 2.50. It is difficult to draw conclusions from this type of analysis because of the nature in which the tests are performed. Each composition is cycled at a percentage of its respective yield point; however, this value is different for each composition. It is not possible to cycle all the compositions at the same peak stress because the apparent yield stress for EP58.1R is substantially lower than that of EP79.8R. As a result of a biased testing procedure, it is difficult to determine the morphological influence on the steady-state energy dissipation value.

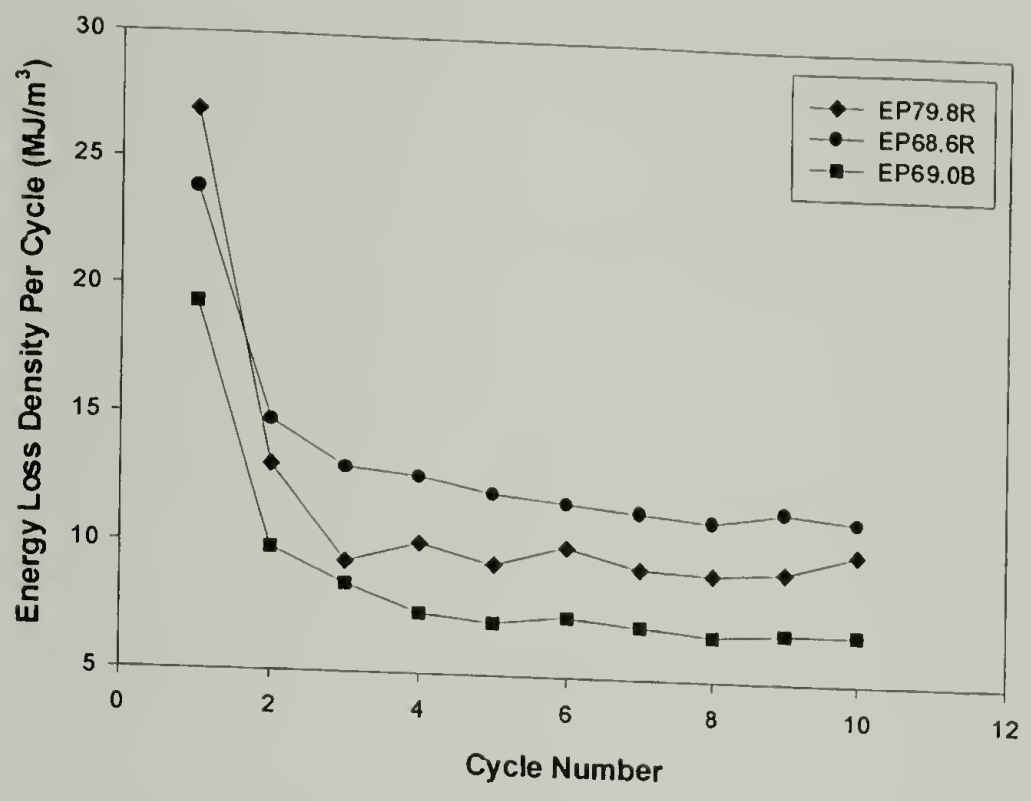

Figure 2.50: Compositional comparison of energy loss density at day 14

The Mullins effect or stress-softening is also investigated under cyclic loading conditions. Another way of examining data collected under cyclic loading is with a Mullins plot. A Mullins plot indicates the amount of energy lost as a function of the energy input. For a traditional crosslinked filled elastomer, the amount of energy dissipated increases linearly with the amount of mechanical energy put into the system. Figures 2.51 and 2.52 are Mullins plots in tension and compression, respectively for several of the copolymer compositions at maturity. It appears that EP58.1R, EP68.6R, EP69.0B, and EP79.8R do not exhibit a monotonically increasing relationship between energy dissipation and energy input. In this regard, they behave differently than their more traditional counterparts. However, when the same type of analysis is performed in compression (Figure 2.52) a monotonic relationship is observed. As such, it appears that stress-state plays an important role in the dissipative process of these thermoplastic elastomers.

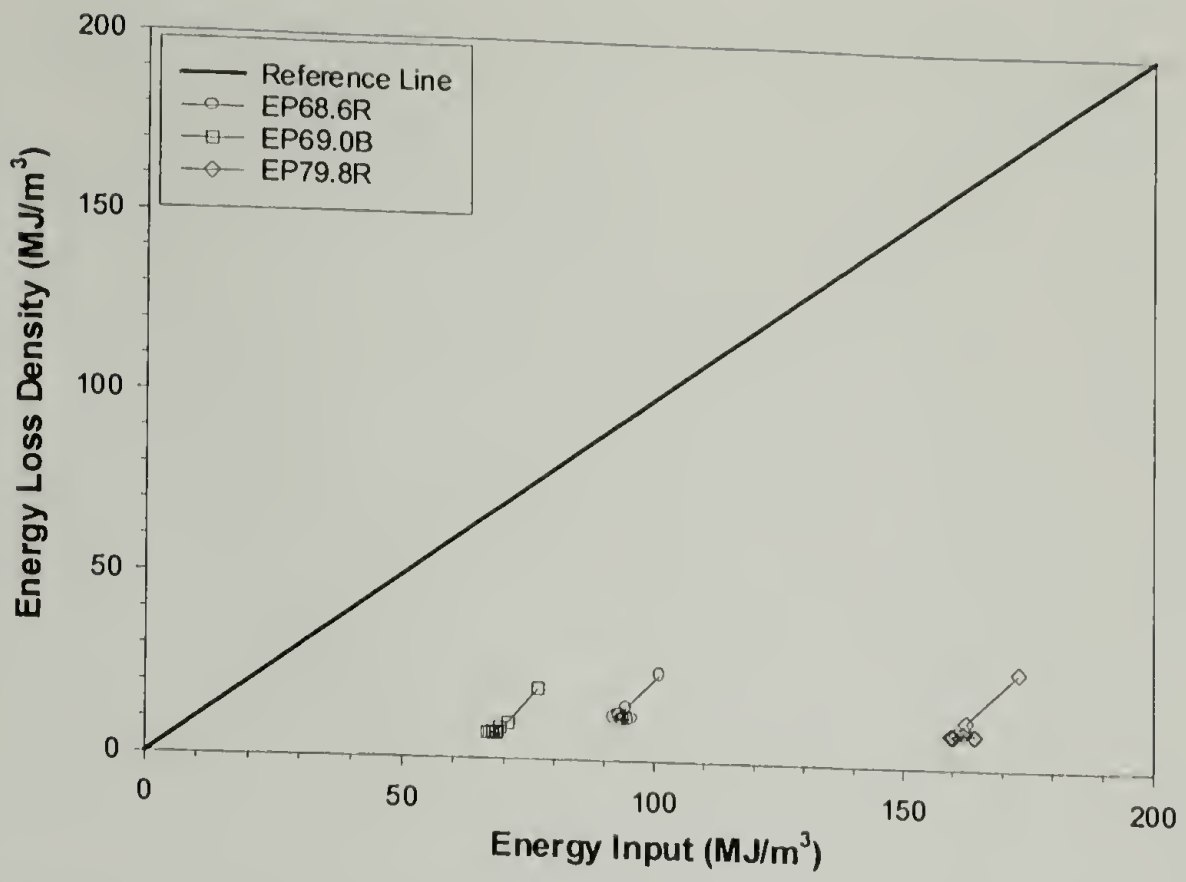

Figure 2.51: Mullins plot for EP68.6B and EP69.0B when cycled in tension

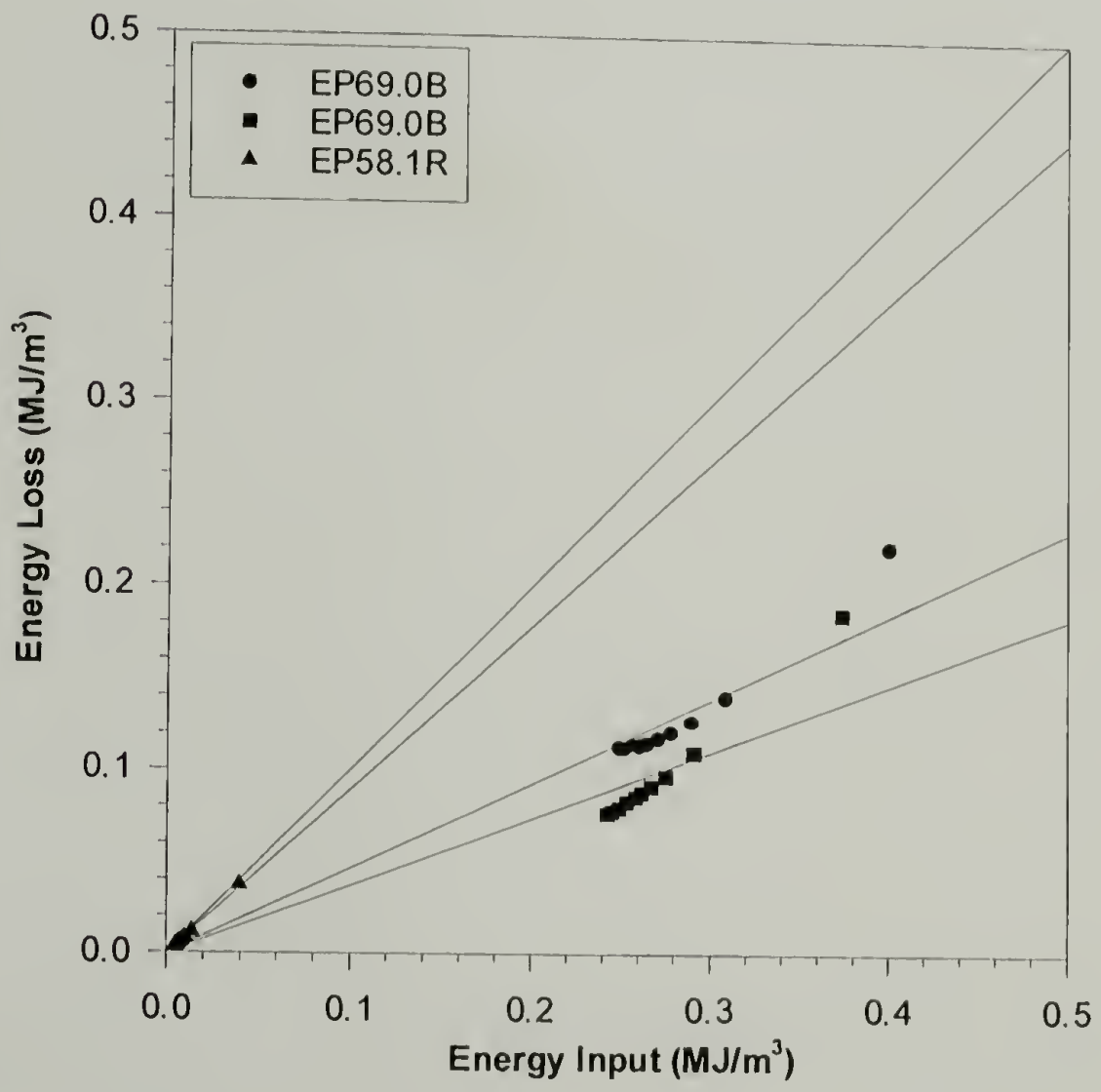

Figure 2.52: Mullins plot for EP58.1R, EP68.6B, and EP69.0B when cycled in compression

2.3.4 Dynamic Loading

In order to further examine their elastomeric nature, the copolymers are investigated under dynamic loading conditions. As mentioned earlier, the Mullins effect must be removed in order to investigate reversibility in terms of the Payne effect. In other words, a steady-state response must be reached. Dynamic mechanical loading is achieved using the modified Dynastat. A sinusoidal loading pattern is imposed under displacement control. Figure 2.53 shows experimental stress-strain data for EP79.8R at maturity. It appears that these copolymers do not exhibit stress-softening to any appreciable degree as the peak load in Figure 2.53(a) does not decease as the sample is cycled. Using this type of testing protocol, oscillatory stress and strain can be collected at a variety of strain amplitudes. Storage modulus can then be calculated according to equation 2.4 where ε_a is the amplitude of the imposed oscillatory strain and σ_a is the amplitude of the resulting oscillatory stress.

$$E' = \frac{\sigma_a}{\varepsilon_a}\cos\theta \qquad (2.4)$$

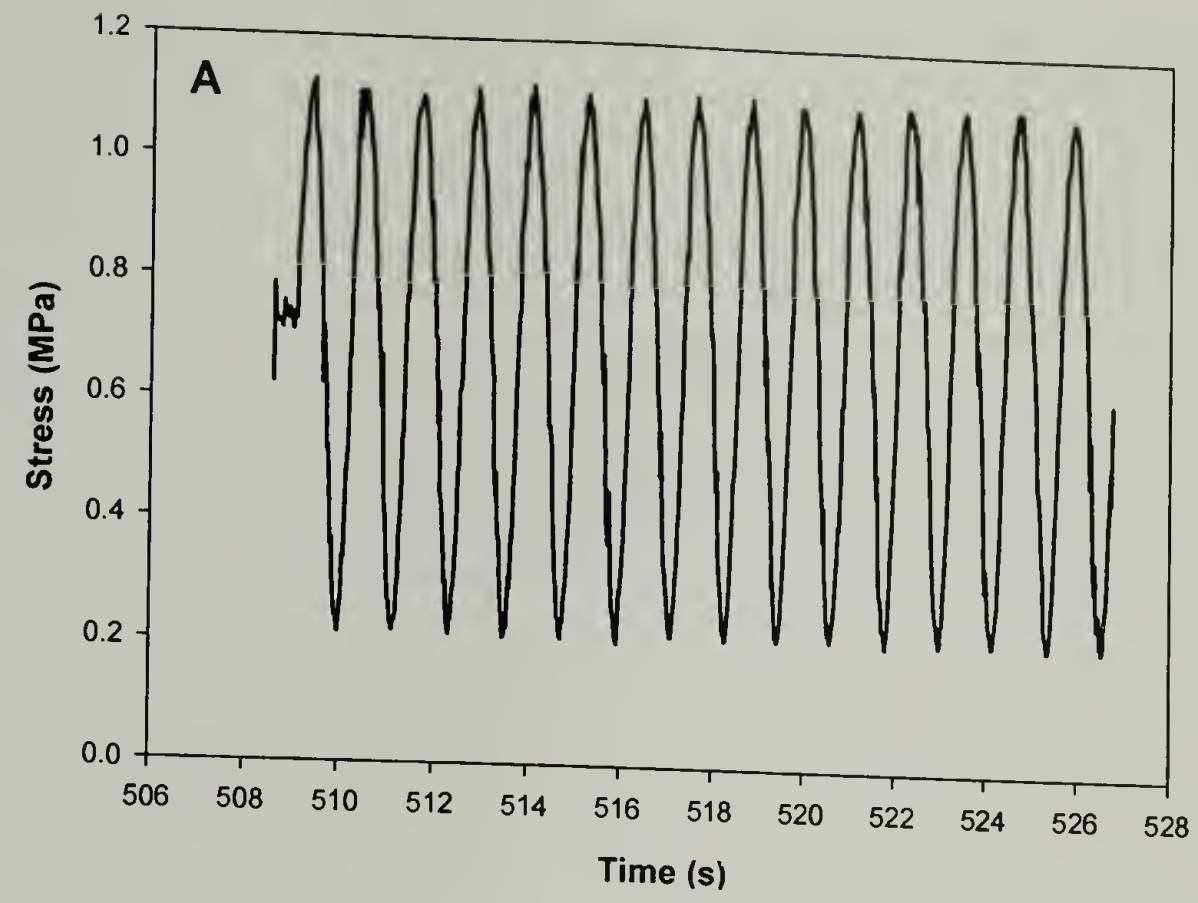

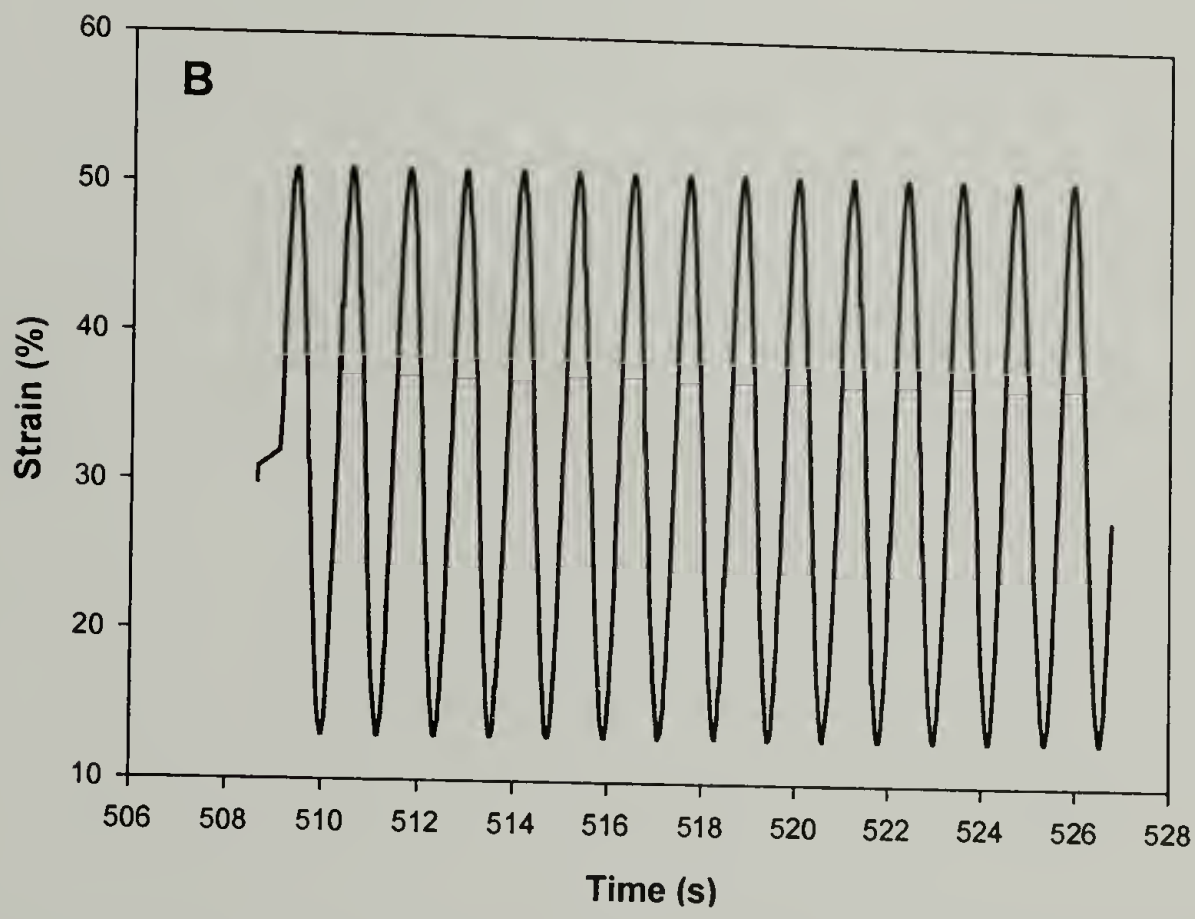

Figure 2.53: Sinusoidal waveforms for (a) stress and (b) strain from Dynastat illustrating lack of stress-softening in EP79.8R

Figure 2.54 is a plot of the storage modulus as a function of dynamic double strain amplitude for EP79.8R, EP69.0B, and EP68.6R all at maturity. The storage modulus exhibits a sigmoidal dependence on dynamic strain amplitude in keeping with the Payne effect. At maturity the magnitude of E'_0-E'_∞ appears to be related to the amount of

crystallinity and not crystal structure. Both EP79.8R and EP68.6R have only orthorhombic crystals yet exhibit different sigmoidal responses. As discussed earlier, the degree of crystallinity at maturity increases with increasing ethylene content as does the decrease in storage modulus. At maturity, E'_o-E'_∞ appears to be related to the amount of heterogeneity or crystal concentration. The influence of crystallinity on the sigmoidal behavior is also evident in Figure 2.55 where storage modulus is plotted as a function of dynamic strain amplitude and sample age. The open symbols correspond to initial behavior and the closed symbols correspond to mature behavior. As crystallization occurs, E'_o-E'_∞ increases for all compositions studied.

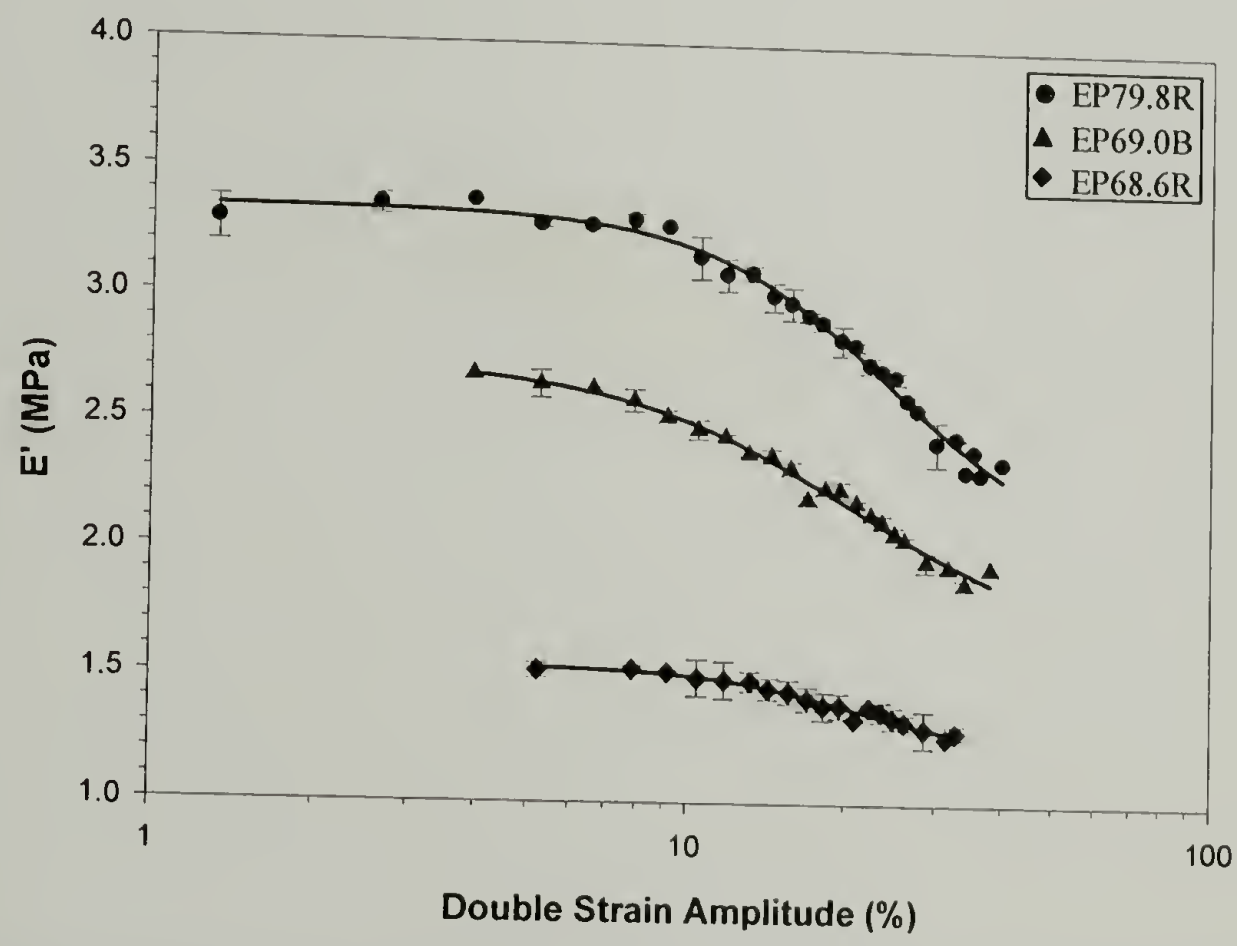

Figure 2.54: Payne effect response at maturity for EP68.6R, EP69.0B, and EP79.8R

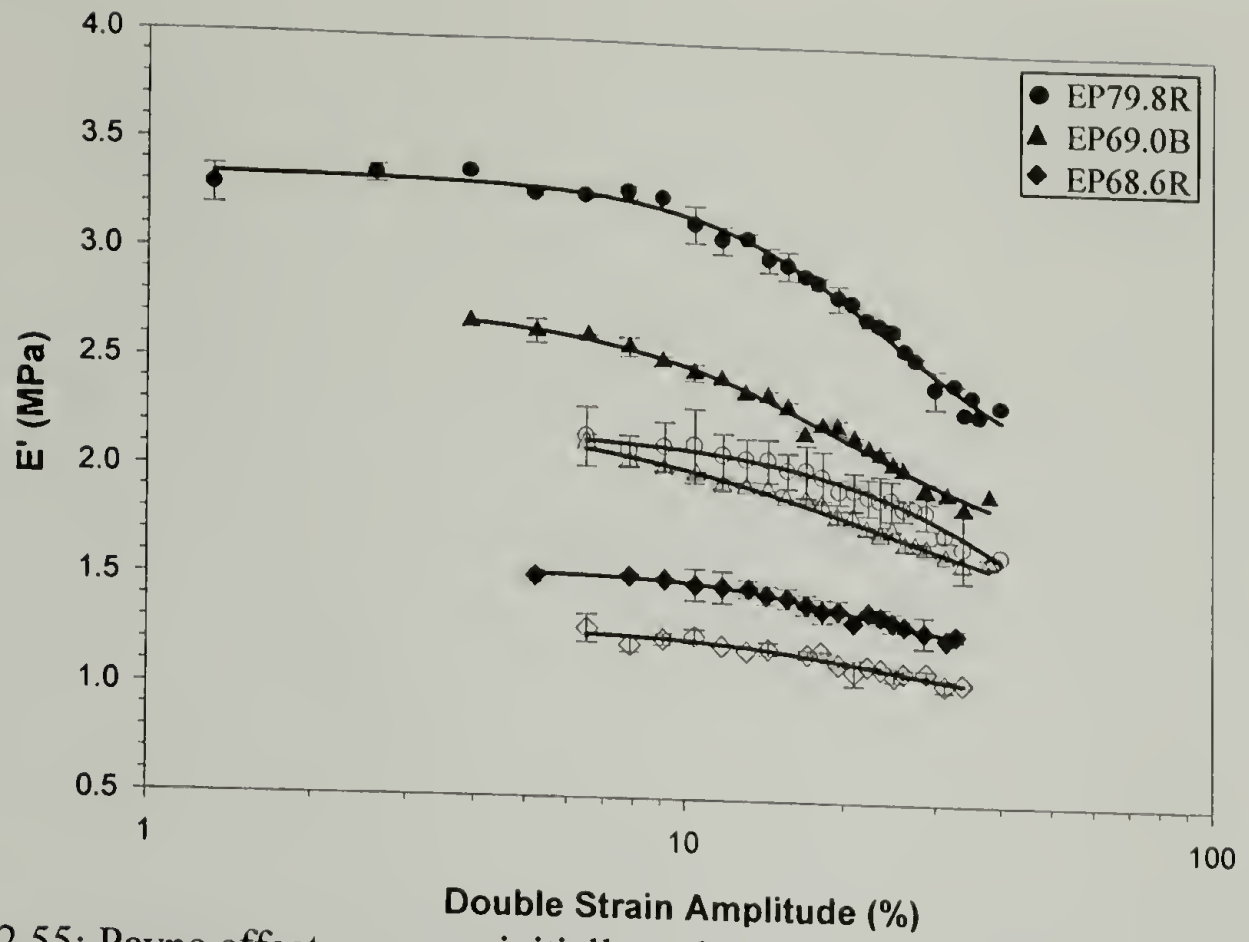

Figure 2.55: Payne effect response initially and at maturity for EP68.6R, EP69.0B, and EP79.8R

This behavior is very similar to that of more traditional crosslinked filled elastomers if the crystals are viewed as physical crosslinks or "filler." The characteristic strain or the strain where maximum change in E' occurs also increases with as the copolymers age. EP68.6R and EP79.8R are both initially amorphous yet they still show a slight sigmoidal dependence of storage modulus on dynamic strain amplitude. The sigmoidal response of the copolymers follows very closely with initial and mature density. The sigmoidal response of EP79.8R is greater than that of EP68.6R even though they are both initially amorphous. This may be further evidence to support a densified amorphous phase that may also act as physical crosslinks. The decline in storage modulus of the copolymers occurs at lower strain amplitudes than that of crosslinked systems. The copolymers reach a high amplitude plateau close to 35% double strain whereas crosslinked elastomers may not plateau until 75% or 100% double strain. There

has been much debate about the origins of the Payne effect in filled rubbers. The fact that these copolymers and other "unfilled" thermoplastic elastomers[66] exhibit the same phenomenological response indicates that filler/filler and filler/matrix interactions may not be the principal causes.

2.4 Morphological Influence on Deformation

2.4.1 Experimental Procedures

In situ wide angle X-ray diffraction (WAXD) measurements are performed on a Rigaku RU-H3R rotating anode X-ray diffractometer equipped with an Osmic multilayer focusing optic and an evacuated Statton-type scattering camera. The incident beam wavelength is 1.54 Å, corresponding to 8 keV Cu Kα radiation. Scattering patterns are acquired with 10 cm x 15 cm Fuji ST-VA image plates in conjunction with a Fuji BAS-2500 image plate scanner. Intensity profiles are obtained from radial averages of the scattering pattern intensities.

In situ Fourier Transform Infrared (FTIR) spectroscopy is performed on a BioRad 175C spectrometer with incident radiation at a wavelength of 632.8 nm. The instrument has a resolution of 2 cm^{-1} and 64 scans are signal averaged. A 25 mm x 2 mm CaF_2 polarizer from International Crystal Labs is used to perform infrared dichroism measurements.

Samples for *in situ* WAXD and FTIR are compression molded into films approximately 0.5 mm thick at 190 °C for 10 minutes and then water-cooled. Samples are then placed in a stretching apparatus that grips one side of the sample and winds the

other around a spindle. Thus large deformations are achieved within a confined geometry.

2.4.2 Origins of Ductility

The monotonic stress-strain behavior of the five ethylene-propylene copolymers at maturity is plotted in Figure 2.56. It is immediately evident that the main difference between the materials is their ductility. They all exhibit a yield-like response at approximately 175% engineering strain. After yielding only EP79.8R continues to draw and strain harden and eventually fails at a strain that is an order of magnitude greater than the other compositions.

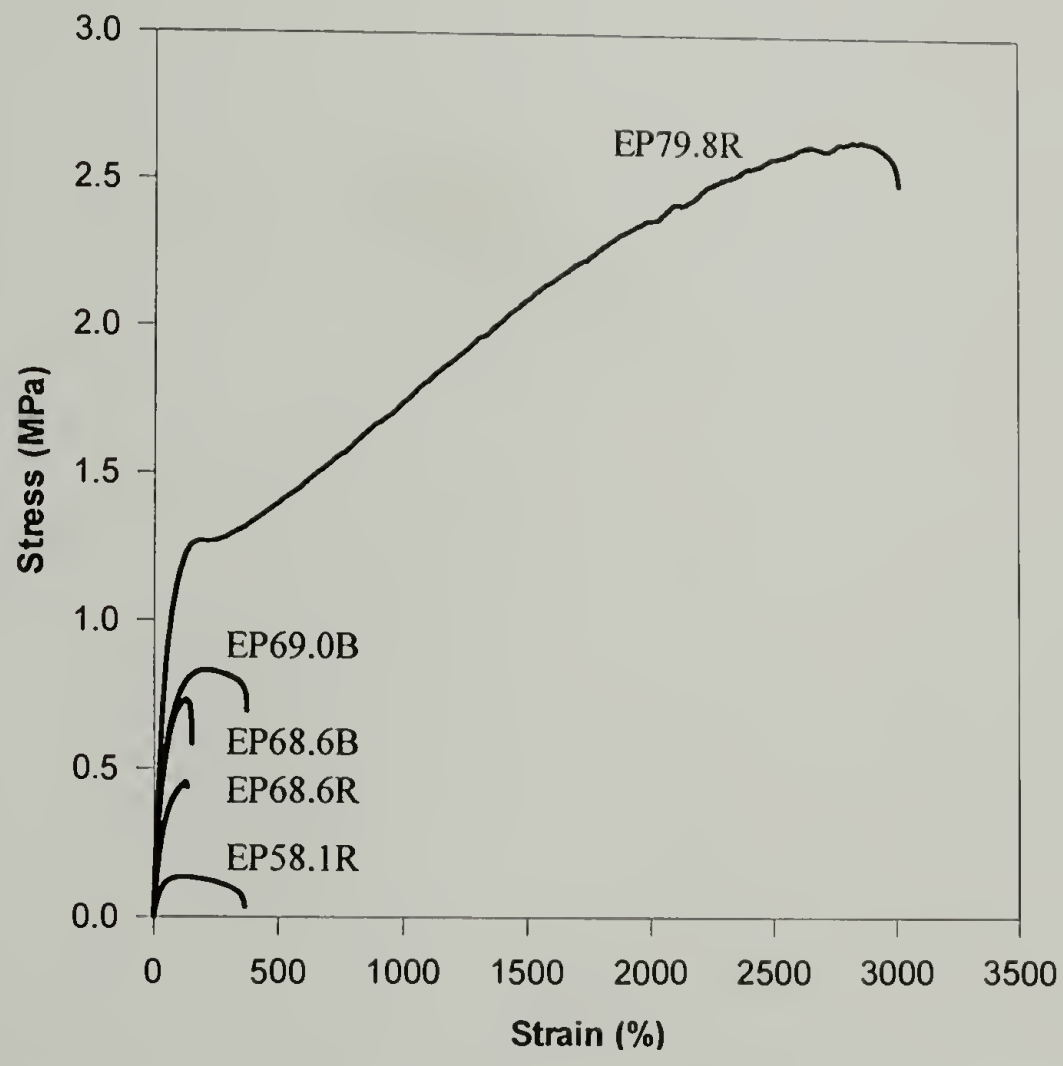

Figure 2.56: Compositional comparison of ductility at maturity

The origins of this ductility are of great interest. For polymeric systems, ductility is generally thought to be proportionally related with molecular weight. However, the molecular weights of these materials are all very similar (see Table 2.1). In fact, the molecular weight of EP79.8R is actually one of the lowest. Some other factors that could affect ductility include: crystallization kinetics and/or crystal structure. Crystallization kinetics can be eliminated because ductility does not change as crystallization occurs. Crystal structure is also not a factor because EP68.6R and EP79.8R both possess identical crystal structures, namely, hexagonal with no orthorhombic. EP79.8R is extremely ductile while EP68.6R fails at 225%.

In order to investigate possible origins of ductility tensile tests are conducted at elevated temperatures. Figure 2.57 shows the melting behavior of EP68.6R, EP69.0B, and EP79.8R at maturity. As discussed earlier, the endotherm at 45 °C is due to the melting of hexagonal crystals whereas the endotherm at 125 °C is due to the melting of orthorhombic crystals. The onset of hexagonal crystal melting occurs between 34 °C and 36 °C.

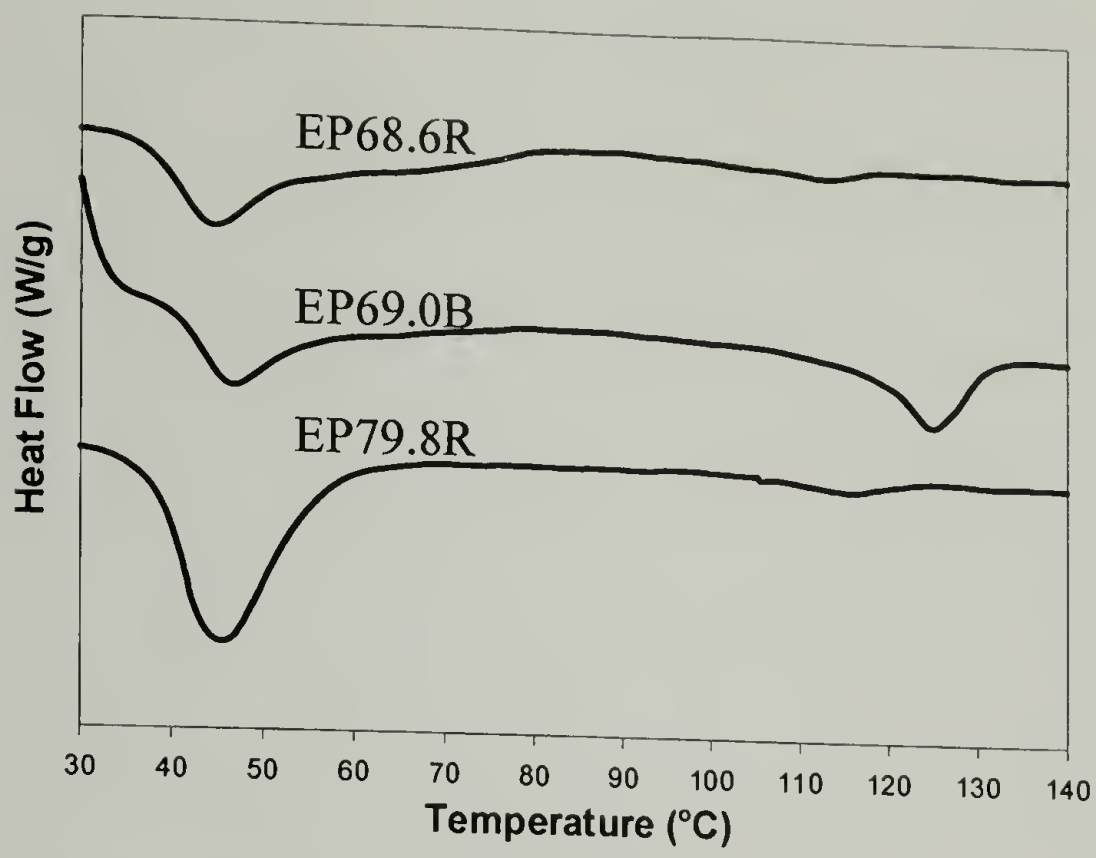

Figure 2.57: Compositional comparison of melting behavior at maturity for EP68.6R, EP69.0B, and EP79.8R

Monotonic stress-strain curves of mature EP79.8R, EP69.0B, and EP68.6R at elevated temperatures are plotted in Figures 2.58, 2.59, and 2.60, respectively. By increasing the temperature from 25 °C to 33 °C the ductility of EP79.8R decreases by 70% although distinct yielding is still observed. Note that the stress-strain behavior at 25 °C is not to failure due to limited stroke in the environmental chamber; at room temperature failure occurs at 3000%. Even though a distinct yield point is observed in keeping with a neck-like phenomenon, no neck formation is visibly observed. Possible origins of this distinct yield point are examined in section 2.4.3. At 40 °C and 48 °C the ductility continues to decrease while a distinct yield point is not longer evident.

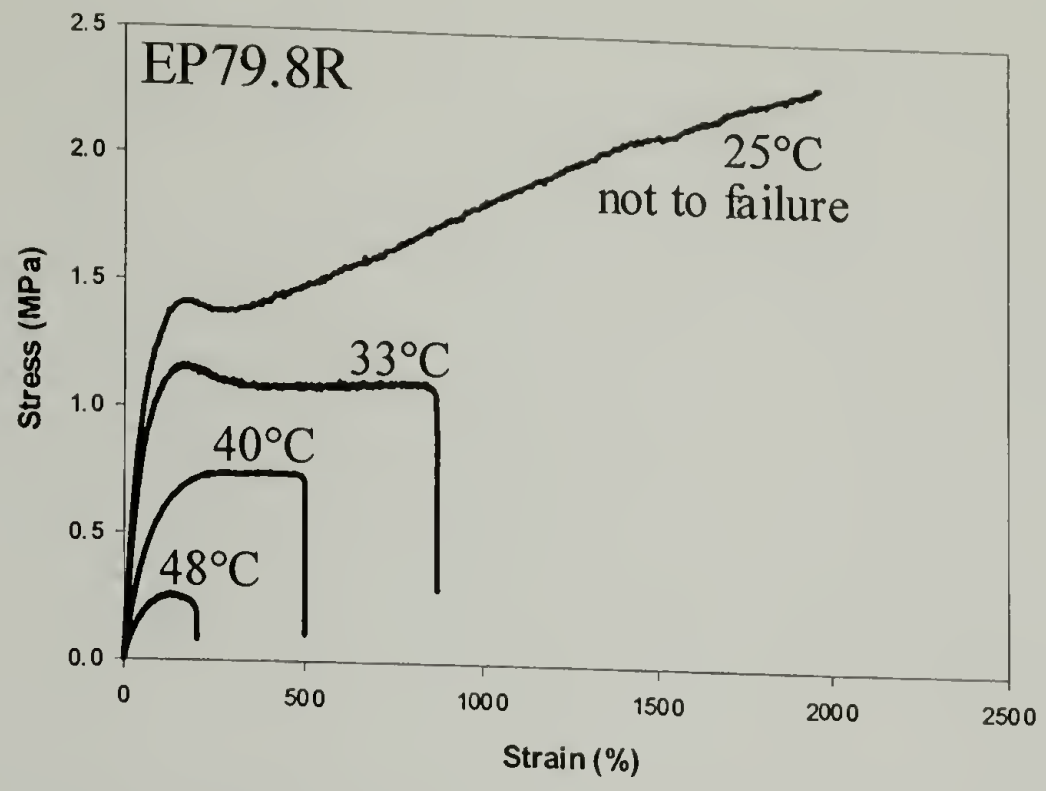

Figure 2.58: Mechanical behavior of EP79.8R at various temperatures

The mechanical behavior of EP69.0B and EP68.6R at elevated temperatures (shown in Figures 2.59 and 2.60) is similar despite the presence of different crystal structures. No dramatic change is observed as temperature decreases other than a decrease in stiffness. At 40 °C the ductility decreases by approximately 25% but then slightly increases again at 48 °C.

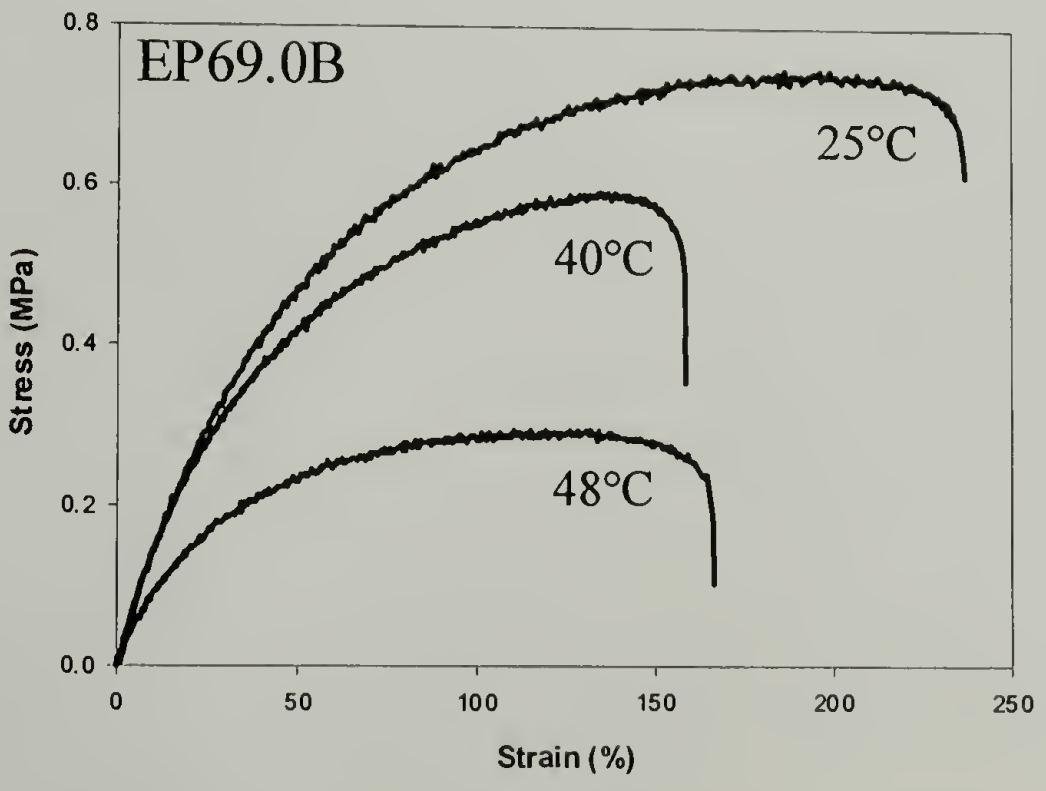

Figure 2.59: Mechanical behavior of EP69.0B at various temperatures

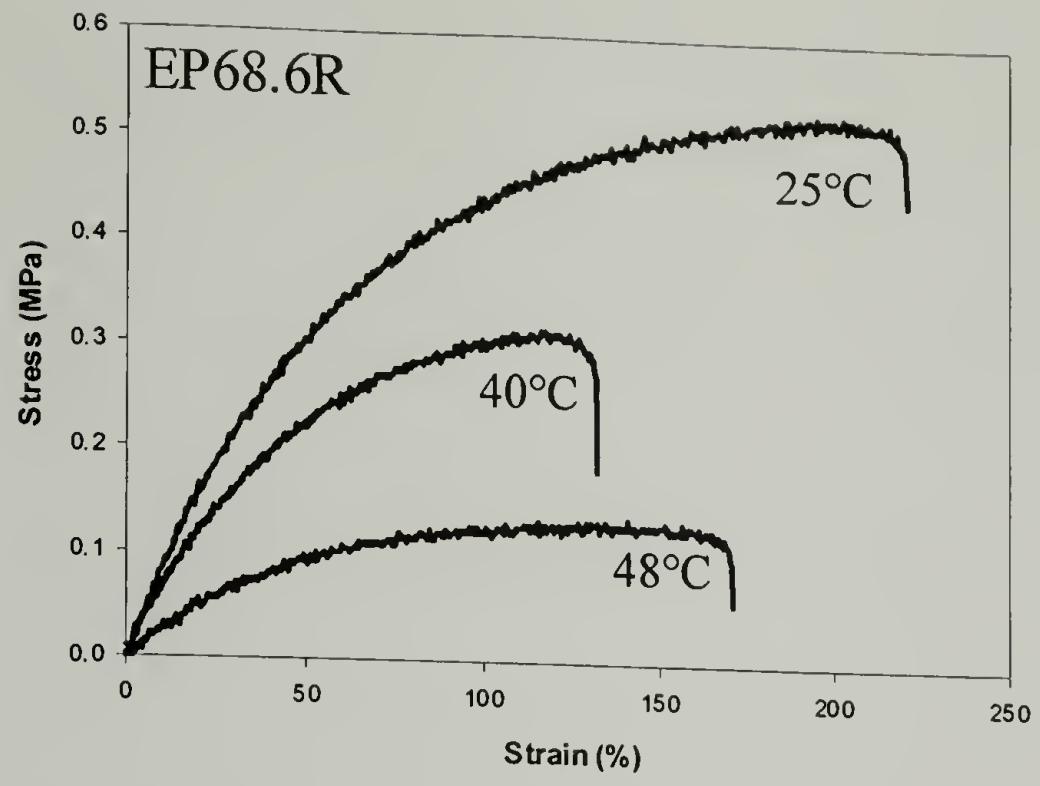

Figure 2.60: Mechanical behavior of EP68.6R at various temperatures

Figure 2.61 plots modulus as a function of temperature. The moduli of EP69.0B and EP68.6R decrease at the same rate due to similar amounts of hexagonal crystals. EP79.8R has a larger amount of hexagonal crystals and its modulus decreases more rapidly. At 48 °C their moduli are commensurate indicating nearly complete melting of the hexagonal crystals. A modulus inversion exists at 40 °C where the modulus of EP69.0B becomes greater than that of EP79.8R. This is due to the remaining orthorhombic crystals in EP69.0B.

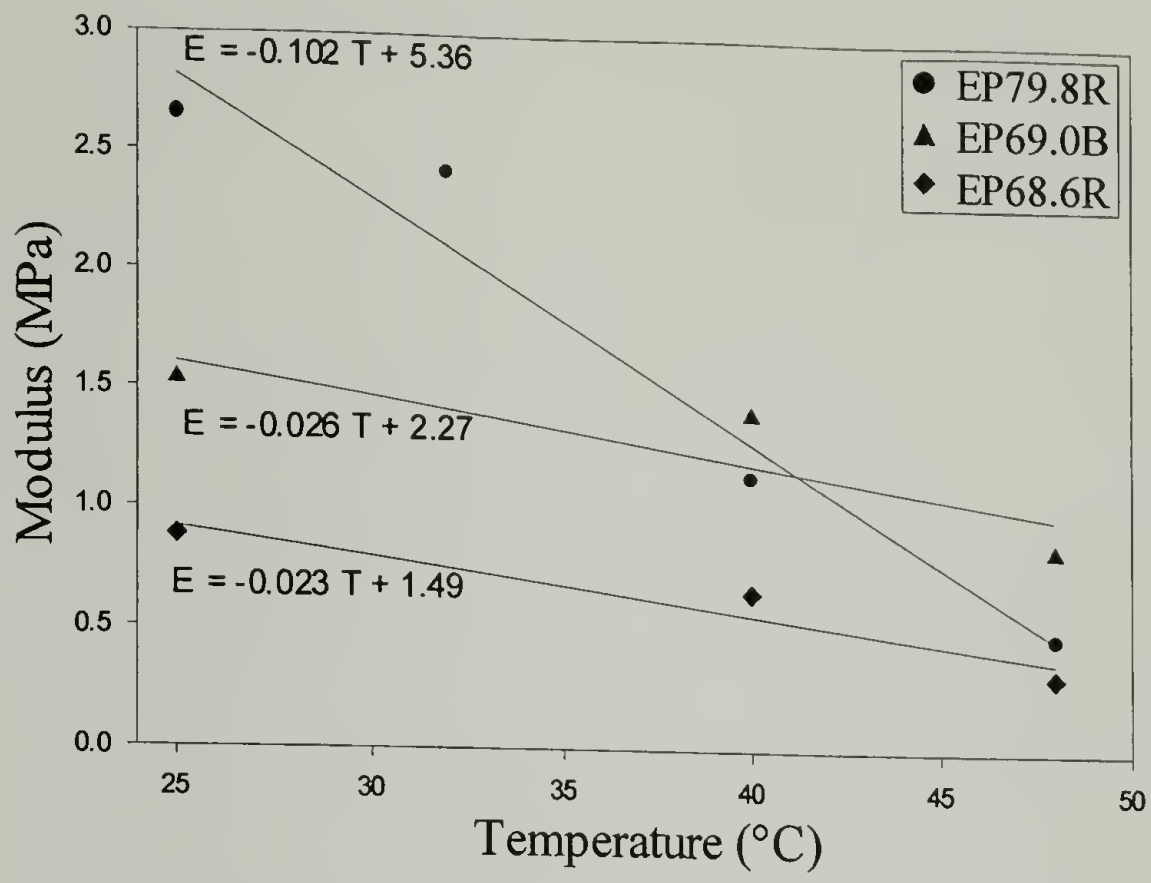

Figure 2.61: Modulus as a function of temperature for EP68.6R, EP69.0B, and EP79.8R

The pronounced temperature dependence on the ductility of EP79.8R may indicate that strain hardening and ductility are due to a critical effective molecular weight between physical crosslinks or some type of selective strain-induced crystallization phenomenon. In order to further investigate the origins of ductility, *in situ* WAXD studies are conducted. Figure 2.62 shows WAXD patterns at 0%, 45%, 105%, and 300% strain. Note the high levels of orientation achieved as deformation is imposed. Also, notice the outer reflection achieves high levels of orientation as well, which as discussed earlier may be indicative of a densified amorphous phase. Angular averages of WAXD patterns at various strains are shown in Figure 2.63. The intensity of the hexagonal reflection at a 2θ of 20.6° decreases as the material is strained to 300%. Upon unloading no change in the WAXD patterns is observed. The peaks are deconvoluted using WinIR software to calculate the degree of crystallinity. Prior to stretching the crystallinity is approximately 14%. The crystallinity steadily decreases until a value of 5% is reached

while substantial levels of orientation are achieved. Although it is difficult to obtain a scattering pattern at very high strains, data indicates that additional crystallinity is not achieved even as high as 1000% strain. This does not support a selective strain induced crystallization phenomenon. Even though other studies on ethylene – α - olefin copolymers suggest the possibility of strain induced crystallization,[67-71] no evidence is found in this study. As a result, the enhanced ductility of EP79.8R is most likely due to a critical molecular weight between physical crosslinks. However, the exact nature of the physical crosslinks is unknown. EP79.8R has the highest density; perhaps the physical crosslinks are a direct consequence of this increased density or perhaps they are simply due to entanglements.

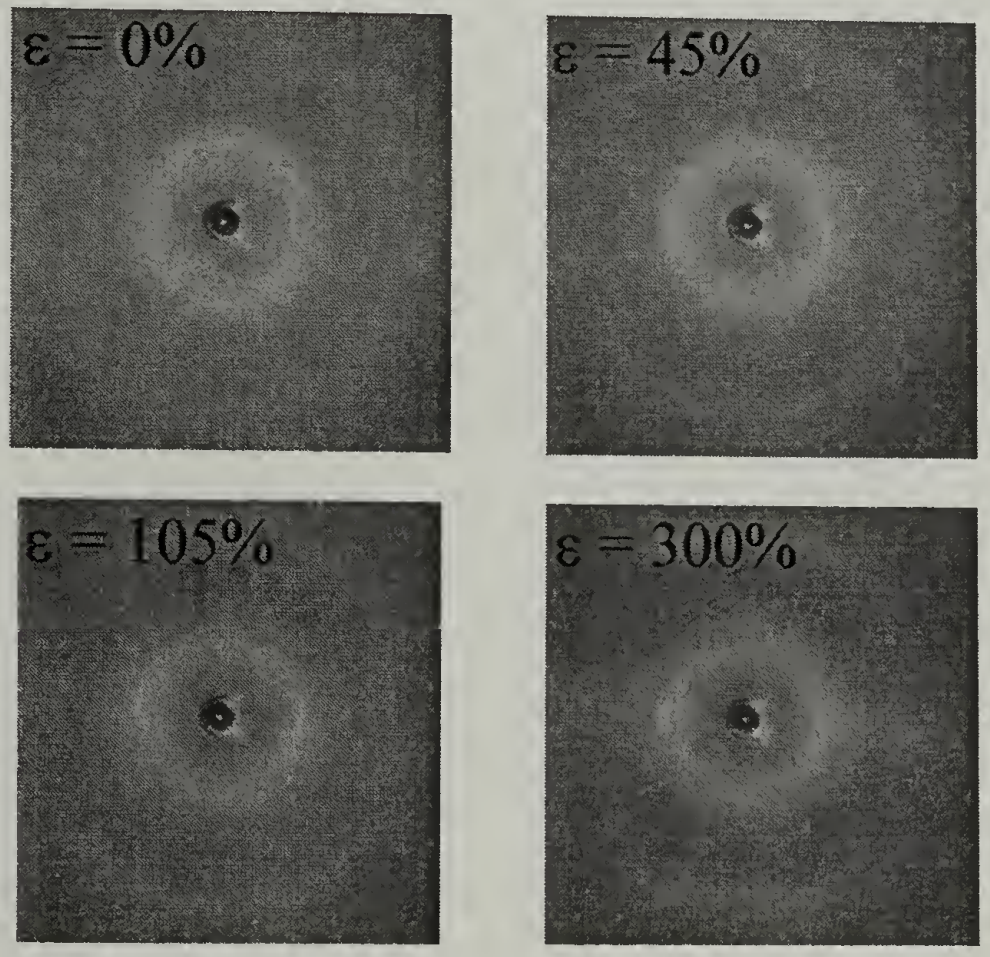

Figure 2.62: WAXD images of EP79.8R at 0%, 45%, 105%, and 300% strain

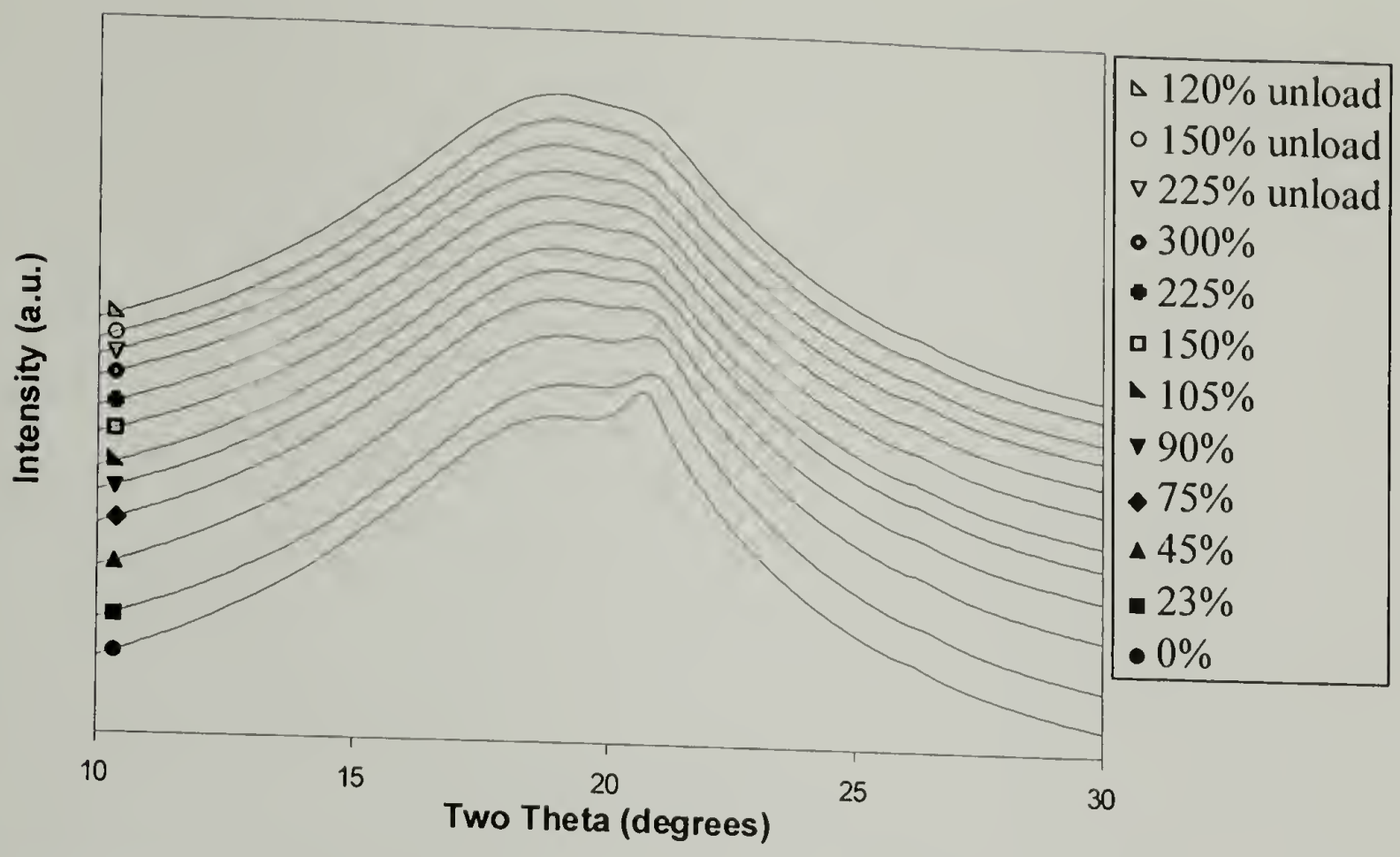

Figure 2.63: WAXD patterns as a function of strain for EP79.8R at maturity post-yield

No change in crystallinity is observed upon unloading from 300% strain. The WAXD patterns upon unloading are shown as the open symbols in Figures 2.63 and 2.64. This behavior is in contrast to when EP79.8R is loaded and unloaded prior to yielding as in Figure 2.64. When unloaded prior to yielding some crystallinity is recovered. This indicates that as the material is stretched and crystallinity is destroyed, the crystal registry is not fully disrupted until after the yield point.

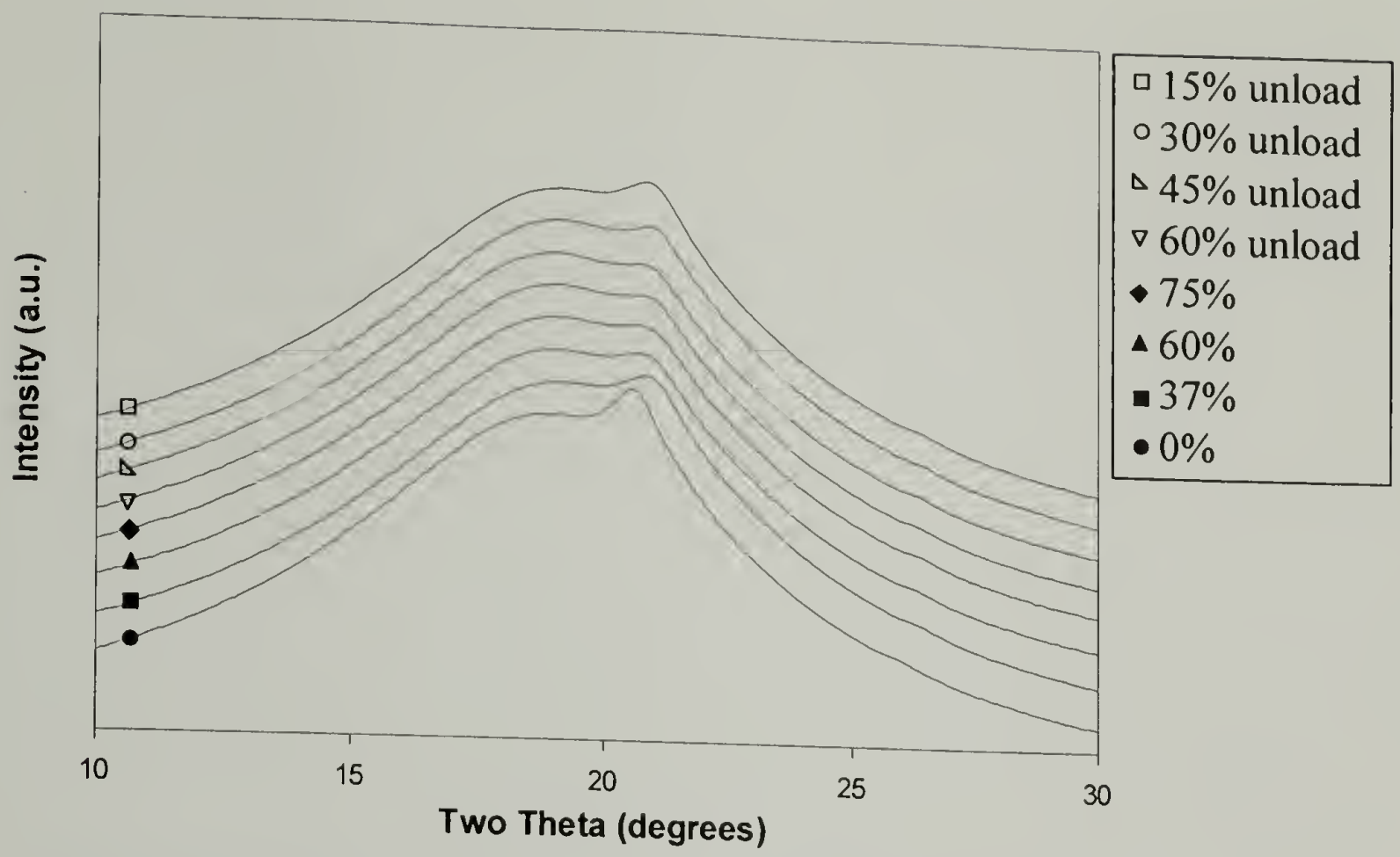

Figure 2.64: WAXD patterns as a function of strain for EP79.8R at maturity pre-yield

In order to investigate the levels of crystalline and amorphous orientation that are evident in the WAXD patterns, *in situ* FTIR dichroism is performed. The Herman's orientation function (f) is calculated as shown in equation 2.5.[72-75]

$$f = \frac{3\langle \cos^2 \theta \rangle - 1}{2} = \frac{D-1}{D+2}\frac{D_o+2}{D_o-1} \qquad (2.5)$$

In equation 2.5 D is the dichroic ratio defined as $A_{\parallel}/A_{\perp}$, $D_o = 2\cot^2\beta$, and β is the angle between the transition moment of the vibrational mode and the chain axis. $A_{\parallel}$ is the absorbance of a relevant IR band with the incident radiation polarized parallel to the draw direction and $A_{\perp}$ is the same with the incident radiation polarized perpendicular to the draw direction. For polyethylene and ethylene – α-olefin copolymers, the band at 1894 cm^{-1} is due to CH_2 rocking of trans C-C bonds within the crystalline unit cell.[72,74] The band at 1078 cm^{-1} is due to trans and gauche vibrations of amorphous material.[72,76] As a

result, the Herman's orientation function calculated using the 1894 cm^{-1} band will provide information regarding crystalline orientation while that calculated using 1078 cm^{-1} will be due to amorphous orientation. Herman's orientation function ranges between –0.5 and 1 where a value of –0.5 indicates complete orientation perpendicular to the draw direction and a value of 1 indicates complete orientation parallel with the draw direction. Figure 2.65 is an FTIR spectrum of EP79.8R showing the bands at 1894 cm^{-1} and 1078 cm^{-1}. When sample thickness is adjusted properly a single band at 720 cm^{-1} is observed. Polyethylene general exhibits a doublet at 720 cm^{-1} and 730 cm^{-1} due to vibrations of all trans C-C bonds within the unit cell. However, a sequence of more than 5 CH_2 units long is necessary in order to observe this splitting.[77-79] As discussed earlier, EP79.8R only has hexagonal crystals. A hexagonal crystal is composed of gauche and trans conformations where the trans units consist of five or fewer CH_2 units in length. This would account for not observing the traditional splitting in the infrared spectrum at 720 cm^{-1} and 730 cm^{-1}.

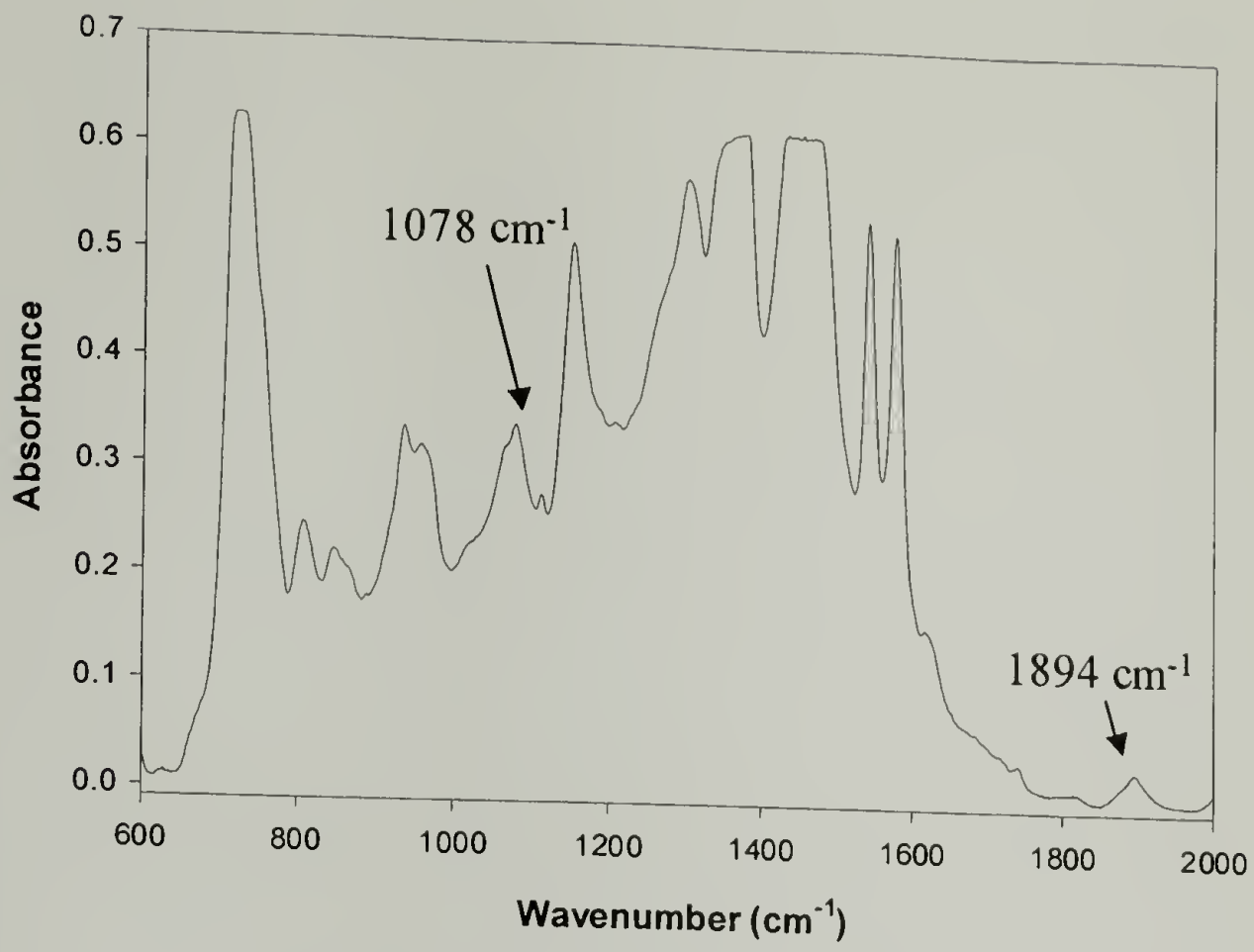

Figure 2.65: FTIR spectrum of EP79.8R

Figure 2.66 is a plot of the initial loading, unloading, and reloading stress-strain response of EP79.8R prior to yielding. Herman's orientation functions corresponding to crystalline (1894 cm^{-1}) and amorphous (1078 cm^{-1}) orientation are plotted on the same graph as a function of strain. During the initial loading excursion, crystalline orientation is achieved to a level of f = 0.6. Upon unloading some permanent orientation remains, and upon reloading the orientation level is reproduced. The amorphous orientation achieves a level of f = 0.2 and appears to be completely reversible prior to yielding. From this analysis the crystallites appear to be mobile crosslinks that rotate during drawing and then translate as amorphous orientation is achieved. Upon unloading the amorphous material becomes completely unoriented while the crystallites retain some permanent level of orientation.

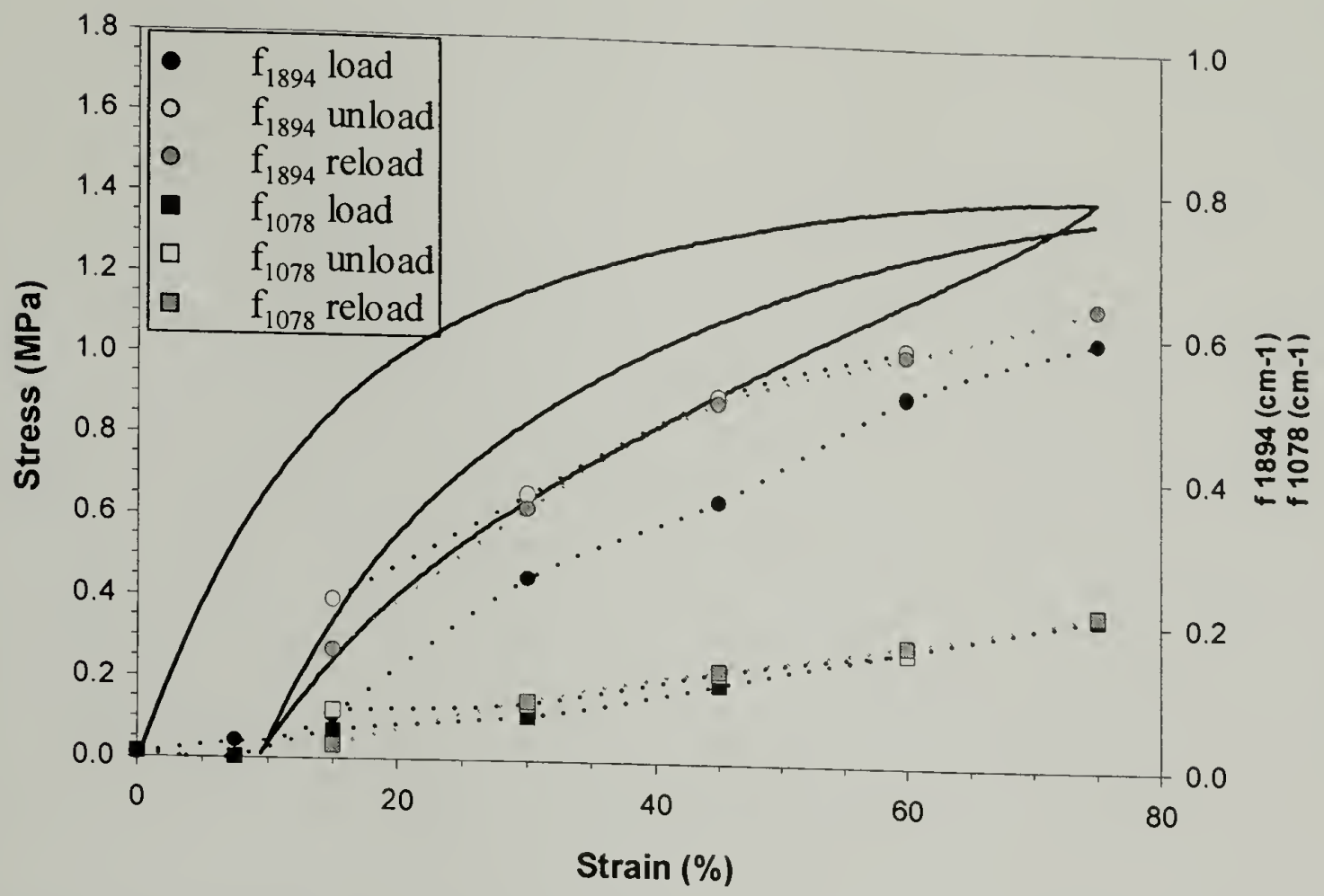

Figure 2.66: Crystalline (1894 cm^{-1}) and amorphous (1078 cm^{-1}) orientation of EP79.8R prior to yielding

Figure 2.67 shows the same type of analysis only now subsequent to yielding. It is immediately evident that the majority of crystalline orientation is achieved prior to yielding while the majority of amorphous orientation is achieved after yielding. Substantial hysteresis is observed in the amorphous orientation upon unloading and reloading while the crystalline orientation function ranges between 0.7 and 0.9.

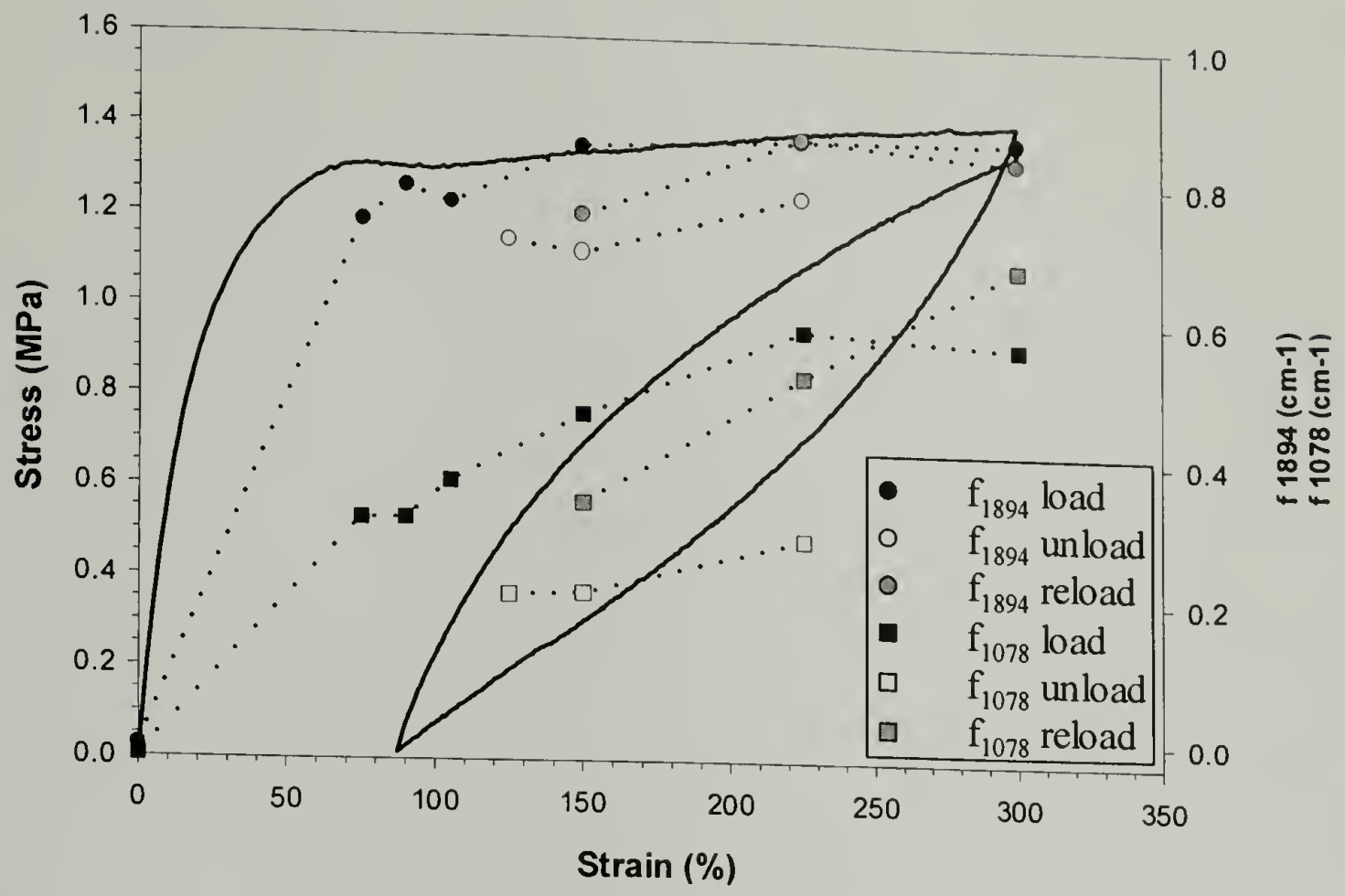

Figure 2.67: Crystalline (1894 cm^{-1}) and amorphous (1078 cm^{-1}) orientation of EP79.8R after yielding

The cartoon in Figure 2.68 illustrates the morphological changes that occur upon deformation. Prior to deformation no orientation exists in the amorphous or crystalline regions. Orientation appears to occur in a two-stage process. As deformation occurs prior to yielding the majority of crystalline orientation is achieved as the crystalline network is destroyed. After yielding the majority of amorphous orientation is achieved and a high level of both amorphous and crystalline orientation exist.

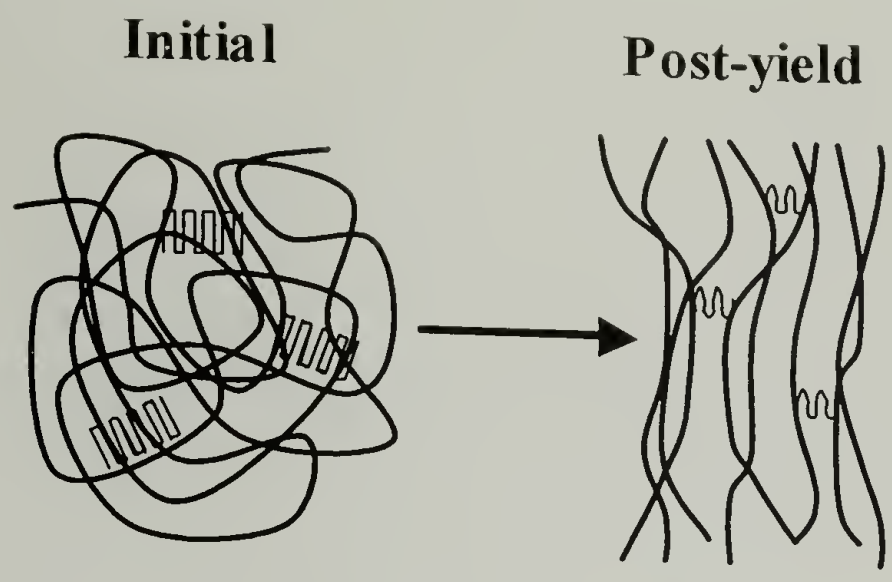

Figure 2.68: Cartoon showing change in crystallinity and amorphous and crystalline orientation as observed through WAXD and FTIR prior to and subsequent to yielding

The enhanced ductility of EP79.8R may be due to a critical molecular weight between physical crosslinks. However, these physical crosslinks cannot be crystals given that ductility is not a function of the crystallization kinetics of EP79.8R. The physical crosslinks may be related to the enhanced density or branching content.

2.4.3 Apparent Yielding Behavior of EP79.8R

Heterogeneous deformation (*i.e.*, neck formation and propagation) is generally observed for a thermoplastic material as yielding occurs. On an engineering stress-strain curve, heterogeneous deformation is manifested as a distinct yield point followed by strain softening and elongation at a constant draw stress. Strain softening typically occurs due to the formation of a geometric instability that occurs as a neck begins to form at a region of stress concentration. The neck then propagates at a constant draw stress. Once the neck has stabilized or fully consumed the gauge length, strain hardening occurs. The yielding region observed in the engineering stress-strain behavior of EP79.8R resembles that of a thermoplastic with strain softening even though necking is not

visually observed. It is unusual for a material to exhibit a distinct yield point with any degree of strain softening without the formation of a neck. As such the nature of yielding in EP79.8R warrants further study.

If heterogeneous deformation occurs, the ratio of the yield stress to the draw stress generally becomes more apparent at lower temperatures and higher strain rates. Figure 2.69 shows the engineering stress-strain behavior of EP79.8R at crosshead speeds ranging from 5 mm/min to 500 mm/min. As strain rate is increased, the yielding behavior is unaffected except for an increase in magnitude as expected. As strain rate is increased the strain hardening slope and ductility decrease. This may be due to heating affects destroying physical crosslinks thus diminishing the entropic contribution to strain hardening. A distinct yielding peak with strain softening has also been observed in ethylene – hexene copolymers.[58] This behavior has shown a trend with molecular weight where necking is observed visually for compositions with low molecular weight. As the molecular weight is increased the deformation appears to become homogeneous in nature similar with that observed for EP79.8R. The critical molecular weight where necking is no longer observed in ethylene – hexene copolymers is between 80,000 and 200,000 g/mol.[58] The molecular weight of EP79.8R is within that range at 111,000 g/mol.

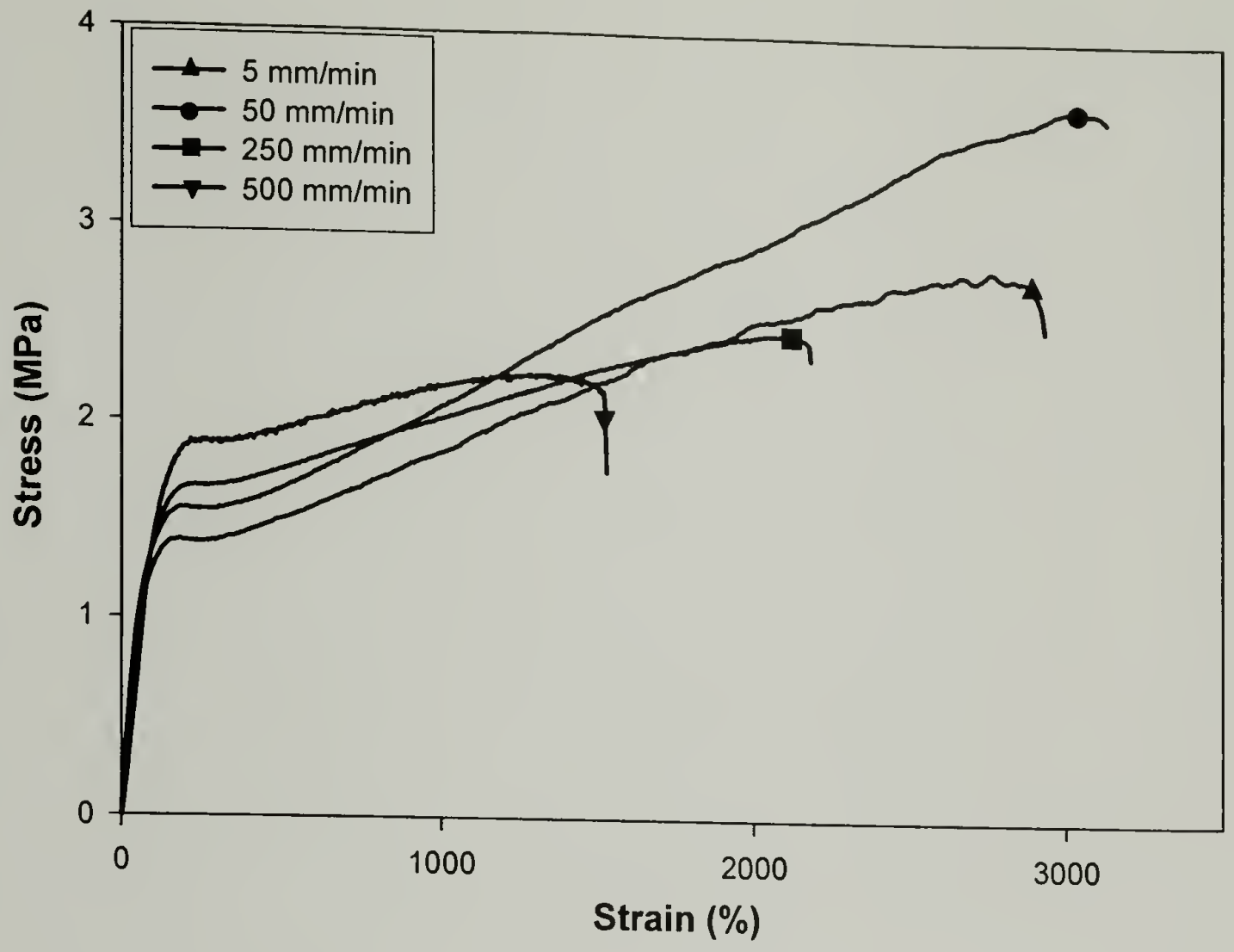

Figure 2.69: Yield behavior of EP79.8R as a function of strain rate

Figure 2.70 shows the engineering stress-strain behavior at 25 °C, 0 °C, and –20 °C at a crosshead speed of 2 mm/min. As temperature is decreased the strain softening response completely disappears and the yielding region resembles that of an elastomer instead of a thermoplastic. These results do not support a true heterogeneous deformation which would become more pronounced at lower temperatures and higher strain rates. It has been speculated that the yielding behavior of polyethylene is possibly due to a melting and recrystallization phenomenon.[59] If this occurs at room temperature, perhaps there is not enough thermal energy supplied at 0 °C to melt the crystals.

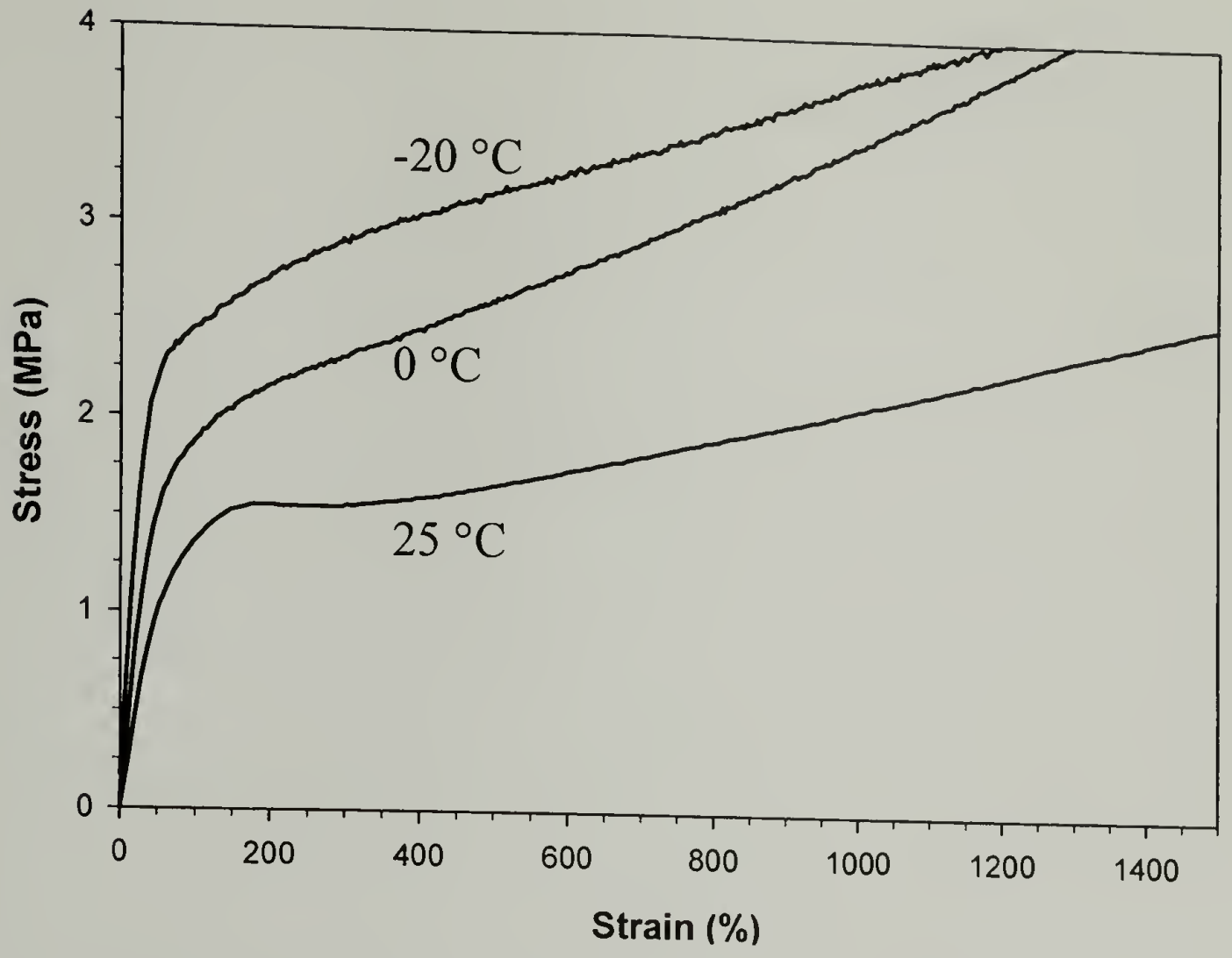

Figure 2.70: Yield behavior of EP79.8R as a function of temperature

The initial portion of the stress-strain behavior and the corresponding degree of crystallinity for EP79.8R is shown in Figure 2.71. As yielding occurs crystallinity decreases steadily and appears to reach a constant value at approximately 225% strain. Recalling the mechanical behavior evolution as a result of crystallization, the distinct yield point only emerges as hexagonal crystals form. Initially after solidification EP79.8R is essentially amorphous with monotonically increasing stress-strain behavior. As a result, the distinct yielding process may originate from destruction of crystals. The deformation then appears to stabilize which allows further drawing and strain hardening.

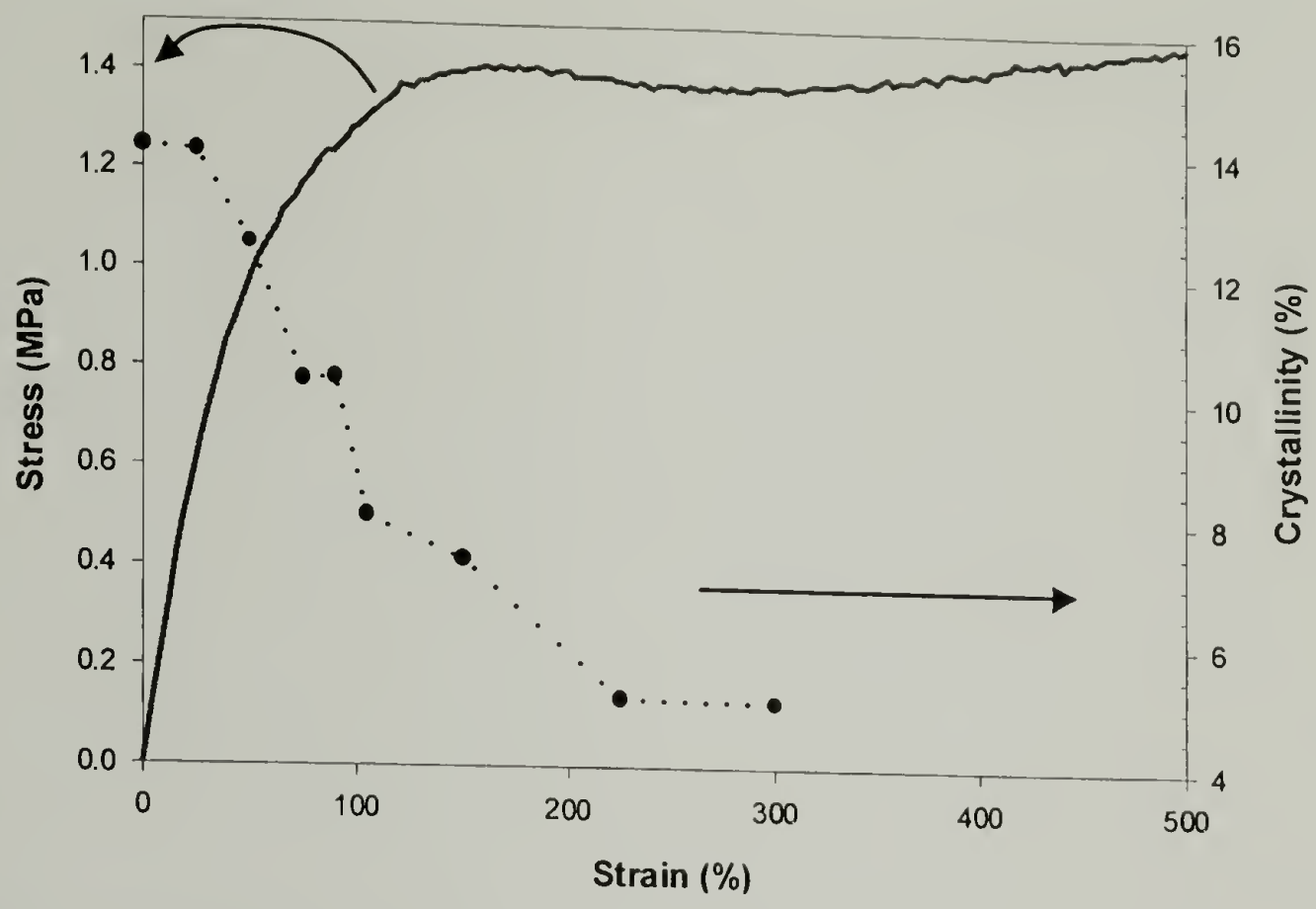

Figure 2.71: Crystallinity as a function of strain for EP79.8R illustrating destruction of crystals as yielding occurs and reformation of crystals after yielding is complete

2.5 Effect of Rigid Fillers

The stiffness of elastomeric materials can be enhanced by the introduction of rigid filler particles.[80] There has been interest in understanding how particles of different shape enhance the stiffness, apparent yield behavior, and elastomeric response in terms of reversibility and stress softening. In this vein some initial studies are conducted with mature EP68.6B as the matrix material. Ceramic fillers with a constant particle volume (1700 μm^3) and various shapes (spheres, rods, and plates) are compounded into the matrix with a DACA twin-screw microcompounder. A barrel temperature of 190 °C and a screw rpm of 100 are used. Batch compounding with a residence time of 3 minutes provides the most homogeneous filler dispersion. Figure 2.72-2.74 and 2.75-2.77 show SEM micrographs of the resulting morphologies with 5 and 10 volume % filler,

respectively. The spherical particles are an alkalialuminosilicate provided by 3M. The rod shaped particles are wollastonite provided by NYCO Minerals. The plate shaped particles are mica provided by Whittaker, Clark, and Daniels.

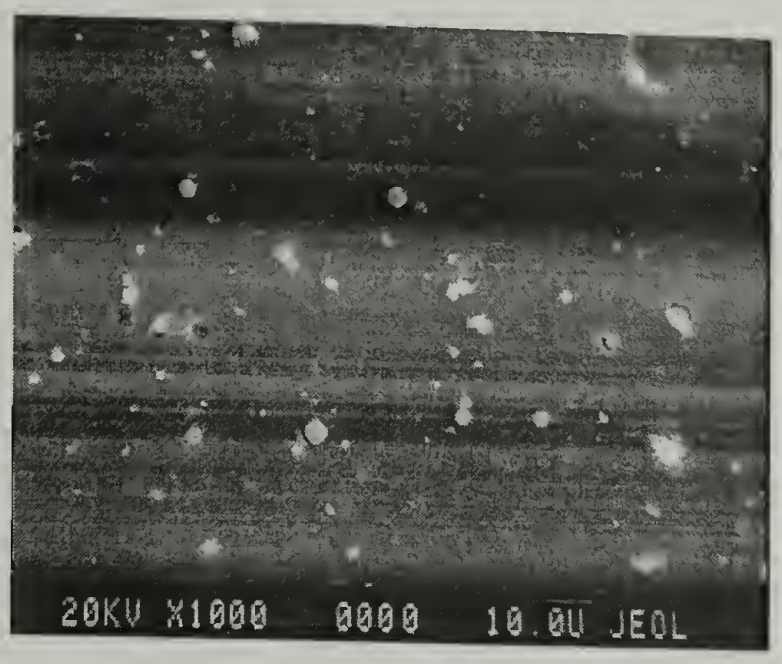

Figure 2.72: Morphology of EP68.6B with 5% spheres

Figure 2.73: Morphology of EP68.6B with 5% rods

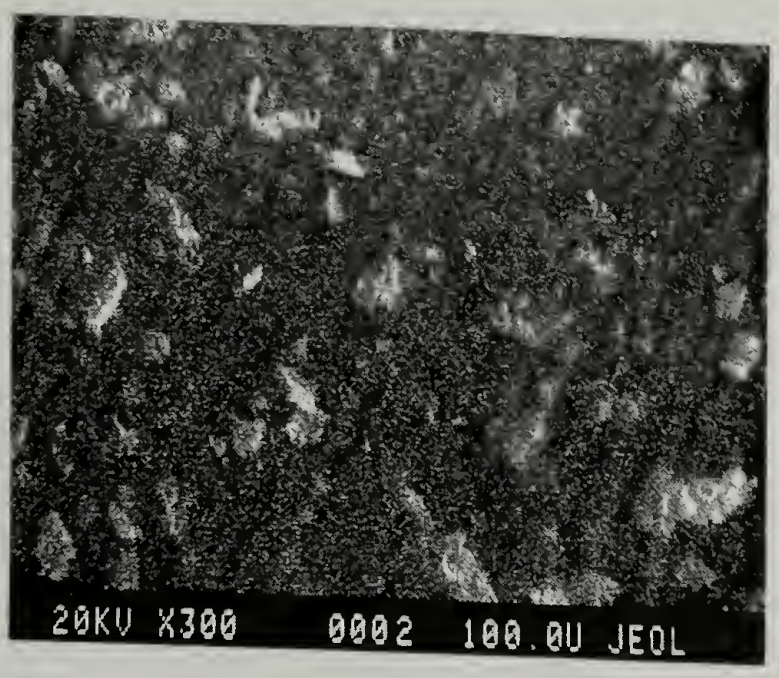

Figure 2.74: Morphology of EP68.6B with 5% plates

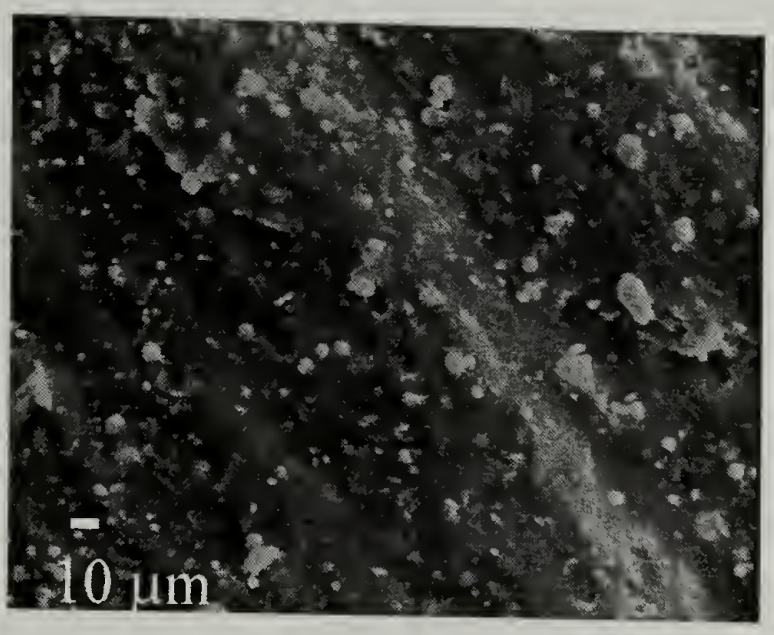

Figure 2.75: Morphology of EP68.6B with 10% spheres

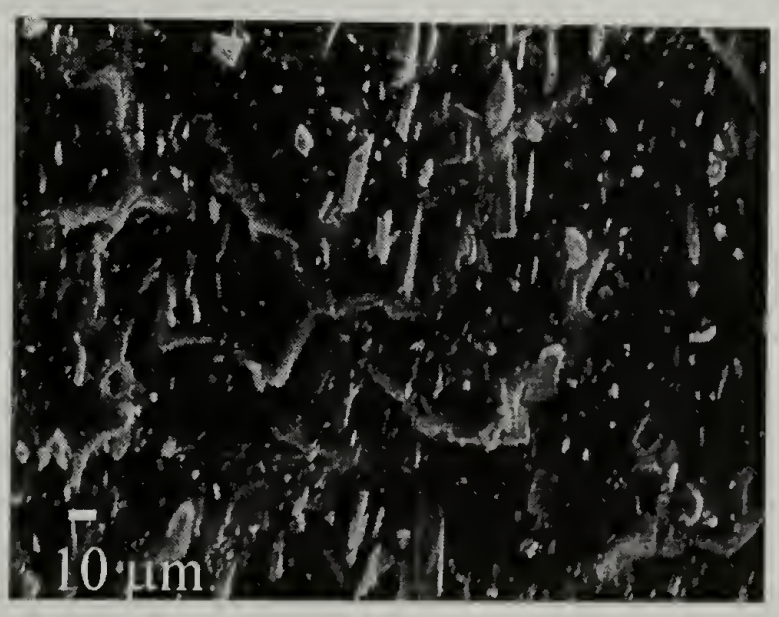

Figure 2.76: Morphology of EP68.6B with 10% rods

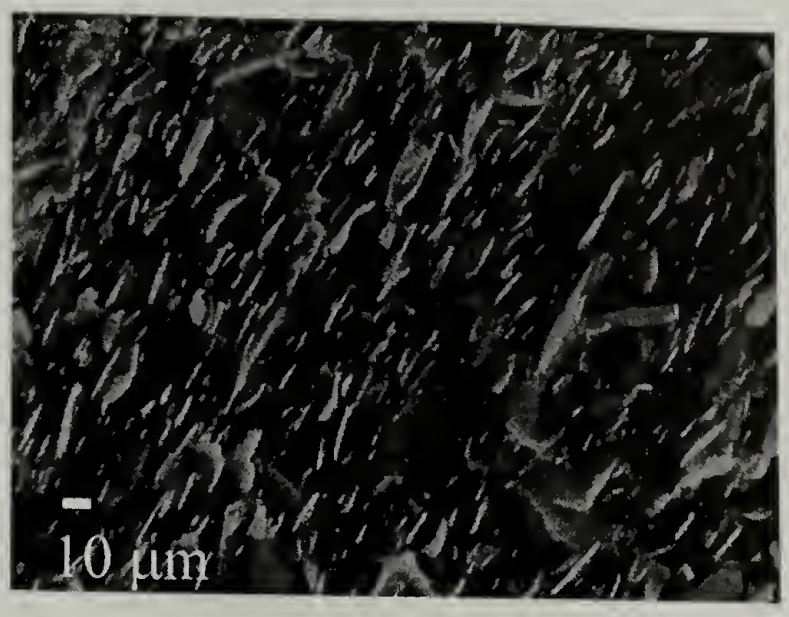

Figure 2.77: Morphology of EP68.6B with 10% plates

The engineering stress-strain behavior is shown in Figure 2.78 for unfilled EP68.6B along with particulate composites of 5 and 10 volume % spheres, rods, and plates. As filler is introduced stiffness increases while ductility decreases. Figure 2.79 plots modulus as a function of filler content.

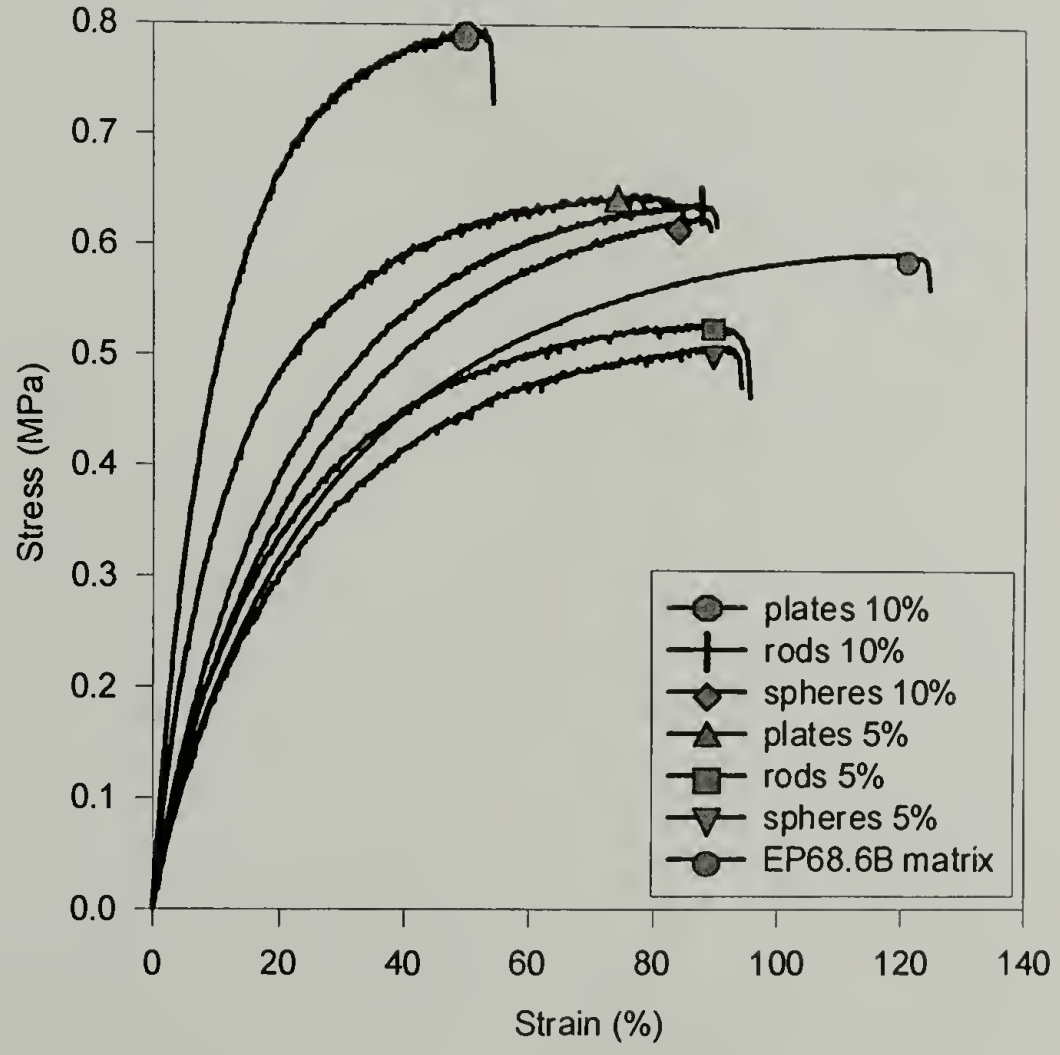

Figure 2.78: Stress-strain curves as a function of filler content with EP68.6B as the matrix

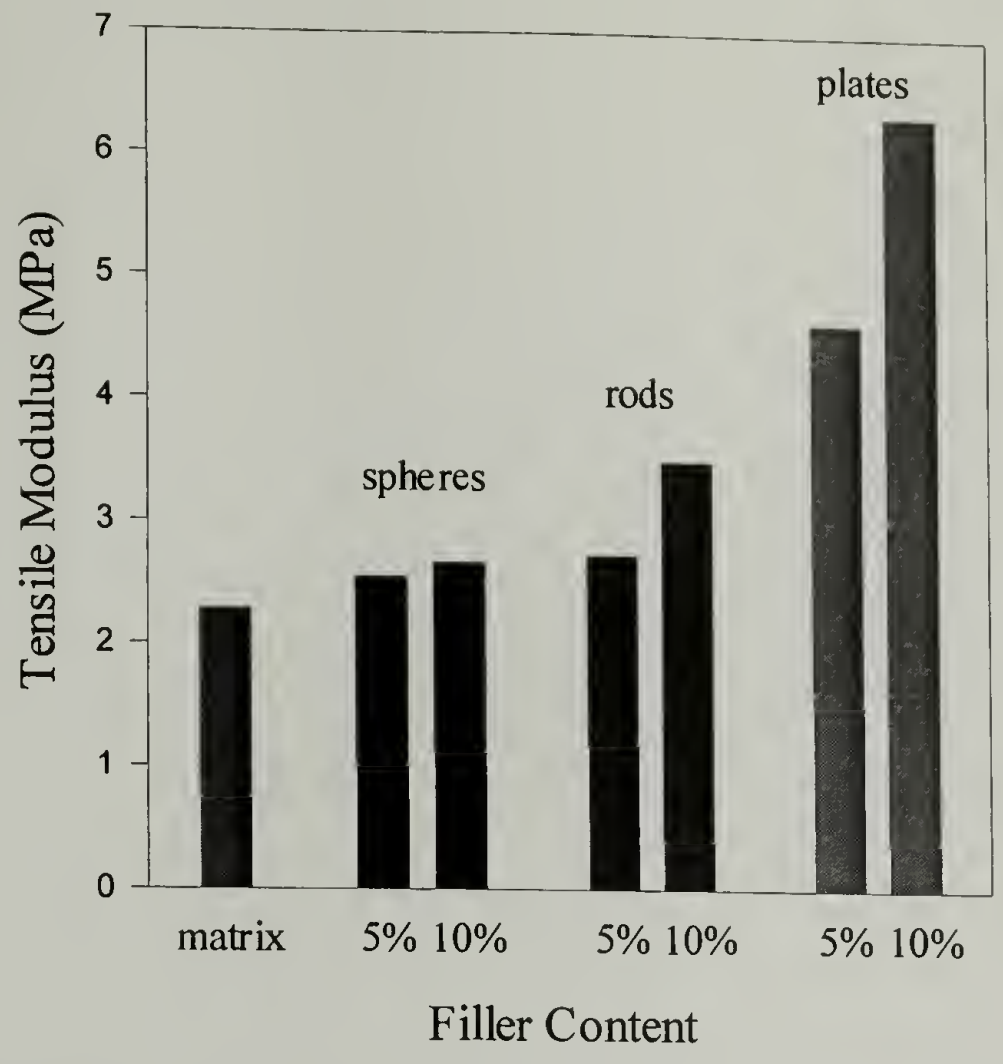

Figure 2.79: Tensile modulus as a function of filler content with EP68.6B as the matrix

The effect of higher filler loadings on the stress-strain behavior is shown in Figure 2.80 and Figure 2.81 shows the influence on modulus. The 15 and 25 volume % particulate composites were compounded at the ExxonMobil Chemical Company. However, EP68.6R was used as the matrix material instead of EP68.6B. As a result, the modulus enhancement of the various filler shapes cannot be directly compared since EP68.6B and EP68.6R have different initial moduli. Since they have the same type of yielding behavior and ductility (see Figure 2.36) the filled moduli are normalized by the respective unfilled matrix moduli. Thus Figure 2.82 provides an accurate comparison of the effect of particle shape on reinforcement. At the same volume concentration, particle shape enhances modulus in the order of spheres < rods < plates which indicates that surface

area is the most important factor in modulus enhancement given that all fillers have approximately the same volume.

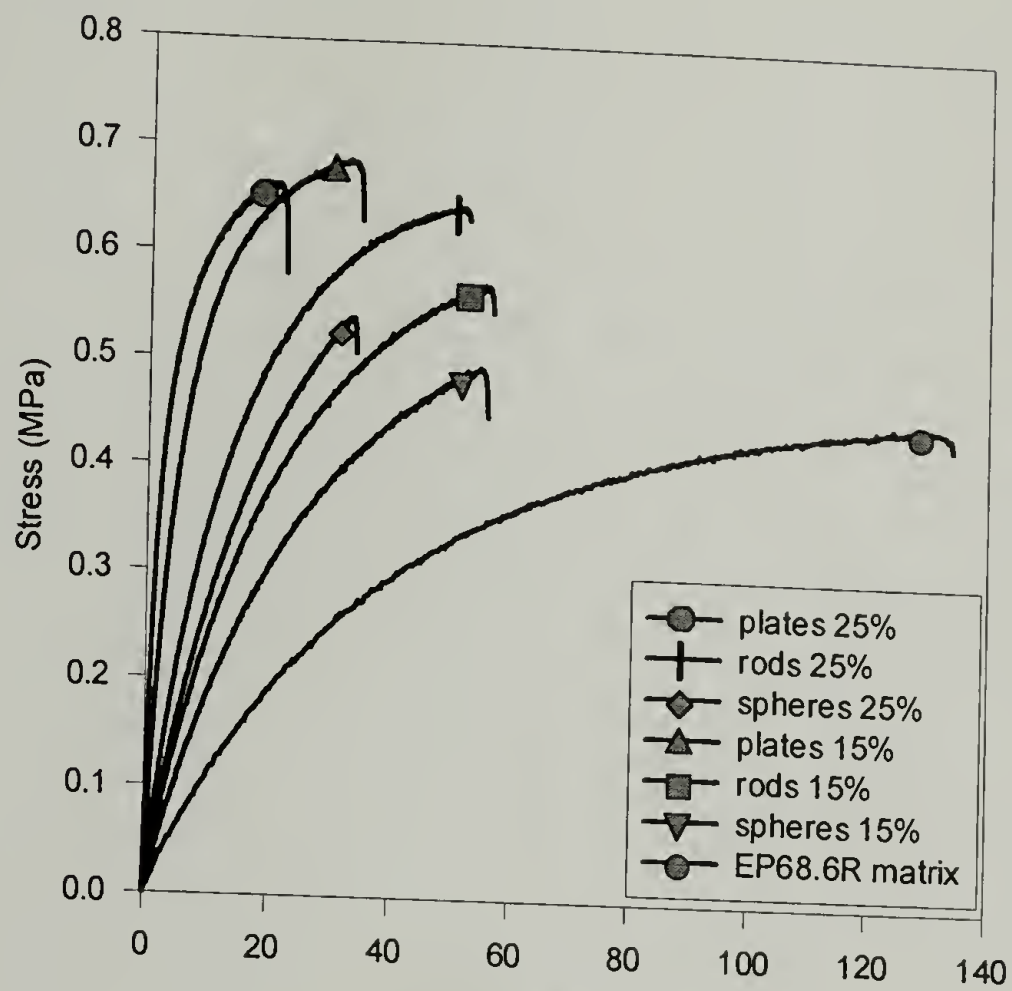

Figure 2.80: Stress-strain curves as a function of filler content with EP68.6R as the matrix

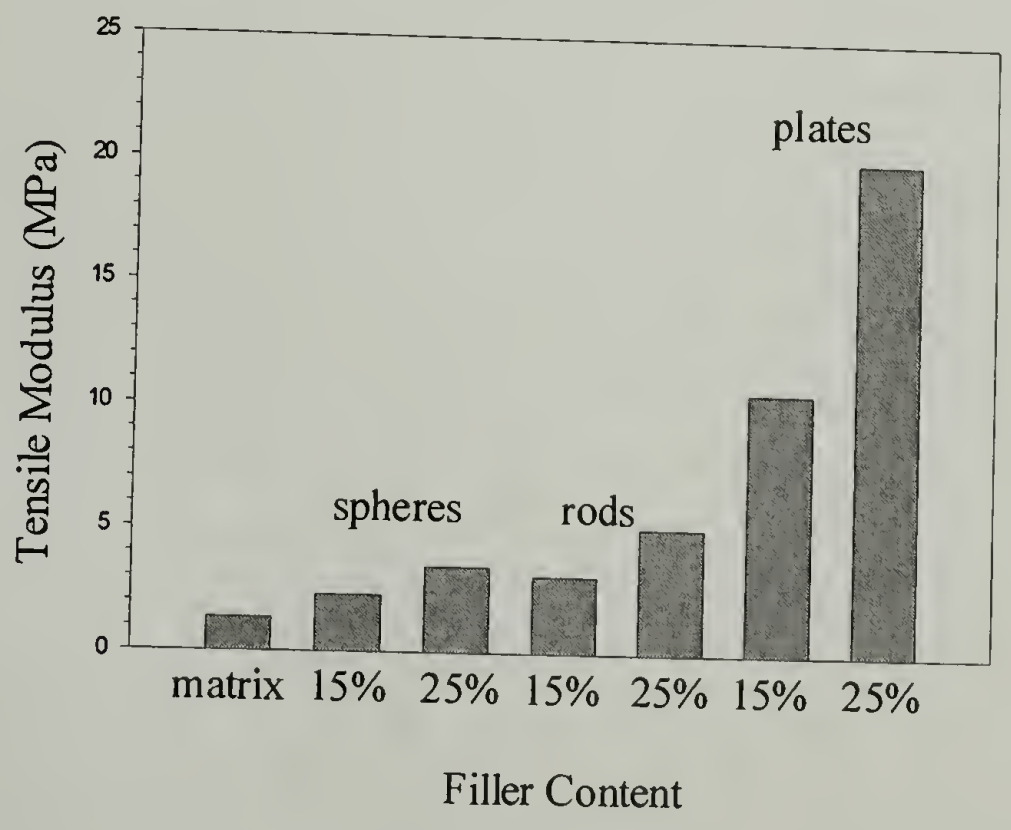

Figure 2.81: Tensile modulus as a function of filler content with EP68.6R as the matrix

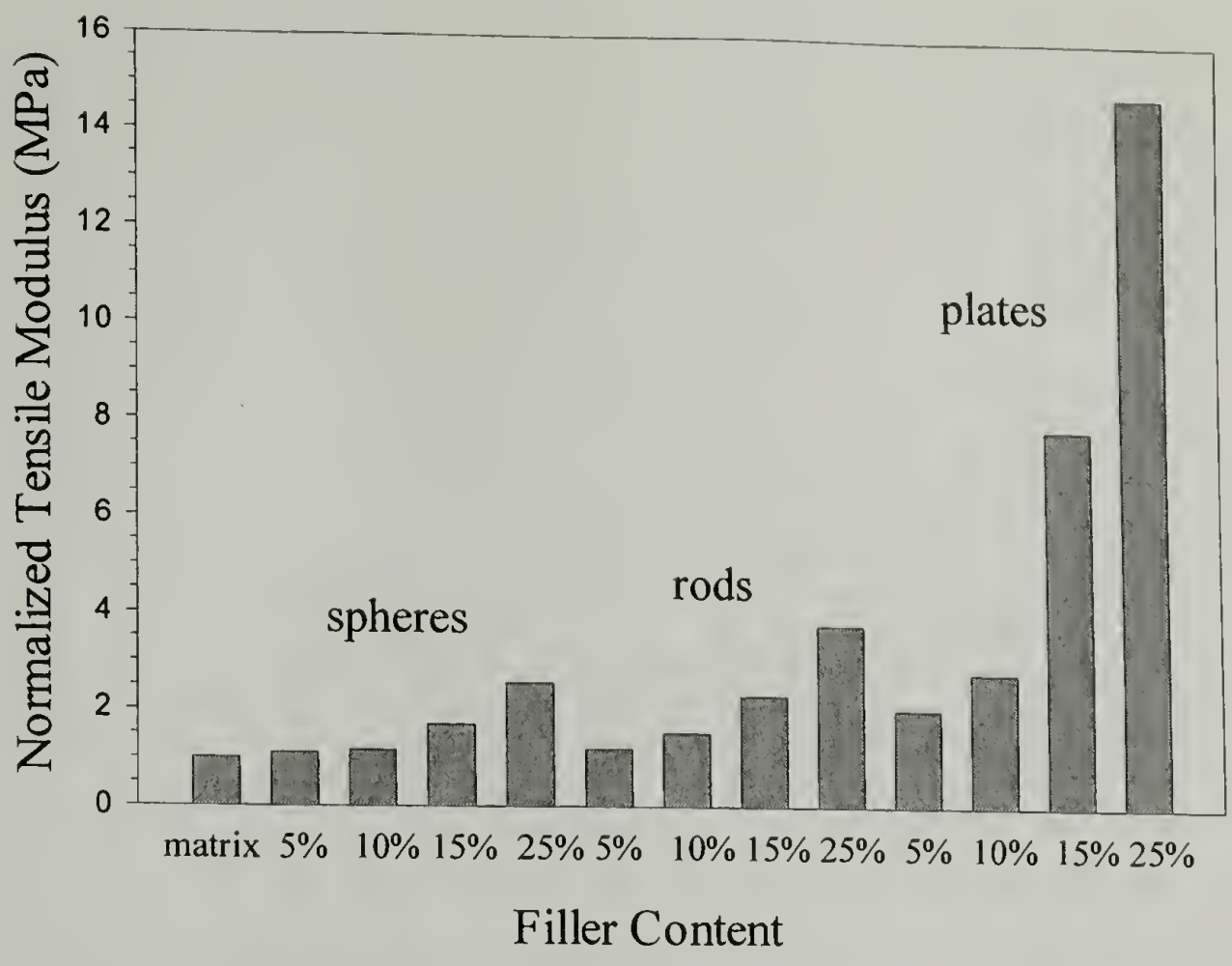

Figure 2.82: Normalized tensile modulus as a function of filler content based on EP68.6B and EP68.6R as matrices

Stress state is also thought to influence the mechanical behavior of filled elastomers. As such the elastomeric behavior of composites with 5 and 10 volume % filler loadings are compared under cyclic tensile and compressive loading conditions. When cycled in tension under load control the peak stress is held at 70% of the apparent yield stress. In compression the peak stress is equal to the stress at 50% strain. Figure 2.83 is a plot of permanent set per cycle as a function of filler shape and loading. Irreversible deformation decreases as the surface area of the filler particles increase.

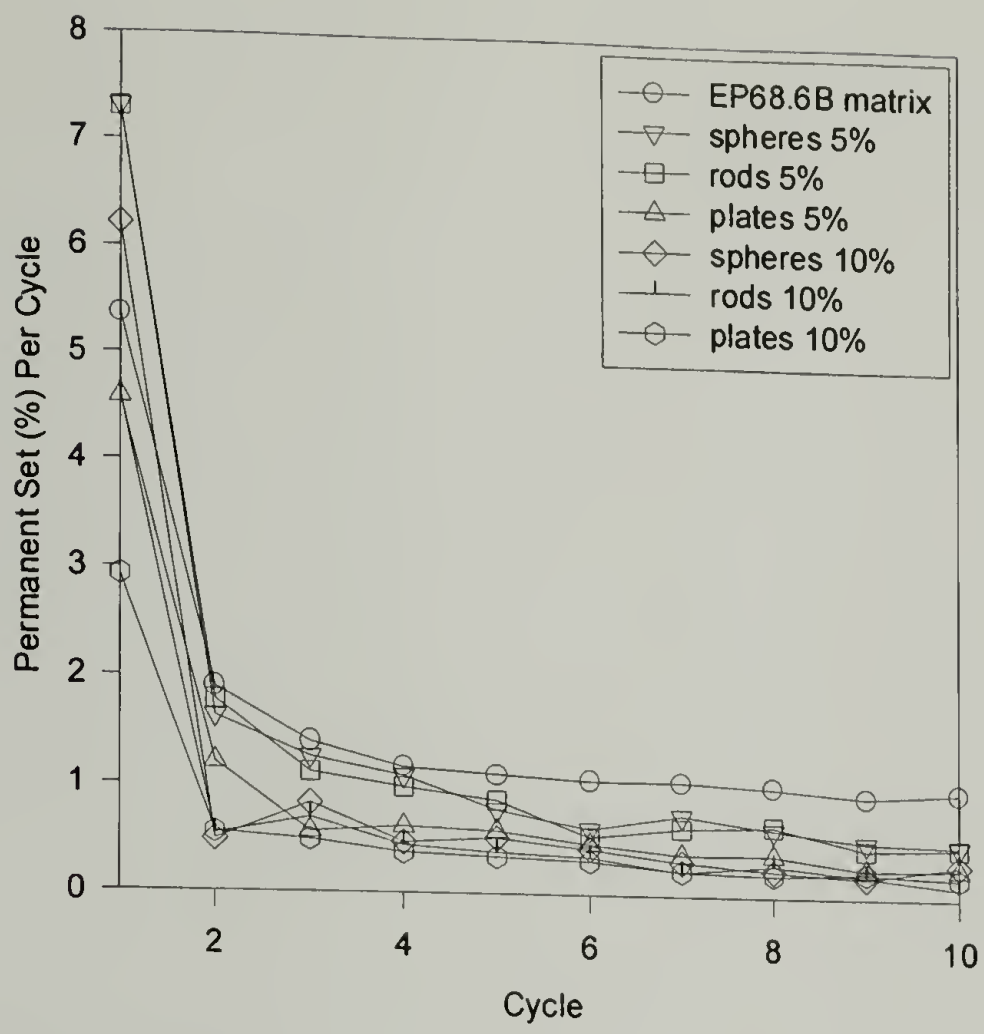

Figure 2.83: Permanent set per cycle as a function of filler content

Figure 2.84 is a Mullins plot for the same concentrations. As discussed earlier, the energy loss of filled crosslinked elastomers generally increases with increasing energy input. As such the slope of the line indicates the percentage of dissipated energy. However, from Figure 2.84 it can be seen that energy loss does not increase monotonically with energy input in a tensile loading geometry. Instead when sufficient conditioning takes place and a steady-state response is reached, the energy loss remains constant while energy input increases slightly.

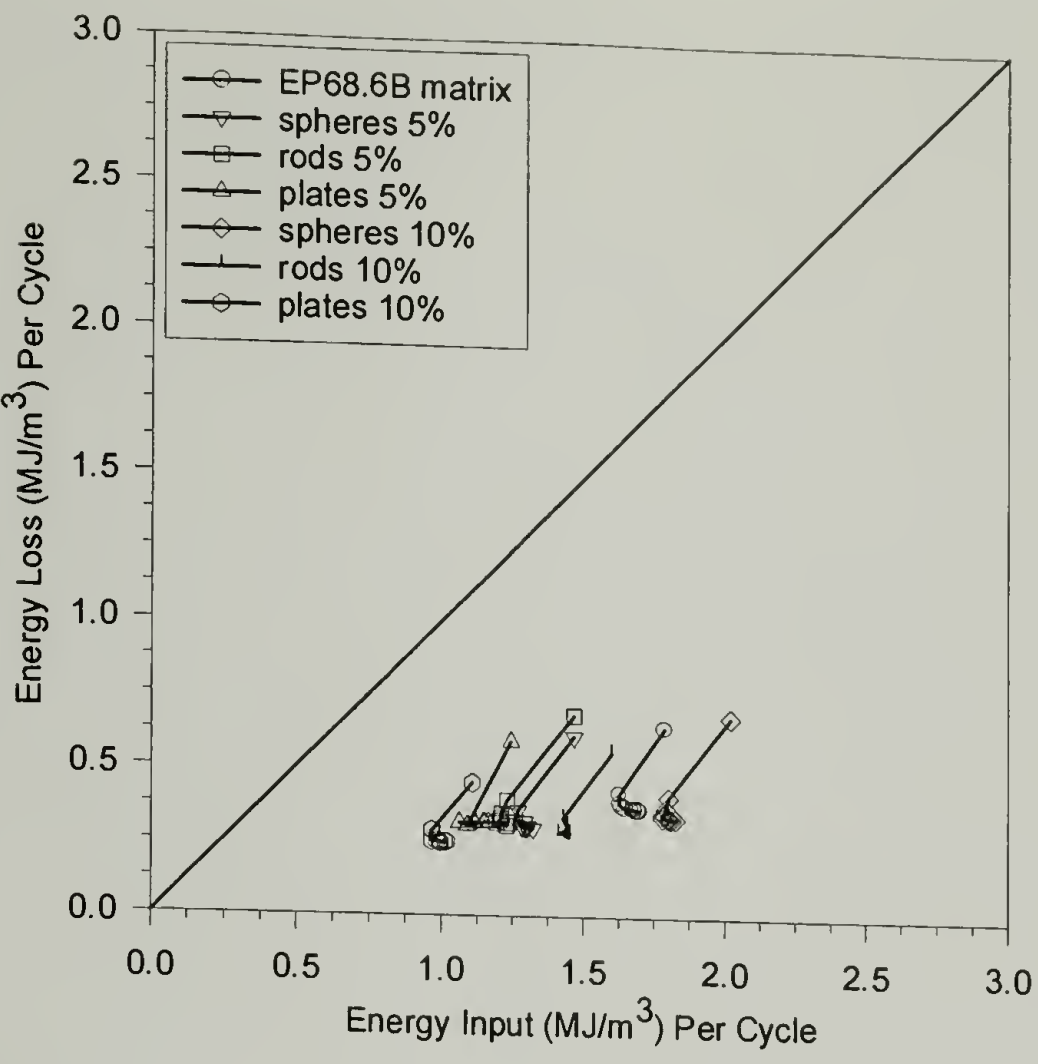

Figure 2.84: Mullins plot when cycled in tension as a function of filler content

When examined under uniaxial cyclic compression, the composites with 5 % filler loading reach a steady-state response after approximately five cycles. Figure 2.85 plots the energy loss per cycle while Figure 2.86 plots the permanent set per cycle. It appears that the addition of filler does not change the elastomeric nature of the EP68.6B to any appreciable degree in compression.

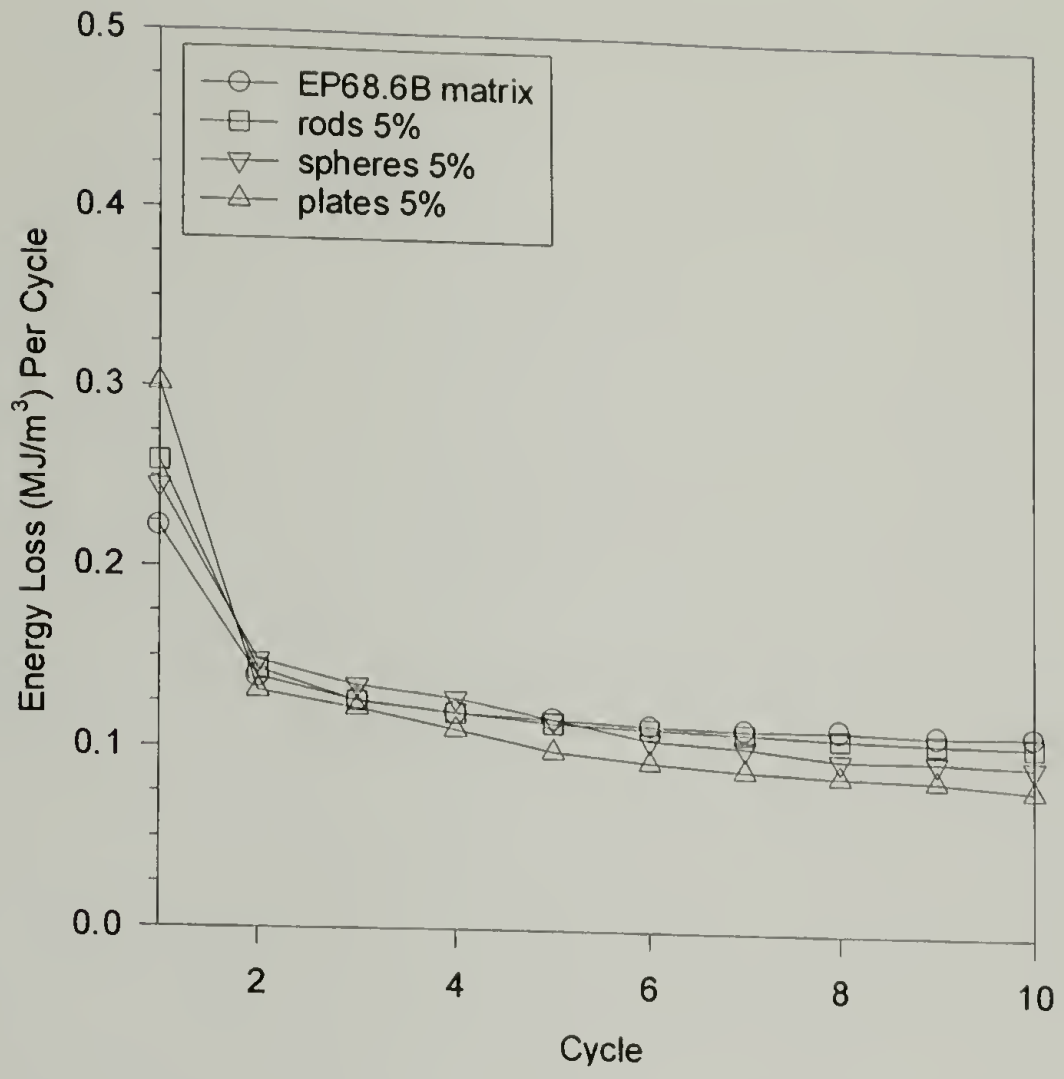

Figure 2.85: Energy loss as a function of filler content in compression

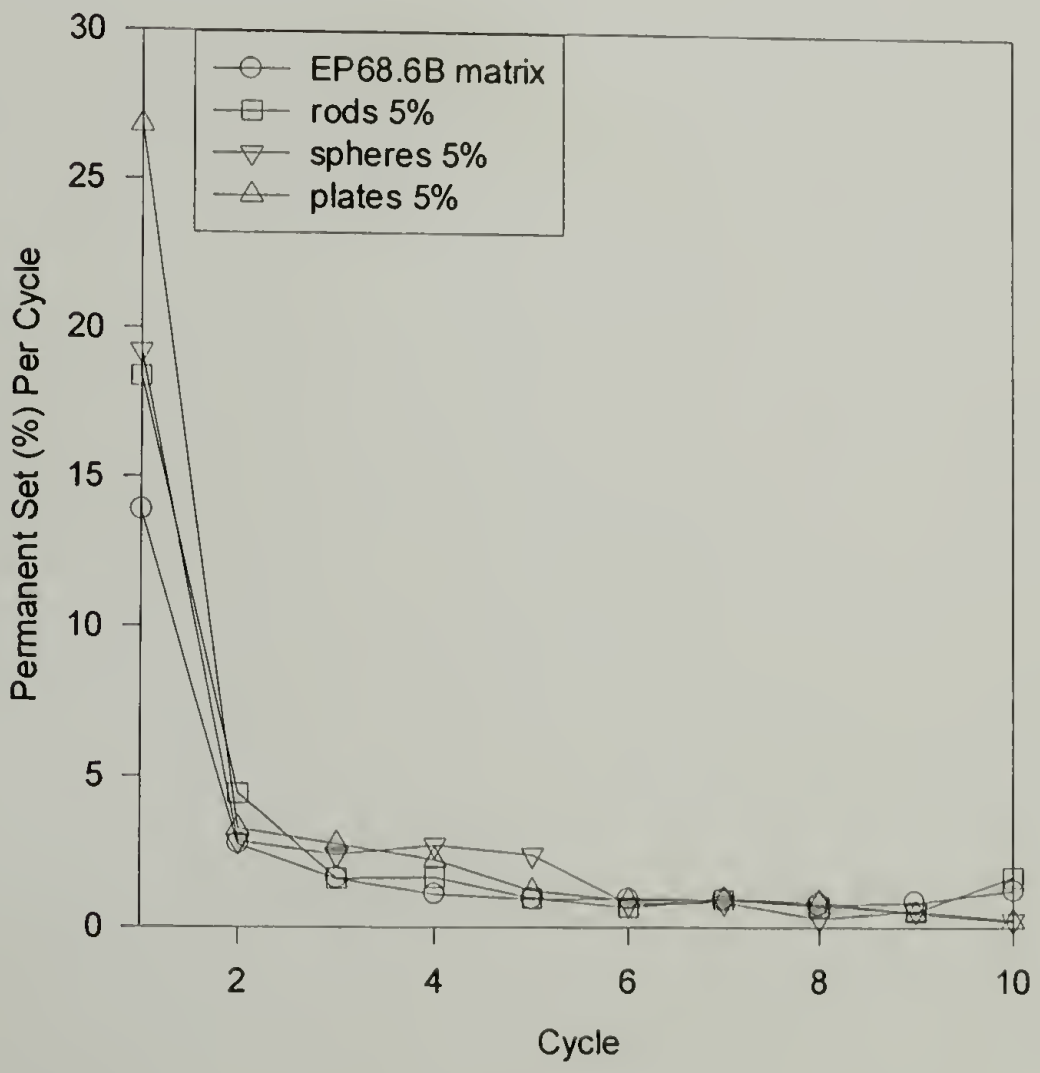

Figure 2.86: Permanent set as a function of filler content in compression

Figure 2.87 is a Mullins plot for the particulate composites with 5% filler tested in compression. Now a monotonic relationship exist between the energy lost due to hysteresis and the energy supplied to the deformation. This is in contrast to the behavior observed in tension. This same type of stress state dependence is observed for the unfilled ethylene –propylene copolymers as described earlier in section 2.3.3. As a result, it appears that stress-state plays a significant role in the steady-state dissipation mechanisms of this class of thermoplastic elastomers.

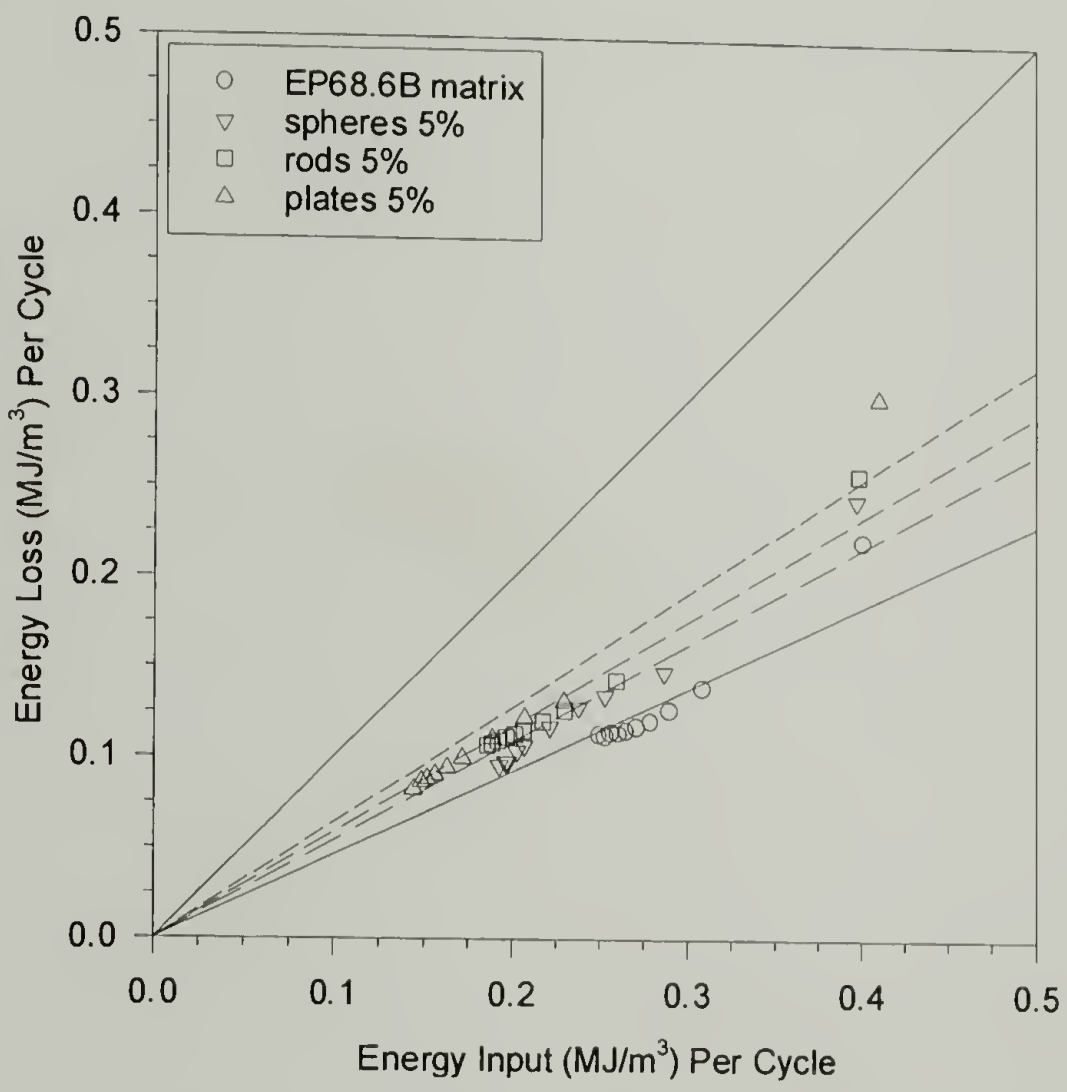

Figure 2.87: Mullins plot as a function of filler content when cycled in compression

2.6 Conclusions

Crystal evolution and resulting mechanical behavior of five ethylene – propylene copolymers are examined. As the materials age at room temperature their crystal

structures evolve. The presence of the hexagonal and orthorhombic structures is directly related to the comonomer distribution. Hexagonal and orthorhombic crystals coexist together in EP68.6B and EP69.0B while only the hexagonal phase is observed in EP68.6R and EP79.8R. EP68.6B and EP69.0B both have a more blocky structure with longer ethylene segments that can form the orthorhombic structure while EP68.6R and EP79.8R have a more random comonomer distribution. As ethylene content increases, the final degree of crystallinity also increases.

Initial density does not obey a rule of mixtures in terms of crystallinity but is linearly related to branching content. This may be due to the presence of a densified amorphous phase that has previously been observed in quenched polypropylene as well as drawn polyethylene. This densified amorphous phase may be evident as the uniformly granular structure observed in TEM. As aging occurs, density increases commensurately with the formation of crystals in the hexagonal phase.

These materials exhibit mechanical behaviors in between that of traditional elastomers and that of thermoplastics. The mechanical behavior evolution of these copolymers is characteristic of increasing crystallinity. The moduli increase as the samples age while the elongation at failure decreases. All samples show a "yield-like" behavior at approximately 175% strain. Increases in yield stress and decreases in rupture energy density are a due to the incorporation of hexagonal crystals. The distinct yield point of EP79.8R appears to be related to the destruction of the crystalline network. The main difference between the compositions is their post-yield behavior. Only EP79.8R continues to draw and strain harden after yielding. Data suggests that the origins of enhanced ductility are not due to molecular weight effects, initial crystal structure,

crystallization kinetics, or changes in crystal structure upon drawing. No evidence has been found that directly supports strain induced crystallization. As a result, enhanced ductility may originate from a critical molecular weight between physical crosslinks. The physical crosslinks may be related to density in the form of a densified amorphous phase.

Ethylene – propylene copolymers exhibit a Payne effect response similar to more traditional crosslinked elastomers despite a fundamentally different morphology. This response differs slightly from more traditional systems in that the characteristic strain occurs at lower strain amplitudes. Even though these copolymers exhibit a Payne effect, a stress-softening response is not directly evident. The origins of elastomeric behavior appear to be related to the amount of heterogeneity as the sigmoidal dependence (E'_o-E'_∞) is influenced initially by density and ultimately by crystallinity.

CHAPTER 3

DYNAMICALLY VULCANIZED EPDM/IPP BLENDS

3.1 Materials

Three formulation parameters are generally thought to control the final morphology of dynamically vulcanized EPDM/iPP blends: the compositional ratio of EPDM to iPP as well as the amount of oil incorporated, the iPP molecular weight, and the cure state of the EPDM phase. For this study these three parameters are chosen in such a way to allow examination of a broad range of compositions and morphologies. Advanced Elastomer Systems provided six compounds listed in Table 3.1 where all compositions are given in weight percent. The oil listed in the formulations is a hydrocarbon paraffin oil and is incorporated as a processing aid. High and low molecular weight iPP is used in the formulations. The molecular weight of the iPP is characterized by melt flow rate (MFR) in accordance with ASTM D1238. Molecular weight is inversely proportional to MFR. Low, medium, and high EPDM cure states are also examined.

Table 3.1: Dynamically vulcanized EPDM/iPP blend compositions

Sample	EPDM	i-PP	Oil	i-PP MFR	Cure State
PHXM	25%	50%	25%	0.7	Medium
PLXM	25%	50%	25%	20	Medium
EHXL	40%	20%	40%	0.7	Low
EHXM	40%	20%	40%	0.7	Medium
EHXH	40%	20%	40%	0.7	High
ELXH	40%	20%	40%	20	High

As a result of these variables, a sample naming system is adopted for ease of comparison. The sample name consists of four letters in which the first letter refers to the majority volume fraction: P for iPP rich or E for EPDM rich. The second letter refers to the molecular weight of the iPP: H for high molecular weight or L for low molecular weight. The third and fourth letters refer to the crosslinking density of the EPDM rubber: XL for a low, XM for a medium, or XH for a high. For example, a composition referred to as PHXM is iPP rich with high molecular weight iPP and has a medium crosslinking density of the EPDM rubber.

3.2 Morphology Characterization

3.2.1 Experimental Procedures

Blend morphology is examined using scanning electron microscopy (SEM). The samples are faced smooth using a cryogenic microtome, etched in a permanganic etch for two hours, gold coated, and imaged under SEM (JEOL 35CX). The permanganic etch[81] involves mixing sulfuric acid, orthophosphoric acid, and potassium permanganate crystals. This etching procedure preferentially removes amorphous rubbery domains leaving behind raised regions of crystalline iPP.

Further morphological evaluation is conducted using tapping mode atomic force microscopy (AFM). Samples are faced smooth using a cryogenic microtome prior to AFM analysis. AFM analysis is performed using a Digital Instruments Dimension 3100 at a scanning rate of 0.2 Hz. The instrument is equipped with an integrated silicon tip/cantilever. Phase imaging is used to differentiate the crosslinked rubber domains

from the semicrystalline matrix. Digital image analysis was performed on the phase images using Zeiss Image software version 1.0 to determine average domain size.

3.2.2 Morphology Results

In all compositions the paraffin oil has been shown to have equal affinities for the EPDM rubber and the amorphous iPP and has been shown to be equally distributed between both constituents.[23,30,31] Figures 3.1 and 3.2 show the morphologies of the iPP rich samples, PHXM and PLXM, respectively. The only difference between these samples is the molecular weight of the iPP. In these compositions the EPDM exists as discrete rubbery domains on the order of 1-3 μm in diameter which is consistent with the process of dynamic vulcanization. The iPP is the continuous phase. The spacing between nearest domains ranges between 1 and 2 μm. These two compositions have very similar morphologies indicating that the molecular weight of the iPP has little effect on morphology.

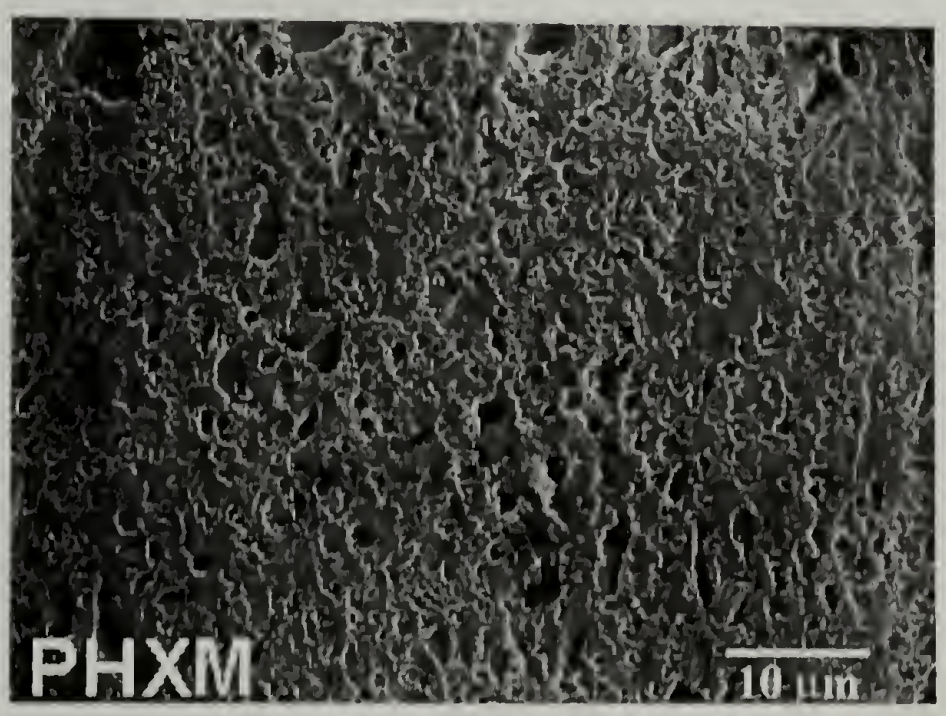

Figure 3.1: SEM micrograph of etched PHXM

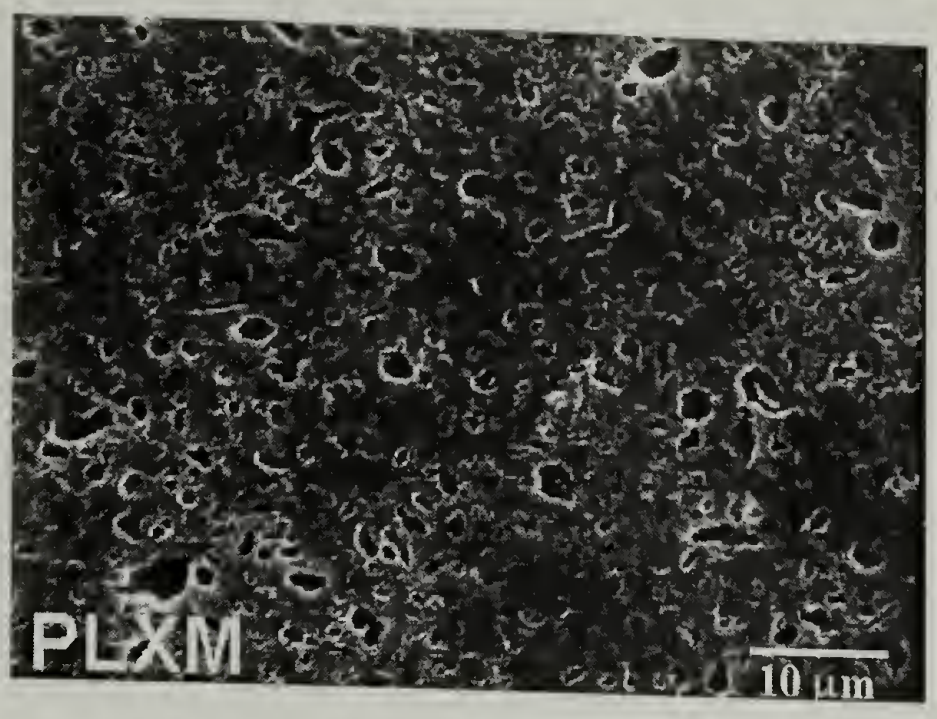

Figure 3.2: SEM micrograph of etched PLXM

The morphologies of the EPDM rich compositions are shown in Figures 3.3-3.7. All micrographs have been taken at the same magnification and are shown in order of increasing cure state. Figure 3.3 is an SEM micrograph of etched EHXL while Figure 3.4 is an AFM image of the same composition. In both images the morphology appears very fine. While the etched morphology appears cocontinuous, the AFM analysis clearly shows that the iPP is the continuous phase. In the medium cure state (Figure 3.5) the structure has coarsened and the EPDM domains have coalesced into slightly larger structures. The morphology of EHXL and EHXM cannot truly be cocontinuous as indicated by the etching analysis and remain processable as a thermoplastic. During the process of dynamic vulcanization the processing oil has equal affinity for the EPDM and molten iPP. Upon solidification, the paraffin oil must be partitioned out of the crystalline regions and into the rubber. It is feasible that the domains with lower crosslinking densities are able to swell to a greater degree when the paraffin oil is forced out of the crystalline iPP regions. This would give the appearance of a cocontinuous structure when

in reality domains are simply impinging on one another and not necessarily connected across their interfaces.

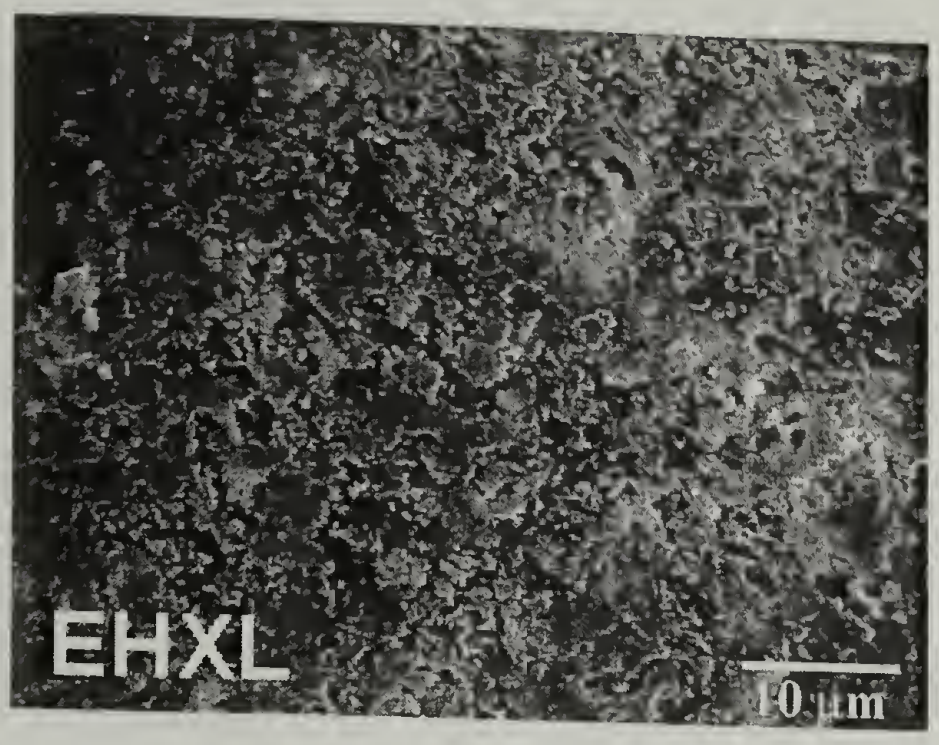

Figure 3.3: SEM micrograph of etched EHXL

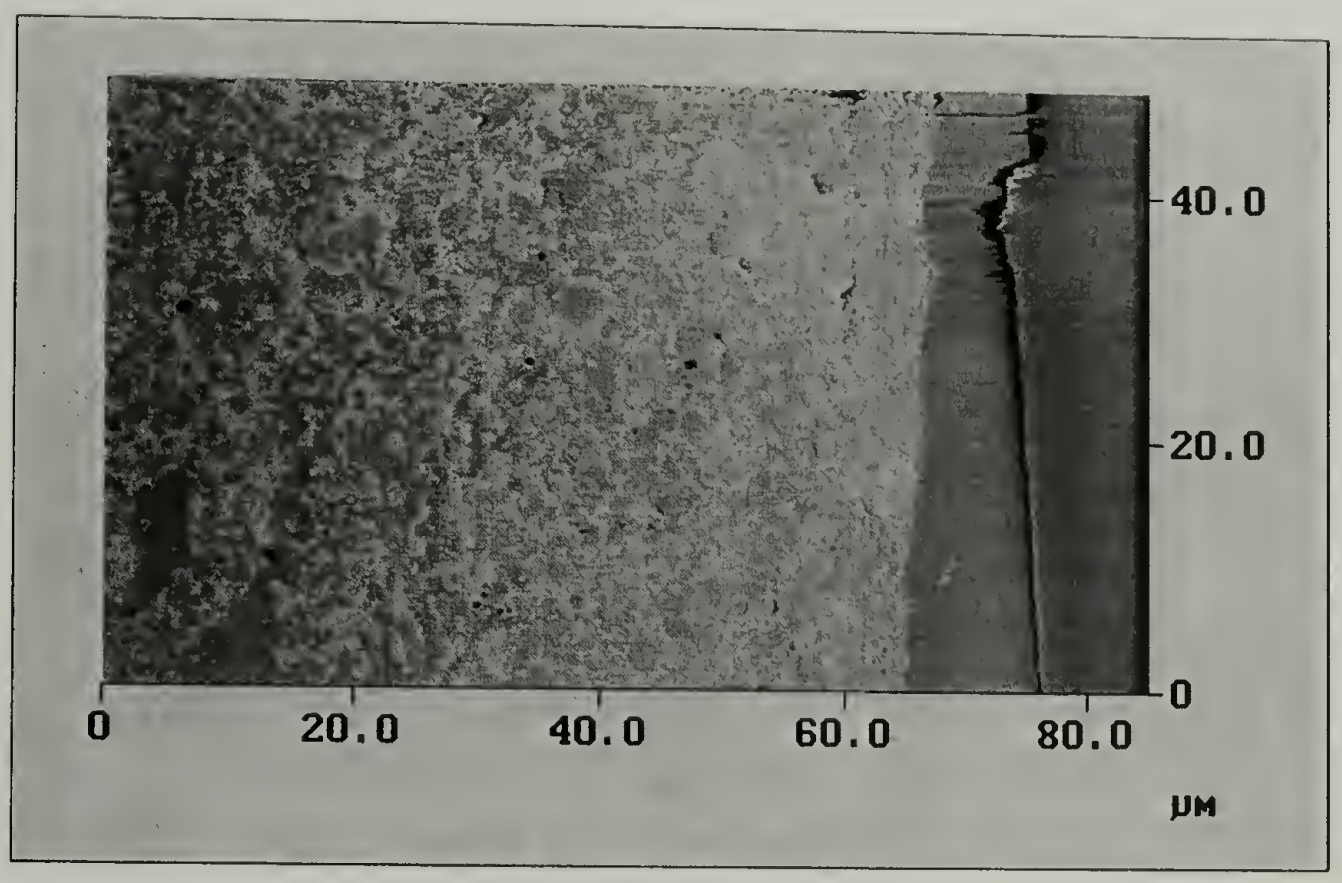

Figure 3.4: AFM image of EHXL

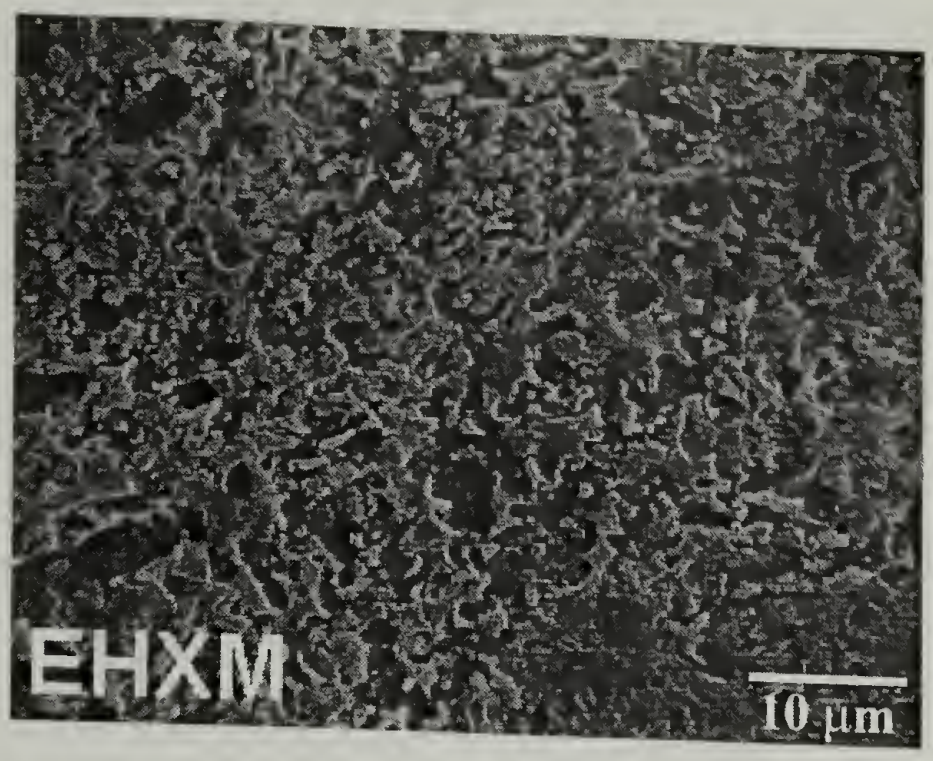

Figure 3.5: SEM micrograph of etched EHXM

A different morphology is observed for the high cure state shown in Figure 3.6. The iPP is again the continuous phase and there appears to be a bimodal distribution of EPDM domains. The large domains range in diameter from 5 – 10 μm while the small domains are on the order of 0.5 – 1 μm. The morphology of the EPDM phase in the medium cure state appears to be in between the seemingly cocontinuous structure of the low cure state and the discrete domain structure of the high cure state. The effect of iPP molecular weight is compared in Figures 3.6 and 3.7. Again, molecular weight plays an insignificant role in the overall morphology. The morphologies of the high cure state EPDM rich compositions are very similar to those of the iPP rich compositions; the major difference being the length scale of the elastomer domains.

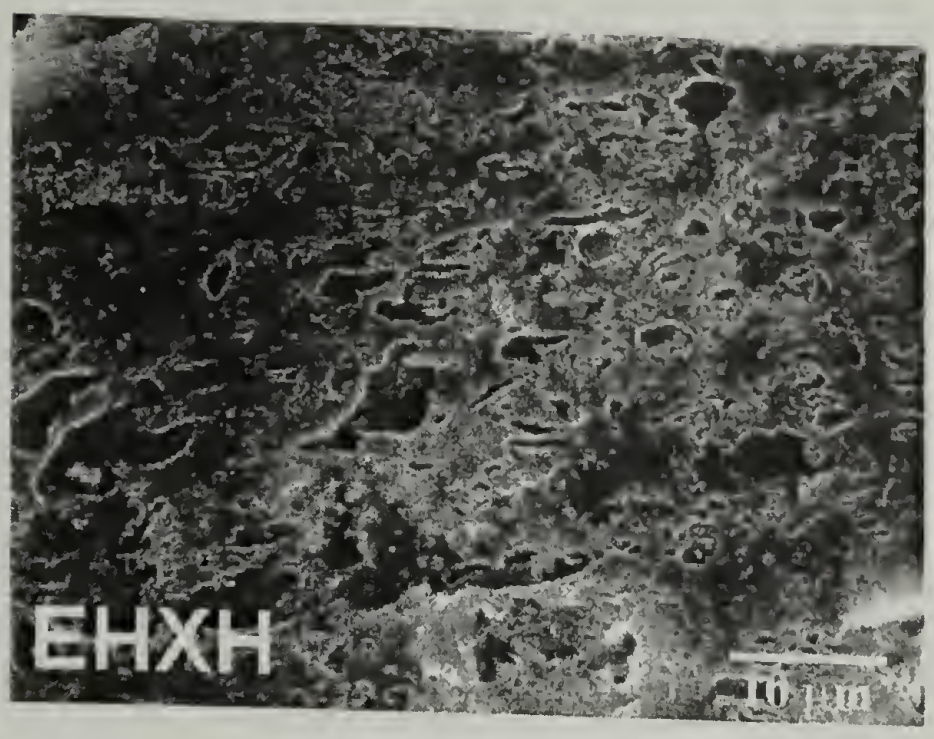

Figure 3.6: SEM micrograph of etched EHXH

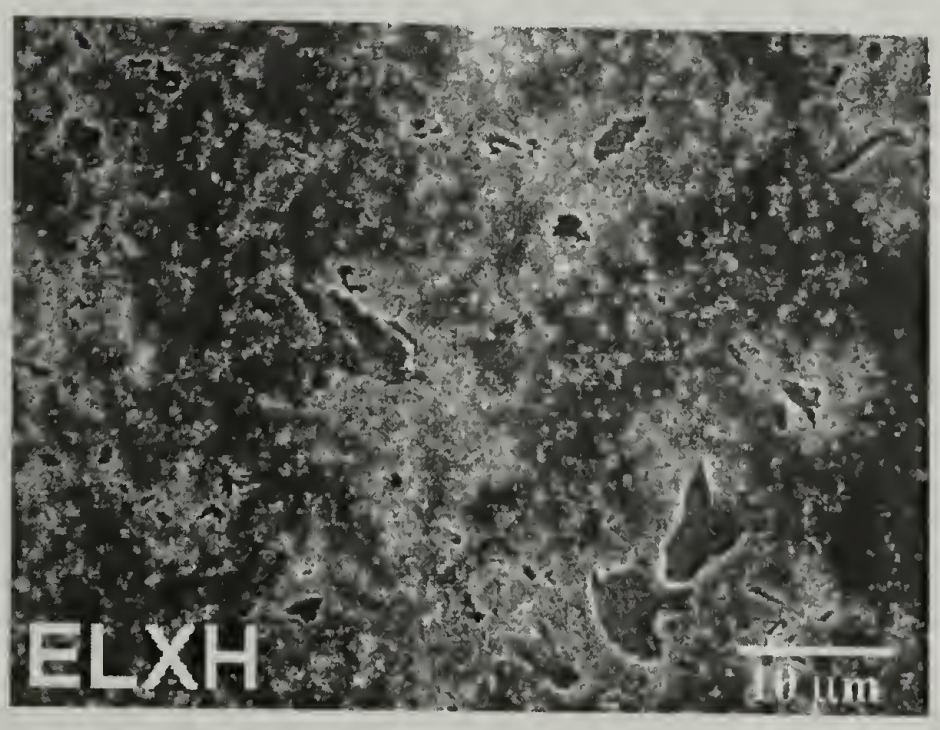

Figure 3.7: SEM micrograph of etched ELXH

Table 3.2 lists the average domain size and standard deviation for five of the compositions. It is apparent that the two dimensional size distributions are very broad given that in most cases the standard deviation is on the order of the average particle size.

Table 3.2: EPDM domain size analysis

Sample	EHXL	EHXM	ELXH	PHXM	PLXM
Ave Diam (um)	2.37137	0.76188	0.69433	1.59207	2.7798
Std Dev (um)	1.65494	0.5637	0.81492	1.17946	2.00887

3.3 Mechanical Behavior Evaluation

3.3.1 Experimental Procedures

Samples are compression molded into 3 mm thick plaques at 200 °C and a pressure of 3.5 MPa for approximately 30 minutes and then water-cooled in the melt press. Tensile specimens are cut to an ASTM D638 type I geometry and tested on an Instron 1123. Monotonic tensile tests are conducted at a crosshead speed of 5 mm/min. Successive loading and unloading under a triangular waveform is performed at a crosshead speed of 50 mm/min. These loading and unloading experiments are performed in the elastic region of the monotonic stress-strain curve as well as at higher strain levels. For tests performed in the elastic regime, the peak stress is 70% of the apparent yield stress. For tests performed at higher strains, the peak stress corresponds to 90% of the ultimate strength. All reported strains are calculated using crosshead displacement.

Test samples are also examined using dynamic mechanical thermal analysis (DMTA) performed on a Rheometric Scientific DMTA IV. Samples for tensile mode DMTA analysis are pressed into films ranging in thickness from 7 to 17 mm at 210 °C and then water-cooled. All dynamic strain sweep tests are conducted at room temperature, under a sinusoidal waveform at 2 Hz, and with a gauge length of

approximately 1.5 mm. The hex bolts on the grips holding the films are torqued to 5 cN-m. In order to prevent the samples from buckling, an initial static force of 10g is applied to each sample.

To study the Payne effect using the DMTA software, the test protocol must be modified as shown in Figure 3.8. Instead of applying a constant static force, the static force is adjusted during the experiment together with the dynamic force. This is required because the DMTA has a limited dynamic strain amplitude that is not sufficient to reach high amplitude strains. Thus, in order to make measurements of the high amplitude modulus using this apparatus, the static strain is systematically adjusted during the experiment. This is achieved by adjusting the static to dynamic force ratio (S/D). The S/D was varied from 1.01 to 3. A low S/D corresponds to a standard experiment probing only the low strain regime, and a high S/D allows a broader range of strains to be examined. The samples are probed over two decades of dynamic strains ranging from 0.1% to approximately 25% at an interval of seven points per decade.

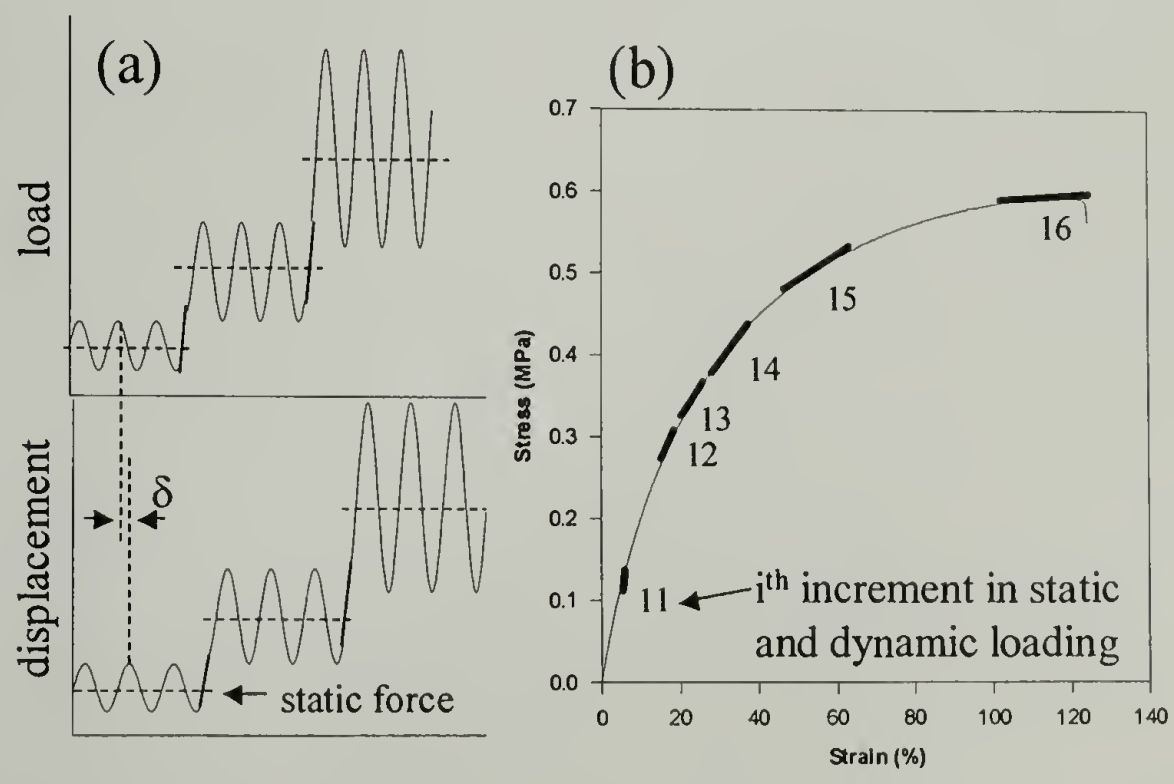

Figure 3.8: Non-standard DMTA protocol (a) dynamic loading and (b) static loading

3.3.2 Static Loading

As would be expected, both the morphology and therefore the mechanical behavior of the thermoplastic vulcanizates under investigation are highly dependent on composition. This is illustrated through the examination of two formulations with varying amounts of iPP keeping all other variables constant: PHXM and EHXM. Figure 3.9 shows the monotonic engineering stress versus engineering strain curves for each of these compositions as well as a typical curve for pure iPP. The mode of deformation for iPP is altered upon the addition of rubbery domains. Pure iPP exhibits heterogeneous deformation through neck formation. Upon the addition of EPDM, affine deformation is observed and no neck is formed. When comparing both elastomers with pure iPP, the apparent yield stresses of both compositions are much lower and less distinct. Both PHXM and EHXM have an apparent "elastic-plastic" response with apparent strain hardening occurring in the plastic regime. The ductility of PHXM is greatly superior to that of EHXM. As iPP concentration increases the ductility and plastic flow stress increase while the plastic modulus decreases.

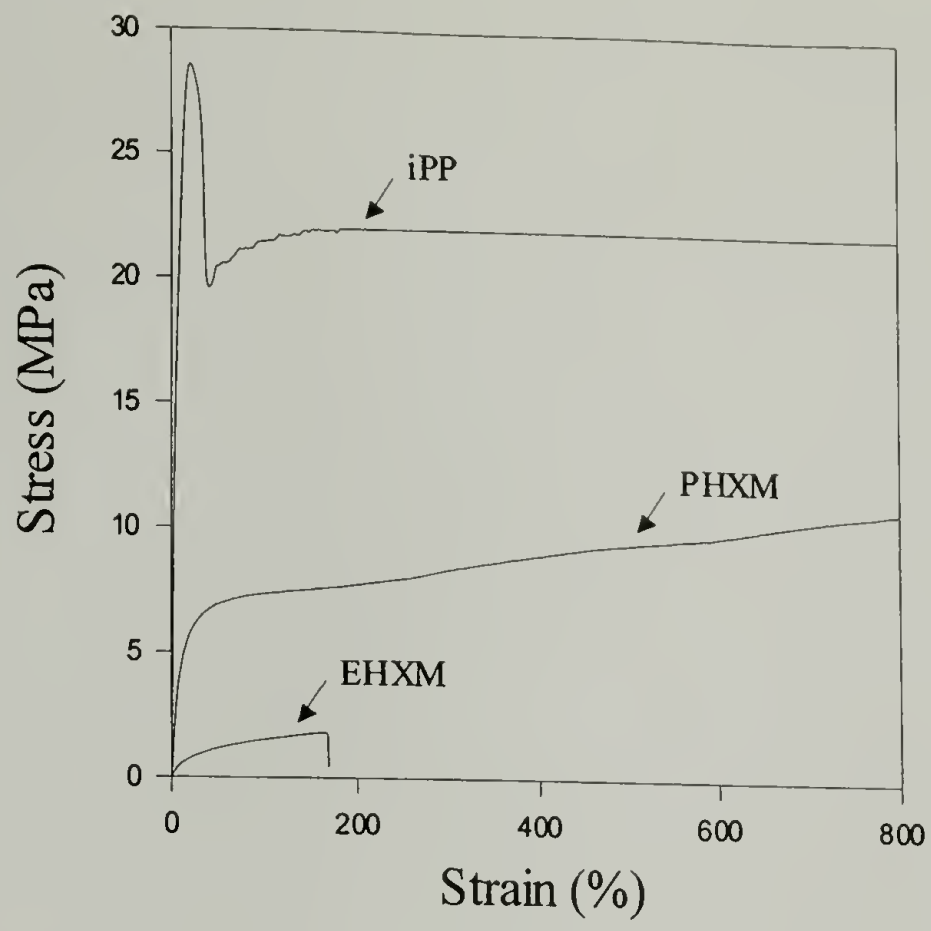

Figure 3.9: Mechanical behavior of EHXM and PHXM in comparison with neat iPP

3.3.3 Quasi-static Loading

Cyclic loading is conducted to investigate mechanical reversibility of the compositions. From the hysteresis loops shown in Figures 3.10, the energy loss per cycle is calculated and plotted in Figure 3.11. When the two compositions are cycled below their apparent yield points, they respond similarly even though they are compositionally different. However, when they are cycled subsequent to yielding (Figures 3.12 and 3.13), the response is drastically different. Note the very strong Mullins effect[34] in the first cycle which is more pronounced in the iPP rich system. These materials exhibit a behavior typically seen in crosslinked materials; they are mechanically reversible and thermodynamically irreversible. Once the initial stress softening is removed a similarity can again be observed between the two systems: the permanent set per cycle is similar

and a steady-state value of energy loss is reached. The iPP rich system strain hardens to a greater degree on subsequent cycles but also dissipates more energy.

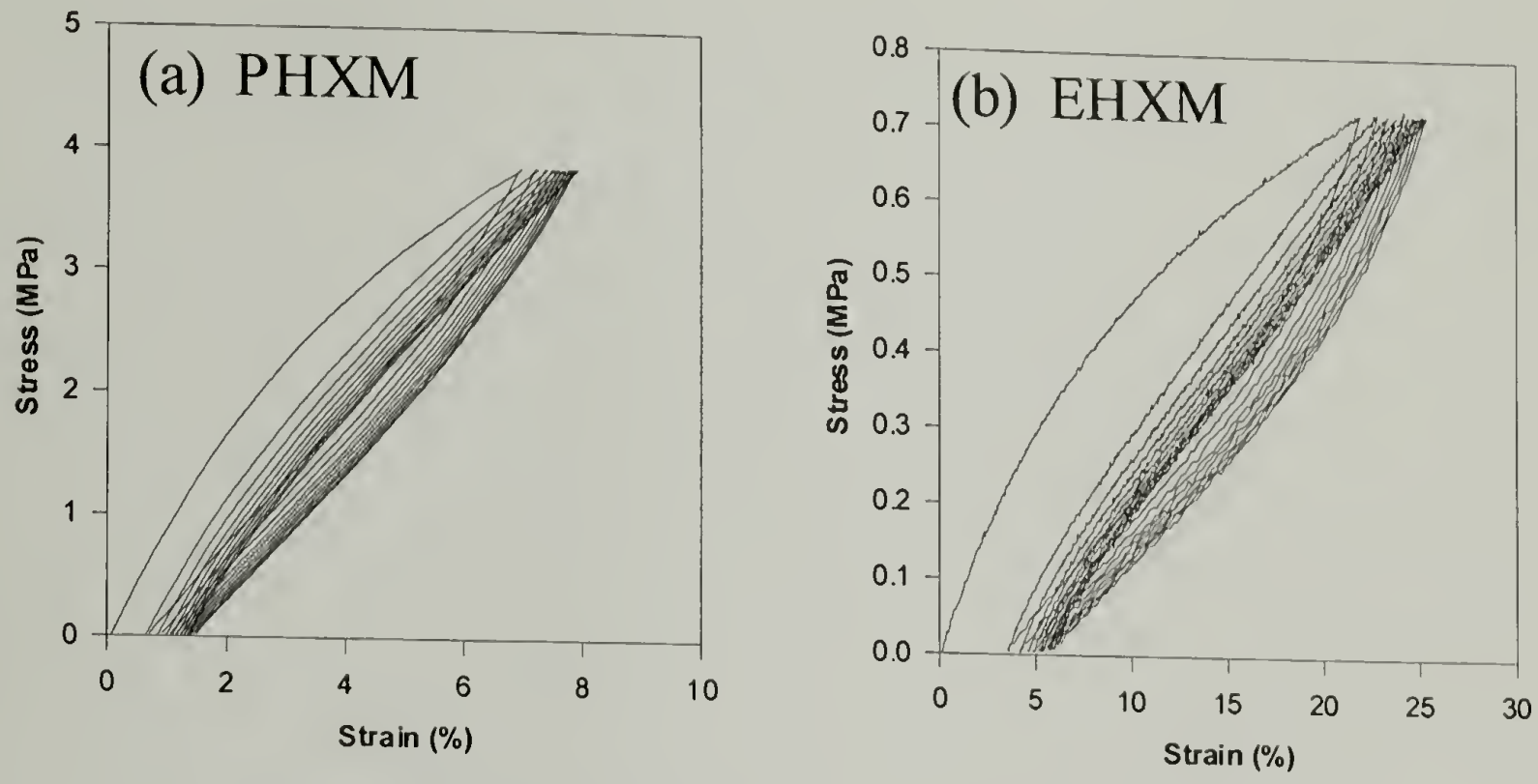

Figure 3.10: Pre-yield hysteresis for (a) PHXM and (b) EHXM

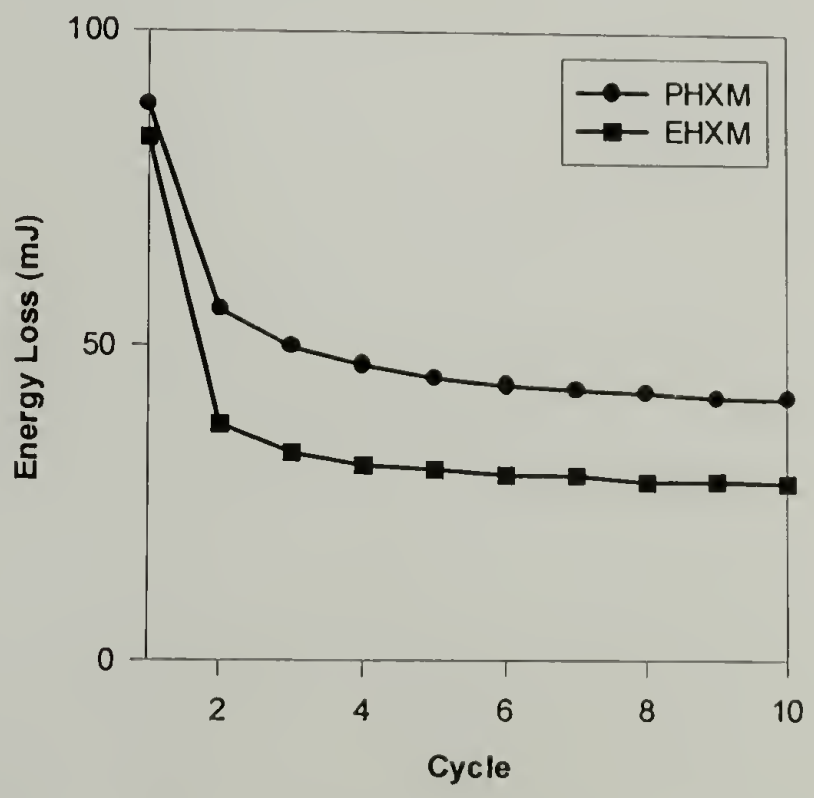

Figure 0.11: Pre-yield energy dissipation for PHXM and EHXM

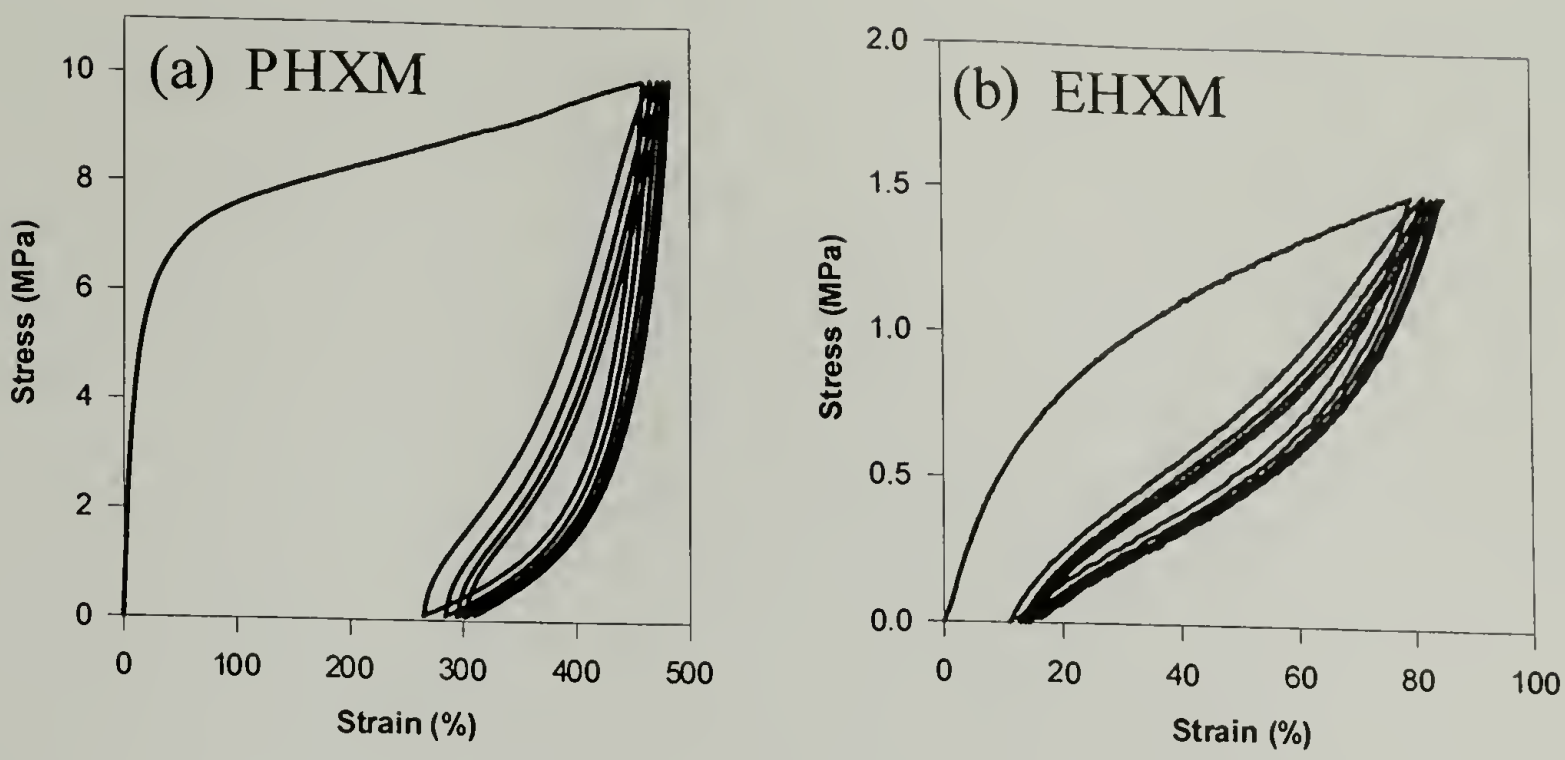

Figure 0.12: Post-yield hysteresis for (a) PHXM and (b) EHXM

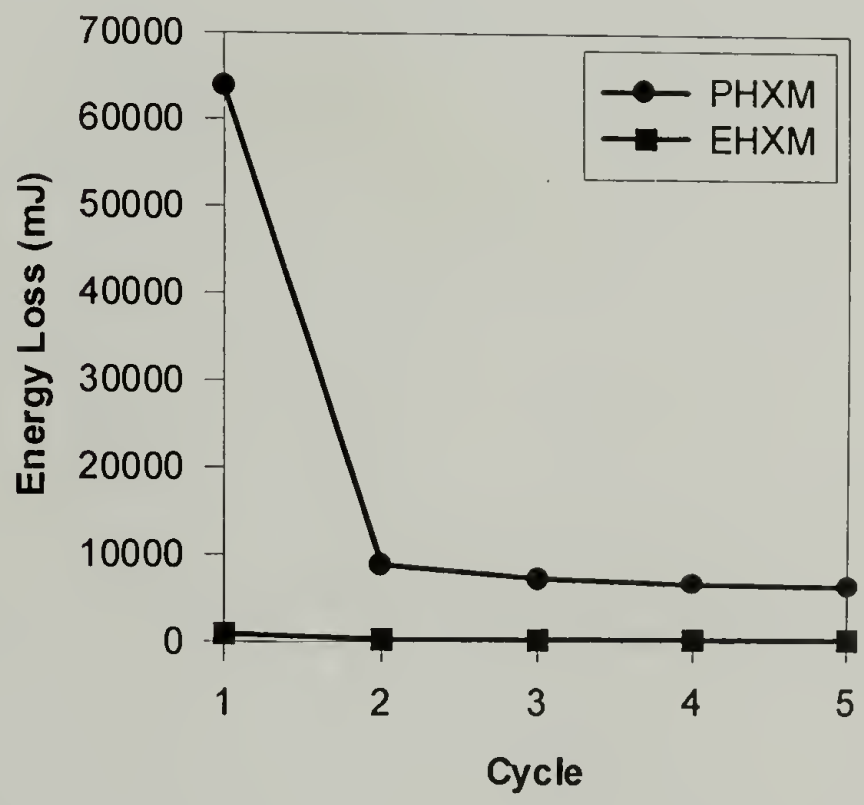

Figure 3.13: Post-yield energy dissipation for PHXM and EHXM

3.3.4 Dynamic Mechanical Behavior

The Kraus model[42] is used to explain the sigmoidal dependence of the storage modulus on dynamic strain typically observed in crosslinked elastomers that show the Payne Effect as described in section 1.3. For the purposes of data analysis the Kraus model is used as a tool to guide the eye through the data by extracting parameter values. These parameters are examined in terms of composition and morphology. Figure 3.14 shows E' as a function of dynamic strain amplitude for the EPDM rich samples, and Figure 3.15 shows the same for the iPP rich samples. Note that the curves fit to the data are taken from the Kraus model. For the EPDM rich blends a critical S/D ratio (approximately 2.5) is observed at which point a plateau in E' occurs.

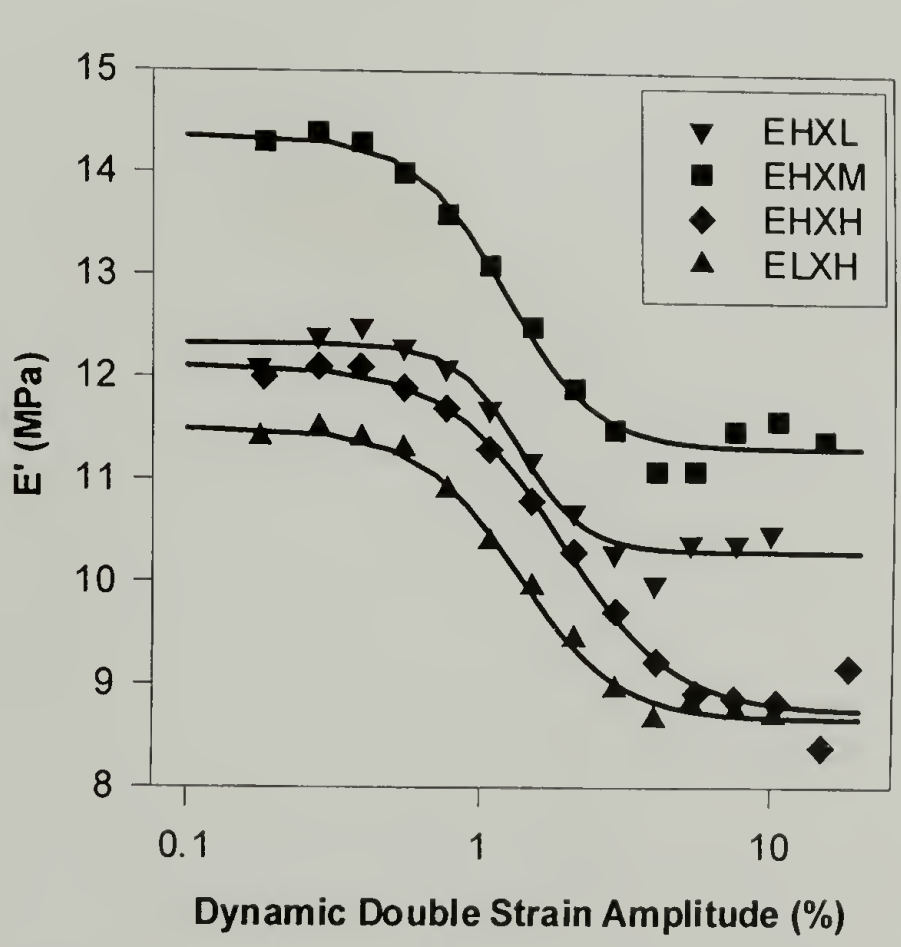

Figure 3.14: Storage modulus as a function of dynamic strain amplitude of EPDM rich compositions illustrating Payne effect response

The iPP rich samples did not plateau at the strains examined in the DMTA due to its limited stroke. It is necessary to use the modified Dynastat described earlier to achieve large enough dynamic strains to capture the high amplitude plateau shown in Figure 3.16.

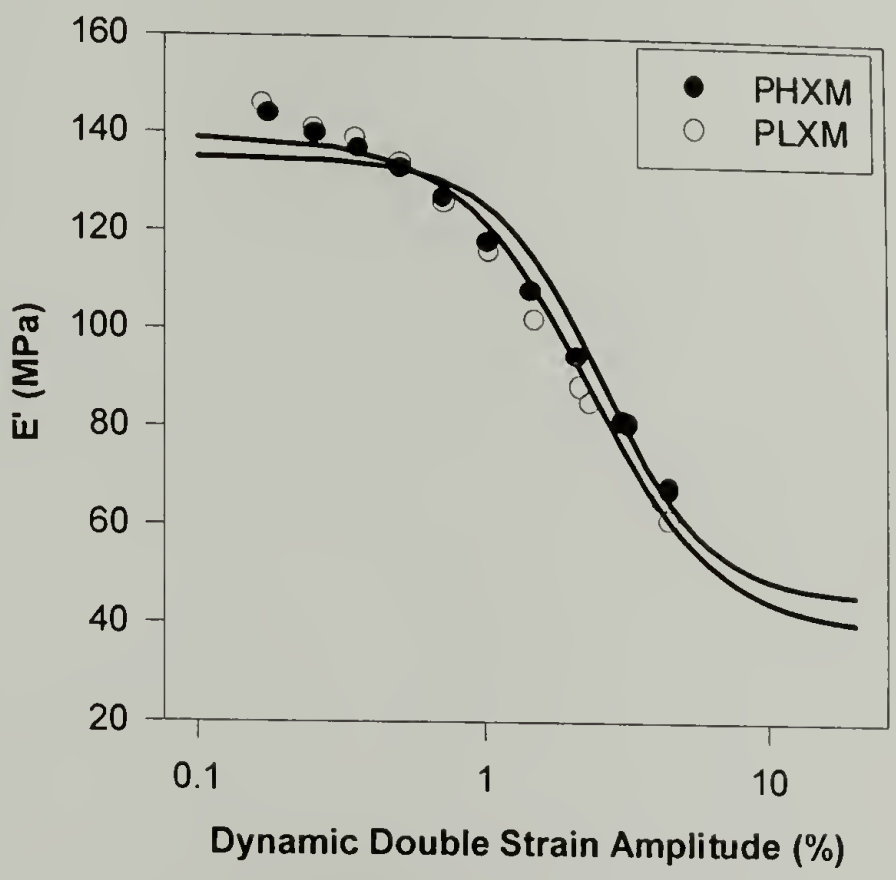

Figure 3.15: Storage modulus as a function of dynamic strain amplitude of iPP rich compositions (measured using the DMTA)

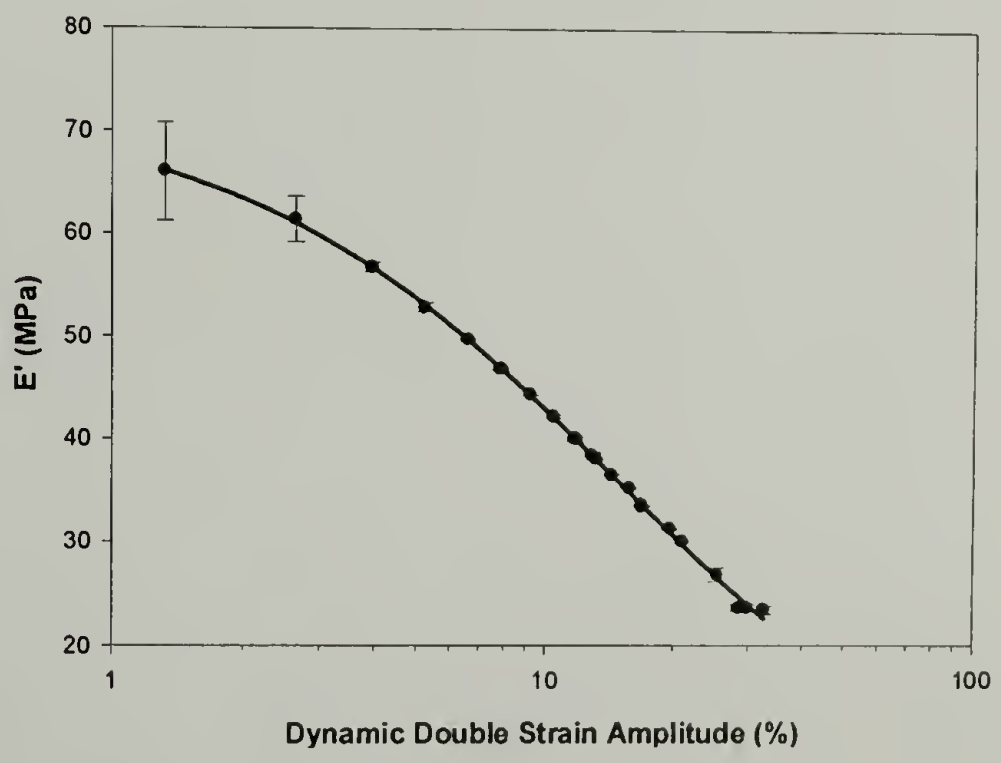

Figure 3.16: Storage modulus as a function of dynamic strain amplitude of PHXM illustrating high amplitude plateau (measured using the Dynastat)

Figure 3.17 shows E'' as a function of dynamic strain for the EPDM rich samples, and Figure 3.18 shows the same for the iPP rich samples. Again the curves fit to the data are taken from the Kraus model. Distinct peaks are observed for the iPP rich systems as well as for the EPDM rich systems with the highest cure states. Less defined peaks are also observed for the low and medium cure states. The E''_m values for the low and medium cure states are nearly identical; their morphologies are also very similar. Whereas E''_m for the higher cure state is much lower. It is also evident that as the iPP molecular weight increases, E''_m slightly decreases. However, this trend is overshadowed by the difference in E''_m as a function of composition. As iPP concentration is increased E''_m drastically increases by a factor of ten.

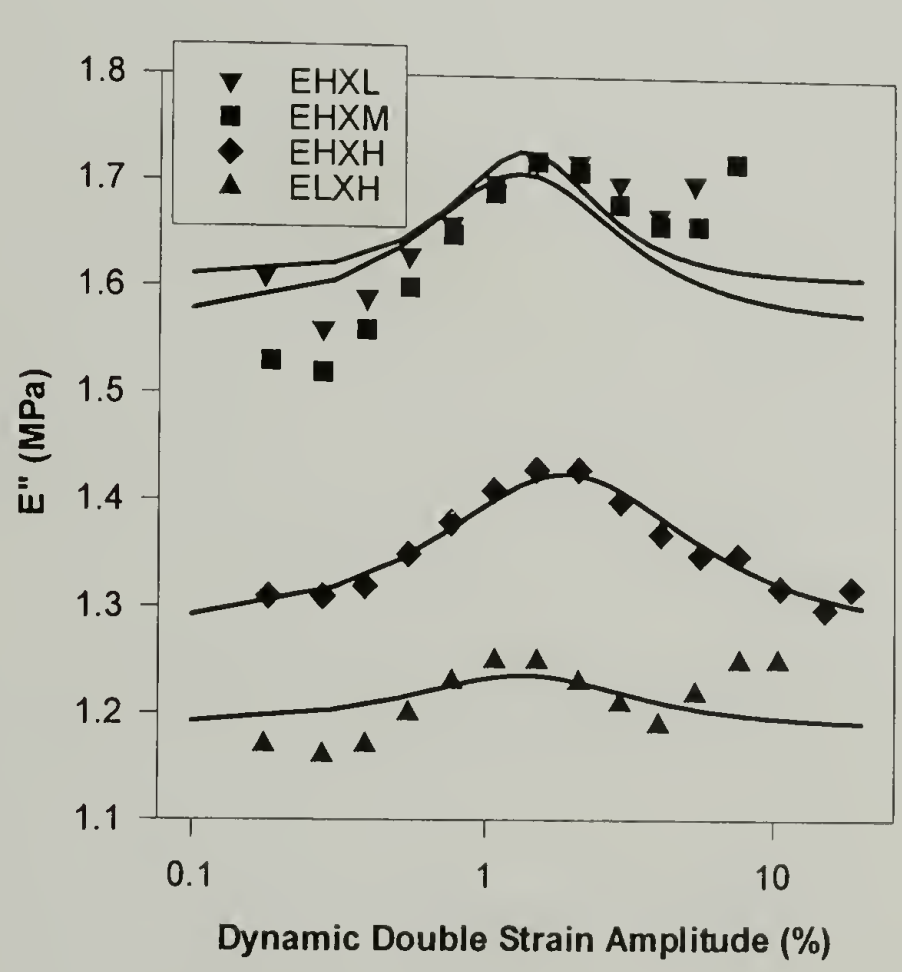

Figure 3.17: Loss modulus as a function of dynamic strain amplitude of EPDM rich compositions

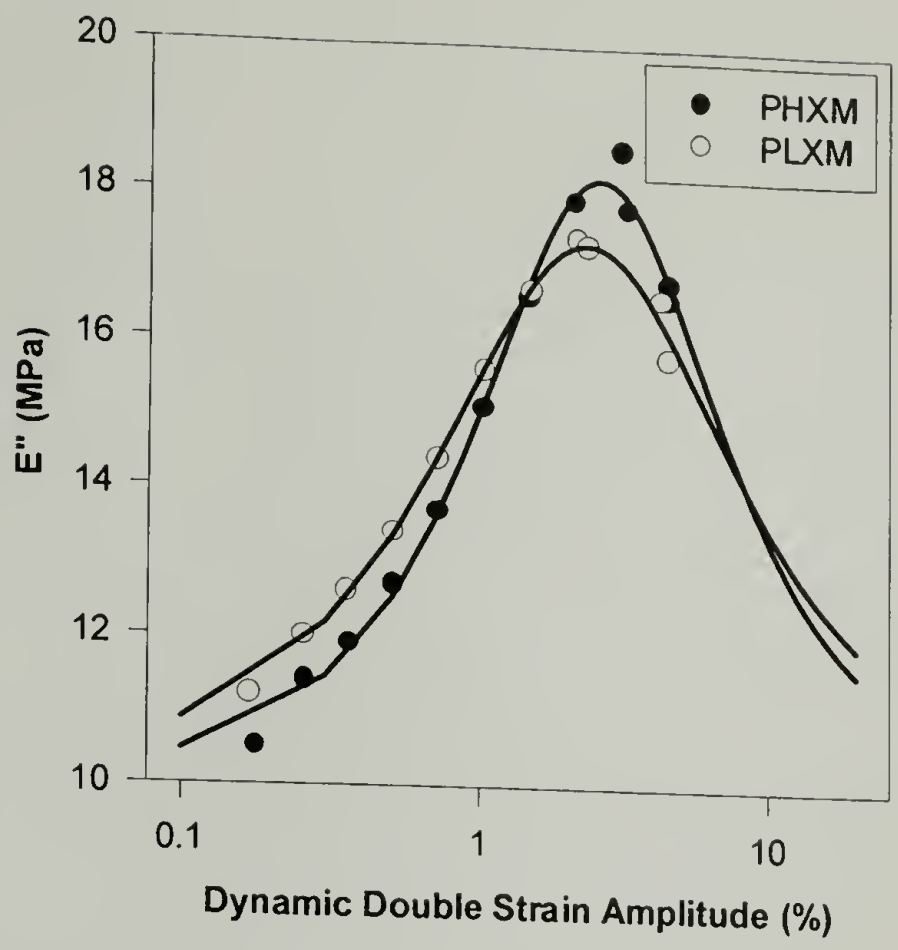

Figure 3.18: Loss modulus as a function of strain amplitude of iPP rich compositions

The Kraus model has been applied to the data as mentioned above using a least squares fitting process. Steps were taken during the fitting process to maintain consistency between the fits (ε_o and m being equal for the E' and E'' regressions). For the elastomer rich compositions, the E' data is well behaved and was fit with the Kraus model first. The resulting ε_o and m parameters were applied to the E'' fit constraining them to be identical. However, the E'' data is more well behaved for the iPP rich compositions in that a distinct maximum is observed in the E'' data and no plateau in E' is observed over the strain range tested using the DMTA protocol. As a result, the E'' data was fit first for the iPP rich compositions and the resulting ε_o and m were then constrained in the E' regression. The parameters extracted from the Kraus model are listed in Table 3.3. The first column is the fractional drop in storage modulus, ε_o is the characteristic strain, and m is the shape parameter. As cure state increases, EPDM domain size and the drop in

storage modulus also increase. As iPP concentration increases, the drop in storage modulus increases by approximately 40% while ε_o increases substantially.

Table 3.3: Compositional comparison of fitting parameters from Kraus model

	$1-\frac{E'_\infty}{E'_o}$	ε_o	m
EHXL	0.163	1.35	1.96
EHXM	0.215	1.30	1.42
EHXH	0.279	1.87	1.11
PHXM	0.644	14.49	0.49

Figure 3.19 shows tanδ as a function of dynamic strain amplitude. Once again, iPP concentration appears to be the dominant parameter in controlling the amount of energy dissipation. Tan δ_m is much higher for the iPP rich compositions than for the EPDM rich blends.

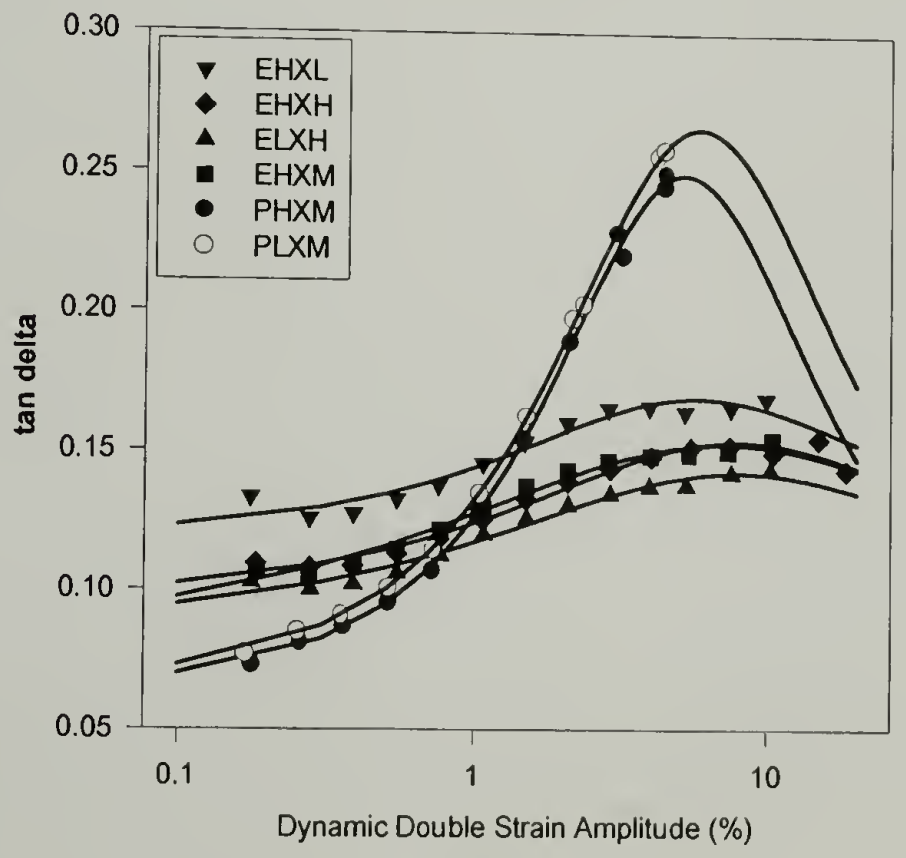

Figure 3.19: Tan delta as a function of dynamic strain amplitude of EPDM/iPP blends

3.4 Structure-Property Relationships

Figure 3.20 shows that the difference in low and high amplitude storage moduli (E'_o-E'_∞) obeys a trend set by cure state. As cure state increases E'_o-E'_∞ substantially increases indicating that E'_o-E'_∞ may be a function of domain size since the morphology coarsens with cure state.

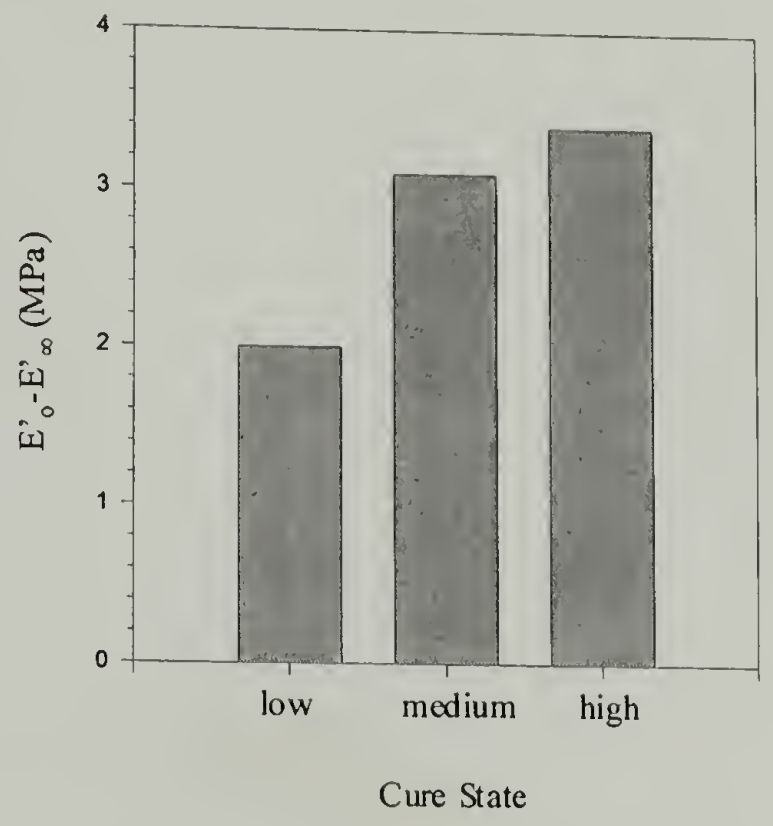

Figure 3.20: Increasing trend of E'_o-E'_∞ with cure state

Figure 3.21 demonstrates that EHXL and EHXM have essentially the same ε_o; however, as cure state increases ε_o also increases. This trend is similar to the connectivity of the morphology in that EHXL and EHXM both appear seemingly cocontinuous while EHXH has a distinct domain structure. Characteristic strain also increases as iPP concentration increases. For all compositions tested, the dynamic double strains at which the decrease in E' begins is approximately an order of magnitude smaller than more traditional crosslinked elastomers in which a decrease in E' does not begin until around 10%. In the EPDM rich samples E' reaches a plateau at a double strain of 10%.

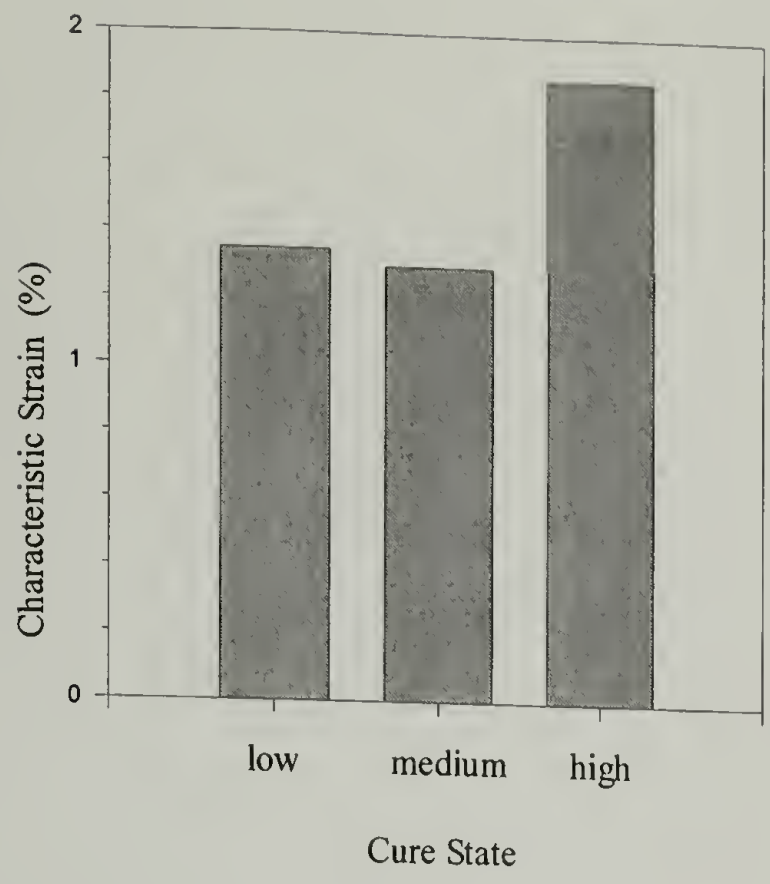

Figure 3.21: Characteristic strain as a function of cure state

Figures 3.22 and 3.23 demonstrate that the iPP molecular weight has very little effect on the observed behavior. E'_o-E'_∞ slightly decreases with decreasing iPP molecular weight for the iPP rich and EPDM rich compositions.

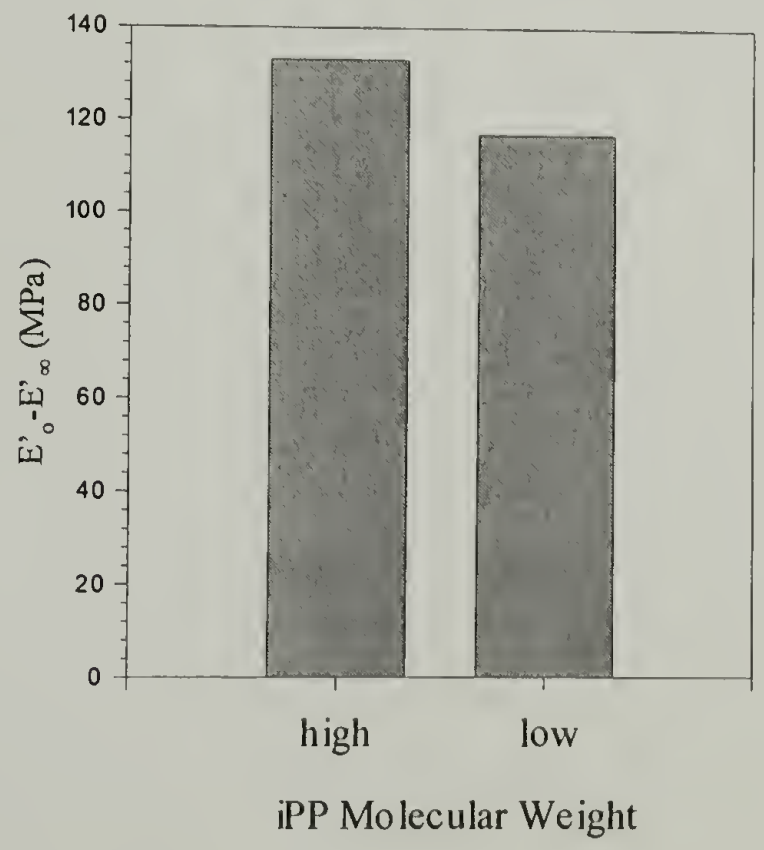

Figure 3.22: E'_o-E'_∞ as a function of iPP molecular weight (iPP rich compositions)

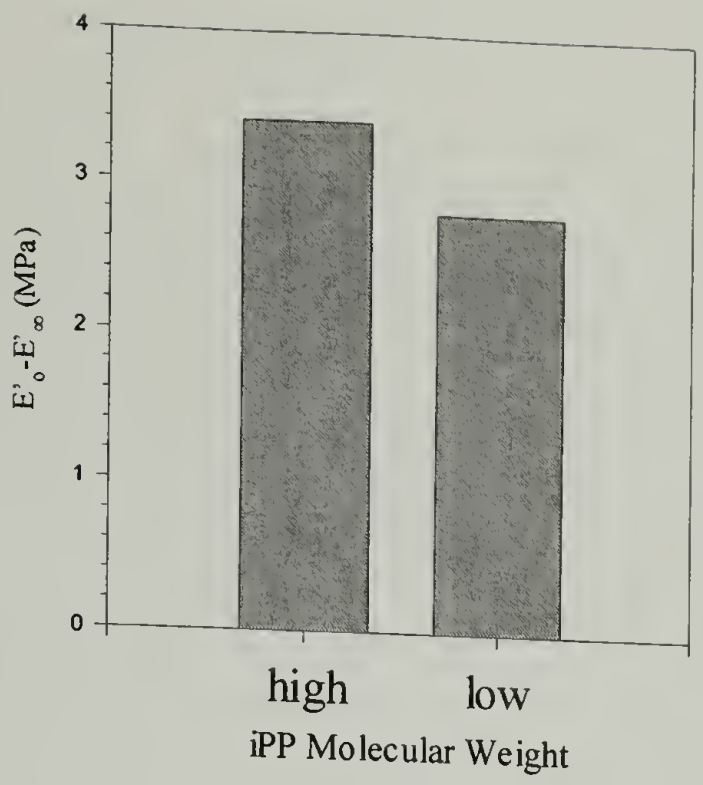

Figure 3.23: $E'_o-E'_\infty$ as function of iPP molecular weight (EPDM rich compositions)

E''_m slightly decreases with increasing cure state and decreasing iPP molecular weight. However, these trends are overshadowed by the effect of iPP concentration as seen in Figure 3.24.

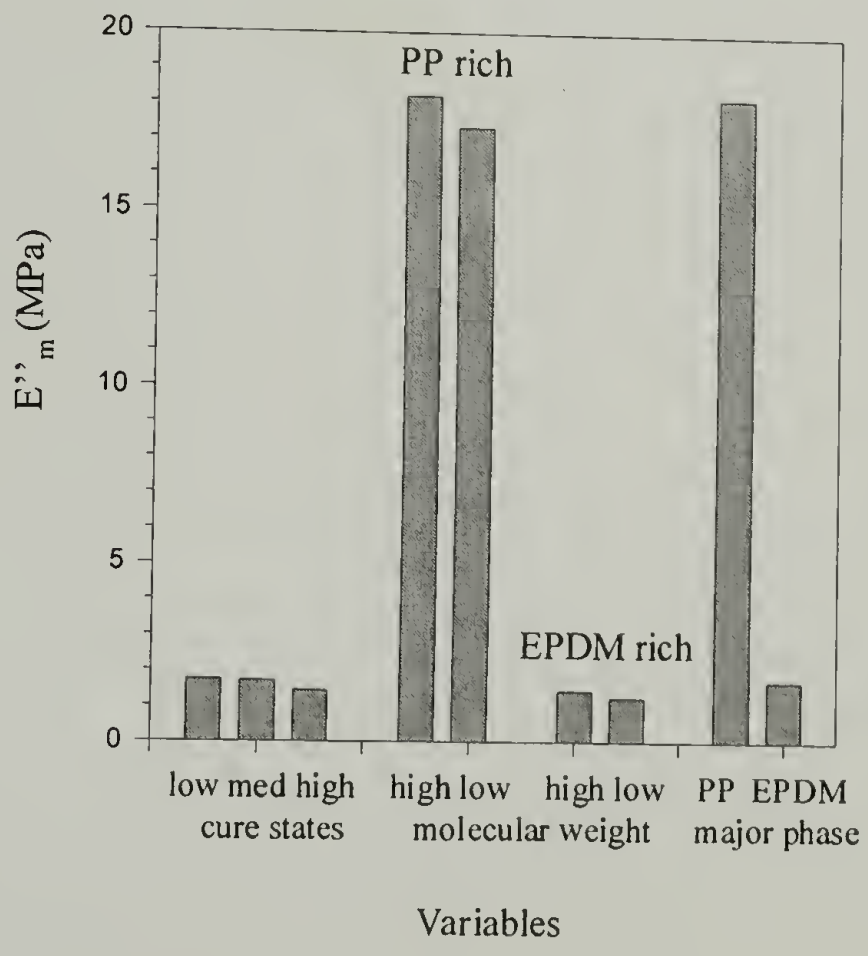

Figure 3.24: Maximum loss modulus as a function of compositional variables for EPDM/iPP blends

A Payne plot consists of the maximum loss modulus plotted as a function of the difference in low and high amplitude storage moduli. Payne plots have been reported that compare many types of traditional crosslinked elastomers with many types of fillers all tested in shear.[82,83] All systems regardless of composition, cure state, filler type, and filler loading reduce to a line with a slope of approximately 0.17. Figure 3.25 is a Payne plot for the six compositions examined in this study under tensile loading. It is apparent that iPP concentration is the most influential parameter in this type of analysis as a clear distinction is observed between the iPP rich and EPDM rich systems. It is reasonable that intermediate compositions may lie in between these extremes. Clustering of the data indicate that EPDM cure state and iPP molecular weight have very little effect on this type of analysis. The data clusters fall on a line of slope 0.13 which indicates that these thermoplastic vulcanizates are exhibiting the same type of phenomenological behavior as traditional filled crosslinked elastomers.

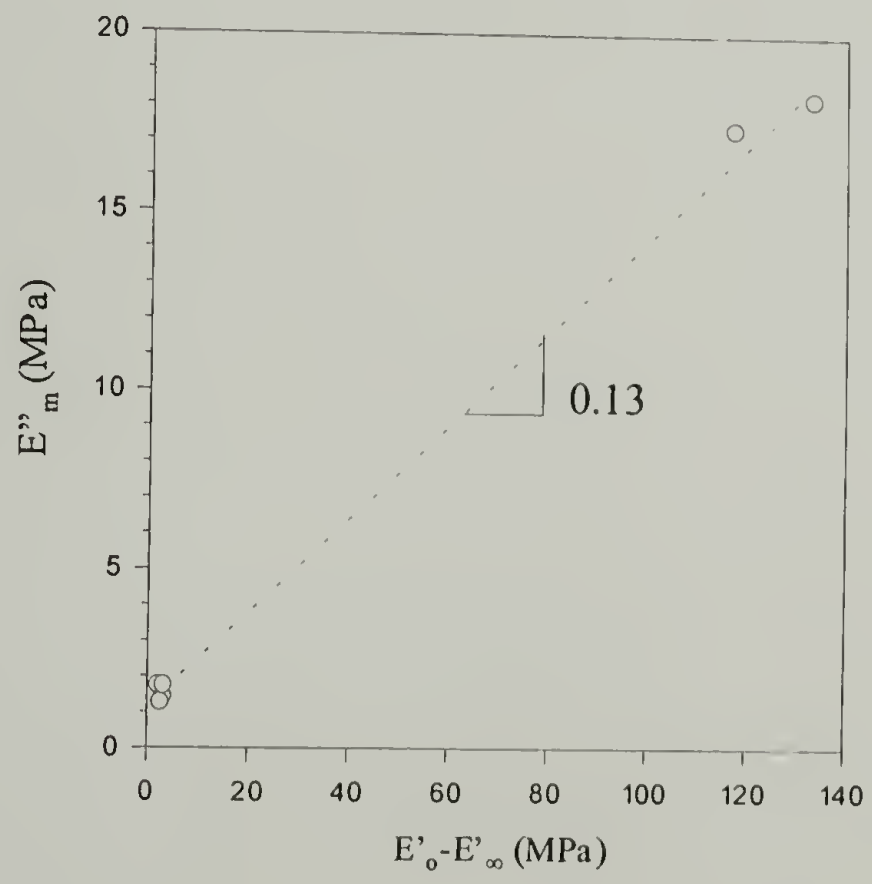

Figure 3.25: Payne plot – maximum loss modulus as a function of E'_0-E'_∞

Similar structure-property trends are observed for tan δ. Figure 3.26 shows that tan δ_m decreases with increasing cure state while iPP concentration is again the most influential variable. However, the characteristic strain from the tan δ analysis is influenced equally by EPDM cure state and iPP concentration as observed in Figure 3.27.

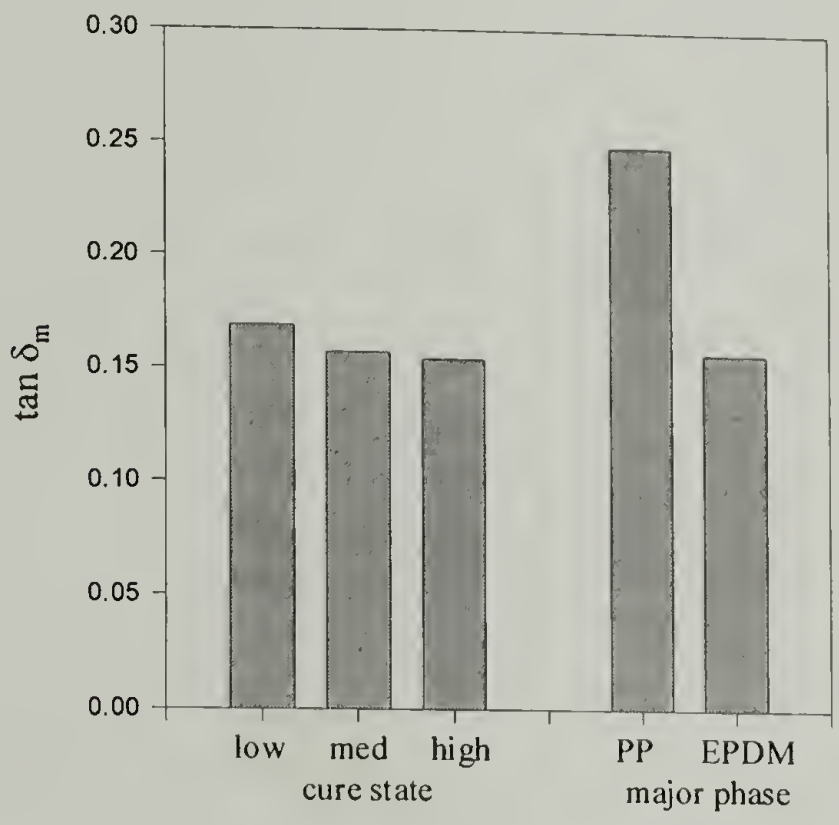

Figure 3.26: Maximum tan delta as a function of compositional variables for EPDM/iPP blends

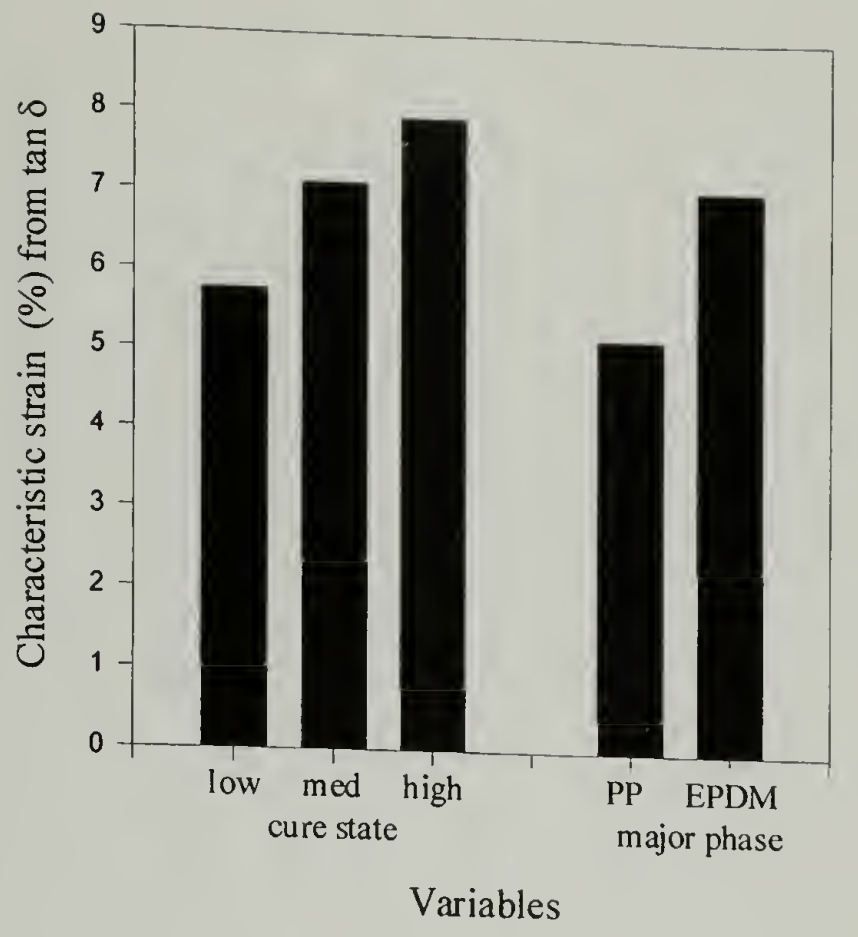

Figure 3.27: Characteristic strain from tan delta as a function of compositional variables for EPDM/iPP blends

The energy dissipation density under sinusoidal oscillatory strain is given by equation 3.1.

$$W_i = \oint \sigma_{ij} d\varepsilon_{ij} = \int_0^{2\pi/\omega} \sigma_o \sin(\omega t + \delta)[\varepsilon_o \cos \omega t] dt \qquad (3.1)$$

Upon evaluation and simplification, the normalized energy dissipation density is given by

$$\frac{W_i}{\sigma_o \varepsilon_o} = \pi \sin \delta \qquad (3.2)$$

At small static strains (<5%) the rate of energy dissipation is constant for all six compositions. At approximately 5% static strain this rate decreases and at 10% plateaus to a constant value as shown in Figure 3.28. Plateau values are a function of composition and morphology and are plotted in Figure 3.29. As cure state increases the energy dissipation density decreases. iPP molecular weight has little effect on the energy

dissipation if all other variables are held constant. As expected a large increase in the energy dissipation density is observed as iPP concentration increases.

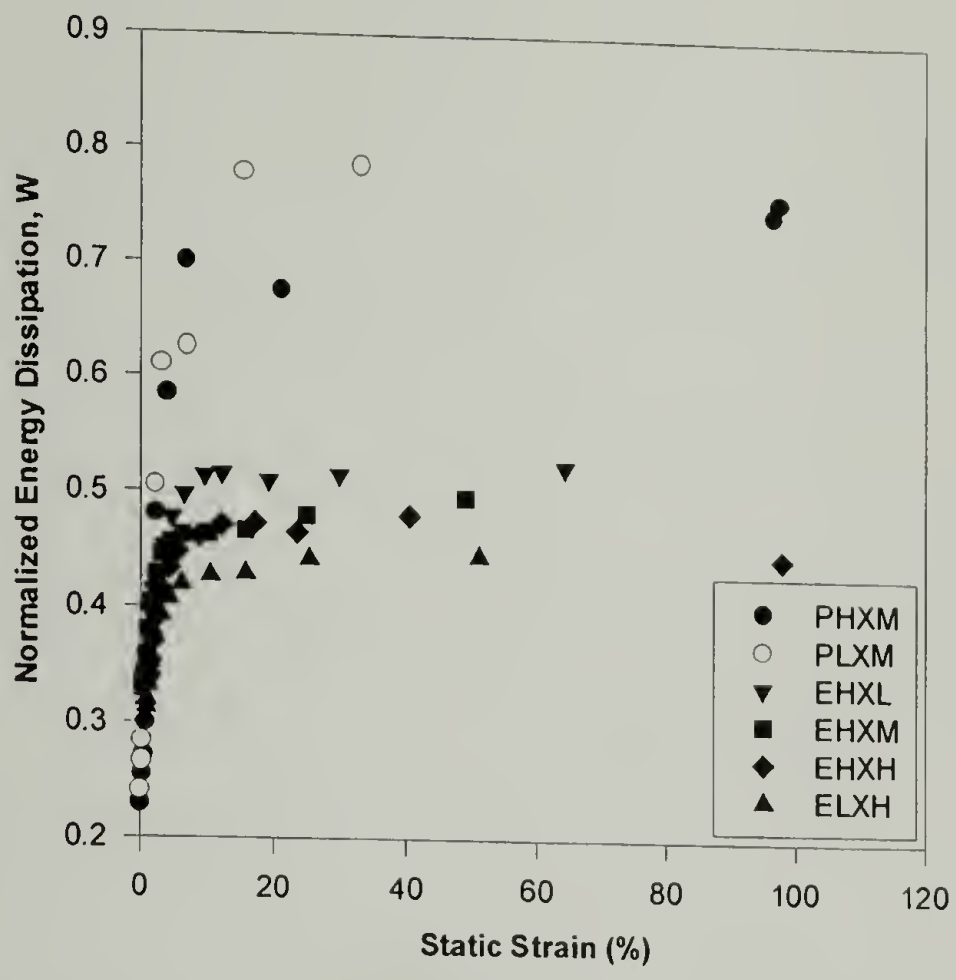

Figure 3.28: Normalized energy dissipation density versus static strain

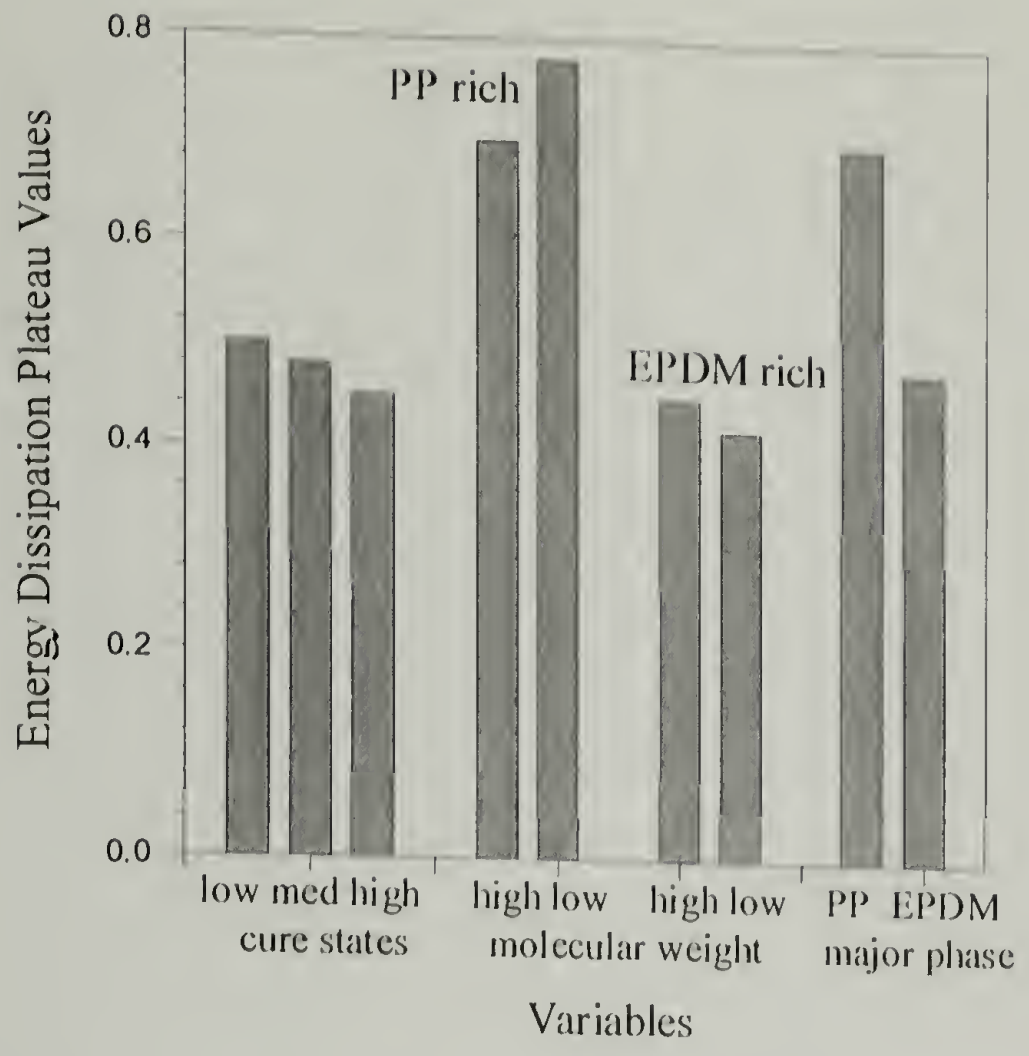

Figure 3.29: Energy dissipation density plateau value as a function of compositional variables for EPDM/iPP blends

3.5 Conclusions

Structure-property relationships are shown for EPDM/iPP blends of varying composition. Formulation variables are chosen to examine a range of morphologies. Even though the length scale of heterogeneity is drastically different from traditional crosslinked elastomers and the matrix is a semicrystalline thermoplastic, these thermoplastic vulcanizates exhibit a "Payne Effect" response similar to traditional crosslinked elastomers. The Kraus model is used as a tool to describe the data.

The mechanical properties of these dynamic vulcanizates have clear similarities under quasi-static loading and distinct differences under dynamic loading. Dramatic stress softening is observed at high loading levels for the iPP rich compositions. These materials exhibit a behavior typically seen in crosslinked elastomers, that is mechanical

reversibility and thermodynamic irreversibility. Energy loss in the iPP rich systems during the first cycle is orders of magnitude greater than that lost by the EPDM rich system. However, once the initial stress softening occurs the recovery is again on the same order of magnitude regardless of composition. The iPP rich system strain hardens to a greater degree on subsequent cycles but also dissipates more energy.

The dynamic moduli show a dependence on strain amplitude analogous with the Payne effect; however, the mechanisms of dissipation are different from traditional crosslinked systems. As morphology evolves with cure state, the dynamic mechanical properties similarly evolve. As cure state increases, E'_o-E'_∞ also increases indicating the decline in E' may be related to domain size. In contrast E''_m decreases as cure state increases. These observations are directly linked to the changes in morphology. The low cure state has a very fine structure that almost appears to be cocontinuous while the high cure state has a coarser morphology with discrete phase separation. The medium cure state has a morphology in between these two. Molecular weight of the iPP affects the overall morphology and resulting mechanical properties very little.

CHAPTER 4

EVALUATION OF A MICROCELLULAR MODEL

4.1 Modeling Objectives

Even though the matrix of dynamically vulcanized EPDM/iPP blends is a semicrystalline thermoplastic, dynamic vulcanizates behave elastically. Over the past several decades, the origins of this elasticity have been debated and several finite element studies and constitutive models have been proposed.[47-51] A primary limitation of these studies is that none clearly identify how composition and morphology influence deformation characteristics. This feasibility study presents and evaluates a new modeling approach to describe the steady-state deformation behavior of dynamically vulcanized EPDM/iPP blends. An analytical expression is developed by combining concepts from microcellular solids with plastic hinge formation and strut yielding to approximate the deformational response of these elastomers. Contributions from iPP concentration and EPDM cure state are included.

The first objective of the proposed model is to describe the steady-state loading and unloading of EPDM/iPP blends including contributions from composition and morphology. The second objective is to determine if the proposed model can be used to predict the steady-state behavior over a broad range of compositions.

4.2 Proposed Model

Idealized strut models are typically used as a morphological tool to describe mechanical and physical responses of non-ideal microcellular geometries.[84,85] The composite foam response is assessed in terms of strut geometry and intrinsic polymer properties. The collapse or failure mechanisms of microcellular foams generally occur in one of two forms, either through strut buckling or through the formation of localized plastic hinges at the strut junction points.[85] Both failure mechanisms were explored in developing the proposed microcellular model. Microcellular collapse through plastic hinge formation requires the least amount of energy and as such is incorporated in the deformation behavior. One would expect a viscoelastic material to dissipate energy to different degrees when exposed to various loading rates. Figure 4.1 illustrates the irreversible work exhibited under two loading conditions for EHXM.

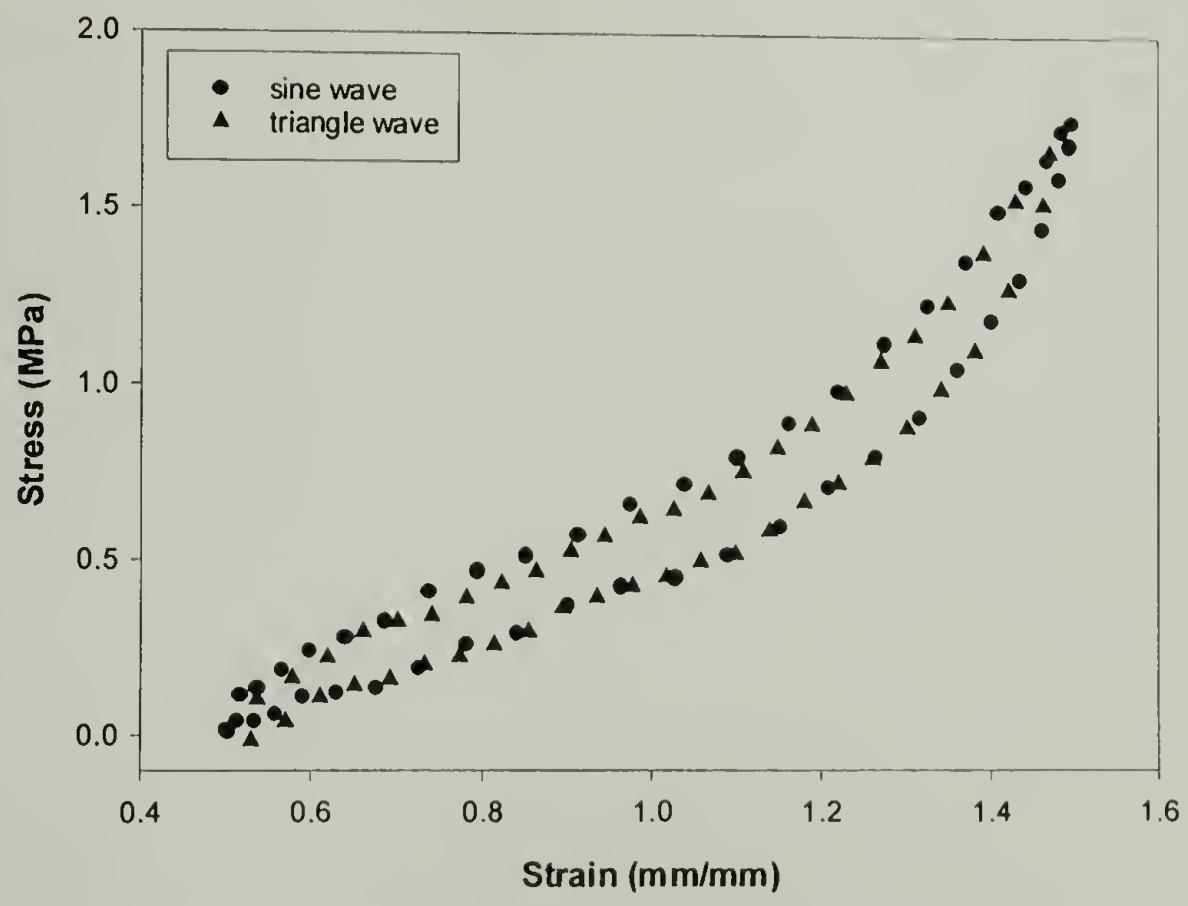

Figure 4.1: Steady-state hysteresis loops for EHXM under sinusoidal and triangular loading patterns

Triangular loading deforms the materials at a constant strain rate while sinusoidal loading applies a constantly changing strain rate. It is evident that the hysteresis exhibited by EPDM/iPP vulcanizates is similar under these two loading conditions. Therefore, it can be assumed that some mechanisms other than viscoelasticity are responsible for dissipation in these systems. In the proposed model, the work required to rotate the plastic hinges provides a possible mechanism for dissipation. The origins of elasticity from a microcellular analysis arise from a competition between the restoring force of the elastically deformed rubber and iPP struts and the strain energy necessary to rotate the plastic hinges. The proposed model may also capture geometrical strain hardening to some degree due to alignment of the struts as the hinges rotate and the struts align into a parallel configuration.

By imposing a microcellular representative volume element (RVE) and ensuing deformation, the proposed model will have some of the same limitations as finite element analysis: the geometry and kinematically admissible displacement field are both prescribed and the displacement may not be a lower bound solution. However, an analytical solution will result possibly allowing the microcellular model to be used as a formulation tool. The RVE is shown in Figure 4.2 where the morphology is considered as a *filled* foam; the foam struts are regions of iPP and the foam interstices are filled with EPDM rubber. In this geometry, t is the strut thickness, ℓ is the strut length, and 2θ is the angle at the junction of two iPP struts.

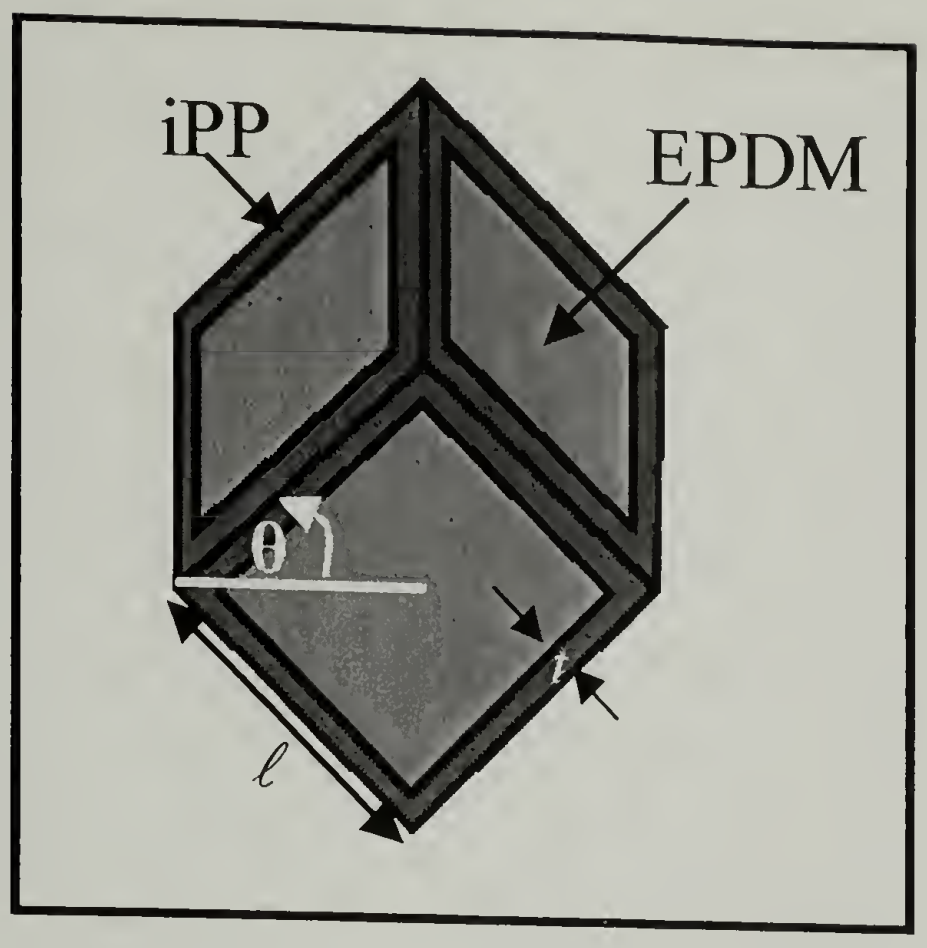

Figure 4.2: Schematic of representative volume element for microcellular model development

For a microcellular geometry, the volume fraction of strut material (C) is directly proportional to the strut density (S) as well as the square of the thickness to length ratio given by equation 4.1 (17).

$$\frac{V_{pp}}{V_{Tot}} = S\left(\frac{t}{\ell}\right)^2 = C \qquad (4.1)$$

A two-dimensional uniaxial deformation is imposed on the RVE as shown in Figure 4.3.

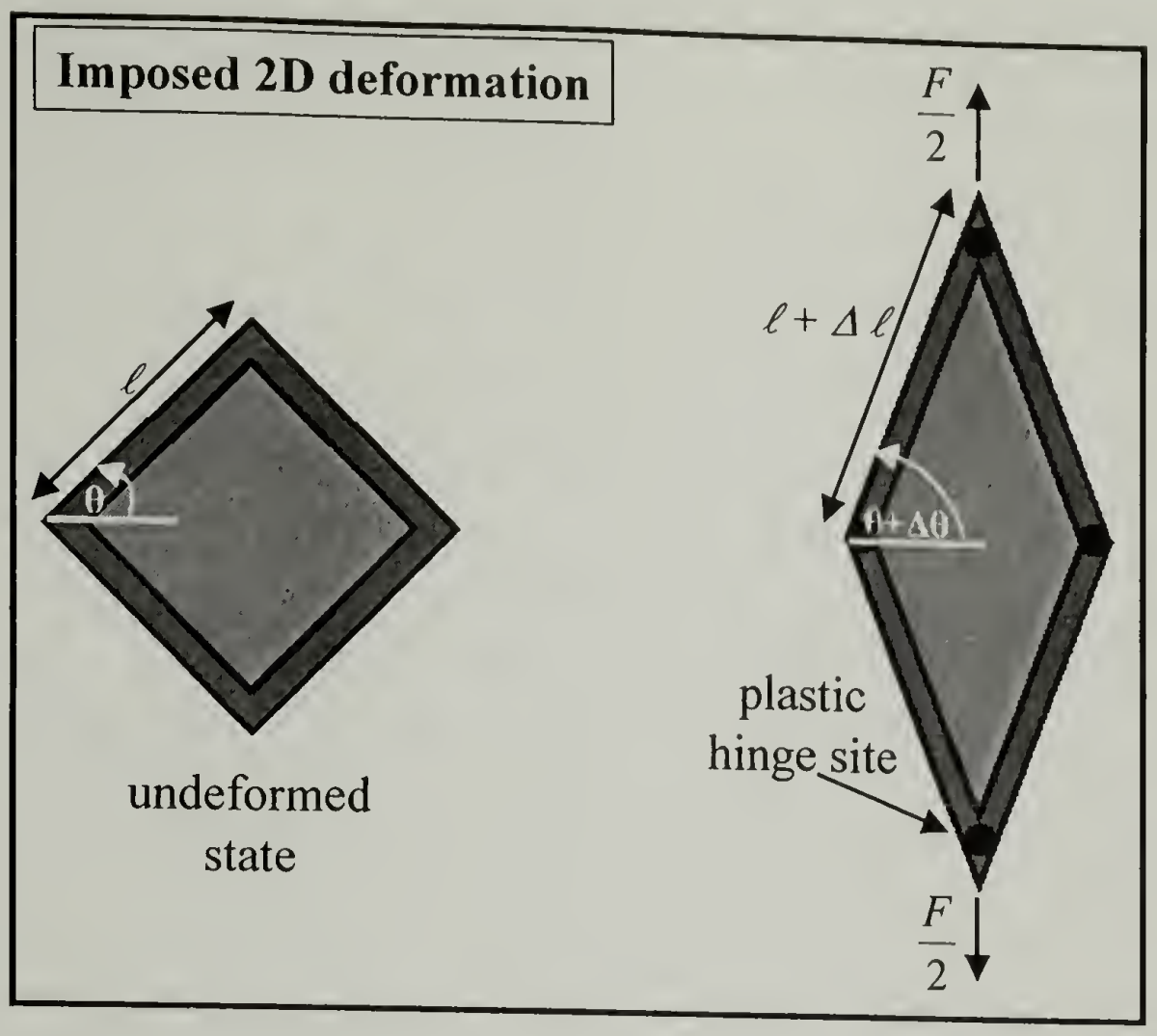

Figure 4.3: Two-dimensional uniaxial deformation imposed on representative volume element

The total force acting on the RVE is given by equation 4.2 where σ_∞ is the far-field stress and $\sqrt{2}\ell^2$ is the cross-sectional area of the RVE center plane.

$$F = \sigma_\infty \sqrt{2}\ell^2 \qquad (4.2)$$

A free body diagram of one strut is shown in Figure 4.4 where F is the total force acting on the RVE, T is the shear force acting on the elastomer, M is the rotational moment about hinge sites, and F_{x1}, F_{x2}, and F_y are unknown reaction forces. F_y and F_{x1} are determined as in equations 4.3 and 4.4, respectively.

$$\Sigma F_y = 0 \qquad F_y = \frac{F}{4} - \frac{T}{2} \qquad (4.3)$$

$$\Sigma M_B = 0 \qquad F_{x1} = \frac{T}{2} - F_y \cot\theta + \frac{2M}{\ell \sin\theta} \qquad (4.4)$$

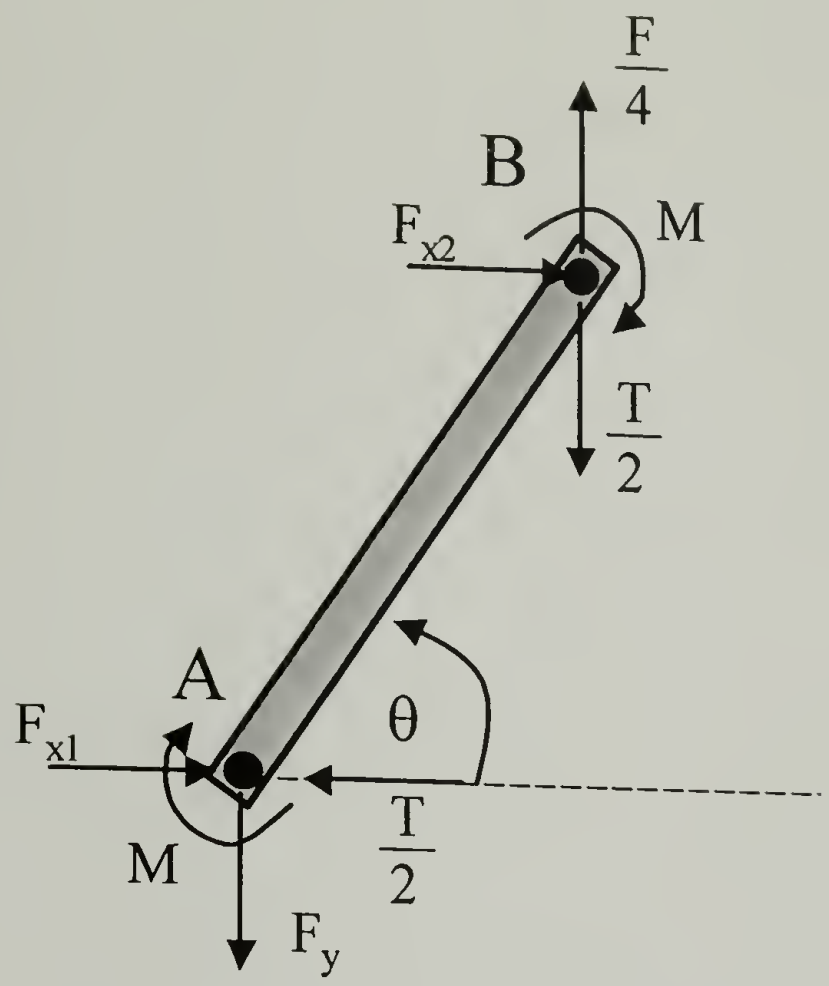

Figure 4.4: Free body diagram of iPP strut

The axial force acting on the strut at point A is given by equation 4.5.

$$F_a = \left(\frac{T}{2} - F_{x1}\right)\cos\theta + F_y \sin\theta \qquad (4.5)$$

By combining equation 4.3, 4.4, and 4.5, the axial force acting on a strut becomes:

$$F_a = \left(\frac{F}{4} - \frac{T}{2}\right)\left(\frac{\cos^2\theta}{\sin\theta} + \sin\theta\right) - \frac{2M}{\ell}\cot\theta \qquad (4.6)$$

The shear force on the elastomer is given by equation 4.7 where G is the shear modulus of the EPDM, $\tan(\theta - \pi/4)$ is the shear strain, and $(1 - C)^{2/3}$ is the area fraction of elastomer.

$$T = (1 - C)^{2/3}\ell^2 G \tan(\theta - \pi/4) \qquad (4.7)$$

An expression for the axial strain in a strut is given by equation 4.8 where E is the tensile modulus of iPP and A is the cross sectional area of a strut.

$$\varepsilon = \frac{F_a}{AE} = \frac{F_a}{t^2 E} \qquad (4.8)$$

By combining equations 4.2, 4.6, and 4.7 and substituting into equation 4.8 an expression for the axial strain in a strut is given by equation 4.9.

$$\varepsilon = \frac{S}{EC}\left\{\left[\frac{\sqrt{2}}{4}\sigma_\infty - \frac{(1-C)^{2/3}}{2} G \tan(\theta - \pi/4)\right]\left[\frac{1}{\sin\theta}\right] \mp \frac{2M}{\ell^3}\cot\theta\right\} \qquad (4.9)$$

The first term in equation 4.9 is due to deformation of iPP struts. The second term is due to shear deformation of the EPDM. The third term of equation 4.9 is due to iPP plastic hinge rotation. The minus sign is used for loading and the plus sign is used for unloading. The rotational moment (M) will have two values: one corresponding to initial deformation that is within and elastic regime (M_e) and one corresponding to high levels of deformation within the plastic regime (M_p). M_e is given by equation 4.10 where σ is the maximum stress in the strut due to elastic bending.

$$M_e = \frac{1}{6}\sigma t^3 \qquad (4.10)$$

A constraint is imposed so that the curvature of the strut remains constant. The strut curvature is given by equation 4.11 where I is the moment of inertia.

$$\frac{1}{\rho} = \frac{M}{EI} = \frac{(\theta - \pi/4)}{\ell} \qquad (4.11)$$

Upon substitution of equation 4.10 into 4.11, the maximum stress in the strut due to elastic bending is determined as equation 4.12.

$$\sigma = \frac{E}{2}\left(\frac{t}{\ell}\right)(\theta - \pi/4) \qquad (4.12)$$

In the plastic regime deformation takes place through the formation of plastic hinges at the strut junction points. The plastic moment (M_p) of a fully plastic hinge is given by equation 4.13 where σ_y is the yield stress of iPP.

$$M_p = \frac{1}{4}\sigma_y t^3 \qquad (4.13)$$

The normalized rotational moment (m) is defined as M/t^3. m_e is found by substituting equation 4.1 into 4.12 and combining with equation 4.10. The elastic and plastic values of m are given by equation 4.14 where the first term corresponds to m_e and the second corresponds to m_p.

$$m = \begin{Bmatrix} \alpha\sqrt{\frac{C}{S}}E(\theta - \pi/4) \\ 1/4\,\sigma_y \end{Bmatrix} \qquad (4.14)$$

In equation 4.14, α is a factor that defines the degree of constraint on the struts and its value determines when plastic hinges form.

Assuming the elastomer to be incompressible, a relationship between θ and ε can be determined. Since there is no deformation in the third dimension, this can be derived by keeping the area constant as in equation 4.15 where A' is the deformed area and A_o is the undeformed area.

$$\frac{A'}{A_o} = \frac{2(\ell + \Delta\ell)^2 \sin\theta\cos\theta}{\ell^2} = 1 \qquad (4.15)$$

Upon rearrangement, the relationship between θ and ε is found as equation 4.16.

$$\theta = 1/2 \sin^{-1}\left(\frac{1}{1+\varepsilon}\right)^2 \qquad (4.16)$$

When equations 4.9, 4.14 and 4.16 are combined and rearranged an expression for the far-field stress can be written as in equation 4.17. The plus portion refers to the loading curve while the minus portion refers to the unloading curve.

$$\sigma_\infty = \sqrt{2}\left\{\frac{2EC\sin\theta}{S}\left(\frac{1}{\sqrt{\sin 2\theta}}-1\right)+(1-C)^{2/3}G\tan(\theta-\pi/4)\pm 4m\left(\frac{C}{S}\right)^{3/2}\cos\theta\right\} \qquad (4.17)$$

The corresponding uniaxial extension ratio (λ) is given by equation 4.18 where δ_o is the original RVE height and δ the deformed RVE height. Upon rearrangement λ is given by equation 4.19.

$$\lambda = \frac{\delta}{\delta_o} = \frac{2(\ell+\Delta\ell)\sin\theta}{\sqrt{2}\ell} \qquad (4.18)$$

$$\lambda = \sqrt{2}(1+\varepsilon)\sin\theta \qquad (4.19)$$

At large deformations the iPP struts undergo plastic yielding. As a result, the deformation response of the RVE will be dependent on the strain history. As such it is necessary to calculate the imposed strain in relation to the maximum previous strain. The new unstrained length of a drawn strut (ℓ'_o) is given by equation 4.20 where ε_f is the maximum previous strain and ℓ_o is its original length.

$$\ell'_o = \ell_o\left(1+\varepsilon_f-\frac{\sigma_y}{E}\right) \qquad (4.20)$$

A relationship between the new length of the drawn strut and its original length is given by equation 4.21.

$$\ell'_o + \Delta\ell' = \ell_o(1+\varepsilon) \qquad (4.21)$$

The elastic strain in a newly drawn strut (ε') is then given by equation 4.22.

$$\frac{\Delta \ell'}{\ell'_o} = \varepsilon' \qquad (4.22)$$

By combining equations 4.20, 4.21, and 4.22, an expression for the elastic strain in a newly drawn strut in terms of the maximum previous strain and strut material properties is given by equation 4.23.

$$\varepsilon' = \frac{\frac{\sigma_y}{E} + \varepsilon - \varepsilon_f}{1 + \varepsilon_f - \frac{\sigma_y}{E}} \qquad (4.23)$$

The resulting stress-strain behavior of the RVE can be calculated using equations 4.9, 4.17, 4.19, and 4.23. This analytical result to describe the steady-state mechanical behavior is in terms of iPP concentration (C), basic constituent properties (E, σ_y, and G), and geometric parameters (θ and α). Two critical conditions result from this type of analysis. The critical angle for plastic hinge formation occurs when $m_e = m_p$ and is given by equation 4.24.

$$\theta_{cp} = \left(\frac{\sigma_y}{4}\right) \frac{1}{\alpha \sqrt{\frac{C}{S} E}} + \frac{\pi}{4} \qquad (4.24)$$

A critical angle also exists for the onset of strut yielding. This is derived by including the yield strain in equation 4.16 and is given by equation 4.25.

$$\theta_{cs} = \pi - \sin^{-1}\left[\frac{1}{1 + \left(\frac{\sigma_y}{E}\right)}\right]^2 \qquad (4.25)$$

Once the critieal angle is reached, the iPP struts begin to plastically yield and draw as they oricnt in the direction of the applicd load. This strut oricntation may eapture geometrical strain hardcning to somc degrcc.

4.3 Experimental Procedures

In order to evaluate the proposcd model in terms of steady-state dcformation the eompositions are examined under eyelic loading. First samples are comprcssion molded into 3 mm thick plaqucs at 210 °C at a prcssure of 3.5 MPa for approximatcly 20 minutes and then water-cooled. Tcnsile specimens are eut to an ASTM D638 type V geometry and tested on a servohydraulic Instron 8511. Specimens are gripped so that only the 7.62 mm gauge length is between the grips. This gripping geometry is used to mcasurc strain morc accuratcly than the traditional tab gripping. All samples experiencc the samc loading condition. A ramp function, followcd by 30 oscillatory sinc waves and 30 triangular waves is imposed on the samples under displacement eontrol. Various static offsets and amplitudcs are examined with the condition that thc material unloads to approximately zero stress during the fourth quarter of each sine and triangle wavc. Sinee the current goal is to deseribe the steady-state behavior after removal of thc Mullins effcct, only the 30^{th} sine and triangle wave are analyzcd. From previous investigations, it is known that these materials reach a steady-state response upon rcmoval of the Mullins effeet which oeeurs after approximately 10 cycles.

The proposed model includes basic properties of the eonstituent matcrials. As such these basic mechanical properties are measurcd. Advanced Elastomcr Systems providcd ncat iPP resin of 0.7 and 20 MFR as well as virgin EPDM samples of various

cure states. The stress-strain behavior of the neat iPP is investigated using an Instron 1123. Samples are first compression molded at 210 °C and 3.5 MPa of pressure for 20 minutes. Samples are then water-cooled in the melt press. Tensile specimens are cut according to ASTM D638 on a Tensile Kut router in a type IV geometry. The shear behavior of crosslinked virgin EPDM samples is examined using an ARES Rheometric Scientific rheometer with a parallel plate geometry. A frequency sweep is performed and shear storage modulus is measured. Monotonic and cyclic tensile tests are conducted using an Instron 1123 and at a crosshead speed of 5 mm/min.

4.4 Model Evaluation

4.4.1 Constituent Properties

The mechanical behavior of virgin crosslinked EPDM rubber is evaluated. Figure 4.5 shows the engineering stress-strain response as a function of crosslinking density. It appears that crosslinking density does not affect the deformation characteristics to any appreciable degree.

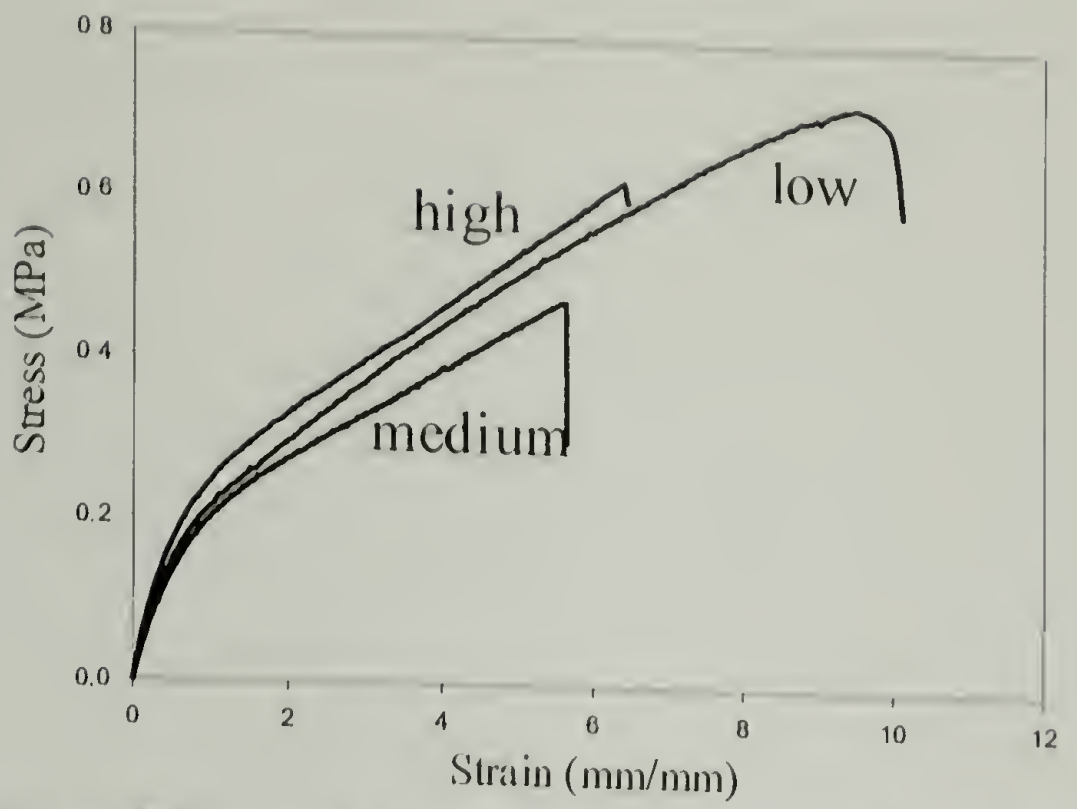

Figure 4.5: Virgin EPDM tensile behavior with low, medium, and high crosslinking densities

The energy loss density and permanent set per cycle are shown in Figures 4.6 and 4.7, respectively, as a function of EPDM cure state. As crosslinking density increases the steady-state energy dissipation and initial permanent deformation decrease. Crosslinking density does not affect the steady-state permanent deformation to any appreciable degree. Once the samples have been conditioned the permanent set is negligible for all three cure states.

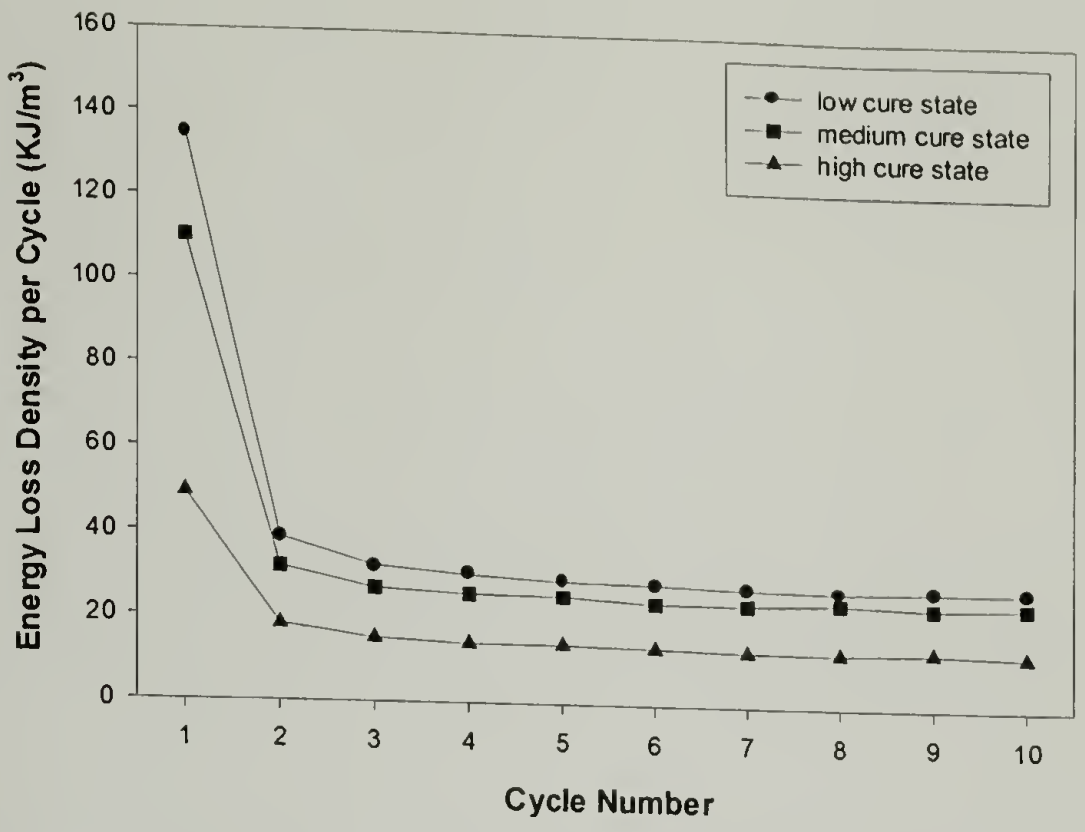

Figure 4.6: Virgin EPDM energy loss as a function of cure state

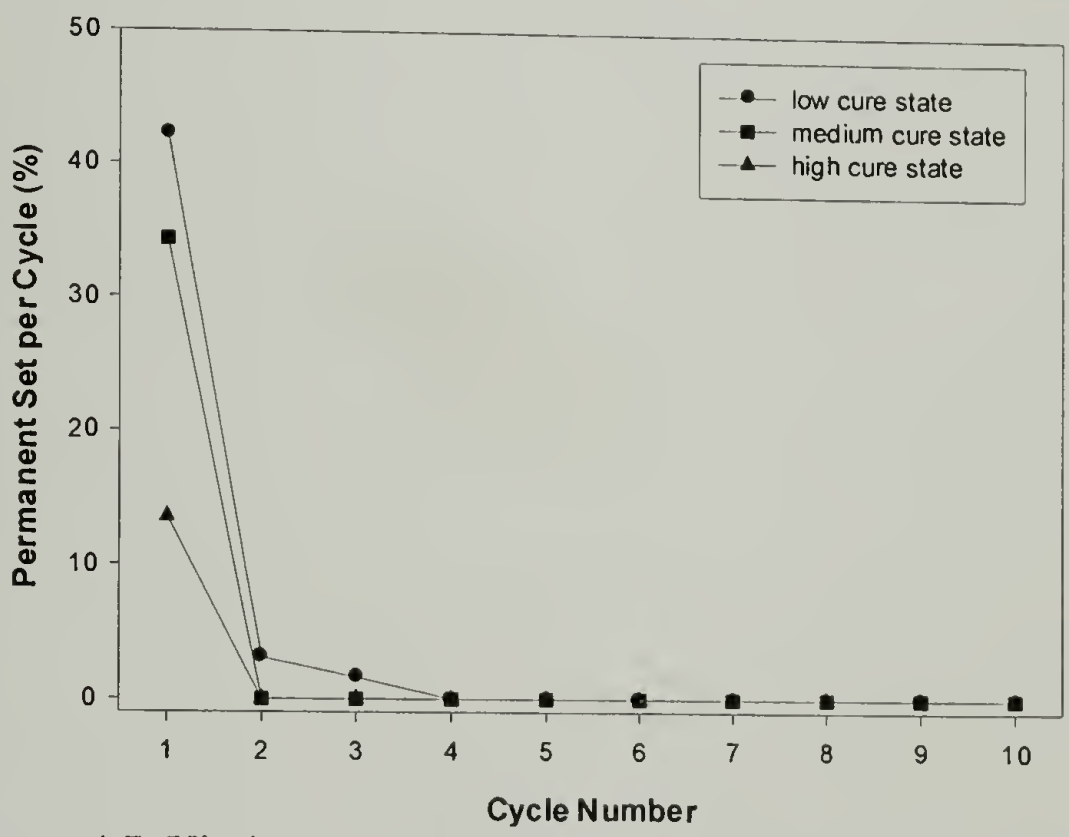

Figure 4.7: Virgin EPDM permanent set as a function of cure state

The shear modulus behavior in Figure 4.7 is similar to that observed under tensile loading; the shear modulus does not obey an explainable trend with increasing crosslinking density. Presumably the shear modulus should be a function of cure state; however, this is not observed for the limited amount of sample provided.

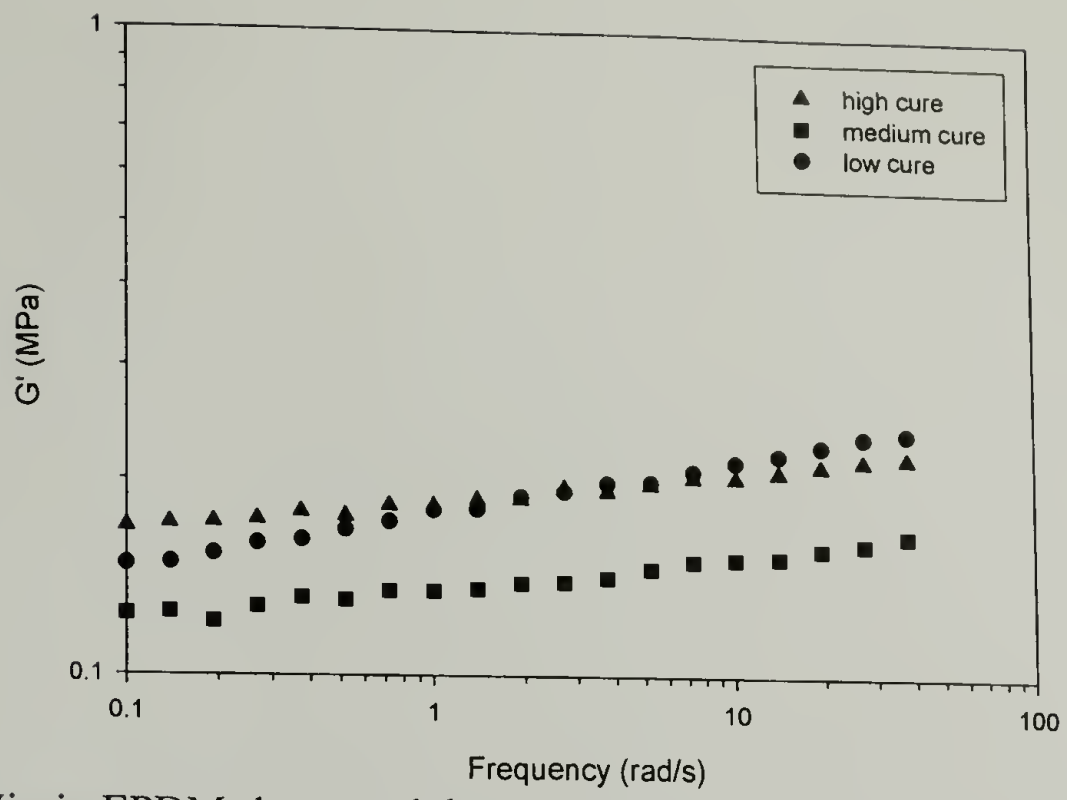

Figure 4.8: Virgin EPDM shear modulus as a function of frequency with low, medium, and high cure states

Table 4.1 lists the material properties of interest for the constituent materials. The stiffness and yield stress of neat iPP are independent of molecular weight within experimental error. The shear moduli of crosslinked virgin EPDM samples all have similar values at 1 Hz. As a result the constituent properties used in the model simulations are as follows: E = 200 MPa, σ_y = 35 MPa, and G = 0.2 MPa and G = 0.25 for medium and high crosslinking densities, respectively. It has been shown that the paraffin oil has an equal affinity for the EPDM and amorphous iPP regions and as such it is ignored when estimating iPP concentration. Since volume fraction cannot be measured due to the presence of the processing oil, concentration values are estimated as C = 0.33 and C = 0.67 for EPDM rich and iPP rich blends, respectively. The factor α determines the amount of constraint on the system and affects when plastic hinges form; in all cases an α value of 100 is used.

Table 4.1: Constituent properties of iPP and EPDM

Constituent	E_p (MPa)	σ_y (MPa)	G' (MPa)*
0.7 MFR iPP	192	36	----
20 MFR iPP	170	36	----
EPDM low cure	----	----	0.21
EPDM med cure	----	----	0.15
EPDM high cure	----	----	0.20

*values at 1 Hz

In order to evaluate the proposed microcellular model in terms of the steady-state deformational characteristics, it is first necessary to understand how the various compositional parameters influence this behavior. Figure 4.9, 4.10, and 4.11 show steady-state hysteresis loops as a function of EPDM cure state, iPP molecular weight, and iPP concentration, respectively. Figure 4.9 shows that as cure state increases, the amount of irreversible work increases slightly as does the strain hardening response. Of the available compositions, EHXL is the only composition with a low cure state. However, EHXL has poor fatigue life and as such a steady-state response cannot be reached prior to failure. iPP molecular weight shows very little affect on the overall steady-state response as seen in Figure 4.10. As such, its influence on steady-state behavior is not incorporated into the proposed model. It is evident from Figure 4.11 that iPP volume fraction is the compositional parameter that influences hysteresis and strain hardening to the greatest degree.

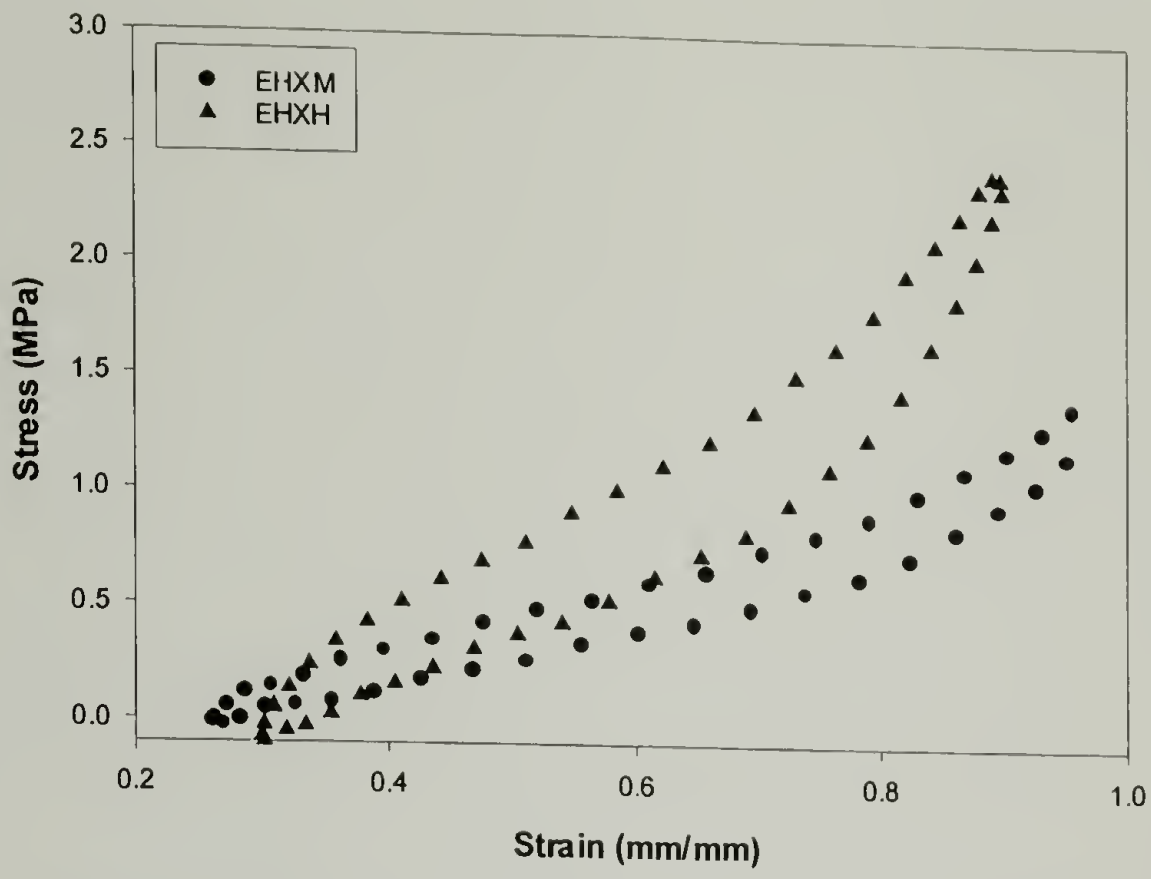

Figure 4.9: Steady-state hysteresis loops for EHXM and EHXH

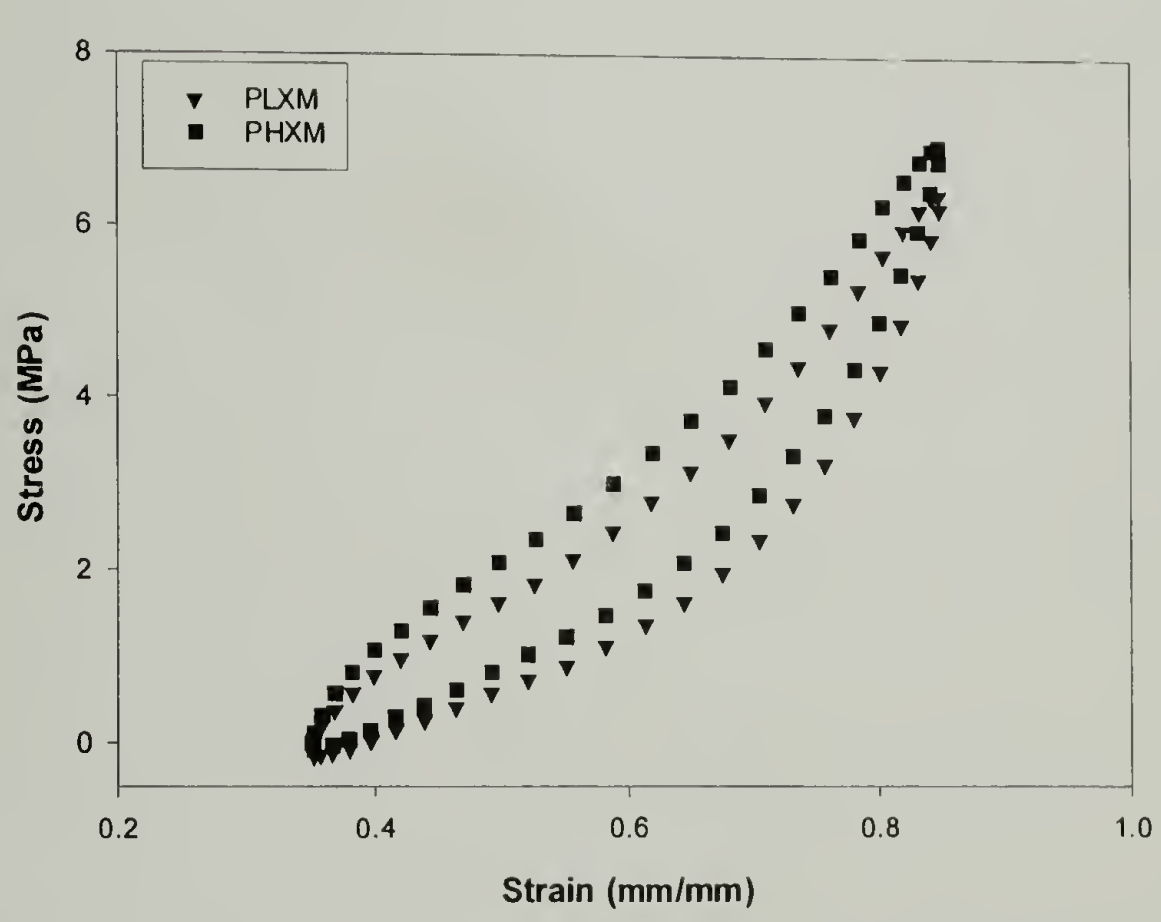

Figure 4.10: Steady-state hysteresis loops for PHXM and PLXM

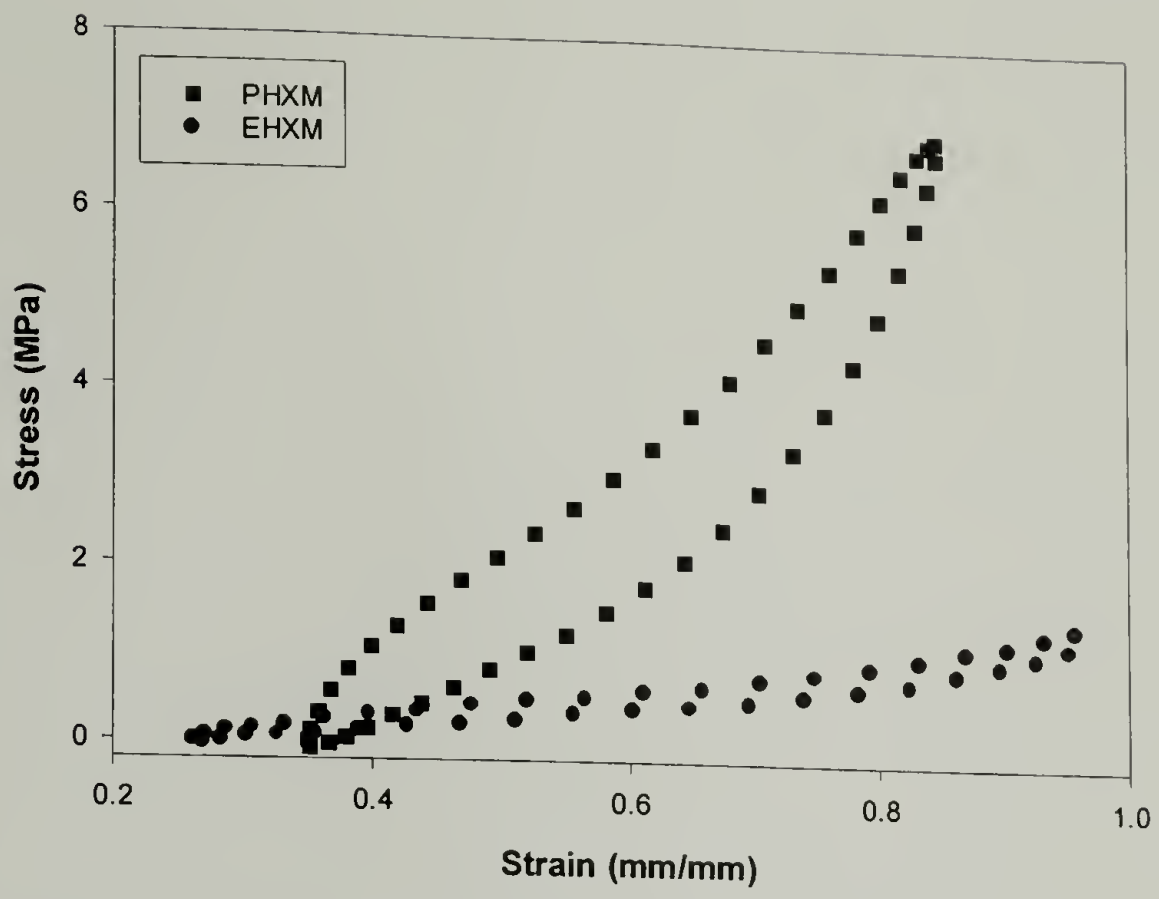

Figure 4.11: Steady-state hysteresis loops for EHXM and PHXM

4.4.2 EPDM Cure State

Four experimental steady-state hysteresis loops for EHXM and EHXH are shown in Figures 4.12 and 4.13 as the open symbols. The solid curves are the predicted stress-strain responses calculated from the microcellular model using S = 14. A strut density of 14 represents a volume element close to a cubic structure, as S would equal 12 for a true cubic structure as drawn in Figure 4.2. Three slopes are observed upon unloading and two upon reloading. The initial negative unloading slope is due to reversal of direction at the plastic hinge sites. During unloading, the iPP struts unload elastically first followed by lateral expansion of the EPDM domains. These modes of deformation are responsible for the two positive slopes that occur upon unloading. The inflection point occurs when the iPP struts are completely unloaded and there is competition between the compressive force on the struts and lateral expansion of the rubber phase.

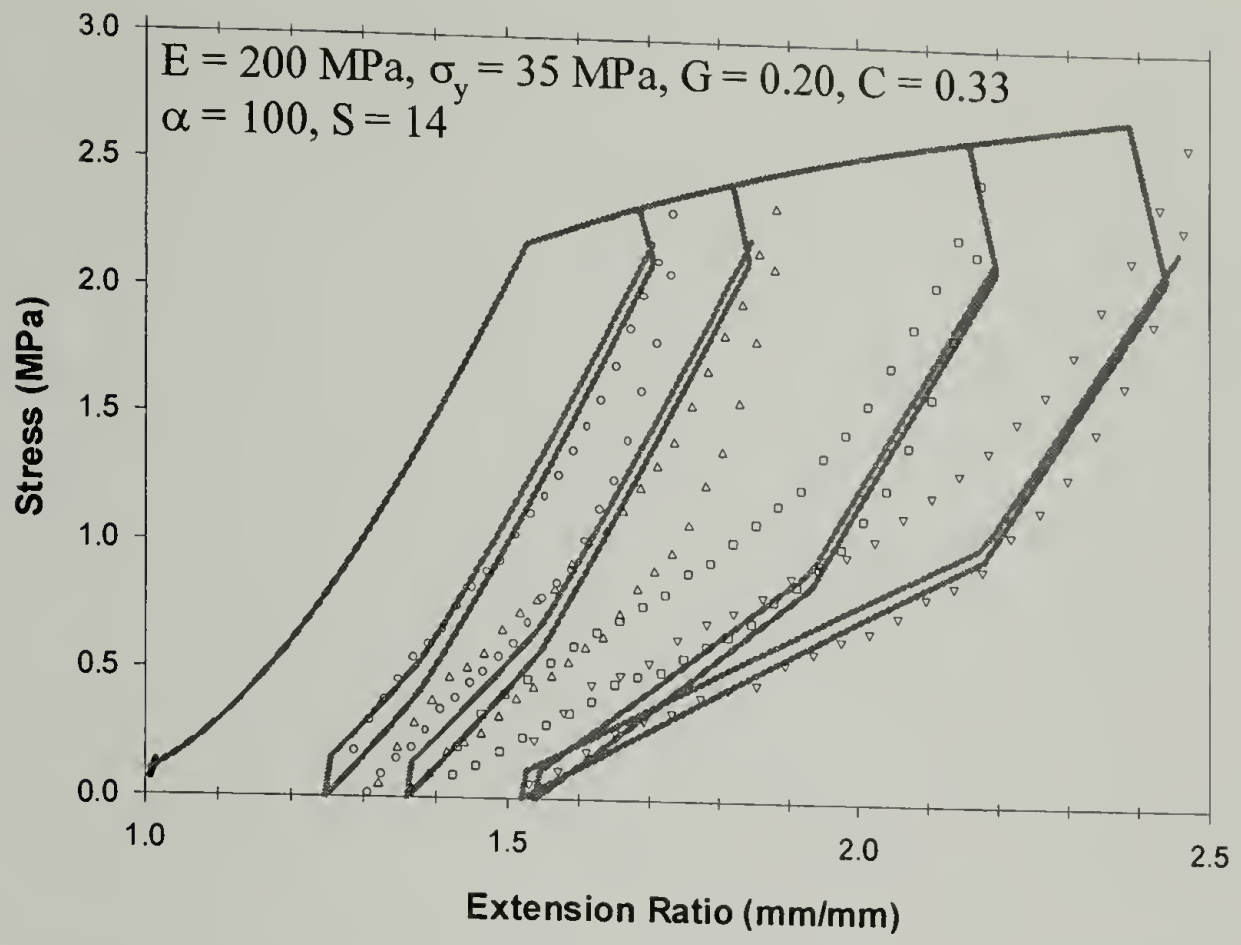

Figure 4.12: Application of microcellular model to steady-state behavior of EHXM

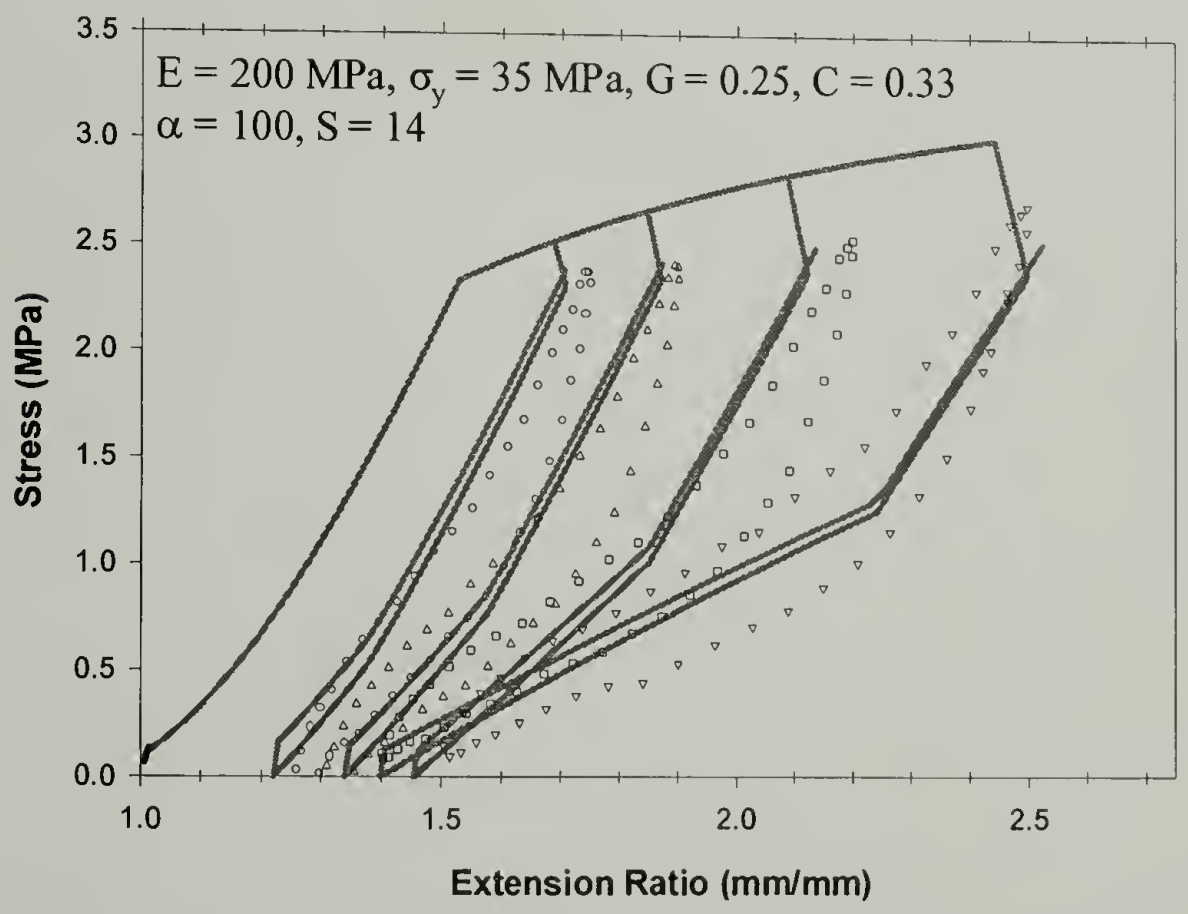

Figure 4.13: Application of microcellular model to steady-state behavior of EHXH

Some general observations can be made regarding the modes of deformation by comparing the experimental stress-strain curves with those calculated from the microcellular model. For the EPDM rich compositions, the microcellular model provides a reasonable estimate of critical stress, permanent deformation, and stiffness at small and large strains. The experimental hysteresis loops exhibit two slopes. These slopes or stiffnesses are approximated reasonably well. The model indicates that the higher stiffness is due to deformation of the iPP struts while the lower stiffness is due to deformation of the rubber domains. However, at all strains the irreversible work or hysteresis is not capture by the proposed model.

4.4.3 iPP Concentration

Figure 4.14 shows experimental hysteresis loops, again as open symbols, along with the deformational response of the microcellular model. All parameters remain the same except for strut density and iPP concentration. Strut density is reduced from 14 to 7 in order to obtain an accurate description of experimental data. A strut density of 7 corresponds to a non-cubic representative volume element. This indicates that the microcellular model cannot be extrapolated to describe the steady-state behavior of iPP rich compositions.

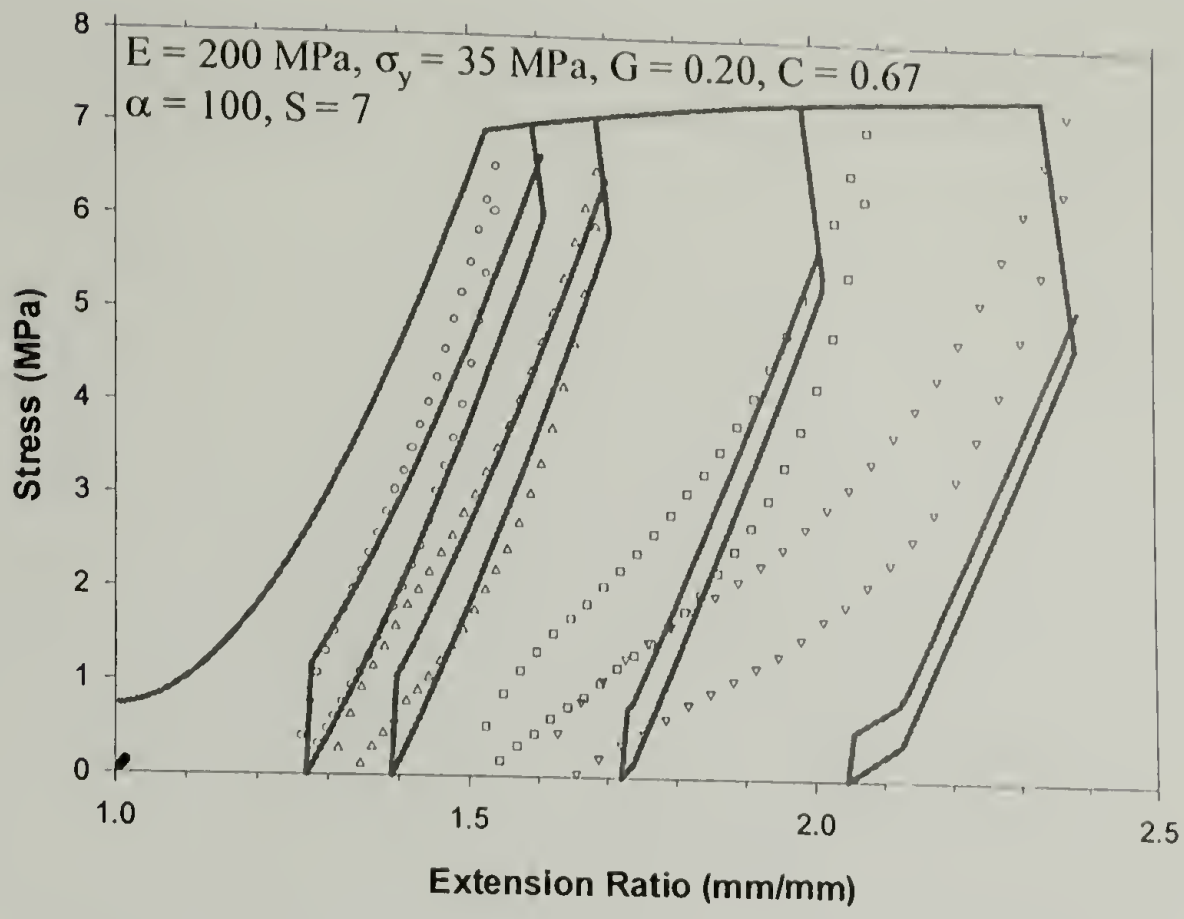

Figure 4.14: Application of microcellular model to steady-state behavior of PHXM

By comparing the responses described by the microcellular model of EHXM (Figure 4.12) with that of PHXM (Figure 4.14) some general observations can be made. The overall strain hardening response is primarily due to the deformation of the rubber domains as EHXM exhibits a much higher degree of overall strain hardening than does PHXM. The stiffness, critical stress, permanent deformation, and irreversible work of PHXM are approximated reasonably well at low strains ($\lambda < 1.7$). However at high strains, the modeled stress-strain response is very different from that observed experimentally. Very little hysteresis and a higher degree of permanent deformation are predicted. It appears that for an iPP rich composition the predicted response at large strain is more highly dominated by iPP strut deformation than that observed experimentally. As such, it can be deduced that not all of the iPP is in the form of deformable struts. In fact there may be a large amount of dead volume or regions of iPP

merely undergoing a rigid body motion instead of inelastic deformation. This is similar to the FEM findings of Boyce and coworkers.[50,51]

4.5 Conclusions

The proposed microcellular model can provide insight regarding the mode of deformation when the deformation is dominated by the rubber phase. However, when the majority of the deformation occurs in the iPP struts, as in PHXM, the predicted stress-strain response becomes very inaccurate at large deformation. In all cases the magnitude of irreversible work is not captured. The objective of developing an analytical model was to be able to predict the steady-state behavior over a range of compositions. However, this is not achieved, as the proposed microcellular model does not capture the response for iPP rich systems upon large deformations. As such this approach does not reveal how composition and morphology influence the deformation characteristics any more than previous finite element studies. It appears that at high levels of iPP concentration, the model predicts too much deformation in the iPP struts and not enough deformation in the EPDM. As such, it is apparent that not all of the iPP deforms in the representative volume element. It is possible that there is a considerable degree of dead volume, or iPP that is simply undergoing rigid body motion, which is similar with the findings of Boyce and coworkers.[50,51]

CHAPTER 5

SUMMARY

The influences of composition and morphology on the physical and mechanical characteristics of two commercial TPE systems are investigated. Both of these systems utilize new architectures and morphologies to produce elastomeric behavior. Heterogeneity at various length scales plays an essential role in determining their mechanical responses. Heterogeneity in the ethylene – propylene copolymers consists of nanoscale crystallites of hexagonal and/or orthorhombic structure embedded within an amorphous rubbery matrix. This crystallinity influences density, stiffness, and mechanical reversibility. Ductility appears to be dictated by entropic effects due to a critical molecular weight between physical crosslinks. Heterogeneity in the dynamically vulcanized EPDM/iPP blends consists of crosslinked EPDM domains embedded within a continuous semicrystalline iPP matrix. As crosslinking density increases the morphology evolves from a very fine structure to a coarser structure with discrete phase separation. Even though mechanical behavior evolves with cure state, the most important parameter in determining the mechanical behavior in terms of stiffness and stress softening is iPP concentration. The iPP rich systems exhibit a pronounced Mullins effect with substantial reversibility under steady-state conditions. An attempt to understand the micromechanisms of deformation responsible for elasticity is made by developing a morphological model. The proposed microcellular model successfully describes stiffness of the EPDM rich blends through shear deformation in the rubber and elastic deformation in iPP struts. However, rotation of plastic hinges does not accurately capture the

dissipation in the blends. The proposed microcellular model cannot be extrapolated to describe the behavior of iPP rich systems. However, the short comings of the model serve to corroborate some earlier finite element findings by Boyce and coworkers.[50,51] These findings indicate that all of the iPP is not deforming; some may simply undergo rigid body motions.

Both TPE systems are also examined in comparison with traditional crosslinked elastomers in terms of the Payne effect. Both systems exhibit a Payne effect response similar with traditional filled crosslinked elastomers despite fundamentally different types and length scales of heterogeneity. The Payne effect responses exhibited by the ethylene – propylene copolymers and EPDM/iPP blends are controlled by the amount of heterogeneity. This behavior is similar to that observed for filled crosslinked elastomers. As crystallinity increases in the copolymer systems the decline in storage modulus increases commensurately. It appears that initial density also plays a role in this behavior. For the EPDM/iPP blends, both domain size and connectivity appear to influence the decline in storage modulus while iPP concentration remains the most influential parameter. Table 5.1 compares the percentage decline in storage modulus of various types of filled crosslinked rubbers with that of PHXM and EP79.8R where the amount of heterogeneity is given in weight percent.

Table 5.1: Payne effect comparison for TPEs and traditional crosslinked elastomers

Rubber	% heterogeneity	Type of heterogeneity	$1-\frac{E'_{\infty}}{E'_{o}}$
SBR*	41	ISAF black	83%
NR*	41	ISAF black	75%
EPDM/iPP	**33**	**EPDM rubber**	**64%**
NR*	31	HAF black	62%
NR*	23	ISAF black	37%
EP copolymer	**14**	**PE crystals**	**30%**
NR*	6	PBNA crystals	50%

*Styrene butadiene rubber and natural rubber data are taken from reference 35.

It appears that the TPE systems studied herein exhibit very similar behavior to filled crosslinked elastomers in terms of the amount of heterogeneity and ensuing drop in storage modulus. This occurs despite fundamentally different types and length scales of heterogeneity. The exact origins of the Payne effect are uncertain and have been debated for several decades.[82] This study suggests that the Payne effect is dictated primarily by the amount of heterogeneity and not necessarily the structure of that heterogeneity. However, structure does play some role which is evident in the behavior of natural rubber (NR) with 6% phenyl-β-naphthylamine (PBNA) crystals. Even with a small amount of PBNA the storage modulus drops by 50%. This is most likely due to the structure of PBNA crystals that form large fern-like structures on the order of 0.2 mm.[35] These fern-like crystals provide a highly connected filler network that appears to influence the sigmoidal behavior to a large degree. The most important result is that the Payne effect is not only observed in filled crosslinked elastomers as previously believed; the TPEs examined herein also exhibit the same type of phenomenological response due to the presence of heterogeneity.

BIBLIOGRAPHY

(1) M-H. Kim, P.J. Phillips, *Journal of Applied Polymer Science* **70**, 1893 (1998).

(2) D. Wilfong, G.W. Knight, *Journal of Polymer Science Polymer Physics* **28**, 861 (1990).

(3) B. Crist, E.S. Claudio, *Macromolecules* **32**, 8945 (1999).

(4) B. Crist, D.N. Williams, *Journal of Macromolecular Science—Physics* **B39**, 1 (2000).

(5) S. Bensason, J. Minick, A. Moet, S. Chum, A. Hiltner, E. Baer, *Journal of Polymer Science Polymer Physics* **34**, 1301 (1996).

(6) J. Wendling, U.W. Suter, *Macromolecules* **31**, 2516 (1998).

(7) M-H. Kim, P.J. Phillips, J.S. Lin, *Journal of Polymer Science Polymer Physics* **38**, 154 (2000).

(8) R.G. Alamo, E.K.M. Chan, L. Mandelkern, *Macromolecules* **25**, 6381 (1992).

(9) S. Vanden Eynde, V. Mathot, M.H.J. Koch, H. Reynaers, *Polymer* **41**, 3437 (2000).

(10) J. Minick, A. Moet, A. Hiltner, E. Baer, S.P. Chum, *Journal of Appl. Polym. Science*, **58**, 1371 (1995).

(11) S. Bensason, J. Minick, A. Moet, S. Chum, A. Hiltner, E. Baer, *Journal of Appl. Polym. Science*, **34,** 1301 (1996).

(12) P.R. Swan, *Journal of Polymer Science* **56**, 409 (1962).

(13) A. Alizadeh, L. Richardson, J. Xu, S. McCartney, H. Marand, *Macromolecules* **32,** 6221 (1999).

(14) S. Rastogi, L. Kurelec, P.J. Lemstra, *Macromolecules* **31**, 5022 (1998).

(15) A. Galeski, Z. Bartczak, A.S. Argon, R.E. Cohen, *Macromolecules* **25**, 5705 (1992).

(16) Z. Bartczak, A. Galeski, A.S. Argon, R.E. Cohen, *Polymer* **37**, 2113 (1996).

(17) J.W. Turley, X-ray Scattering Patterns of Polymers Chemical Physics Research Laboratory: Michigan, 1965.

(18) K. Tashiro, S. Sasaki, M. Kobayashi, *Macromolecules* **29**, 7460 (1996).

(19) L. Kurelec, S. Rastogi, R.J. Meier, P.J. Lemstra, *Macromolecules* **33**, 5593 (2000).

(20) J.D. Barnes, B.M. Fanconi, *Journal of Chemical Physics* **56** (10), 5190 (1972).

(21) K. Kuwabara, F. Horii, *Macromolecules* **32**, 5600 (1999).

(22) R. Androsch, J. Blackwell, S.N. Chvalun, B. Wunderlich, *Macromolecules* **32**, 3735 (1999).

(23) M.D. Ellul, Plastics, Rubber and Composites Processing and Applications **26** (3),137 (1997).

(24) J. Karger-Kocsis, in Polymer Blends and Alloys, G.O. Shonaike and G.P. Simon, Eds., Marcel Dekker, Inc., New York, 1999, ch. 5, p. 125.

(25) A.Y. Coran, in Thermoplastic Elastomers – A Comprehensive Review, N.R. Legge, G. Holden, and H.E. Schroeder, eds., Hanser Publishers, Munich, 1987, ch. 7, p. 133.

(26) A.Y. Coran, *Rubber Chemistry & Technology* **53**, 141 (1980).

(27) J. Karger-Kocsis, A. Kallo, A. Szafner, G. Bodor, *Polymer* **20**, 37 (1979).

(28) V. Choudhary, H.S. Varma, I.K. Varma, *Polymer* **32**, 2534 (1991).

(29) M.D. Ellul, *Rubber Chemistry Technology* **68**, 573 (1995).

(30) M.D. Ellul, *Rubber Chemistry Technology* **71**, 244 (1998).

(31) M.D. Ellul, *Rubber Chemistry Technology* **71**, 1087 (1998).

(32) N.R. Legge, *Rubber Chemistry Technology* **62**, 529 (1989).

(33) J.S. Bergstrom, M.C. Boyce, *Rubber Chemistry & Technology* **72**, 633 (1999).

(34) J.A.C. Harwood, L. Mullins, A.R. Payne, *JIRI* **1**, 17 (1967).

(35) A.R. Payne, R.E. Whittaker, *Rubber Chemistry & Technology* **44**, 440 (1971).

(36) A.R. Payne, R.E. Whittaker, in Interactions Entre Les Elastomeres Et Les Surfaces Solides Avant Une Action Renforcante, Editions du Centre National de la Rechereche Scientifique, Anatole, 1975, p. 233.

(37) L.R.G. Treloar, *Transaction of the Faraday Society* **39**, 241 (1943).

(38) M. Mooney, *Journal of Applied Physics* **11**, 582 (1940).

(39) P.J. Flory, Principles of Polymer Chemistry, Cornell University Press, 1953, ch. 11.

(40) R.W. Ogden, *Proceedings of the Royal Society of London* **A326**, 565 (1972).

(41) R.W. Ogden, *Proceedings of the Royal Society* **A328**, 567 (1972).

(42) S. Vieweg, R. Unger, K. Schroter, E. Donth, *Polymer Networks Blends* **5** (4), 199 (1995).

(43) R.P. Brown, Physical Testing of Rubber, Elsevier Applied Science Publishers, London, 1986.

(44) S. Bensason, E.V. Stepanov, S. Chum, A. Hiltner, and E. Baer, *Macromolecules*, **30**, 2436 (1997).

(45) R.C. Ball, M. Doi, S.F. Edwards, M. Warner, *Polymer*, **22**, 1010 (1981).

(46) S.F. Edwards, Th. Vilgis, *Polymer*, **27**, 483 (1986).

(47) Y. Kikuchi, T. Fukui, T. Okada, T. Inoue, *Journal of Applied Polymer Science* **50**, 261 (1992).

(48) M. Okamoto and K. Shiomi, *Polymer* **35** (21), 4618 (1994).

(49) M.C. Boyce, K. Kear, S. Socrate, and K. Shaw, *Journal of the Mechanics and Physics of Solids*, **49**, 1073 (2001).

(50) M.C. Boyce, S. Socrate, K. Kear, O. Yeh, and K. Shaw, *Journal of the Mechanics and Physics of Solids*, **49**, 1323 (2001).

(51) M.C. Boyce, O. Yeh, S. Socrate, K. Kear, and K. Shaw, *Journal of the Mechanics and Physics of Solids*, **49**, 1343 (2001).

(52) E.M. Arruda, M.C. Boyce, *Journal of the Mechanics and Physics of Solids*, **41** (2), 389 (1993).

(53) E.M. Arruda, M.C. Boyce, *International Journal of Plasticity*, **9**, 697 (1993).

(54) G.M. Brown, J.H. Butler, *Polymer*, **38**, 3937 (1997).

(55) C. Le Fevere de Ten Hove, Thesis: Controlling Solid-State Microstructure of Semi-Crystalline Polymers Through Chemical Design of Chains, Department of Chemistry, Catholic University of Louvain (2001).

(56) W.O. Statton, *Journal of Polymer Science: Part C*, **18**, 33 (1967).

(57) K.H. Illers, H. Hendus, *Kunststoffe*, **57**, 193 (1967).

(58) Polymer Handbook, Third Edition; J. Brandrup, E.H. Immergut, John Willey & Sons: New York, p. V28.

(59) J.T. Grahan, R.G. Alamo, L. Mandelkern, *Journal of Polymer Science: Part B: Polymer Physics*, **35**, 213 (1997).

(60) V. Gaucher-Miri, C. Depecker, R. Seguela, *Journal of Polymer Science: Part B: Polymer Physics*, **35**, 2151 (1997).

(61) W.P. Slichter, in Growth and Perfection of Crystals: R.H. Doremus, B.W. Roberts, D. Turnbull, John Wiley & Sons: New York, p. 558.

(62) R.L. Miller *Polymer*, **1**, 135 (1960).

(63) G. Natta, *Society of Plastics Engineering Journal*, 373 (1959).

(64) D.E. Turek, B.G. Landes, S. Chum, *Conf. Proceedings of ANTEC*, **2**, 2270 (1995).

(65) S.S. Sternstein, C.D. Weaver, J.W. Beale, *Materials Science and Engineering*, **A215**, 9 (1996).

(66) K.J. Wright, A.J. Lesser, *Rubber Chemistry and Technology*, **74**, 677 (2001).

(67)S. Bensason, E.V. Stepanov, S. Chum, A. Hiltner, E. Baer, *Macromolecules*, **30**, 2436 (1997).

(68) A. Chang *Polymeric Materials: Science & Engineering*, **84**, 354 (2001).

(69) O.R. de Ballesteros, F. Auriemma, G. Guerra, P. Corradini, *Macromolecules*, **29**, 7141 (1996).

(70) I.W. Bassi, P. Corradini. G. Fagherazzi, A. Va.vassori, *European Polymer Journal*, **6**, 709 (1970).

(71) G. Guerra, O.R. de Ballesteros, V. Venditto, M. Galimberti, F. Sartori, R. Pucciariello, *Journal of Polymer Science: Part B: Polymer Physics*, **37**, 1095 (1999).

(72) B.E. Read, R.S. Stein, *Macromolecules*, **1**, 116 (1968).

(73) T.A. Huy, T. Luepke, H. Radusch, *Journal of Applied Polymer Science*, **80**, 148 (2001).

(74) C.P. Lafrance, P. Chabot, M. Pigeon, R.E. Prud'homme, M. Pezolet, *Polymer*, **34**, 5029 (1993).

(75) S. Elkoun, R. Seguela, C. Depecker, *Applied Spectroscopy*, **53**, 1398 (1999).

(76) C. Zhang, T. Mori, M. Ishioka, Y. Cheng, *Journal of Polymer Science: Part B: Polymer Physics*, **39**, 1741 (2001).

(77) C. Hongjun, L. Xiaolie, M. Dezhu, W. Jiamin, T. Hongsheng, *Journal of Applied Polymer Science*, **71**, 93 (1999).

(78) L.E. Skaare, P. Klaeboe, C.J. Nielsen, *Vibrational Spectroscopy*, **3**, 23 (1992).

(79) D. Daoust, S. Bebelman, N. Chaupart, R. Legras, J. Devaux, J. Costa, *Journal of Applied Polymer Science*, **75**, 96 (2000).

(80) A.E. Oberth, *Rubber Chemistry & Technology*, **40,** 1337 (1967).

(81) M. Patrick, B.V. Bennett, M.J. Hill, *Polymer*, **37**, 5335 (1996).

(82) L. Chazeau, J.D. Brown, L.C. Yanyo, S.S. Sternstein, *Polymer Composites*, **21**, 202 (2000).

(83) A.R. Payne, in Reinforcement of Elastomers: G. Kraus, Interscience Publishers, New York, 1965, p. 69.

(84) K.A. Aurora, T.J. McCarthy, A.J. Lesser, *Polymer Engineering and Science*, **38**, 2055 (1999).

(85) L.G. Gibson, M.F. Ashby, Cellular Solids: Structure and Properties, Pergamon Press, Oxford, 1988.